5-2016

Low Cost, Carbon-Based Micro- and Nano-Structured Electrodes for High Performance Supercapacitors

Kryssia Pamela Díaz Orellana
Clemson University, kryssiadiaz@gmail.com

LOW COST, CARBON-BASED MICRO- AND NANO-STRUCTURED ELECTRODES FOR HIGH PERFORMANCE SUPERCAPACITORS

A Dissertation
Presented to
the Graduate School of
Clemson University

In Partial Fulfillment
of the Requirements for the Degree
Doctor of Philosophy
Chemical Engineering

---

by
Kryssia Pamela Díaz Orellana
May 2016

Accepted by:
Dr. Mark E. Roberts, Committee Chair
Dr. David A. Bruce
Dr. Stephen H. Foulger
Dr. Christopher L. Kitchens

ABSTRACT

Advances in the development of sustainable, low-cost, and reliable energy storage technologies have become a high priority as the demand for high power, and high energy storage devices has risen with emerging technologies in electronics, transportation, and renewable energy systems. Supercapacitors, due to their relatively high energy density and power density, provide an attractive alternative to bridge the gap between conventional batteries and capacitors. Materials ranging from high surface area, inert carbons to Faradaic metal oxides and conducting polymers have been used to achieve a range of performance properties in supercapacitors. However, the development of new technologies faces many challenges, such as sustainability, charge efficiency, capacity, cycle stability and scalable manufacturing processes.

In this work, to overcome some of these challenges, we developed straightforward, low-cost approaches for the design of micro- and nano-structured electrodes with enhanced electrochemical performance. Two main pathways were taken (1) manipulation of the electrode composition through the incorporation of lignin, as a redox polymer, into the active electrode material, for enhanced energy density, and (2) modification of the electrode structure through changes in the synthesis process of the electrode materials to improve the electrochemical performance.

For the first approach, lignin polymers were incorporated into a conducting polymer during electrochemical polymerization, providing increased Faradaic charge storage from the phenolic lignin groups. Polypyrrole (PPy) electrodes were prepared with alkali lignin (AL) and sulfonated lignin (SLS), and the electrochemical performance was

compared with pure PPy films. We demonstrated an increase in capacitance of 30% in PPy/AL compared to PPy/SLS and 56% to PPy. Subsequently, AL and SLS were combined with porous carbon, which is electrochemically inert and non-reactive with lignin to improve the electrode stability and study the electrochemical performance of lignin without possible chemical/physical interactions with PPy. We found that intermediate pore sizes (>40 nm) led to optimal redox activity as lignin cannot get inside small pores, and large pores do not adsorb significant amounts of polymer.

In the second approach, lignin was used as a precursor to make high surface area carbon fibers, in which the structure of conventional fibers (polyacrylonitrile) was manipulated to produce porous materials. Decreasing the fiber diameter (115 to 8.5 μm) led to an increase in capacitance from ~2 F g^{-1} to ~70 F g^{-1} and a chemical activation process resulted in capacitances of ~192 F g^{-1}. Under the same scope, high surface area resorcinol–formaldehyde carbon aerogels reinforced with a backbone material allowed the fabrication of free-standing electrodes, eliminating the need for a binder and current collector during supercapacitor assembly. Finally, we developed a template-free synthesis method for creating microstructured electrodes to improve ion transport within thick conducting polymer films (~16 μm) while maintaining high energy storage capacity. Electrodes comprising these materials validate low cost, high energy density and innovative ways to manipulate the chemical composition and physical structure of Faradaic and non-Faradaic materials.

DEDICATION

Esta tesis doctoral está dedicada a todas las personas que a través de estos años me han brindado su apoyo y me han alentado a culminar mis estudios de doctorado, especialmente:

- A Dios y a la Virgen de Guadalupe que me han dado las fuerzas necesarias para siempre seguir adelante y cumplir mis metas.
- A mis padres, José Rigoberto y Haydee, quienes han estado a mi lado en todo momento proporcionándome su amor, dedicación, apoyo, ánimo, guía, consejos y oraciones.
- A mi hermana, Yessika María y mis sobrinas, Camina María y Ximena María, por todo su amor, ánimo, oraciones, compañía y cartas.
- A mi tío, Emmanuel de Jesús Orellana, por todo su apoyo, dedicación y amor hacia mí y mi familia.
- A mis amigos por su apoyo incondicional.

"Valor y Confianza"

José Antonio Plancarte y Labastida

This dissertation is dedicated to all the people that through all these years supported and encouraged me to accomplish my doctoral studies.

- God and Lady of Guadalupe that gave me the strength I needed to accomplish my goals.
- My parents, Jose Rigoberto and Haydee, who have always been side by side giving me their love, dedication, support, encouragement, guidance, advice and prayers.
- My sister, Yessika María and my nieces, Camila María and Ximena María, for all of their love, support, prayers, company and letters.
- My uncle, Enmanuel de Jesús Orellana, for all his support, dedication, and love to me and my family.
- My friends for their unconditional support.

"Courage and Trust"

José Antonio Plancarte y Labastida

ACKNOWLEDGEMENTS

Words are not enough to express how deeply grateful I am to my advisor, Professor Mark E. Roberts, for guiding and supporting me to be a better researcher and encouraging me to always give my best in my research projects, presentations and papers. These research projects would not have been possible without his mentorship, guidance and knowledge. He supported me in each of my career goals, and I greatly appreciate his and his family's friendship.

I would like to thank my research group Dr. Jesse Kelly, Dr. Margarita Arcila-Vélez, and Robert Emmett for their advice, assistance, friendship, and support. Also, I appreciate the undergrads who collaborated with me on different projects: Nick Wegner, Andrew Carlin and especially, Samuel Leguizamon for his dedication and commitment in each of the projects on which we worked together. I appreciate the opportunity to collaborate with wonderful people including Dr. Mark Thies, Dr. Julian Vélez, Dr. Amond Ogale and Jing Jin from Clemson University; Andrew Cain and Madison Parks from Southern Research Institute and the special collaboration of Kim Ivey from Material Science and George Wetzel from the Electron Microscopy Laboratory.

I want to thank the members of my dissertation committee, Dr. David Bruce, Dr. Christopher Kitchens and Dr. Stephen Foulger for their commitment and willingness to collaborate on my research and give their time to providing encouragement, valuable suggestions, and feedback.

Finally, I would like to thank the Department of Chemical and Biomolecular Engineering for the opportunity to pursue my Ph.D. at Clemson University, and all the great people that work in there, especially, Joy Rodatz, Terri Mcallister, Diana Stamey and Bill Coburn; they are a fundamental part and make the department feel like home as soon as you step in.

TABLE OF CONTENTS

Page

Table of Contents (Continued)

Page

Table of Contents (Continued)

Page

Table of Contents (Continued)

Page

LIST OF TABLES

LIST OF FIGURES

List of Figures (Continued)

Figure Page

List of Figures (Continued)

Figure Page

List of Figures (Continued)

Figure Page

List of Figures (Continued)

Figure Page

List of Figures (Continued)

Figure Page

List of Figures (Continued)

Figure Page

List of Figures (Continued)

Figure Page

List of Figures (Continued)

Figure Page

List of Figures (Continued)

Figure Page

CHAPTER ONE

INTRODUCTION

The world's electricity demand is projected to increase more than 70% by 2040 according to the World Energy Outlook 2015 released by the International Energy Agency in November. Efforts will be focused on the expansion of renewable energy sources, which will represent about the 25% of the energy produced in U.S. and 50% of the energy generated in the European Union.[1] Just in U.S from 2014 to 2017 the energy produced by solar is expected to increase by 90%, wind in 28%, geothermal in 9%, and hydropower by 5% while waste biomass and wood biomass are expected to decrease.[2] Because, geothermal and hydropower are fixed resources due to limited locations, the current drive is to increase the energy generation capacity of wind and solar, sources that are naturally intermittent. Accordingly, sustainable energy storage also becomes an urgent need.

Currently, batteries and systems that can store electricity come from limited sources, energy-intensive fabrication processes or hazardous materials, mainly relying on the global mineral reserves.[3] This leads us to the fundamental question of whether or not it is better to mine the materials used to store energy generated from renewable resources or simply mine the energy itself (in the form of fossil fuels). The obvious solution is creating energy storage systems from renewable or sustainable materials, to ensure we are indeed minimizing our impact on the environment. In recent years, concepts like sustainability and green chemistry, have found their way to the scientific community and now influence research motivation and pathways. Sustainability is defined by the U.S.

Environmental Protection Agency (EPA) as "*to create and maintain conditions under which humans and nature can exist in productive harmony to support present and future generations.*"[4] While Green chemistry (also known as sustainable chemistry) is defined by EPA as "*the design of chemical products and processes that reduce or eliminate the use or generation of hazardous substances; it applies to the life cycle of a product, including its design, manufacture, use, and ultimate disposal.*"[5]

Both descriptions seek the same purpose: develop materials and processes that offer improvements over existing technology with respect to environmental impact, energy consumption during extraction and synthesis, recyclability, natural abundance, and toxicity to preserve the environment and protect human health.[6, 7] The selection of a greener or lower-cost materials does not necessarily indicate that the final product will be green and/or low-cost as many factors affect the overall impact and cost, such as raw material extraction processes, location, abundance, synthesis methods, device fabrication and recyclability.[6, 8] As a result, most current electrochemical energy storage technologies do not necessarily meet the criteria for either sustainability or green chemistry; therefore, it is imperative to focus research efforts in these directions to support the expected growth of energy consumption by 2040. This review highlights the recent developments in sustainable materials for electrochemical energy storage, including active materials, separators, binders, electrolytes, and current collectors.

1.1 Electrochemical energy storage mechanism

Electrochemical energy storage devices are mainly classified as batteries and capacitors; however, supercapacitors, have steadily been attracting interest due to their higher power capabilities. Batteries provide energy for long time periods (high energy density) but take several hours to recharge (low power density) due to slow reaction kinetics and diffusion processes involved in their energy storage mechanism. They are classified in primary and secondary batteries. Primary batteries undergo irreversible redox reactions and cannot be recharged (i.e. Zinc-MnO_2, Lithium primary, Zinc-Carbon). Secondary batteries undergo in a reversible redox reaction that once is discharged can be restored to its initial state by charging it (i.e. nickel-cadmium, nickel-metal hydride, lithium-ion, lead-acid).[9] Conventional capacitors, on the other hand, deliver energy and recharge in seconds (high power density) but the amount of charge delivered is very small (low energy density).[10] Possessing high power and relatively high energy density, supercapacitors are attractive intermediates between batteries and conventional electrostatic. Due to versatile material design, they can be assembled in various configurations depending on the application; for instance, as flexible devices for wearable electronics or rigid, robust cells for regenerative braking system in electric buses.[11]

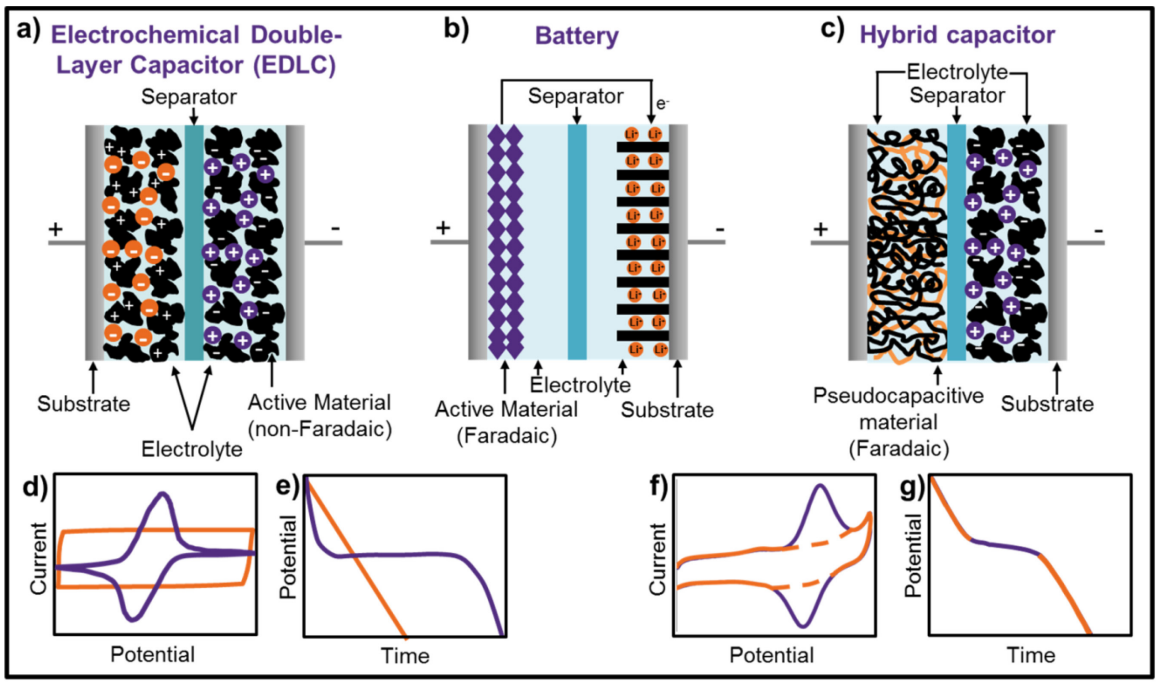

Figure 1.1 Electrochemical energy storage devices in the charged state. (a) Electrochemical Double-Layer Capacitor (EDLC), (b) Li-ion battery, (c) Hybrid capacitor. Cyclic voltammetry profiles for EDLC (orange line) and battery (purple line) (d), hybrid capacitor (f) and discharge profiles (e), (g), respectively.

Supercapacitors and batteries have, roughly, similar configurations comprising of two electrodes (cathode and anode) separated by an electrolyte-soaked separator. The electrodes consist of active charge storage material and, depending on the preparation process, can also have a binder that holds the electrode together and a conductivity enhancer, all of which are coated on a foil current collector. The separator prevents both electrodes from making contact and the electrolyte allows the transport of ions within the cell. Even though both rely on electrochemical processes to store and deliver energy, the electrochemical mechanisms that determine the energy and power density are quite different.

A conventional electrostatic capacitor is a passive device with two electrodes that are separated by a dielectric layer. Static charge is stored by polarizing the electrodes within an electric field, providing a mechanism for delivering very high power density, but low energy density (few microFarads per gram).[12] Electrochemical double layer capacitors (EDLCs) (**Figure 1.1a**) store charge electrostatically by reversible adsorption of ions from the electrolyte onto the active material, which is commonly a high surface area carbon-based material. Ions are adsorbed on the surface of a polarized active material forming a double layer at the electrode-electrolyte interface. The absence of a redox reaction (non-Faradaic process) allows fast charge/discharge cycles, which produce high power density and long cycle life since there is no mechanical stress caused by changes in the volume of the electrode. However, as the energy storage depends on the surface area of the active material, they exhibit limited energy density.[12-15]

The mechanism for energy storage in batteries can vary depending on the electrode chemistry, but each type requires ion diffusion and reaction within the electrode masses. For example, lithium-ion batteries (**Figure 1.1b**), operate by transporting lithium ions (Li^+) from the cathode, which is typically a lithium-intercalated metal oxide, to the anode, which is typically graphite, during charging and then back to the cathode during discharge (energy release). The amount of energy stored (by mass or volume) and the power are function of the voltage between the electrodes and directly dependent on the chemistry selected.[16] They can store a large amount of energy (10-250 Wh kg^{-1} for Li-ion batteries) but are often limited by short cycle life and slow charge/discharge rates (low power density).[10, 12, 17]

Pseudocapacitive electrode materials (**Figure 1.1c**) store charge based on a fast and reversible surface oxidation-reduction reaction (Faradaic process) by electron transfer in addition to the formation of the double layer. Common pseudocapacitive materials are conducting polymers (e.g. polypyrrole, polyaniline, polythiophenes) and metal oxides (e.g. MnO_2, RuO_2). The capacitance of these electrodes is between 10-100 times higher than EDCLs; however, the power density and cycle life are lower because Faradic processes are slower than electrostatic processes and changes in the volume of the electrode upon cycling (swelling and shrinking) tend to cause mechanical stress, degrading the materials.[12, 14, 15, 18, 19] When electrodes of different nature are used as the cathode (e.g. pseudocapacitive material) and the anode (e.g. capacitive material) the supercapacitor is called hybrid capacitor.[20]

The differences between the energy storage mechanisms in batteries and supercapacitors are evident by cyclic voltammetry (CV) and galvanostatic cycling (charge-discharge) profiles. EDLCs are characterized by a rectangular profile, that is, a constant current over the voltage scan range (**Figure 1.1d** orange) and a constant slope (voltage *vs.* time) in the discharge profile (**Figure 1.1e** orange). Batteries are characterized by redox peaks at a specific voltage in the CV profiles (**Figure 1.1d** purple) and a constant voltage plateau discharge profile (**Figure 1.1e** purple).[10] Hybrid capacitors exhibit a combination of battery and EDLC mechanisms, as shown in the CV and discharge profiles (**Figure 1.1f** and **1.1g,** respectively).[21]

The two key parameters to evaluate the performance of electrical energy storage devices are energy density (Wh kg^{-1}) and power density (W kg^{-1}) which are calculated

from the discharge curves in the charge-discharge experiments utilizing **Eqs. 1.1** and **1.2**, respectively, for supercapacitors: [14, 15, 22]

$$E = \frac{1}{2m} CV^2 \quad \text{Eq. 1.1}$$

$$P = \frac{V^2}{4mR} \quad \text{Eq. 1.2}$$

where C represents the capacitance (F), m is the mass of the electrodes (kg), V is the operating voltage that depends on the stability window of the electrolyte (V), and R is the equivalent series resistance (Ω, ESR). ESR is a combination of the electrolyte resistance, contact resistance between current collector and electrode material, intrinsic resistance of the electrode material, and diffusion resistance of ions.[22] The relationship between energy and power density for various devices is typically presented as a Ragone plot (**Figure 1.2a**). To improve the performance of current supercapacitors, three different approaches can be taken or combined: (1) increase the cell's operation voltage range, which is directly related to the stability of the electrolyte, (2) increase the capacitance of the active material (C), and (3) reduce the equivalent series resistance (R).

In the case of batteries, the discharge voltage is constant as described by Ohm's law; therefore, **Eqs. 1.3** and **1.4** are used for the Ragone plot (**Figure 1.2b**):

$$P = \frac{I \, x \, V}{m} \quad \text{Eq. 1.3}$$

$$E = P \, x \, t \quad \text{Eq. 1.4}$$

where I is the discharge current (A), V is the cell voltage (V), t is the discharge time (h), and m is the mass of the electrodes (kg). The energy density and power can be improved by (1) developing electrode chemistry to increase the voltage difference between the two

electrodes, (2) avoiding electrolyte consumption during the reaction process, and (3) optimizing the mass or volume of the active materials.[16]

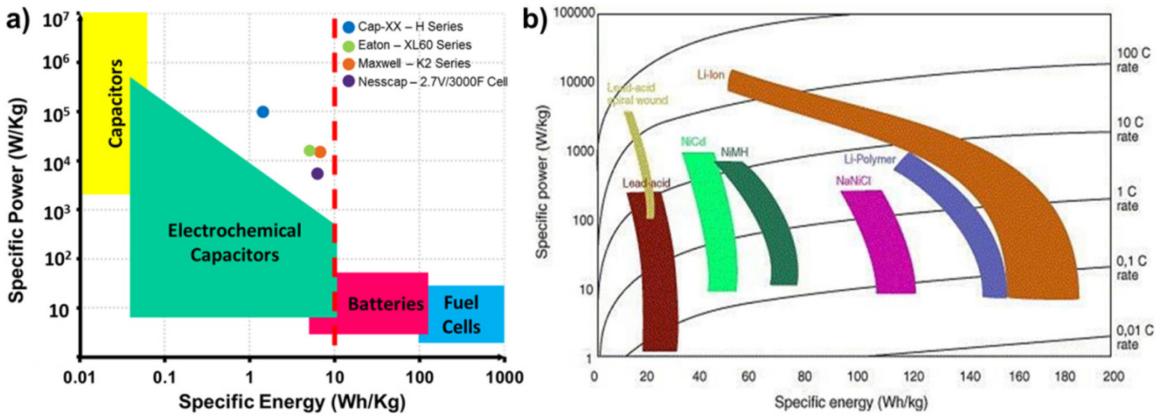

Figure 1.2 Ragone plot: specific power (W kg^{-1}) *vs.* specific energy (Wh kg^{-1}) for electrical energy storage devices, highlighting current commercial supercapacitors (a) and current battery technologies (b) (Figure 1.2b reprinted from ref. [23], Copyright 2006, with permission from Elsevier).

The global market of supercapacitors is expected to grow over the next five years (2015-2020) at a compound annual grow rate of 19.1% to reach $4.8 billion in 2020 from $1.8 billion market in 2014 according to current market research reports.[24] EDLCs are the most widely commercialize supercapacitors. Commonly, the technology consist of high surface area carbon electrodes in an organic electrolyte (i.e. acetonitrile or propylene carbonate). The major players in the market of commercial supercapacitor technologies are companies such as Maxwell Technologies (USA),[25] Cap-XX (Australia),[26] Eaton PowerStor (USA),[27] Nesscap (South Korea),[28] AVX (USA), and Panasonic (Japan). The performance metrics of the current technologies are depicted in **Figure 1.2a** which shows

cycle life between 0.5 to 1 million cycles. Currently, these technologies are limited in energy density to less than 10 Wh kg^{-1} (**Figure 1.2a**), and the primary challenge is to overcome this limit using sustainable materials and processes.[22]

On the other hand, the global market for batteries produces $80 billion in annual revenue and is expected to grow at a rate of ~8% per year to $120 billion in 2019.[29, 30] Secondary batteries will grow more than primary batteries, and Li-ion batteries will present the fastest grow rate due to increased use of consumer electronics. The major companies in this market are Procter & Gamble (USA), Energizer (USA), Spectrum Brands (USA), Foxlink (Taiwan), GP Batteries (Singapore), GS Yuasa Corporation (Japan) and Saft Groupe (France).[29, 30] **Figure 2b** shows the performance of the most common battery technologies.

1.2 Materials for electrochemical energy storage devices

In this section, we will discuss the different types of sustainable materials available for each of the components in supercapacitors and batteries *i.e.* active materials, binders, conductivity enhancers, current collectors, and electrolytes.

1.2.1 Active materials for electrodes

The active material is one of the main components of supercapacitors and batteries. It stores charge based on a Faradaic or non-Faradaic processes. The most common materials used for this purpose are carbon materials (**Figure 1.3a** and **1.3b**), metal oxides (**Figure 1.3c**), lithium-intercalation metal oxides (**Figure 1.3d**), conducting polymers

(**Figure 1.3e** to **1.3g**) and composites thereof. The options for composite materials in energy storage are vast; therefore, we will limit the scope to biomass-based redox molecules or polymers as the organic components.

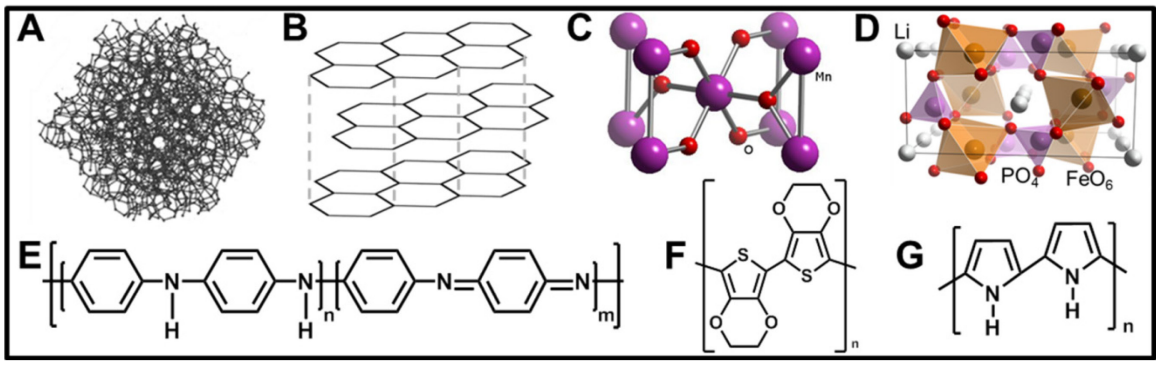

Figure 1.3 Electrode active materials. (a) Amorphous carbon, (b) Graphite, (c) Manganese oxide,[31] (d) Lithium iron phosphate,[32] (e) Polyaniline, (f) Poly(3,4-ethynlenedioxythiophene), (g) Polypyrrole. (a) Reprinted from ref. [33] with permission of Nature Publishing Group.

Lithium-based batteries

Secondary Li-ion batteries store charge base on reversible insertion and extraction of Li^+ from one electrode to the other during charge and discharge.[16] One of the highlights compared with traditional battery chemistries (i.e. lead-acid, nickel-cadmium, nickel metal hydride) is the versatility; a wide variety of chemistries can be developed which opens the possibility for sustainable materials.[6, 34] For instance, lithium iron phosphate ($LiFePO_4$) (**Figure 1.3d**) is safer and cheaper than $LiCoO_2$, which is widely used in commercial Li-ion batteries due to its high energy density, while $LiFePO_4$ is the most attractive material for large scale applications due to its safety and cost.[6] However,

truly suitable and green materials are organic electrodes derived from oxocarbons ($Li_2C_6O_6$)[35] or carboxylates ($Li_2C_8H_4O_4$) which are synthesized from renewable sources or recyclable metal oxides.[6, 9, 36]

Li-air batteries are another option for primary batteries which offer good gravimetric energy density but lower volumetric energy density compared with Li-ion because they need pure oxygen without CO_2 and moisture. Recent efforts are focusing on developing rechargeable Li-air batteries by encapsulating Li_2O formed during the discharge process into a conductive substrate.[36, 37] More sustainable alternatives to Li^+ are Na^+, Mg^{2+}, Ca^{2+} from which Na^+ represents the best alternative due to its natural abundance, price, and low environmental impact. Sodium is heavier than lithium which reduces the potential volumetric and gravimetric capacity; however, it is worthwhile to pursue Na chemistries as a reliable substitute for Li.[6]

Carbons

Carbon materials store energy base on the electrostatic accumulation of ions on the surface upon the application of a voltage difference (EDLCs) or by ion insertion (Li-ion batteries).[38] They are is widely used in commercial EDLCs and batteries due to high electrical conductivity, low cost, easy synthesis process, versatility, temperature stability, widely abundant and environmentally friendly precursors.[15, 18, 22, 38] The versatility of carbon leads to the formation of different types of materials that are tailored to fit specific applications.

In commercial EDLCs, activated carbon is the most commonly used material (**Figure 1.3a**), which can be derived from biomass, such as wood, lignin, seaweeds, waste coffee beans, paper, and coconut shells, among others.[22, 39-42] The capacitance is highly dependent on the specific surface area, pore size distribution, pore structure, surface wettability, and electrical conductivity,[22, 38] and it increases proportionally to the specific surface area for values up to 1500 $m^2 g^{-1}$. At higher surface areas, the capacitance tends to plateau because the average pore size increases with the specific surface area.[43] Thus, the interactions of ions with the walls of the pores are weaker as the pore size increases.[38] To obtain an optimal capacitance and high-power rates, a balance between micro-, meso- and macro-pores within the porous carbon structure is needed.[22] In commercial Li-ion batteries, graphite is widely used as anode material because it stores Li-ions in the interstitial sites between two graphite planes showing moderate capacity (373 mA h g^{-1}). Moreover, it presents low expansion upon charge-discharge, long cycle life and is cheap.[44]

Other types of carbon materials are also suitable for electrodes. Carbon gels have a significant presence of mesopores and can be synthesized from renewable materials like lignin,[45, 46] polysaccharides, tannin, bacterial cellulose[46] (**Figure 1.4a** and **1.4b**), among others.[47] Carbon nanotubes (CNTs) have good electrical conductivity, pore structure, mechanical, chemical and thermal stability.[22] They can be derived from leaves, grasses, and natural oils;[42] however, the life-cycle assessment (LCA) of the current technologies and products show that improvements are still needed with respect to their synthesis process, which is energy intensive, low yield, requires high purity of precursors, and

information about their toxicity and disposal is lacking.[48] Templated carbons, which are fabricated via hard- or soft-template methods to produce a well-ordered nanostructures (**Figure 1.4c** and **1.4d**);[22, 40, 49] activated and nanostructured carbon fibers,[50, 51] activated carbon cloths,[52-54] and reduce graphene oxide / cellulose paper electrodes[53] can also be derived from biomass precursors.[38] Efforts to reduce the environmental impact of biomass-based carbon material synthesis processes have focused on lower energy-intensive technologies, such as low-temperature nonequilibrium plasma for the production of carbon nanostructures[42] and low-temperature hydrothermal synthesis to produce carbon materials ranging from hydrogels and carbon nanofibers (**Figure 1.4e** and **1.4f**).[40, 55, 56]

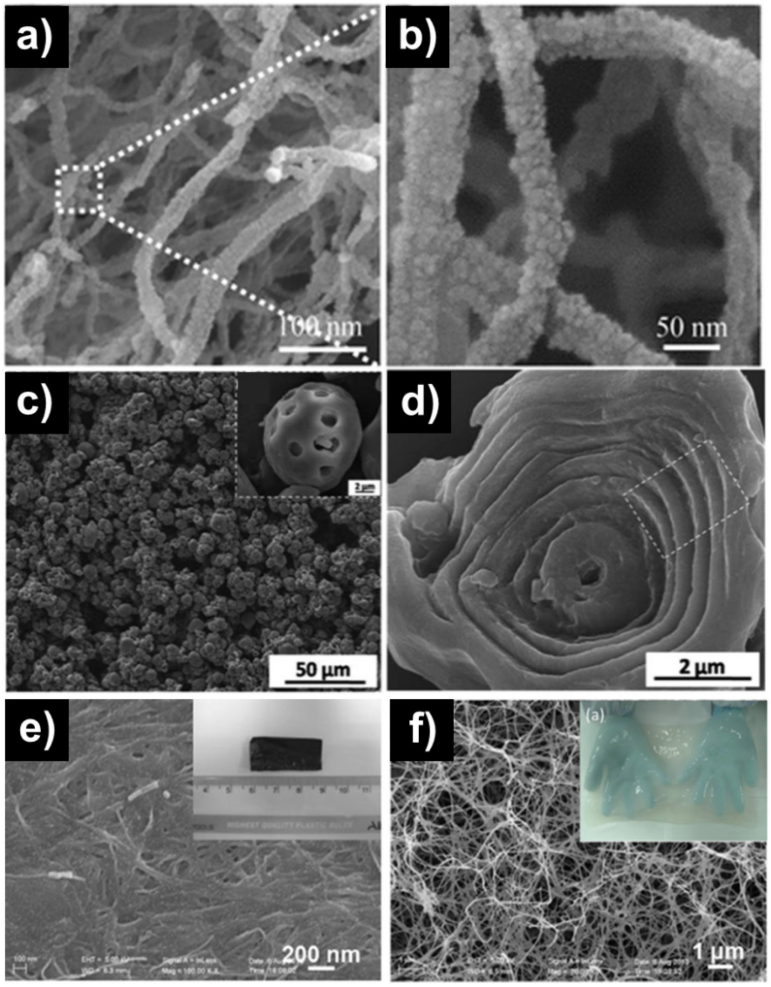

Figure 1.4 (a) Bacterial cellulose / Lignin / Resorcinol / Formaldehyde carbon aerogel and (b) high magnification. (c) Hierarchical porous carbon microspheres (Inset: high magnification) and (d) internal ladder-like structure. (e) Bacterial cellulose (BC) carbon nanofibers (CNFs) (Inset: sample photograph) and (f) SEM image of the internal structure of the BC-CNFs (Inset: Photograph of a BC pellicle). (a) and (b) Reprinted from ref. [46], Copyright 2015, Wiley-VCH Verlag GmbH & Co. KGaA. (c) and (d) Reproduced from ref.[49], with permission of The Royal Society of Chemistry. (e) and (f) Reprinted from ref.[56], Copyright 2015, Wiley-VCH Verlag GmbH & Co. KGaA.

Conducting polymers

Electrically conducting polymers (ECPs) are conjugated molecules with delocalized π electrons along the polymer backbone resulting from adjacent sp^2 hybrid orbitals. These polymers can be partially oxidized or reduced, and stabilized with the respective counter ion, to store charge via a pseudocapacitive mechanism.[19, 22, 57] Advantages over alternative materials include simple synthesis processes, wide conductivity range, light weight, low cost, flexibility, nanostructure tailorability, and process scalability. As supercapacitor electrodes, ECPs typically exhibit higher energy densities than EDLCs due to the fast redox reaction.[7, 57] Still, some of the main drawbacks are poor stability upon cycling due to the swelling and shrinking of the polymer film upon charge and discharge, low coulombic stability and self-discharge.[22, 57]

The most well-studied ECPs are polyaniline (PANI) (**Figure 1.3e**), polythiophenes, especially poly(3,4-ethynlenedioxythiophene) (PEDOT) (**Figure 1.3**f), and polypyrrole (PPy) (**Figure 1.3g**) which have demonstrated good performance as pseudocapacitor materials. They have interesting applications in the organic photovoltaics as a low-cost alternative to solid-state solar cells; hydrogel electrodes for Li-ion batteries and capacitors;[58] water remediation[59] and applications as biodegradable biosensors and tissue engineering due to their biocompatibility with biological molecules.[60, 61]

In supercapacitors, ECPs wide versatility allows the synthesis of various electrodes configurations. ECPs can be synthesized with a particular micro or nanostructure to increase surface area and capacitance utilizing hard-templates,[62, 63] soft-

templates[62, 64] or free-template[65, 66] methods (**Figure 1.5a**); or also combined with redox molecules to increase the energy density [67, 68] (**Figure 1.5b**). Additionally, several composite materials with metals oxides[69, 70] (**Figure 1.5c**) and/or carbon materials[71, 72] (**Figure 1.5d**) have recently been developed. However, ECPs are derived from petroleum resources and information is lacking regarding their environmental impact. Nonetheless, most reports agree that their low cost, scalability, and easy processability are sufficient evidence for classification as "sustainable."

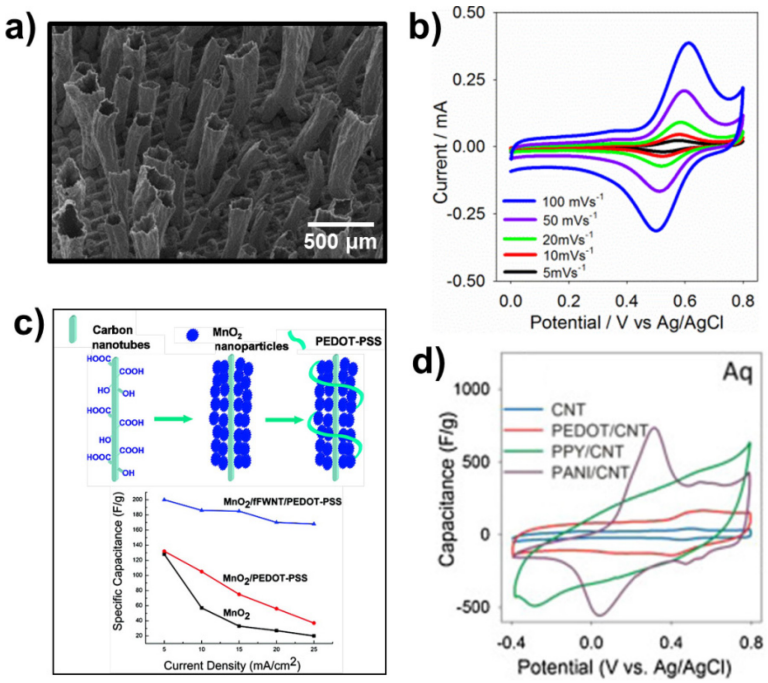

Figure 1.5 (a) Free-template synthesis of polypyrrole microtubes on stainless steel mesh.[65] (b) Cyclic voltammetry profile of Polypyrrole-Alkali lignin electrode.[61] (c) Carbon nanotube/MnO_2/PEDOT:PSS composite electrodes (Adapted with permission from Ref. [70]. Copyright 2010 American Chemical Society) (d) Cyclic voltammetry profile normalized to specific capacitance of carbon nanotube composite electrodes with PEDOT, PPy, and PANI (Reprinted from ref.[71], Copyright 2016, with permission from Elsevier).

Metal oxides

Metal oxides are pseudocapacitor materials that store charge based on a fast, reversible electron transfer reaction along with electro-adsorption of protons onto the surface, changing between the different oxidation states.[13, 18] The most widely studied metal oxides in literature are manganese (IV) oxide (MnO_2) and ruthenium (IV) oxide (RuO_2), which have been commercialized by Nesscap[73] and Evans Capacitor Company,[74] respectively. Due to the high cost of RuO_2 (43.5 \$ g^{-1}), MnO_2 (8.68 \$ g^{-1})[75] results more appealing for energy storage applications. However, these materials are often scarce and extracted through energy-intensive mining processes from the earth, suggesting it is unlikely the can meet sustainability requirements.

Redox molecules for composite electrodes

Redox molecules or polymers have moieties in their chemical structure that can be reversibly oxidized and reduced upon the application of an electric field.[76] However, they required the presence of a conducting network (e.g. carbon, conducting polymers) to facilitate the electron transfer in applications requiring more than an extremely thin film, e.g. supercapacitor or battery electrodes. Conjugated carbonyl compounds are well-known to have good redox activity. For example, quinone (Q) derivatives such as benzoquinone (BQ)[77, 78] and anthraquinone (AQ)[79, 80] have been studied in applications for supercapacitors due to their high theoretical capacity (496 mAh g^{-1} for 1,4 benzoquinone[68] and 257 mAh g^{-1} for anthraquinone[7]), fast reaction kinetics, structural diversity.[7] However, over time, these molecules will diffuse out of the electrode[77]

resulting in a decreased capacitance, which suggests that redox polymers will be necessary to achieve the same increases in capacitance while remaining trapped within an entangled polymer network.

Lignin is a renewable polymer obtained as a by-product of the pulping process of wood to produce paper.[81] Aside from its heat content, it possesses very little value. Recently, it has become attractive for applications in supercapacitors and batteries due to the presence of quinone type moieties within the polymer structure that can undergo redox processes at a given electrochemical potential. Within a properly designed electrode, lignin may provide a sustainable and greener option compared to synthetic organic molecules and metal oxides (**Figure 1.6a**). Different types of lignin have been incorporated into conducting polymer networks (**Figure 1.6b**) to increase capacitance over the pure conducting polymer electrode.[67, 68, 82-86] For instance, polypyrrole / alkali lignin electrodes prepared in 15.3M Acetic Acid showed a capacitance of ~400 F g^{-1} and a charge capacity of 80 mAh g^{-1} at 0.14 mA cm^{-2} while polypyrrole / sulfonated lignin electrodes showed a capacitance of ~300 F g^{-1} and charge capacity of 60 mAh g^{-1} at 0.14 mA cm^{-2}.[67] Moreover, composites with CNTs[87] or different types of porous carbons have been prepared to improve the energy density.[85] Milczarek and Nowicki[87] prepared CNTs surface-functionalized with Kraft lignin which exhibited a specific capacitance of 143 F g^{-1} compared with 75 F g^{-1} for the unmodified CNTs (**Figure 1.6c**).

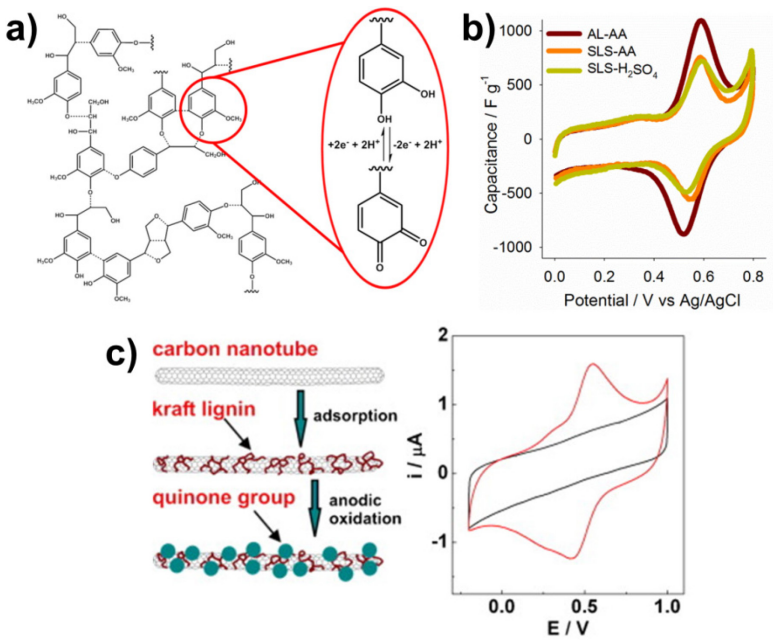

Figure 1.6 (a) Illustrative schematic of lignin structure along with the redox processes that occurs when phenolic and methoxy phenolic functional groups are converted into reversible quinone/hydroquinone redox couple. (b) Cyclic voltammetry profiles normalized to specific capacitance (10 mV s^{-1}) for alkali lignin/polypyrrole and sulfonated lignin/polypyrrole electrodes prepared in acetic acid (AL-AA, SLS-AA, respectively) and sulfonated lignin/polypyrrole electrodes in sulfuric acid (SLS-H_2SO_4).[67] (c) MWCNTs surface-functionalized with kraft lignin scheme and cyclic voltammetry profiles of unmodified (black line) and functionalized (red line) MWCNTs at 50 mV s^{-1} (Reprinted from ref.[87], Copyright 2013, with permission from Elsevier)

1.2.2 Binders

The binder holds together the active material, conductivity enhancer and provides adhesion to the current collector to maintain the structural integrity of the electrode.[88] Ideally, the binder would be a good ion and/or charge conductor, otherwise, their use can increase the internal resistance of the electrode.[89] Binders are often classified based on their interactions with the active material. Dot-to-surface binders, such as

polytetrafluoroethylene (PTFE) and styrene butadiene rubber (SBR), stick to the surface of the materials by point connection and have a weak adherence (**Figure 1.7a**).[88] Segment-to-surface binders have moderate adherence binders due to polymer chain segments that stick to the surface of the materials. Examples include polyvinylidene fluoride (PVDF), polyvinyl alcohol (PVA), polyacrylic acid (PAA), carboxymethyl cellulose (CMC), among others (**Figure 1.7b**).[88] Network-to-surface binders, such as PVA and polyvinyl acetate (PVAc) block copolymer crosslinked with sodium tetraborate ($Na_2B_4O_7$), provide strong adherence by forming a 3D-network via thermal or chemical crosslinking of the polymer (**Figure 1.6c**). [11, 88]

Fluoride-derived binders (e.g. PTFE or PVDF) are the most common binders utilized in electrode formulations and require the use of organic solvents (e.g. N-Methyl-2-pyrrolidone) to be dissolved into the slurry.[6] Because of these reasons, and that volatile fluorocarbons that are formed during incineration at the end of the device life, fluoride-derived binders do not meet sustainability criteria.[11] Ideally, aqueous soluble binders will provide a more environmentally friendly option.[88] Current research has focused on CMC, which is produced by incorporating carboxymethyl groups in natural cellulose to make it water soluble since it is non-toxic, nevertheless, the final electrode lacks elasticity (**Figure 6e**).[90] Sodium alginate (**Figure 6d**) is a polysaccharide derived from brown seaweed, which has shown to have a good affinity for activated carbon while also reducing the internal resistance compared with CMC and PVDF.[91] SBR is another common binder utilized in Li-ion batteries and supercapacitors due to its low viscosity and is usually combined with CMC to improve the wetting of the slurry on the current

collector (**Figure 6f**).[92] PVA has shown better binder properties than PVDF and PAA (**Figure 6g**)[93] and is known to form flexible free-standing electrodes when using a 95% hydrolyzed PVA solution.[11] Other examples of sustainable biomass-derived binders that can be used in Li-ion batteries include Xanthan Gum, which is a polysaccharide used as food additive,[89] β-cyclodextrin and gelatin.[88]

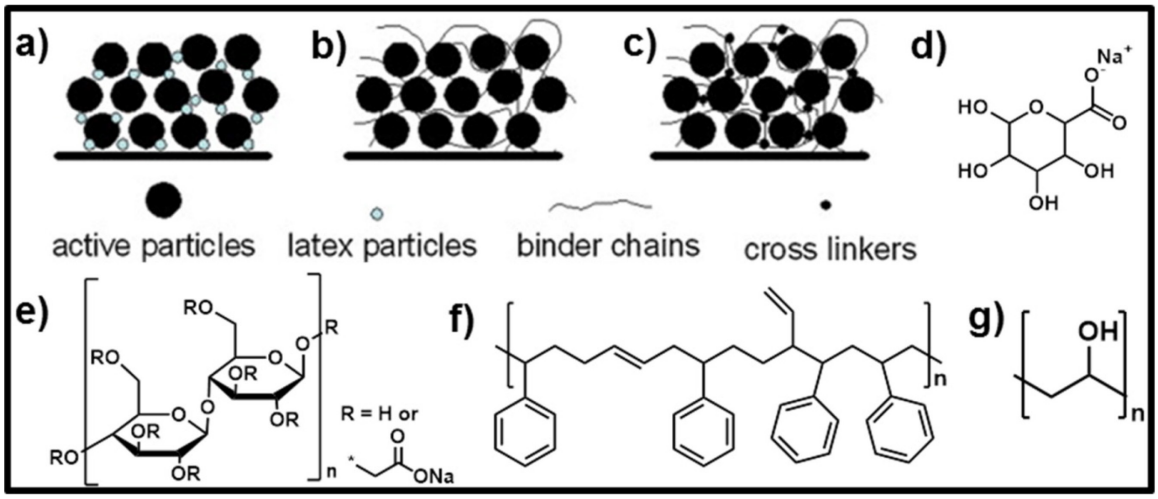

Figure 1.7 Types of binders (a) dot to surface, (b) segment to surface, (c) network to surface. Reprinted from ref. [88], Copyright 2015, with permission from Elsevier. Common binders chemical structure (e) CMC, (d) sodium alginate, (f) SBR, (g) PVA.

1.2.3 Conductivity enhancers

Conductivity enhancers are often added to the preparation of the slurries used to make electrodes (Active material + binder + conductivity enhancer + solvent) in low quantities (5-10wt.%) for the purpose of enhancing the conductivity cast electrode film. The conductivity can be increased by improving the contact between the active material particles and between the particles and the current collector. Usually, graphite or

acetylene black, which can be derived from biomass, are used as the conductivity enhancer. As previously discussed, improvements in material synthesis and processing are needed to reduce the energy consumption to create the material.

1.2.4 Current collectors

The current collector is often a metal foil that supports and connects the active material with the external circuit to shuttle electrons into and out of the active energy storage electrodes. Therefore, they should have excellent electrochemical and chemical stability, inert toward the electrolyte, low cost, wide availability and simple manufacturability.[22] Good contact between the current collector and electrode material is crucial to keep the internal resistance of the device low, as shown in **Eq. 1.2**;[22] hence, it must be carefully selected. Commercial cells typically use, metal foils as the current collector, such as aluminum and copper, but other metals commonly used in a research setting include stainless steel, titanium, and nickel their low cost, high conductivity, wide availability and easy handling. However, more sustainable materials like graphite foil,[11] carbon cloth,[94] CNFs,[56] and cotton cloth[95] have become more commonly used in laboratory research, especially as concerns for environmentally friendly technologies rise. These are low weight materials, which represents an advantage to reduce the overall weight of the complete cell.

1.2.5 Separators

Separators are a porous membrane films placed between the two electrodes of an electrochemical device to prevent physical contact while allowing the transport of ions within the electrolyte between electrodes.[15, 88] A good separator must be an electronic insulator but have a good ion conductivity, mechanical strength, and high chemical and electrochemical stability.[96] These characteristics are influenced by the series resistance, hydrophilicity, pore shape and volume, and surface area.[11] Some of the most used separators in supercapacitors and batteries are derived of polyolefins such as polyethylene (PE), polypropylene (PP) and copolymers, which have good mechanical strength, stability, pore structure and low cost; however, their thermal stability limit is around 100°C and exhibit wettability issues with aqueous electrolytes (hydrophobic) (**Figure 8a**).[88] Other separators like nafion (**Figure 8b**) and nylon (**Figure 8c**) membranes will produce sulfur oxides, nitrogen oxides, and cyanide compounds during the incineration process at the end of the life of the device leading to considerable environmental concerns.[11] Therefore, biomass-derived separators represent a more environmentally friendly option.

Among biomass derived separators, the leading material is cellulose due to its good hydrophilicity, versatility, and thermal stability.[88] Dreamweaver International, for instance, produces nonwoven separators containing a combination of cellulose fibrillated nanofibers with microfibers that demonstrate good thermal stability, wettability, narrow pore size distribution and a wide variety of thickness (25-80 μm) suitable for various applications (supercapacitor, batteries, organic or aqueous systems) (**Figure 8d**).[97] Most

of the literature to date regarding sustainable separators includes a cellulose-based composite material.[88, 98]

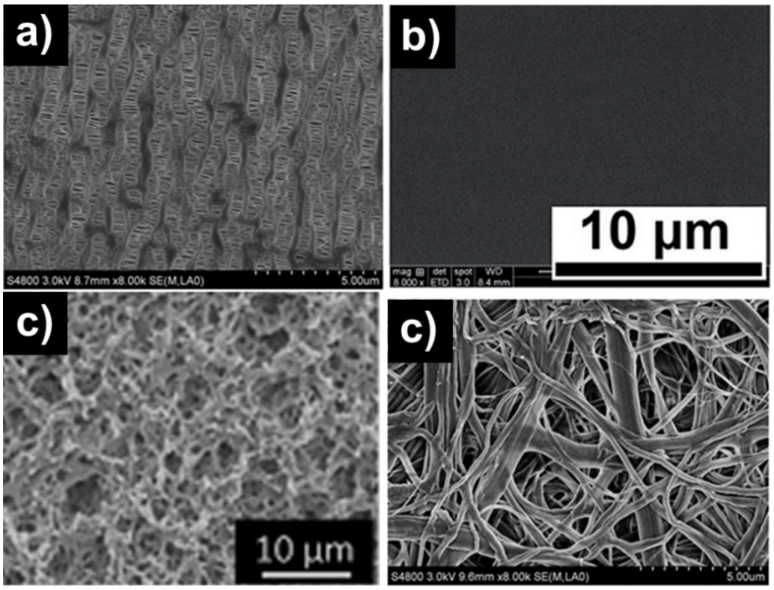

Figure 1.8 SEM images of different types of separators (a) Polypropylene (PP). (b) Nafion. (c) Nylon. (d) Cellulose nanofibers. (a) and (c) Reprinted from ref. [98], with permission of Nature Publishing Group (b) Reproduced from ref. [99], with permission of The Royal Society of Chemistry. (c) Reprinted from ref. [11], Copyright 2013, Wiley-VCH Verlag GmbH & Co. KGaA

1.2.6 Electrolytes

The electrolyte facilitates the transport of ions through the separator between the electrodes and within the internal structure of the electrode, as in the case of porous carbons. The main characteristics to take into account when selecting an electrolyte are the voltage stability range, electrochemical stability, ion conductivity, low volatility, low toxicity, low viscosity, low cost and high purity availability.[14, 22] These characteristics are

extremely important for Li-ion batteries, as the Li+ conductivity affects the overall power density, and for electrical double layer capacitors (supercaps), where the energy density in an is directly proportional to the operating voltage range to the square power (**Eq. 1.1**). Accordingly, the most effective approach to increasing the energy density in supercapacitors is increasing the operating voltage range, which is primarily limited to the stability of the electrolyte.[13] In general, electrolytes are classified in aqueous electrolytes, organic electrolytes and ionic liquids (ILs).

Aqueous electrolytes

Aqueous electrolytes can be either acidic (e.g. H_2SO_4, HCL, $HCLO_4$), basic (e.g. NaOH, KOH) or a neutral medium (e.g. K_2SO_4, Na_2SO_4, Li_2SO_4).[14] The advantages of aqueous solvents are high ionic concentration (high conductivity), low cost, non-flammable, low viscosity, safety, environmentally friendly and relatively small solvated ions compared with organic solvents.[22, 100] Usually devices will exhibit a higher capacitance and power than organic electrolytes due to higher conductivity, even though the operating voltage range is limited by water electrolysis, which occurs around 1.23V.[14] The voltage range can be expanded by utilizing electrolytes with different electrochemical stabilities in each electrode in hybrid devices[100, 101] (**Figure 9a**). Another approach is using neutral aqueous electrolyte (i.e. 1M Li_2SO_4), which opens the voltage operating range up to 2.2V (**Figure 1.9b** and **1.9c**). Supercapacitors with these electrolytes exhibit specific capacitance values of 140F g^{-1} for 2-electrode cell and good stability up to 15000 cycles (17% decrease in capacitance).[102]

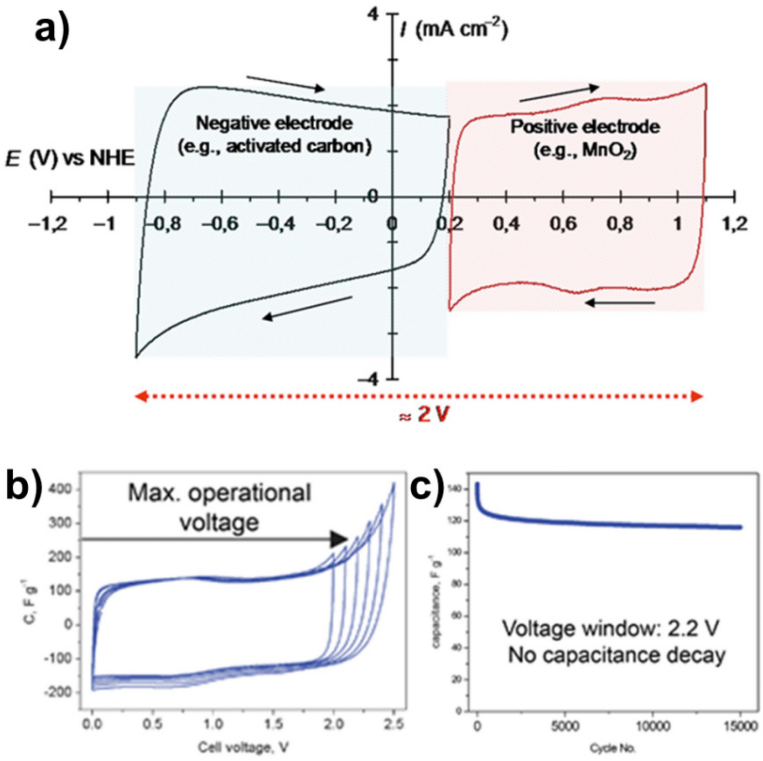

Figure 1.9 (a) Schematic representation of cyclic voltammetry profiles for aqueous based supercapacitor where the shaded areas in red and blue represent the voltage window of the positive and negative electrode for asymmetric activated carbon/MnO_2 in 0.5M K_2SO_4 vs. NHE. Reproduced from ref. [101], with permission of Cambridge University Press (b) Cyclic voltammetry profiles at 10 mV s^{-1} and gradual 100 mV voltage shift of symmetric activated carbon device in 1M Li_2SO_4 aqueous solution (c) Cyclability (1 A g^{-1}) at a voltage range 2.2V for 1500 cycles. Reproduced from ref. [102], with permission of The Royal Society of Chemistry.

Organic electrolytes

The main advantage of organic electrolytes is their wide voltage window, which can be as high as 3.5V.[14] However, they raise significant health and environmental concerns due to the toxicity, safety, and cost, along with the use of fluorinated salts such as tetraethylammonium tetrafluoroborate, tetraethylphosphonium tetrafluoroborate, and triethylmethylammonium tetrafluoroborate, which are likely to generate volatile fluorocarbons during the incineration process at the end of the device life.[11, 14, 22] The most commonly used organic solvents are acetonitrile (ACN) and propylene carbonate (PC); however, countries like Japan have prohibited the use of ACN in electrochemical devices for safety concerns.[103] As a result, PC has become more widely used due to its lower toxicity, wider electrochemical stability range, and temperature stability range.[14, 22]

Ionic liquids

Ionic liquids (ILs) are molten salts that are liquid at room temperature.[104] They have low vapor pressure, high thermal and chemical stability, low flammability, stability over a wide voltage range (2 to 6V), higher conductivity than organic electrolytes, and well-defined ion size (no solvation shell) due to the absence of solvent.[6, 13, 14, 22] However, some of the main disadvantages are high cost, high viscosity, and low ionic conductivity at room temperature.[22, 102] Commonly used anions in ILs for electrochemical applications are bis(trifluoromethane)sulfonamide ($TFSI^-$) and bis(fluorosulfonyl)imide (FSI^-) which are very expensive; therefore, they can be replaced with less expensive options such as chloride-based[6] or acetate-based[11, 105] anions couple with imidazole-derived cations.

Moreover, since the high cost is a concern, efforts have been made to develop recycle cost-effective processes.[106] In addition, the toxicity of IL increases with the length of the hydrocarbon chain (hydrophobicity).[106, 107] A recent review by A. Jordan and N. Gathergood[108] examined the degradability of current ILs, showing that cholinium cation and organic acid anions are by far the biggest group of readily biodegradable ILs, but the suitability of electrochemical devices is yet to be studied.

1.3 Recycling and recyclable technologies

The EPA encourages the electronics manufacturers and retailers to collect the devices and send them to third-party certified electronics refurbishers and recyclers through the program "Sustainable Materials Management (SMM) Electronics Challenge". Through this program, they offer awards and public recognition to those companies committed to electronics recycle and reuse. Additionally, the program promotes a variety of electronics recycling sources, such as Call2Recycle, Eart911, Electronics Industries Alliance, and GreenerGadgets, to focus on the recycling batteries, cellphones, laptops, among other devices.[109]

Recycle is currently the only way to avoid the detrimental environmental impact of battery technologies. Lead-acid batteries are by far the most widely recycled batteries (95% recycling efficiency[16]) since the recycling process is cheaper than the lead mining process and is relatively easy to recover the different constituents as they are standardized to certain configurations across the market. On the other hand, recycling processes for Li-ion batteries are more complicated due to the wide range of chemistries and cell

configurations making it less economically attractive. Most of the companies that recycle Li-ion batteries currently rely on subsidies.[110] Moreover, primary batteries are not popular for recycling because the mineral content is low which makes material recovery economically unattractive.

In general, recycling processes for Li-ion batteries are classified in pyrometallurgy (high-temperature pyrolysis) and hydrometallurgy (low-temperature solution chemistry) (**Figure 10**). The former uses high-temperature process but yields high purity materials, while the latter uses low-temperature processes but needs ~7 m^3 of water per ton of batteries processed.[6] Other methods actively under consideration to reduce the environmental impact use bio-hydrometallurgy based on microorganisms that perform leaching process,[6] or modifying the leaching step with biomass derived reductants.[111] Larcher and Tarascon[6] show that the production of batteries (Li-ion, Ni-MH and Pb-acid) are the major contributors to the energy cost when compared to the energy consumption during the recycling process, and a lot of emphases is made on the need for more environmentally friendly production and recycling processes.[36] In the literature, there are many examples of electronic devices comprised of entirely degradable components; however, their performance needs considerable improvement to meet technological specifications.[42]

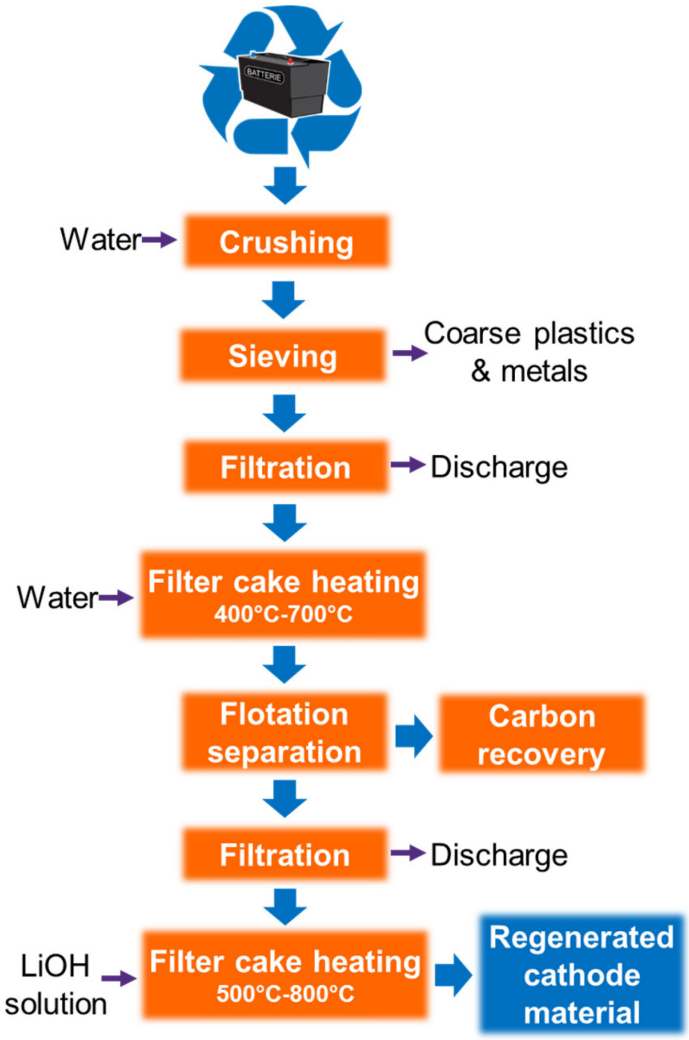

Figure 1.10 Example of recycling process for Li-ion batteries implemented by Retriev Technologies Inc.[112]

1.4 Concluding remarks and future perspective

One tool that can help to determine whether a process, material or product is truly sustainable is the life-cycle assessment (LCA), which is a formal technique to determine the environmental impact of a product from cradle to grave. Along with the green chemistry and sustainability principles, LCA could guide the development of new technology and determine whether a material represents a sustainable option. In the area of batteries, there are reports about the environmental impact of those technologies;[113] however, in the field of supercapacitors there is a lack of information about the environmental effects of metal oxides and conducting polymers from the origin to the final disposal. **Table 1.1**, summarizes the current potentially sustainable options for the assembly of batteries and supercapacitors, as well as, what we think should be the target materials for sustainable energy storage. Nevertheless, these target materials either are not yet available or cannot compete with the commercial state of the art systems. If the goal is true sustainability, we cannot continue to focus solely on renewable energy generation; we must increase research efforts on sustainable energy storage materials to support the increasing energy capacity from intermittent sources.

Table 1.1 Summary of sustainable materials for supercapacitors and batteries

Component	Current options	Target
Active materials	- Biomass-derived carbons - Conducting polymers - MnO_2 - Redox biopolymers - Oxocarbons or carboxylates derived lithium	- Biomass-derived polymers and carbons - Abundant metals (e. g. Mn, Al, Fe, Na, Ca, among others) - Recyclable / degradable materials
Binders	- Cellulose - derived - Xanthan Gum - Polyvinyl alcohol (PVA) - Polyacrylic acid (PAA) - Styrene Butadiene Rubber (SBR) - Sodium alginate	- Biomass-derived polymers / molecules - Biodegradable polymers
Conductivity enhancers	- Graphite - Acetylene black	- Biomass-derived carbons
Current collectors	- Carbon veil / fibers - Graphite foil	- Abundant / Recyclable metals - Biomass-derived carbons
Separators	- Cellulose-derived	- Biomass-derived - Biodegradable materials
Electrolytes	- Aqueous - Fluor - free salts - Fluor - free ionic liquids	- Aqueous - Abundant / non-toxic salts - Biodegradable ionic liquids

1.5 Dissertation outline

As it has been mentioned before, supercapacitors still need improvements in energy and power density, as well as, alternative routes for the synthesis of sustainable electrodes. The overall goal of this doctoral work was to develop straightforward, low-cost approaches for the design of micro- and nano-structured electrodes with enhanced electrochemical performance. The chemical composition or physical structure of conducting polymers, carbons, and composite materials were manipulated through chemical or electrochemical synthesis techniques aiming for enhanced surface area, high electrochemical activity, practical electrode mass and easy processability. This dissertation comprises of five main chapters that compile various approaches taken towards the fulfillment of the main goal. The first two chapters look at the modification of the electrode composition by using lignin as redox polymer and the last three chapters look at the manipulation of the electrode structure in carbon fibers, conducting polymers and carbon aerogels.

Chapter 2, *High charge-capacity polymer electrodes comprising alkali lignin from Kraft process*, was a collaborative effort with Dr. Mark Thies's research group. The objective of this project was to demonstrate the use of the most abundant type of lignin, which is derived from the Kraft pulping process wood (alkali lignin), in supercapacitors through the synthesis of conducting polymer / lignin composite electrodes with enhanced energy density. The first step was to overcome the poor solubility of alkali lignin in aqueous solutions while maintaining the right conditions for the conducting polymer synthesis. Then, the electrochemical activity of polypyrrole/alkali lignin electrodes was

compared with a less abundant but readily soluble in aqueous solutions type of lignin (sulfonated lignin). Finally, the influence of the phenolic content in the electrochemical activity of the composite electrodes was studied, using samples derived from the pH fractionation process to separate lignin from black liquor developed by Dr. Thies and his former student Dr. Julian Vélez. To the best of our knowledge, there were no previous reports of the use of alkali lignin as part of the electrode material in supercapacitors, mainly due to the poor solubility in aqueous solutions, which highlights the relevance of this work.

From the results in chapter 2, it was found that conducting polymer/lignin composite electrodes exhibit relatively lower cycle life than electrodes comprised only of the conducting polymer. To overcome this problem, in Chapter 3, *Lignin-coated Carbon Nanomaterials for Low-Cost Electrical Energy Storage*, the conducting polymer was replaced by different types of porous carbon materials. The main objectives were to study the electrochemical response of lignin in aqueous electrolytes, increase the stability of composite electrodes, select a suitable porous carbon material for the adsorption of lignin within the carbon structure, and examine the influence of the synthesis conditions in the electrochemical response of lignin in supercapacitor electrodes.

After studied the changes in the electrochemical activity of electrodes due to the incorporation of redox polymers, from chapter 4 to chapter 6, the modification of the physical structure of electrodes was studied. In chapter 4, *Nanostructured Polyacrylonitrile/Lignin Carbon Fiber Electrodes for High-Performance Supercapacitors*, lignin is utilized as a source of macro- and mesoporosity in carbon

fibers to enable the use in supercapacitors. This project was a collaborative effort with Dr. Ogale's research group and his graduate student Jing Jin. The primary objective was to determine the synthesis conditions that enable the use of porous carbon fibers in supercapacitor electrodes. First, the ideal fiber diameter was determined by measuring the electrochemical activity of carbon fibers with different diameters. Then, an activation process was developed to produce microspores within the already existing macro- and mesoporosity to increase the surface area, and hence, the capacitance of the electrodes. To the best of our knowledge, this is the first report in taking advantage of lignin as a way to produce porous carbon fibers for supercapacitor applications.

In chapter 5, *Rigid, Non-Pressed, Highly Porous Carbon Aerogel Supercapacitor Electrodes*, a high surface area, free-standing carbon aerogel electrodes were developed to eliminate the need for a current collector and a binder during the electrode preparation and increase the electrochemical performance. This project was in collaboration with Mr. Andrew Cain and Mr. Madison Parks from Southern Research Institute; several details regarding the synthesis process of the carbon aerogels are omitted for proprietary reasons. The objective was to determine the most suitable backbone material that led to the best electrochemical performance while making the synthesis process more efficient and facilitating the handling process of the electrode during the device assembly.

Finally, in chapter 6, *Scalable, Template-Free Synthesis of Conducting Polymer Microtubes*, a free template synthesis method was developed to produce conducting polymer microtubes. This project was divided in two parts. In the first part, the main objective was to understand the microtubes growth mechanism and the influence of the

substrate on the development of the microstructure. The second part was focus in a deeper understanding of the role of the hydrogen gas produced as part of the electrochemical polymerization of the conducting polymer in the growth of the microtubes by examining the influence of the polymerization temperature and electrode set up.

All the chapters are based on the following publications and under review manuscripts at the time of the dissertation submission:

- **Chapter 1:** K. P. Díaz-Orellana, M. E. Roberts, "Sustainable Materials for Electrochemical Energy Storage". Manuscript under review (2016).
- **Chapter 2:** S. Leguizamon*, K. P. Díaz-Orellana*, J. Vélez, M. C. Thies, M. E. Roberts, "High-Charge Capacity Polymer Electrodes comprising Alkali Lignin from the Kraft Process", *Journal of Material Chemistry A*, 2015, 3, 11330-11339. *equal contribution
- **Chapter 3:** K. P. Díaz-Orellana, A. Carlin, M. E. Roberts, "Engineering Lignin-Carbon Composites for Low-Cost, High Charge-Capacity Electrodes". Manuscript under review (2016).
- **Chapter 4:** K. P. Díaz-Orellana*, J. Jin*, A. Ogale, M. E. Roberts, "Nanostructured Polyacrylonitrile/Lignin Carbon Fiber Electrodes for High-Performance Supercapacitors". Manuscript under review (2016). *equal contribution

- **Chapter 5:** K. P. Díaz-Orellana*, M. Parks*, A. Cain, M. E. Roberts, "Rigid, Non-Pressed, Highly Porous Carbon Aerogel Supercapacitor Electrodes". Manuscript under review (2016). *equal contribution
- **Chapter 6:**
  - K. P. Díaz-Orellana, M. E. Roberts, "Scalable, Template-Free Synthesis of Conducting Polymer Microtubes", *RSC Advances*, 2015, 5, 25504-25512.
  - K. P. Díaz-Orellana*, S. Leguizamon*, M. E. Roberts, "Influence of Temperature and Polymerization Conditions on the Synthesis of Conducting Polymer Microtubes". Manuscript under review (2016). *equal contribution

1.6 References

1. International Energy Agency: World Energy Outlook 2015. [cited 2016 March]; Available from: http://www.worldenergyoutlook.org/

2. U.S. Energy Information Administration: Renewables and CO2 Emissions. [cited 2016 March]; Available from: https://www.eia.gov/forecasts/steo/report/renew_co2.cfm

3. U.S. Deparment of the Interior & U.S. Geological Survey: Mineral commodity summaries 2016. 2016 [cited]; 202]. Available from: http://dx.doi.org/10.3133/70140094

4. EPA: Learn about Sustainability. [cited 2016 March]; Available from: https://www.epa.gov/sustainability/learn-about-sustainability#what

5. EPA: Basics of Green Chemistry. [cited 2016 March]; Available from: http://www.epa.gov/greenchemistry/basics-green-chemistry#definition

6. Larcher D, Tarascon JM. Towards greener and more sustainable batteries for electrical energy storage. *Nature Chemistry* **2015**, 7(1)**:** 19-29.

7. Song Z, Zhou H. Towards sustainable and versatile energy storage devices: an overview of organic electrode materials. *Energy Environ. Sci.* **2013**, 6(8)**:** 2280-2301.

8. Zhang J, Terrones M, Park CR, Mukherjee R, Monthioux M, Koratkar N*, et al.* Carbon science in 2016: Status, challenges and perspectives. *Carbon* **2016**, 98**:** 708-732.

9. Poizot P, Dolhem F. Clean energy new deal for a sustainable world: from non-CO2 generating energy sources to greener electrochemical storage devices. *Energy Environ. Sci.* **2011**, 4(6)**:** 2003-2019.

10. Simon P, Gogotsi Y, Dunn B. Where Do Batteries End and Supercapacitors Begin? *Science* **2014**, 343(6176)**:** 1210-1211.

11. Dyatkin B, Presser V, Heon M, Lukatskaya MR, Beidaghi M, Gogotsi Y. Development of a Green Supercapacitor Composed Entirely of Environmentally Friendly Materials. *ChemSusChem* **2013**, 6(12)**:** 2269-2280.

12. Yu G, Xie X, Pan L, Bao Z, Cui Y. Hybrid nanostructured materials for high-performance electrochemical capacitors. *Nano Energy* **2013**, 2(2)**:** 213-234.

13. Simon P, Gogotsi Y. Materials for electrochemical capacitors. *Nat Mater* **2008**, 7(11)**:** 845-854.

14. Wang G, Zhang L, Zhang J. A review of electrode materials for electrochemical supercapacitors. *Chem. Soc. Rev.* **2012**, 41(2)**:** 797-828.

15. Manaf NSA, Bistamam MSA, Azam MA. Development of high performance electrochemical capacitor: a systematic review of electrode fabrication technique based on different carbon materials. *ECS J. Solid State Sci. Technol.* **2013**, 2(10)**:** M3101-M3119.

16. Armand M, Tarascon JM. Building better batteries. *Nature* **2008**, 451(7179)**:** 652-657.

17. Etacheri V, Marom R, Elazari R, Salitra G, Aurbach D. Challenges in the development of advanced Li-ion batteries: a review. *Energy Environ. Sci.* **2011**, 4(9)**:** 3243-3262.

18. Augustyn V, Simon P, Dunn B. Pseudocapacitive oxide materials for high-rate electrochemical energy storage. *Energy Environ. Sci.* **2014**, 7(5)**:** 1597-1614.

19. Snook GA, Kao P, Best AS. Conducting-polymer-based supercapacitor devices and electrodes. *J. Power Sources* **2011**, 196(1)**:** 1-12.

20. Yao F, Pham DT, Lee YH. Carbon-Based Materials for Lithium-Ion Batteries, Electrochemical Capacitors, and Their Hybrid Devices. *ChemSusChem* **2015**, 8(14)**:** 2284-2311.

21. Vlad A, Singh N, Rolland J, Melinte S, Ajayan PM, Gohy JF. Hybrid supercapacitor-battery materials for fast electrochemical charge storage. *Scientific reports* **2014**, 4**:** 4315.

22. Yan J, Wang Q, Wei T, Fan Z. Recent Advances in Design and Fabrication of Electrochemical Supercapacitors with High Energy Densities. *Adv. Energy Mater.* **2014**, 4(4)**:** 1-43.

23. Van den Bossche P, Vergels F, Van Mierlo J, Matheys J, Van Autenboer W. SUBAT: An assessment of sustainable battery technology. *J. Power Sources* **2006**, 162(2)**:** 913-919.

24. Ceskaa: Global Market for Supercapacitors: 2015-2020. [cited 2016 February]; Available from: https://www.ceskaa.com/shop/energy-and-power/global-market-for-supercapacitor-report-2015-2020/

25. Maxwell Tehcnologies, Inc.: Desing Considerations for Ultracapacitors & Ultracapacitors Overview. [cited 2016 February]; Available from: http://www.maxwell.com/products/ultracapacitors/downloads

26. Cap-XX Pty Ltd.: Product Guide 2015. [cited 2016 February]; Available from: http://www.cap-xx.com/wp-content/uploads/2015/10/CAP-XX-Product-Guide-2015-v3.0.pdf

27. Eaton PowerStor: XB, XL60 & XV Series Data Sheet. [cited 2016 Frebuary]; Available from: http://www.cooperindustries.com/content/public/en/bussmann/electronics/products/eaton-supercapacitors/cylindrical1.html

28. Nesscap Co., Ltd.: EDLC & Pseudocapacitor. [cited 2016 February]; Available from: http://www.nesscap.com/ultracapacitor/EDLC/Supercapacitor/Small_cell_supercapacitor_family/Lead_wired_capacitor.jsp

29. Freedonia Group: World Batteries - Demand and sales forecast, market share, market size and market leaders. [cited 2016 March]; Available from: http://www.freedoniagroup.com/World-Batteries.html

30. First Research, Inc.: Battery Manufacturing Industry Profile. [cited 2016 March]; Available from: http://www.firstresearch.com/Industry-Research/Battery-Manufacturing.html

31. Webelements: Manganese dioxide. [cited 2016 March]; Available from: http://www.webelements.com/compounds/manganese/manganese_dioxide.html

32. Chemical Structure: Lithium Iron Phosphate. [cited 2016 March]; Available from: http://chemicalstructure.net/

33. Wang J, Hu Z, Xu J, Zhao Y. Therapeutic applications of low-toxicity spherical nanocarbon materials. *NPG Asia Mater* **2014**, 6**:** e84.

34. Xu H, Zhang H, Mu Y, Feng Y, Wang Y. General and Green Strategy toward High Performance Positive Electrode Materials for Rechargeable Li Ion Batteries with Crop Stalks as the Host Carbon Matrixes. *ACS Sustainable Chem. Eng.* **2015**, 3(7)**:** 1650-1657.

35. Chen H, Armand M, Demailly G, Dolhem F, Poizot P, Tarascon J-M. From Biomass to a Renewable LiXC6O6 Organic Electrode for Sustainable Li-Ion Batteries. *ChemSusChem* **2008**, 1(4)**:** 348-355.

36. Dunn JB, Gaines L, Sullivan J, Wang MQ. Impact of Recycling on Cradle-to-Gate Energy Consumption and Greenhouse Gas Emissions of Automotive Lithium-Ion Batteries. *Environ. Sci. Technol.* **2012**, 46(22)**:** 12704-12710.

37. Evarts EC. Lithium batteries: To the limits of lithium. *Nature* **2015**, 526(7575)**:** S93-S95.

38. Frackowiak E, Abbas Q, Béguin F. Carbon/carbon supercapacitors. *Journal of Energy Chemistry* **2013**, 22(2)**:** 226-240.

39. Jeon J-W, Zhang L, Lutkenhaus JL, Laskar DD, Lemmon JP, Choi D*, et al.* Controlling Porosity in Lignin-Derived Nanoporous Carbon for Supercapacitor Applications. *ChemSusChem* **2015**, 8(3)**:** 428-432.

40. Hu B, Wang K, Wu L, Yu S-H, Antonietti M, Titirici M-M. Engineering Carbon Materials from the Hydrothermal Carbonization Process of Biomass. *Adv. Mater.* **2010**, 22(7)**:** 813-828.

41. Liu D, Zhang W, Lin H, Li Y, Lu H, Wang Y. A green technology for the preparation of high capacitance rice husk-based activated carbon. *J. Clean. Prod.* **2016**, 112, Part 1**:** 1190-1198.

42. Bazaka K, Jacob MV, Ostrikov K. Sustainable Life Cycles of Natural-Precursor-Derived Nanocarbons. *Chem. Rev.* **2016**, 116(1)**:** 163-214.

43. Béguin F, Presser V, Balducci A, Frackowiak E. Carbons and Electrolytes for Advanced Supercapacitors. *Adv. Mater.* **2014**, 26(14)**:** 2219-2251.

44. Miranda D, Costa CM, Lanceros-Mendez S. Lithium ion rechargeable batteries: State of the art and future needs of microscopic theoretical models and simulations. *J. Electroanal. Chem.* **2015**, 739**:** 97-110.

45. Thakur VK, Thakur MK. Recent advances in green hydrogels from lignin: a review. *Int. J. Biol. Macromol.* **2015**, 72**:** 834-847.

46. Xu X, Zhou J, Nagaraju DH, Jiang L, Marinov VR, Lubineau G*, et al.* Flexible, Highly Graphitized Carbon Aerogels Based on Bacterial Cellulose/Lignin: Catalyst-Free Synthesis and its Application in Energy Storage Devices. *Adv. Funct. Mater.* **2015**, 25(21)**:** 3193-3202.

47. White RJ, Brun N, Budarin VL, Clark JH, Titirici M-M. Always Look on the "Light" Side of Life: Sustainable Carbon Aerogels. *ChemSusChem* **2014**, 7(3)**:** 670-689.

48. Upadhyayula VKK, Meyer DE, Curran MA, Gonzalez MA. Life cycle assessment as a tool to enhance the environmental performance of carbon nanotube products: a review. *J. Clean. Prod.* **2012**, 26**:** 37-47.

49. Dutta S, Bhaumik A, Wu KCW. Hierarchically porous carbon derived from polymers and biomass: effect of interconnected pores on energy applications. *Energy Environ. Sci.* **2014**, 7(11)**:** 3574-3592.

50. Li Y, Lu C, Zhang S, Su F-Y, Shen W, Zhou P*, et al.* Nitrogen- and oxygen-enriched 3D hierarchical porous carbon fibers: synthesis and superior supercapacity. *J. Mater. Chem. A* **2015**, 3(28)**:** 14817-14825.

51. Hu S, Zhang S, Pan N, Hsieh Y-L. High energy density supercapacitors from lignin derived submicron activated carbon fibers in aqueous electrolytes. *J. Power Sources* **2014**, 270**:** 106-112.

52. Liu S, Yu T, Wu Y, Li W, Li B. Evolution of cellulose into flexible conductive green electronics: a smart strategy to fabricate sustainable electrodes for supercapacitors. *RSC Adv.* **2014**, 4(64)**:** 34134-34143.

53. Koga H, Tonomura H, Nogi M, Suganuma K, Nishina Y. Fast, scalable, and eco-friendly fabrication of an energy storage paper electrode. *Green Chem.* **2016**, 18(4)**:** 1117-1124.

54. Zhang T, Kim CHJ, Cheng Y, Ma Y, Zhang H, Liu J. Making a commercial carbon fiber cloth having comparable capacitances to carbon nanotubes and graphene in supercapacitors through a "top-down" approach. *Nanoscale* **2015**, 7(7)**:** 3285-3291.

55. Titirici M-M, Antonietti M. Chemistry and materials options of sustainable carbon materials made by hydrothermal carbonization. *Chem. Soc. Rev.* **2010**, 39(1)**:** 103-116.

56. Chen L-F, Huang Z-H, Liang H-W, Gao H-L, Yu S-H. Three-Dimensional Heteroatom-Doped Carbon Nanofiber Networks Derived from Bacterial Cellulose for Supercapacitors. *Adv. Funct. Mater.* **2014**, 24(32)**:** 5104-5111.

57. Abdelhamid ME, O'Mullane AP, Snook GA. Storing energy in plastics: a review on conducting polymers & their role in electrochemical energy storage. *RSC Adv.* **2015**, 5(15)**:** 11611-11626.

58. Ghosh S, Thandavarayan M, Basu RN. Nanostructured Conducting Polymers for Energy Applications: Towards a Sustainable Platform. *Nanoscale* **2016**.

59. Admassie S, Elfwing A, Skallberg A, Inganas O. Extracting metal ions from water with redox active biopolymer electrodes. *Environ. Sci.: Water Res. Technol.* **2015**, 1(3)**:** 326-331.

60. Irimia-Vladu M, Głowacki ED, Voss G, Bauer S, Sariciftci NS. Green and biodegradable electronics. *Mater. Today* **2012**, 15(7–8)**:** 340-346.

61. Guo B, Glavas L, Albertsson A-C. Biodegradable and electrically conducting polymers for biomedical applications. *Prog. Polym. Sci.* **2013**, 38(9)**:** 1263-1286.

62. Xia L, Wei Z, Wan M. Conducting polymer nanostructures and their application in biosensors. *J. Colloid Interface Sci.* **2010**, 341(1)**:** 1-11.

63. Lin H-A, Luo S-C, Zhu B, Chen C, Yamashita Y, Yu H-h. Molecular or Nanoscale Structures? The Deciding Factor of Surface Properties on Functionalized Poly(3,4-ethylenedioxythiophene) Nanorod Arrays. *Adv. Funct. Mater.* **2013**, 23(25)**:** 3212-3219.

64. Bai Y, Xu Y, Wang J, Gao M, Wang J. Interface Effect on the Electropolymerized Polypyrrole Films with Hollow Micro/Nanohorn Arrays. *ACS Appl. Mater. Interfaces* **2014**, 6(7)**:** 4693-4704.

65. Diaz-Orellana KP, Roberts ME. Scalable, template-free synthesis of conducting polymer microtubes. *RSC Adv.* **2015**, 5(32)**:** 25504-25512.

66. Wang Z, Tammela P, Zhang P, Stromme M, Nyholm L. High areal and volumetric capacity sustainable all-polymer paper-based supercapacitors. *J. Mater. Chem. A* **2014**, 2(39)**:** 16761-16769.

67. Leguizamon S, Diaz-Orellana KP, Velez J, Thies MC, Roberts ME. High charge-capacity polymer electrodes comprising alkali lignin from the Kraft process. *J. Mater. Chem. A* **2015**, 3(21)**:** 11330-11339.

68. Milczarek G, Inganäs O. Renewable Cathode Materials from Biopolymer/Conjugated Polymer Interpenetrating Networks. *Science* **2012**, 335(6075)**:** 1468-1471.

69. Bahloul A, Nessark B, Briot E, Groult H, Mauger A, Zaghib K*, et al.* Polypyrrole-covered MnO2 as electrode material for supercapacitor. *J. Power Sources* **2013**, 240**:** 267-272.

70. Hou Y, Cheng Y, Hobson T, Liu J. Design and Synthesis of Hierarchical MnO2 Nanospheres/Carbon Nanotubes/Conducting Polymer Ternary Composite for

High Performance Electrochemical Electrodes. *Nano Lett.* **2010**, 10(7)**:** 2727-2733.

71. Arcila-Velez MR, Emmett RK, Karakaya M, Podila R, Díaz-Orellana KP, Rao AM*, et al.* A facile and scalable approach to fabricating free-standing polymer—Carbon nanotube composite electrodes. *Synth. Met.* **2016**, 215**:** 35-40.

72. Byrne MT, Gun'ko YK. Recent Advances in Research on Carbon Nanotube–Polymer Composites. *Adv. Mater.* **2010**, 22(15)**:** 1672-1688.

73. Lee HY, Kim HS, Seong WK, Kim SW, inventors; Ness Capacitor Co., Ltd., assignee. Manufacturing method for a metal oxide electrode for supercapacitor patent US6616875 B2. 2003.

74. Evans Capacitor Company: Hybrid® Capacitors. [cited 2016 February]; Available from: http://www.evanscap.com/hybrid.htm

75. Sigma Aldrich: 238058 Ruthenium(IV) oxide & 529664 Manganese(IV) oxide. [cited 2016 February]; Available from: https://www.sigmaaldrich.com/united-states.html

76. Gracia R, Mecerreyes D. Polymers with redox properties: materials for batteries, biosensors and more. *Polym. Chem.* **2013**, 4(7)**:** 2206-2214.

77. Arcila-Velez MR, Roberts ME. Redox Solute Doped Polypyrrole for High-Charge Capacity Polymer Electrodes. *Chem. Mater.* **2014**, 26(4)**:** 1601-1607.

78. Vonlanthen D, Lazarev P, See KA, Wudl F, Heeger AJ. A Stable Polyaniline-Benzoquinone-Hydroquinone Supercapacitor. *Adv. Mater.* **2014**, 26(30)**:** 5095-5100.

79. Chen X, Wang H, Yi H, Wang X, Yan X, Guo Z. Anthraquinone on Porous Carbon Nanotubes with Improved Supercapacitor Performance. *J. Phys. Chem. C* **2014**, 118(16)**:** 8262-8270.

80. An N, An Y, Hu Z, Zhang Y, Yang Y, Lei Z. Green and all-carbon asymmetric supercapacitor based on polyaniline nanotubes and anthraquinone functionalized porous nitrogen-doped carbon nanotubes with high energy storage performance. *RSC Adv.* **2015**, 5(78)**:** 63624-63633.

81. Sixta H. *Handbook of Pulp, vol. 1*. Wiley-VCH Verlag GmbH, Weinheim, Germany, **2006**.

82. Admassie S, Elfwing A, Jager EWH, Bao Q, Inganas O. A renewable biopolymer cathode with multivalent metal ions for enhanced charge storage. *J. Mater. Chem. A* **2014**, 2(6)**:** 1974-1979.

83. Ajjan FN, Casado N, Rebis T, Elfwing A, Solin N, Mecerreyes D*, et al.* High performance PEDOT/lignin biopolymer composites for electrochemical supercapacitors. *J. Mater. Chem. A* **2016**, 4(5)**:** 1838-1847.

84. Ajjan FN, Jafari MJ, Rebis T, Ederth T, Inganas O. Spectroelectrochemical investigation of redox states in a polypyrrole/lignin composite electrode material. *J. Mater. Chem. A* **2015**, 3(24)**:** 12927-12937.

85. Rebis T, Nilsson TY, Inganas O. Hybrid materials from organic electronic conductors and synthetic-lignin models for charge storage applications. *J. Mater. Chem. A* **2016**, 4(5)**:** 1931-1940.

86. Nilsson TY, Wagner M, Inganäs O. Lignin Modification for Biopolymer/Conjugated Polymer Hybrids as Renewable Energy Storage Materials. *ChemSusChem* **2015**, 8(23)**:** 4081-4085.

87. Milczarek G, Nowicki M. Carbon nanotubes/kraft lignin composite: Characterization and charge storage properties. *Mater. Res. Bull.* **2013**, 48(10)**:** 4032-4038.

88. Zhang L, Liu Z, Cui G, Chen L. Biomass-derived materials for electrochemical energy storages. *Prog. Polym. Sci.* **2015**, 43**:** 136-164.

89. Courtel FM, Niketic S, Duguay D, Abu-Lebdeh Y, Davidson IJ. Water-soluble binders for MCMB carbon anodes for lithium-ion batteries. *J. Power Sources* **2011**, 196(4)**:** 2128-2134.

90. Lux SF, Schappacher F, Balducci A, Passerini S, Winter M. Low Cost, Environmentally Benign Binders for Lithium-Ion Batteries. *J. Electrochem. Soc.* **2010**, 157(3)**:** A320-A325.

91. Yamagata M, Ikebe S, Soeda K, Ishikawa M. Ultrahigh-performance nonaqueous electric double-layer capacitors using an activated carbon composite electrode with alginate. *RSC Adv.* **2013**, 3(4)**:** 1037-1040.

92. Li C-C, Wang Y-W. Importance of binder compositions to the dispersion and electrochemical properties of water-based LiCoO2 cathodes. *J. Power Sources* **2013**, 227**:** 204-210.

93. Park H-K, Kong B-S, Oh E-S. Effect of high adhesive polyvinyl alcohol binder on the anodes of lithium ion batteries. *Electrochem. Commun.* **2011**, 13(10)**:** 1051-1053.

94. Jost K, Stenger D, Perez CR, McDonough JK, Lian K, Gogotsi Y*, et al.* Knitted and screen printed carbon-fiber supercapacitors for applications in wearable electronics. *Energy Environ. Sci.* **2013**, 6(9)**:** 2698-2705.

95. Liu W-w, Yan X-b, Lang J-w, Peng C, Xue Q-j. Flexible and conductive nanocomposite electrode based on graphene sheets and cotton cloth for supercapacitor. *J. Mater. Chem.* **2012**, 22(33)**:** 17245-17253.

96. Zhong C, Deng Y, Hu W, Qiao J, Zhang L, Zhang J. A review of electrolyte materials and compositions for electrochemical supercapacitors. *Chem. Soc. Rev.* **2015**, 44(21)**:** 7484-7539.

97. Dreamweaver International (DWI)Technical papers: A Comparison of Nonwoven Separators for Supercapacitors [cited 2016 February]; Available from: http://www.dreamweaverintl.com/

98. Zhang J, Yue L, Kong Q, Liu Z, Zhou X, Zhang C*, et al.* Sustainable, heat-resistant and flame-retardant cellulose-based composite separator for high-performance lithium ion battery. *Scientific reports* **2014**, 4.

99. Yu X, Joseph J, Manthiram A. Polymer lithium-sulfur batteries with a Nafion membrane and an advanced sulfur electrode. *J. Mater. Chem. A* **2015**, 3(30)**:** 15683-15691.

100. Zhang J, Zhao XS. On the Configuration of Supercapacitors for Maximizing Electrochemical Performance. *ChemSusChem* **2012**, 5(5)**:** 818-841.

101. Long JW, Bélanger D, Brousse T, Sugimoto W, Sassin MB, Crosnier O. Asymmetric electrochemical capacitors—Stretching the limits of aqueous electrolytes. *MRS Bull.* **2011**, 36(07)**:** 513-522.

102. Fic K, Lota G, Meller M, Frackowiak E. Novel insight into neutral medium as electrolyte for high-voltage supercapacitors. *Energy Environ. Sci.* **2012**, 5(2)**:** 5842-5850.

103. Hall PJ, Mirzaeian M, Fletcher SI, Sillars FB, Rennie AJR, Shitta-Bey GO*, et al.* Energy storage in electrochemical capacitors: designing functional materials to improve performance. *Energy Environ. Sci.* **2010**, 3(9)**:** 1238-1251.

104. Marr PC, Marr AC. Ionic liquid gel materials: applications in green and sustainable chemistry. *Green Chem.* **2016**, 18(1)**:** 105-128.

105. Leones R, Sentanin F, Rodrigues LC, Ferreira RAS, Marrucho IM, Esperança JMSS*, et al.* Novel polymer electrolytes based on gelatin and ionic liquids. *Opt. Mater.* **2012**, 35(2)**:** 187-195.

106. Horowitz AI, Wang Y, Panzer MJ. Reclamation and reuse of ionic liquids from silica-based ionogels using spontaneous water-driven separation. *Green Chem.* **2013**, 15(12)**:** 3414-3420.

107. Coleman D, Gathergood N. Biodegradation studies of ionic liquids. *Chem. Soc. Rev.* **2010**, 39(2)**:** 600-637.

108. Jordan A, Gathergood N. Biodegradation of ionic liquids - a critical review. *Chem. Soc. Rev.* **2015**, 44(22)**:** 8200-8237.

109. EPA: Electronics Donation and Recycling. [cited 2016 February]; Available from: https://www.epa.gov/recycle/electronics-donation-and-recycling

110. Gies E. Recycling: Lazarus batteries. *Nature* **2015**, 526(7575)**:** S100-S101.

111. Chen X, Luo C, Zhang J, Kong J, Zhou T. Sustainable Recovery of Metals from Spent Lithium-Ion Batteries: A Green Process. *ACS Sustainable Chem. Eng.* **2015**, 3(12)**:** 3104-3113.

112. Smith WN, Swoffer S, inventors; Retriev Technologies Inc. , assignee. Recovery of lithium ion batteries patent US8616475 B1. 2013.

113. Majeau-Bettez G, Hawkins TR, Strømman AH. Life Cycle Environmental Assessment of Lithium-Ion and Nickel Metal Hydride Batteries for Plug-In Hybrid and Battery Electric Vehicles. *Environ. Sci. Technol.* **2011**, 45(10)**:** 4548-4554.

CHAPTER TWO

HIGH CHARGE-CAPACITY POLYMER ELECTRODES COMPRISING ALKALI LIGNIN FROM THE KRAFT PROCESS

2.1 Introduction

Energy storage technologies are critical components for the deployment of renewable energy generation systems (e.g. wind, solar), electric transportation, and load-leveling systems.[1] Future applications in these areas will require materials and systems with increasing power and energy densities, long term cycle-ability, and low-cost materials compatible with scalable processing methods. Accordingly, research efforts have focused on inert carbon nanomaterials in supercapacitors, which have been shown to exhibit fast discharge rates with long-term cycle stability over a wide temperature range.[2-5]

High-surface area (porous) carbon materials have been extensively developed and studied due to their chemical stability, long-term cycle stability and rapid electrochemical processes; however, these materials have limited energy densities as a result of the electrochemical double layer (EDL) mechanism, in which charge is stored physically through ion- adsorption at the electrode interfaces.[4, 6] Faradaic (redox) materials, on the other hand, store energy through charge transfer in the bulk of the material in addition to at the material interface, providing opportunities to overcome the low charge capacity of commercial supercapacitors. Metal oxides,[7, 8] such as RuO_2 and MnO_2 yield high capacitance values; however, their cost, material scarcity, and processing variability limit their applicability to large-scale systems. On the other hand, electrically conducting

polymers[1, 4, 9] (ECPs) (*e.g.* polypyrrole) have been the subject of considerable research as electrode materials due to their high conductivity, low-cost and facile synthesis and preparation.[9-11] With high porosity and surface area, ECPs are able to store energy through physical and chemical processes.[9, 12, 13]

One limitation of ECPs, however, is their relatively low charge-capacity. Various approaches have been investigated to increase the energy densities of ECPs, such as incorporating redox-active side groups,[14-17] inorganic molecules,[18, 19] and redox molecule dopants, or creating nanostructured electrodes to increase electrode/electrolyte contact and utilization.[11, 20, 21] Recently, several groups have examined incorporating organic redox molecules or polymers within ECPs networks due to their stability, low cost, and environmental friendliness.[16, 22, 23] Small molecules provide an increased enhancement in capacitance compared to redox polymers[24-28] due to their high charge capacity on a per mass basis. For example, polypyrrole electrodes showed in increase in capacitance from 249 F g^{-1} to 550 F g^{-1} when synthesized with 1,4-benzoquinone.[22] However, the use of polymers leads to more stable confinement of the redox materials, as small molecules diffuse out of the electrodes overtime. Due to the presence of phenolic groups, several groups have integrated sulfonated lignin, a renewable, abundant, and low-cost biopolymer, as part of an electrode. Lota *et al.*[29] showed that a thin layer of lignosulfonate deposited on carbon led to an increase in EDLC from 155 F g^{-1} to 181Fg^{-1}. Later, Milczarek and Inganäs[23] integrated sodium lignosulfonate (SLS) within polypyrrole networks to increase the electrode capacitance up to 450 F g^{-1}, albeit for very thin polymer films. Subsequently, Admassie and co-workers[30] developed a ternary

composite to enhance the capacitance of polypyrrole/lignosulfonate composite with the addition a multivalent metal ion 682 F g^{-1}.

While SLS shows promise for low-cost energy storage, it is a by-product of the sulfite pulping process, which is outdated, environmentally unsound, and being phased out worldwide.[31] Thus, SLS is continuously declining in availability. Alkali lignin, however, which is derived from the modern Kraft pulping process and accounts for ~98% of the world pulp production,[32] is becoming increasingly available with the implementation of processes for the recovery of lignin from the Kraft black liquor (*i.e.*, SLRP™, LignoBoost™, LignoForce Systems™). However, the low solubility of this form of lignin in inorganic acids has limited its use in electrical energy storage. Inorganic acids are typically used to prepare conducting polymer films, which provide electron transport to the redox groups in lignin in mixed polymer films.

In this work, we enable the use of alkali lignin (AL) to increase the capacitance of composite polymer electrodes by utilizing acetic acid solvents as the deposition solvent. Polypyrrole electrodes are synthesized with commercially available AL (Aldrich) and SLS (VWR) in acetic acid to increase the electrode charge capacity, which will ultimately increase device energy density. We report how the concentration of lignin, molarity of acetic acid, and chemical functionality of lignin affect the physical structure, electrode composition and electrochemical properties. Additionally, we present a correlation between lignin phenolic content (redox component) and the electrochemical properties using alkali lignin fractions that are separated based on MW and aromatic content using an elevated-temperature, pH-driven fractionation process developed by Velez *et al.*[33, 34]

2.2 Experimental methods

2.2.1 Materials

All chemicals were purchased from Fisher Scientific, Sigma- Aldrich, VWR, and MTI Corporation, and used as received unless otherwise stated. Pyrrole was purified by fractional distillation. Alkali lignin (AL) was purchased from Sigma-Aldrich and sodium lignosulfonate (SLS) from VWR. Narrow-pH, liquid-lignin fractions were recovered from a softwood Kraft black liquor using a recently reported, pH-based fractionation process, which involves sequential CO_2 addition with black liquor recycle at elevated temperatures to separate a lignin fraction with a desired, narrow-pH region. Briefly, fresh Kraft black liquor (pH= 13.6) was charged to a 2 L batch reactor and the temperature was increased to 115°C. CO_2 gas was fed to decrease the pH to ~13.0; this caused the phase separation of a liquefied, water-solvated, lignin-rich phase. This "liquid-lignin" fraction was collected for analysis, and the spent black liquor was recycled for the next fractionation experiment in which more CO_2 was fed to decrease the pH even lower and produce yet another liquid-lignin fraction. This procedure was repeated to produce seven, narrow-cut, liquid-lignin fractions, each encompassing a pH range of ~0.5 units. Details of this process can be found elsewhere.[33, 34]

2.2.2 Substrate preparation

Platinum substrates were cleaned by the following method: bath sonication in ethanol for 5 min, polished on sandpaper (Emery 500 mesh and 1200 mesh), rinsed with DI water, polished with BASi PK-4 polishing kit, rinsed with DI water, and then

sonicated for 5 minutes in DI water. Stainless steel foil substrates were polished with sandpaper (Emery 500 mesh), dried in vacuum oven at 110 °C for 10 min, and then treated for 30 min in UV–ozone (Novascan PSD-UV). The electrode mass was determined using a semi-microbalance (Ohaus DV215CD, 0.01 mg).

2.2.3 Polypyrrole-lignin film synthesis

Electropolymerization was performed in a 3-electrode cell utilizing a Gamry Instruments Reference 600 Potentiostat/Galvanostat/ZRA and Gamry Framework Software v5. In one setup, the 3-electrode cell was comprised of a platinum working electrode (1.06 mm^2 surface area), a coiled platinum wire as a counter electrode, and a Ag/AgCl (maintained in a 3 M NaCl solution) reference electrode. Polymerization solutions consisted of 0.1 M pyrrole monomer in 0.5 M sulfuric acid (H_2SO_4) or acetic acid (0 M, 1 M, 2 M, 5 M, 10 M, 15.3 M). Standard synthesis solutions for preparing polypyrrole–lignin mixtures were based on a weight ratio of Py : lignin of 1 : 2, which included 0.134 g (10 mL solutions) of either sodium lignosulfonate or alkali lignin. Electrodes were also prepared with varying lignin concentrations (g L^{-1}): 0.67, 1.34, 3.35, 6.7, 13.4, 33.5. These solutions were polymerized at room temperature using chronopotentiometry with a current of 20 μA for 300 s. The resulting films were rinsed with DI water and then placed in 0.5 M H_2SO_4 for testing.

Polymerization on gold substrates (20 mm^2 surface area) consisted of a 3-electrode cell utilizing a high surface area platinum mesh (gauze 52 mesh, Alfa Aesar) as a counter electrode and a Ag/AgCl as a reference electrode. Films were prepared with 0.1

M pyrrole monomer and 0.067 g of sodium lignosulfonate (1 : 1 wt%) in 0.5 M H_2SO_4 and 0.067 g of either sodium lignosulfonate or alkali lignin in 10 mL of 15.3 M acetic acid (1 : 1 wt%) at 0.195 mA for 300 s. Polymerization on stainless steel substrates were also carried out in 3-electrode cells utilizing a Teflon compartment. The Teflon cell created a stainless steel working electrode surface area of 47 mm^2. A platinum mesh was used as a counter electrode and combined with a Ag/AgCl reference electrode. The pyrrole was polymerized from a 0.1 M pyrrole monomer in 0.5 M sulfuric acid using a chronopotentiometry with a current of 2.5 mA for 30 s. The resulting film was rinsed with DI water. Polymerization of Py with SLS used 0.5 M H_2SO_4 and a current of 2.5 mA for 120 s and polymerization of Py with AL used acetic acid with a current of 90 μA for 3333 s. PPy-Kraft lignin samples were prepared using the Teflon cell setup with 5 mL solutions (1 : 1 wt% Py–lignin).

2.2.4 Electrochemical analysis

Electrochemical characterization was performed using a Gamry Instruments Reference 600 Potentiostat/Galvanostat/ZRA in 0.5 M H_2SO_4 using cyclic voltammetry from 0 to 0.8 V at various scan rates (5–100 mV s^{-1}), electrochemical impedance spectroscopy (EIS) at 0.7 V over a frequency range of 10 000 to 0.1 Hz using a perturbation amplitude of 10 mV, and charge–discharge measurements at current densities between 0.14 and 1.08 mA cm^{-2}. The effect of the concentration of H_2SO_4 as testing solution in the electrochemical performance of the electrodes is shown in Appendix A, **Figure A.1**

2.2.5 Surface morphology and elemental analysis

The film surface characterization was performed by scanning electron microscopy (SEM) in a Hitachi SU-6600 Analytical VP FE-SEM at a beam intensity of 5 kV at high resolution; the samples were placed on 45° aluminum sample holders with carbon tape. Images were captured at magnifications of x50k, x22k, x10k, x8k, x4k, x1.20k. Quartz PCI software was used to make the measurements; this software was calibrated with the microscope used. An average film thickness is presented. Elemental analysis was performed by energy dispersive X-ray spectroscopy (EDX).

2.2.6 Inductively coupled plasma atomic emission spectroscopy (ICP-AES)

The sulfur content of the lignin samples was determined by the Agricultural Service Laboratory at Clemson University via ICP- AES.

2.2.7 Device characterization

Supercapacitors were assembled in coin cell apparatus (MTI Corp). Polypyrrole–lignin films on stainless steel substrates were used as the cathode and activated carbon (AC) (MTI Corp, 2000 m^2 g^{-1}) as the anode. The anode was prepared by dispersing 0.01 g conductive graphite (CG), 0.005 g carboxymethyl cellulose (CMC), and 0.085 g activated carbon in 10 mL of DI water. The CMC was first left to dissolve in the DI water for 6 h with periodic agitation, then finely ground CG and AC were added. This solution was sonicated for 40 min and then the required amount was filtered onto a Whatman glass microfiber type A. The mass of the activated carbon was set to 120% the charge of

the cathode determined at a scan rate of 10 mV s^{-1}. The film on the filter paper acted as the anode while the filter paper itself was the membrane separating the anode and cathode. 0.5 M H_2SO_4 was used as an electrolyte. Cyclic voltammetry was performed at scan rates of 5–100 mV s^{-1} and charge–discharge rates at currents of 0.5, 0.25, and 0.125 mA from 0 to 0.8 V. The AL electrode had an approximated mass of 0.21 mg whereas the activated carbon electrode had a mass of 2.23 mg.

2.3 Results and discussion

As the second-most abundant, naturally occurring biopolymer after cellulose, lignin makes up to 20–40% of plant dry mass.[26, 35] Lignin is a co-product of the chemical pulping process of wood with an annual United States production over 2.49 x 10^{10} kg per year.[36] The chemical structure of lignin, in general, consists of a complex network of phenylpropane units with hydroxylated and methoxylated aromatic rings, arranged in a 3D structure (**Figure 2.1**) that depends on the type of plant (softwood or hardwood) utilized as the raw material. The chemical functionality of the recovered lignin is somewhat governed by the pulping process. For example, Kraft cooking generates alkali lignin (AL), which is a hydrophobic polymer with a lower molecular weight and higher aromatic hydroxyl content than the natural lignin, giving rise to solubility in aqueous bases. Acid sulfite cooking leads to sulfonated lignin (SLS), which imparts hydrophobic and hydrophilic properties and, therefore, solubility in water. Of note, the molecular weight of SLS from the sulfite process is generally higher than AL from the Kraft process.[26-28, 35, 37] As shown in **Figure 2.1**, aromatic methoxy substituents are converted

to hydroxyl groups upon voltammetric cycling above 0.6 V, which allow for the reversible oxidation of hydroquinone to quinone to increase charge capacity.[38]

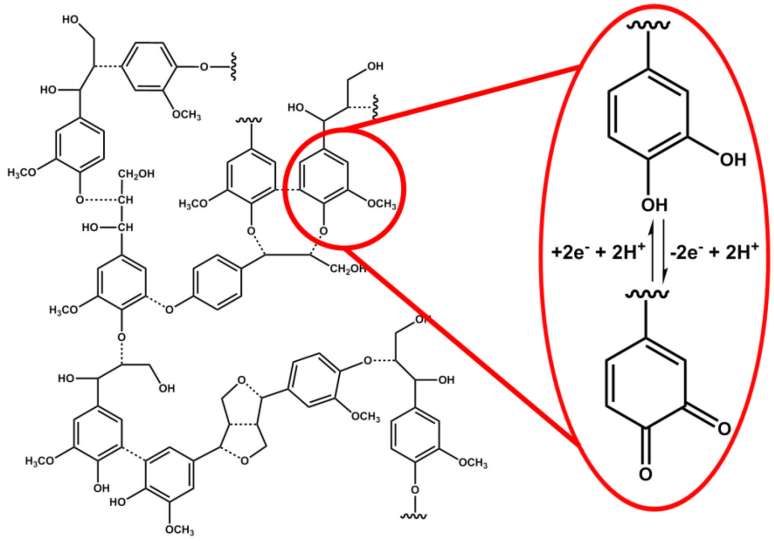

Figure 2.1. Illustrative schematic of lignin structure along with the redox processes occurring between hydroquinone/quinone (QH_2/Q). Aromatic methoxy groups are converted to hydroxyl groups during the initial voltammetric cycles.

Applications in electrochemistry and energy storage arise from the presence of phenolic groups, which give rise to oxidation and reduction processes. Of the different forms of lignin, SLS has been investigated as an electrode component due to its high solubility in acids; however, as stated above, it comprises less than 2% of the total lignin recovered in the various paper-pulping processes,[36] and its supply is in long-term decline. AL accounts for most of the remaining lignin, but its limited solubility in inorganic acids represents a challenge for its integration with ECPs. To enable the use of AL in mixed-polymer electrodes, we explored its solubility in organic acids and found that acetic acid

(AA) with a certain molarity range is suitable for solubilizing AL and also for polymerizing pyrrole.

Acetic acid (AA) was considered for use as an electrolyte for synthesizing polypyrrole–alkali lignin (AL) mixed electrodes because of the improved AL solubility and the availability of protons to assist the electropolymerization of pyrrole. Mixed polymer electrodes were prepared in AA with commercially available lignin materials, which serve as model polymers. In the presence of lignin, pyrrole is electrochemically oxidized to form polypyrrole using chronopotentiometry (**Figure 2.2a**). During the polypyrrole synthesis, AL is entrapped within the growing film, leading to a formation of a pronounced redox couple in the cyclic voltammetry (CV) profile near 0.55 V (**Figure 2.2b**). The peak current – which is a measure of electrode performance – correlates with the lignin composition in the electrode, which is affected by the AA molarity (**Figure 2.2c**) and the polymer concentration (**Figure 2.2d**) of the synthesis solution.

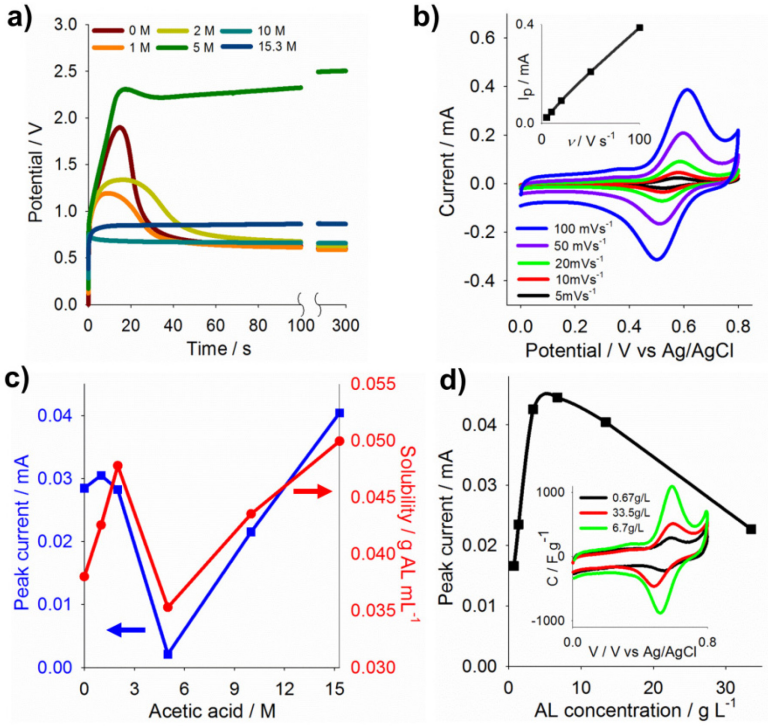

Figure 2.2 Preparation of PPy-lignin composite electrodes. (a) Chronopotentiometry deposition profiles (V *vs.* Ag/AgCl) for PPy/AL films prepared in various [AA]. (b) Cyclic voltammetry profiles for PPy (6.7 g L^{-1}) electrodes polymerized in 15.3 M AA on Pt electrodes (inset: peak current *vs.* scan rate). (c) Peak current of PPy/AL (13.4 g L^{-1}) electrodes (10 mV s^{-1}) as function of [AA] (blue) and AL solubility *vs.* [AA] (red). (d) Peak current of PPy/AL films as function of [AL] (g L^{-1}). Inset: cyclic voltammetry profiles normalized to specific capacitance for various [AL]. Electrochemical measurements are conducted in a 3-electrode configuration with Ag/AgCl reference and Pt counter electrodes.

Figure 2.2b shows the Cyclic Voltammetry (CV) profiles of PPy/AL electrodes (0.1 M Py, 6.7 g L^{-1} AL) synthesized in 15.3 M AA. As the potential scan rate is increased from 5 to 100 mV s^{-1}, the current increases proportionally (inset), indicative of ion-adsorption dependent redox processes. At low electrode potentials (0 to 0.4 V), the

electrode behavior is governed by the PPy, which typically exhibits a constant current with increasing voltage.[23] As the potential increases above 0.5 V, a sharp redox couple is observed resulting from the oxidation of the phenolic groups on the AL, and the intensity of these peaks is associated with the composition of lignin incorporated in the film.

The molarity of the AA electrolyte was shown to affect the solubility of AL and also the electropolymerization of pyrrole, both of which determine the composition of AL in the mixed polymer electrode. As shown in **Figure 2.2a**, the voltage required to maintain the constant current set-point during polymerization increases with [AA] up to 5 M, after which the required voltage decreases. Films were not synthesized in glacial acetic acid (17.4M) due to the low solubility of the AL. The differences in voltage required for polymerization is likely related to the AL solubility, which is presented in **Figure 2.2c**, and shows a minimum in AL solubility for 5 M solutions (highest required voltage). The redox characteristics of PPy/AL electrodes prepared in AA showed a similar trend in redox activity compared to the AL solubility (while keeping constant polymerization charge, [PPy] and [AL]). The peak current from cyclic voltammetry (CV, 10 mV s^{-1}) measurements followed the AL solubility trend, which can be attributed to a lower amount of AL incorporated in the film when prepared from solutions with lower AL solubility. We also observed a lower PPy deposition rate in the AA molarity range of 5 M, which is not yet completely understood. For reference, the electrochemical performance of mixed polymer electrodes prepared in 5 M AA is shown in **Figure A.2**.

The influence of AL concentration ([AL]) on the electrochemical performance of the mixed polymer electrodes was determined by varying [AL] in 0.1 M Py, 15.3 M AA

solutions. The peak current obtained from CV at 10 mV s^{-1} is shown in **Figure 2.2d** for films synthesized in solutions with increasing [AL]. A low peak current is obtained at low [AL] because only a limited amount of AL is incorporated into the growing PPy network. The peak current increases with increasing [AL] as more lignin is integrated into the polymer electrode providing addition redox activity from the phenolic groups. Further increasing [AL] beyond 13.4 g L^{-1} (Py : AL wt% ratio 1 : 2) resulted in a decrease in electrochemical activity of the resultant electrodes. The decrease in performance is a result of the insulating nature of the lignin, which inhibits the electrochemistry in the polymer network. The decrease in redox activity ($C = I/v$) on a per mass basis is shown in the inset of **Figure 2.2d**.

The performance of mixed polymer electrodes comprising electrically conducting polymers and sodium lignosulfonate (SLS) is described in detail in the literature.[16, 23] As discussed above, widespread use of lignin in energy storage systems will require utilization of the abundant alkali lignin. Below, we compare the physical and electrochemical properties of lignin–polypyrrole composite electrodes prepared using our new synthesis process with AL in acetic acid to the current state-of-the-art method utilizing SLS in sulphuric acid.

PPy–lignin electrodes were synthesized with (i) AL and (ii) SLS in 15.3 M AA and with (iii) SLS in 0.5 M H_2SO_4. PPy/AL electrodes could not be obtained in H_2SO_4 due to the poor AL solubility. As a control, PPy electrodes were also synthesized using each electrolyte. Film morphologies were examined using scanning electron microscopy (SEM) and are shown in **Figure 2.3** for PPy (thickness: 0.78 μm, mass: 0.019 mg),

PPy/AL synthesized in AA (2.53 μm, 0.088 mg), and PPy/SLS synthesized in AA (10.65 μm, 0.076 mg) and H_2SO_4 (2.24 μm, 0.068 mg). Interestingly, PPy/AL electrodes synthesized in AA (**Figure 2.3a**) had similar morphology to PPy/SLS electrodes prepared in H_2SO_4 (**Figure 2.3b**) which were similar to the reference PPy electrodes in AA (**Figure2.2c**) and H_2SO_4 (not shown). From the observed structures, we can conclude that polymer–solvent interactions of AL/AA were similar to SLS/H_2SO_4 resulting in film morphologies governed by polypyrrole electropolymerization kinetics. When PPy/SLS was prepared in AA (**Figure 2.3d**), however, films displayed a granular, openly porous structure, with a density much less than similar films synthesized in H_2SO_4 (1.54 g cm^{-3} *vs.* 0.36 g cm^{-3}). The difference in the morphology of PPy/SLS in AA arises because AA acts as a moderate to poor solvent for SLS causing the polymer to act as a surfactant around growing clusters of PPy.

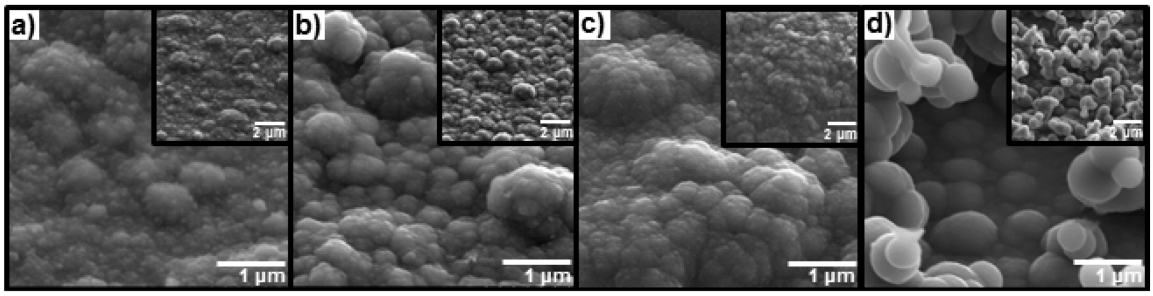

Figure 2.3 Scanning electron microscopy images of films electrochemically polymerized using chronopotentiometry (0.975 mA cm^{-2}) on gold electrodes with a magnification of x22k and inset at x10k. Films synthesized in 15.3 M AA are shown for (a) PPy/AL, (c) PPy, and (d) PPy/SLS; and films synthesized in 0.5 M H_2SO_4 are shown in (b) PPy/SLS. The concentration of lignin was 6.7 g L^{-1} in (a), (b) and (d).

The electrochemical performance of PPy-lignin composite films for cathode materials are obtained from 3-electrode measurements, which are shown in **Figure 2.4**. Cyclic voltammetry profiles are presented as of specific capacitance (F g^{-1}), which is current (A) divided scan rate (V s^{-1}) and electrode mass (g), *versus* voltage (V) to account for the mass variation in each film (**Figure 2.4a**). PPy/SLS electrodes synthesized in 15.3 M AA (red) and 0.5 M H_2SO_4 (blue) exhibited similar redox activity, even with the notably different film morphologies, shown in **Figure 2.3**, indicating similar film composition. When measured in 0.5 M H_2SO_4 electrolytes, PPy/AL electrodes exhibited between 20–30% higher capacitance than the films with SLS. Each mixed polymer films exhibited a fairly linear peak current dependence with scan rate (**Figure 2.4b**) indicating ion-adsorption limiting redox processes, which is typical for redox electrodes comprising polypyrrole rather than an ion diffusion-limit mechanism.

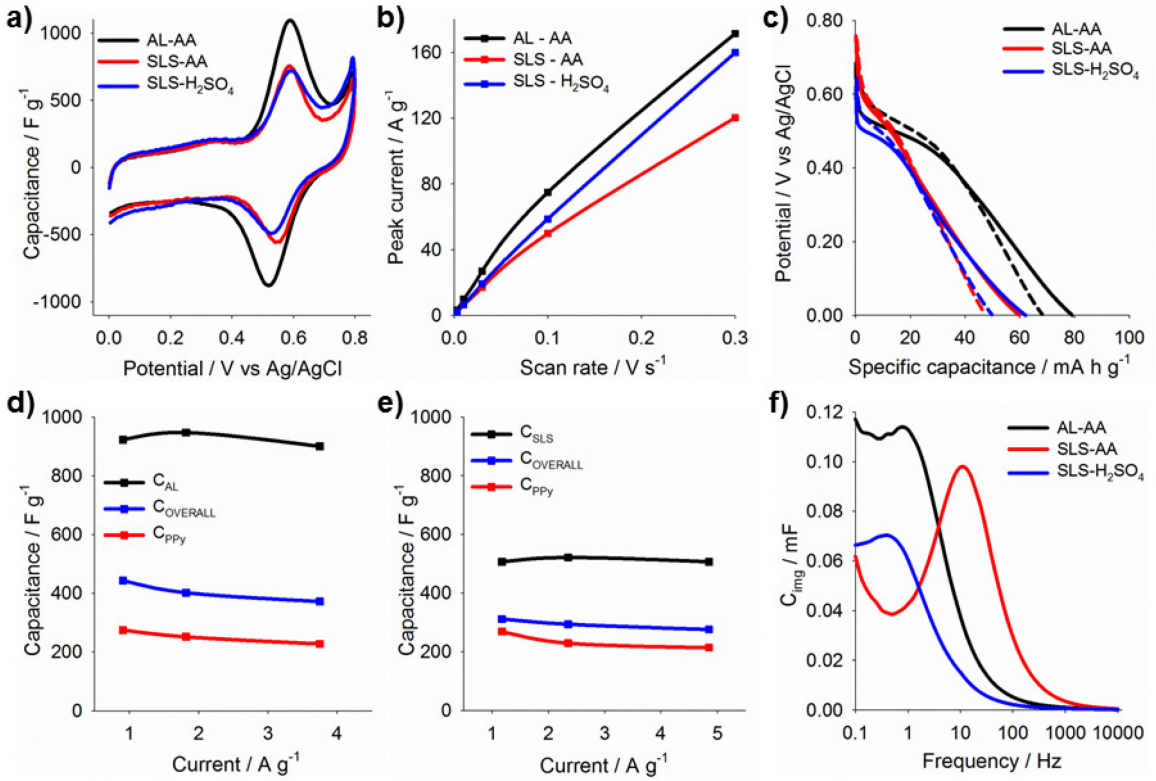

Figure 2.4 Electrochemical properties of PPy/AL, PPy/SLS synthesized in 15.3 M AA and PPy/SLS synthesized in 0.5 M H_2SO_4. (a) Cyclic voltammetry profiles normalized to specific capacitance (10 mV s^{-1}). (b) Peak current normalized by mass as function of scan rate. (c) Discharge profiles at current densities of 0.55 mA cm^{-2} (- - -) and 0.14 mA cm^{-2} (—). Specific capacitance *vs.* discharge current in terms of the two contributing capacitances: polypyrrole (C_{PPy}) and lignin (C_{AL}) or (C_{SLS}) for (d) PPy/AL and (e) PPy/SLS in 0.5 M H_2SO_4. $C_{OVERALL}$ is the total capacitance. (f) Bode plots of the imaginary capacitance (C'') *vs.* frequency. PPy-lignin electrodes were prepared on Au electrodes (20 mm^2) using chronopotentiometry (0.195 mA, 120 mC, ratio 6.7 g L^{-1} lignin). Electrochemical measurements were conducted in a 3-electrode cell with Ag/AgCl references and Pt counter electrodes.

Constant current charge–discharge measurements were performed on the PPy–lignin electrodes and the discharge characteristics are reported in **Figure 2.4c** as electrode voltage *vs.* charge capacity, which is simply the discharge time normalized by applied current and mass. Consistent with the CV profiles, PPy/SLS in H_2SO_4 and AA exhibited similar charge capacities, between 50 and 60 mA h g^{-1}, for discharge currents of 0.14–0.55 mA cm^{-2}, while PPy/AL showed a 30% increase to 70 to 80 mA h g^{-1} for similar currents (**Figure 2.4c**). The capacitance contributions from PPy and lignin (AL or SLS) were calculated from the discharge profiles (**Figure 2.4d** and **2.4e**) using previous methods.[22, 23, 39] Two distinct slopes were observed with a transitioning point around 0.45 V, indicating two separate charge storage mechanisms from lignin (AL or SLS) and polypyrrole. The individual capacitance contributions were calculated from the inverse of the discharge slope obtained from each segment. Alkali lignin (AL) contributed to ~900 F g^{-1} whereas the SLS provided ~500 F g^{-1}. As expected, the polypyrrole contribution remained fairly constant (~250 F g^{-1}) in each film. Furthermore, the overall capacitance could be determined over the entire discharge range, which gave ~400 F g^{-1} and ~300 F g^{-1} for PPy/AL and PPy/SLS, respectively, corroborating the increase in capacitance observed in **Figure 2.4a**.

Although electrodes comprising PPy/SLS synthesized in AA and H_2SO_4 appear similar over the time scales investigated with CV and charge–discharge, these films have notably different relaxation time constants, τ_c, which is determined from electrochemical impedance spectroscopy (EIS). τ_c is a measure of how fast electrodes can discharge with 50% efficiency and is defined as the reciprocal of the peak ($\tau_c = 1/f_{peak}$) in the imaginary

capacitance (C'') from the Bode plot of C'' *vs.* frequency (**Figure 2.4f**).[26] From these measurements, we found that PPy/SLS electrodes synthesized in AA had the shortest relaxation time constant, $\tau_c = 0.1$ s, followed by PPy/AL with $\tau_c = 1$ s, and then PPy/SLS grown in H_2SO_4 ($\tau_c = 1.67$ s). These results are consistent with the morphology differences observed in **Figure 2.3**. PPy/SLS electrodes grown in AA exhibited a granular, openly porous structure that allows for increased electrode/electrolyte contact which is more conducive for rapid ion exchange with the electrolyte. Furthermore, PPy/AL and PPy/SLS electrodes grown in AA also displayed notably lower charge-transfer resistances, as evidenced by the Nyquist plots shown in Appendix A, **Figure A.3**.

Lignin samples with varying phenolic content were recovered from black liquor produced during the Kraft paper pulping process using a recently reported pH-based fractionation process. These lignin fractions provide a means to study the influence of lignin chemistry, *e.g.* phenolic content, on the electrochemical performance of the PPy–lignin samples. Solvated liquid-lignin fractions are separated from the black liquor at an elevated temperature using sequential CO_2 additions that incrementally lower the pH and precipitate lignin with varying MW and phenolic content (details of this process can be found elsewhere [33, 34]). Composite polymer electrodes were prepared as stated above, but here, lignin samples were allowed to dissolve overnight in the 15.3 M AA solution prior to Py addition and polymerization.

The electrochemical characteristics of the PPy–lignin composite electrodes prepared with different lignin fractions (pH 9.5, 10, 10.5, 11), in addition to the non-fractionated sample (all of the lignin precipitated in the pH range 13.6–9.5), are presented

in **Figure 2.5**. The CV profiles normalized to specific capacitance (**Figure 2.5a**) showed that electrodes comprising lignin fractions collected between pH 9.5–10 exhibited the highest redox activity, whereas electrodes prepared with lignin samples collected at high pH exhibited notably lower performance. The estimated phenolic OH content expressed as mmol of OH per mmol of methoxyl (**Figure 2.5c** blue) was shown to increase as the pH of the precipitated lignin fraction decreased,[33] which affects the number of accessible redox sites. As expected, the redox activity of the PPy–lignin electrodes increased with increasing phenolic content, as shown in **Figure 2.5b** (the peak current of the non-fractionated lignin sample is indicated by the dashed line for reference). Non-lignin contaminants (polysaccharides) co- precipitate with the lignin fractions preferentially in the pH range from 11.0–11.5 (**Figure 2.5c** red); thus, the lignin fractions that precipitate in this pH range contained up to 6 wt% polysaccharides. As a result, PPy–lignin electrodes with these samples exhibited inferior performance compared to the non-fractionated lignin sample. As shown in **Figure 2.5d**, each PPy–lignin sample exhibited a linear relationship between the peak current (normalized by mass) and scan rate, indicating that the various lignin fractions do not inhibit ion diffusion within the polymer electrodes for the compositions investigated.

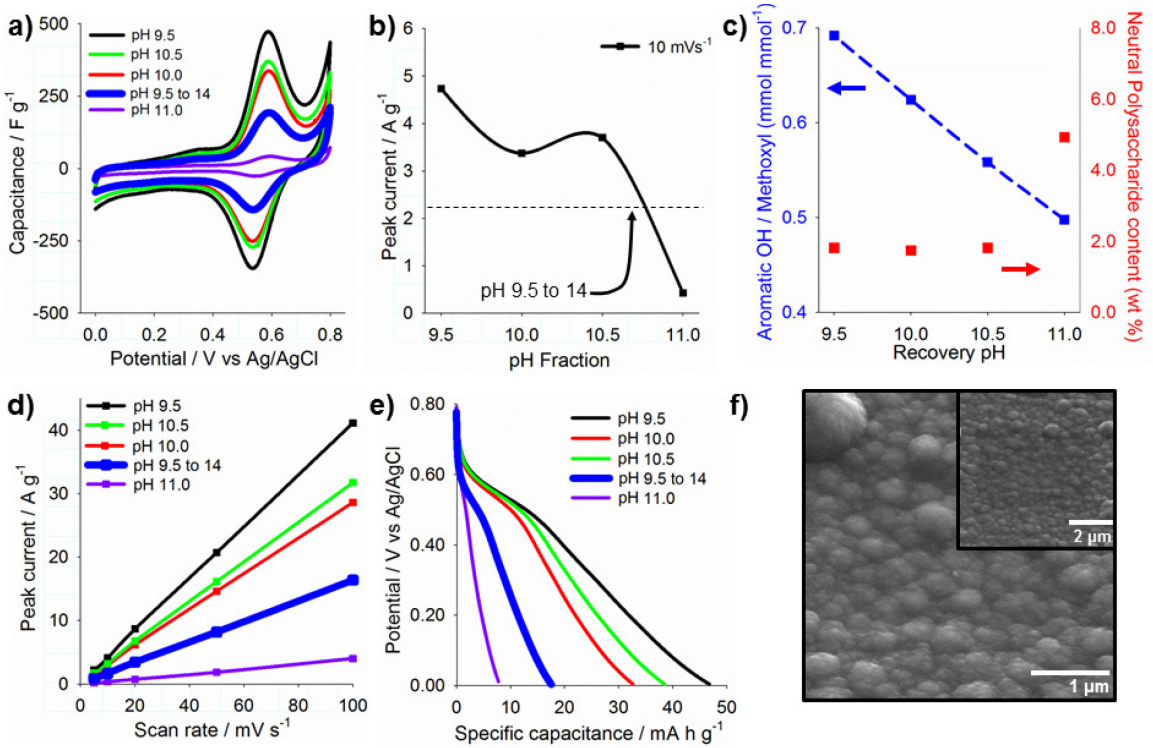

Figure 2.5 Electrochemical properties of PPy-lignin pH fractions (6.7 g L^{-1} lignin) synthesized on Pt electrodes (0.02 mA, 6 mC). (a) Cyclic voltammetry profiles normalized to specific capacitance (10 mV s^{-1}). (b) Peak current normalized by mass (10mV s^{-1}) as a function of the lignin fractionation pH in the PPy-lignin composite films. (c) Aromatic content and quantified non-lignin impurities (*e.g.* polysaccharides) as a function of fractionation pH. (d) Peak current (normalized by mass) *vs.* scan rate. (e) Discharge profiles at 0.14 mA cm^{-2}. (f) Scanning electron microscopy of PPy-lignin (pH 9.5 fraction) at x22k, inset at x10k. Electrochemical measurements were conducted in a 3-electrode cell with Ag/AgCl reference and Pt counter electrodes.

Consistent with the CV characteristics, the charge capacities obtained from the discharge profiles of the electrodes comprising pH fractions (**Figure 2.5e**) showed for pH 9.5 to 10.5 charge capacities between 47 and 33 mA h g^{-1}, while pH 11 showed 8 mA h g^{-1}. As mentioned above, lignin structure and functionality will vary depending on the

plant and the pulping process, and will have an impact on the redox activity. The differences in performance observed are a reflection of the intrinsic chemical functionality variations within the lignin from the black liquor provided directly from an industrial process,[40] which has not undergone any further treatment.

The morphology of pH 9.5 and 10.5 (**Figure 2.5f**) was studied by SEM on gold electrodes. Comparing these images with PPy and PPy/AL films presented in **Figure 2.3a** and **2.2c** showed no morphological differences between the two pH fractions that exhibited similar thicknesses (2.46 and 2.16 μm, respectively). Slight variations in chemical functionality did not affect the solvent behavior of lignin in AA or influence the polymer density. Thus, it was determined that the variations in electrochemical activity were solely a result of the chemical functionality of the various lignin fractions.

The elemental compositions of the various electrodes were measured using elemental analysis (EDX), and these values were used to determine wt% of lignin in the composite polymer electrodes. The dopant level of AA and H_2SO_4 in reference PPy electrodes were calculated from the elemental compositions, and the approximate molecular formulas of AL and SLS were used from data reported in previous studies,[36] where the sulfur content was adapted to fit the one in the lignin reactants. Polypyrrole films synthesized in AA exhibited higher doping levels (by wt%) relative to films grown in H_2SO_4. This has been observed in previous works[41, 42] with weak organic acids. Even with higher doping levels, each film displayed similar electrochemical activity on a per mass basis. Accordingly, PPy films doped with AA counter-ions are able to achieve a higher extent of oxidation (reduction) during the charge (discharge) processes.

To determine the lignin wt% in PPy–lignin electrodes grown in AA and H_2SO_4, elemental compositions from EDX were fit to elemental compositions of PPy–lignin-dopant films, where dopant reflects either AA or H_2SO_4, depending on the growth media. The fitting parameters in this method were the molar ratios of lignin (relative to PPy) and H_2SO_4, which can be incorporated into the films during electrochemical testing. The sum of the error of individual elemental compositions was minimized by changing the fitting parameters (molar compositions). The calculated wt% of each component is presented in **Table 2.1**. The range in compositions reflects a variation of parameter analysis in which the error did not significantly change. For reference, elemental compositions of nitrogen and sulfur from the EDX analysis, as well as the sulfur content in the lignin determined from ICP-AES are presented. The sulfur compositions followed a similar trend as its composition in the integrated lignin, suggesting reasonable parameter fitting. A detailed description of the fitting calculations can be found in Appendix A.

Table 2.1. Estimated mass composition of the different constituents in PPy/Lignin films.

Sample[a]	Polypyrrole [wt.%]	Lignin [wt.%]	Acetic Acid [wt.%]	Sulfate [HSO_4^-/SO_4^{-2}] [wt.%]	EDX, N[a] [wt.%]	EDX, S[a] [wt. %]	Lignin, S[b] [wt. %]
PPy – AA	53.5 – 59.1	-	32.3 – 38.6	7.9 – 8.7	13.3	2.9	-
PPy – SA	87.8 – 88.9	-	-	11.9 – 12.2	19.3	3.9	-
PPy/AL – AA	21.9 – 25.9	51.9 – 55.9	11.9 – 14.2	8.4 – 10.2	5.5	4.0	3.6
PPy/SLS – AA	26.2 – 30.5	42.1 – 51.7	14.3 – 16.6	7.7 – 10.9	6.2	5.6	5.1
PPy/SLS – SA	38.3 – 47.4	45.9 – 56.4	-	5.3 – 6.6	8.7	4.1	5.1
PPy/FXN pH 9.5	31.8 – 35.8	37.6 – 45.2	17.4 – 19.6	4.8 – 5.4	7.7	2.9	2.7
PPy/FXN pH 10.5	30.4 – 33.1	42.2 – 47.4	16.6 – 18.1	5.6 – 6.7	7.2	2.9	2.4

[a] Elemental analysis data from EDX.

[b] Sulfur content in lignin reactant before electrochemical deposition.

The alkali lignins (AL, pH 9.5 and pH 10.5) exhibited a similar range of lignin entrapped within the film, which varies between ~37 to 47 wt%; all these samples showed a small composition of sulfate (HSO_4^-/SO_4^{2-}) between ~5 to 7 wt%, which comes from electrochemical measurements in 0.5 M H_2SO_4. These values are similar to the sulfate content in the reference PPy electrodes polymerized in AA electrolytes. Samples synthesized with SLS showed a similar lignin content to those prepared with AL, with compositions varying between ~42–52 in AA and ~46–56 wt% in H_2SO_4. Because the redox activity of PPy/SLS electrodes was lower than PPy/AL, we can conclude that the AL form of lignin has more accessible phenolic groups contributing to the composite film's redox behavior. Furthermore, the lower molecular weight of AL relative to SLS further supports the conclusion for a higher phenolic content per mass basis (the cleavage of aryl-ether bonds during the pulping process causes an increase in phenolic content and a decrease in molecular weight).[35, 40]

PPy/SLS (0.5 M H_2SO_4) and PPy/AL (15.3 M AA) synthesized on stainless steel foil were used as cathode materials in asymmetric supercapacitors with activated carbon (AC) anodes. An illustrative schematic of the PPy/AL–AC device is presented in **Figure 2.6a**. As a control, a symmetric supercapacitors with AC electrodes was tested. For comparison purposes, the single electrode CV profiles (from 3-electrode measurements) normalized to capacitance are shown in **Figure 2.6b**. AC electrodes seem to exhibit a low capacitance at 10 mV s^{-1}; however, for the purpose of these experiments the mass of the anode was increased up to a point where the CV profile (current vs. potential) of AC single electrode showed about a 20% increase in capacitance relative to PPy–lignin (SLS

or AL) electrodes (at the scan rates investigated, 10–100 mV s^{-1}) to ensure that PPy–lignin (SLS or AL) electrodes were not limiting device performance.

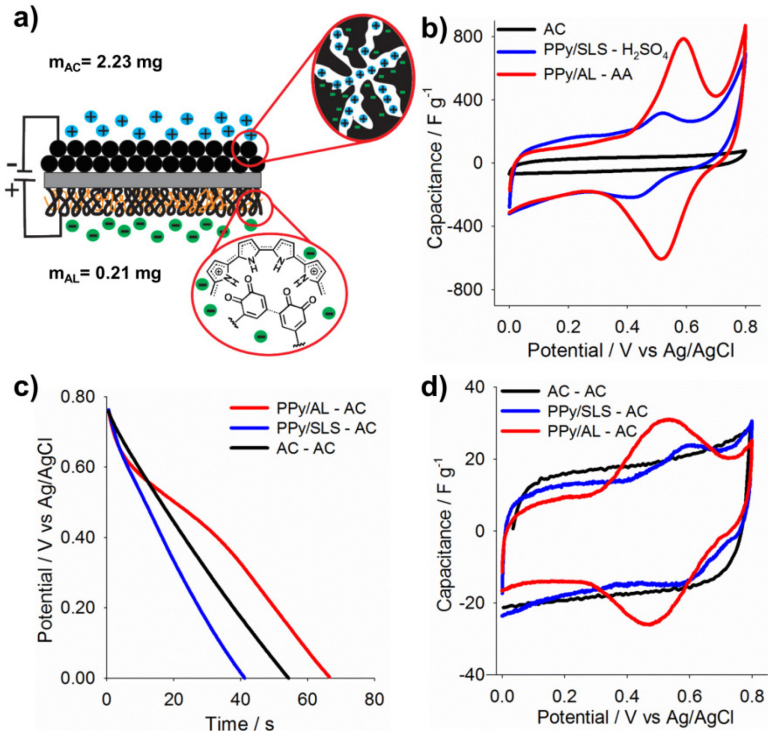

Figure 2.6 Electrochemical performance of asymmetric supercapacitors with PPy-lignin cathodes and activated carbon (AC) anodes (symmetric AC cells presented as a control). (a) Illustrative schematic of PPy/AL-AC cell. (b) Single-electrode CV profiles normalized to specific capacitance (10 mV s^{-1}) of electrodes prepared on stainless steel foil. (c) Supercapacitor (2-electrode) discharge profiles at 0.5 mA. (d) Device CV profiles normalized to specific capacitance (10 mV s^{-1}).

The discharge and cyclic voltammetry profiles of the asymmetric and symmetric cells are shown in **Figure 2.6c** and **2.6d**, respectively. Discharge profiles of cells comprising PPy/AL cathodes exhibited the highest charge capacity due to the added redox capacitance of the AL. It should be noted that the asymmetric cells are not properly

balanced, and higher device performance is expected with improved anode material design. The increase in electrochemical performance of PPy/AL cells is also evident in **Figure 2.6d**, where CV profiles normalized to specific capacitance, are shown. Although these cells are not significantly higher than symmetric AC cells, the redox behavior of the lignin is obvious in the CV profiles, which ultimately provides a higher cell capacitance. Further improvement in anode materials and cell design will enable the use of AL composite electrodes for ultra-low-cost energy storage.

A well-known limitation in redox polymers as the charge storage media for batteries and supercapacitors is cycle-stability. While the mixed polymer electrodes reported here are promising for low-cost energy storage, especially when considering the use of sustainable polymers from renewable sources (i.e. plants and trees), it should be noted that such materials suffer from poor stability (Appendix A, **Figure A.4**). This issue is likely due to irreversible reactions between (i) the two polymers in the electrodes or (ii) the polymers and the electrolyte and is the subject of ongoing research. It is expected that advances in material stability, along with the development of low-cost, polymeric anode materials, will provide exciting opportunities for stationary energy storage.

2.4 Conclusions

Using acetic acid electrolytes, alkali lignin, which accounts for 98% of the available lignin, could be efficiently incorporated into PPy redox electrodes during electrochemical polymerization. Synthesis conditions, including AA molarity and lignin concentration, were shown to strongly influence the resulting electrode properties. In

addition to enabling the use of the low-cost, widely available form of lignin in redox electrodes, we found that PPy/AL composite materials exhibited a 30% increase in capacitance compared with electrodes containing similar compositions of SLS, and 56% higher than PPy electrodes. The individual contributions showed that, in general, lignin comprises between the 40 to 60 wt% of the entire composite electrode, and contributed a higher capacitance than polypyrrole. Using lignin fractions separated directly from Kraft black liquor, we showed that the electrochemical performance of PPy–lignin electrodes could be further improved by increasing the aromatic content of the lignin. Further optimization and developments need to be done in other to deploy the entire potential of lignin as dopant for conducting polymers.

2.5 References

1. Liu C, Li F, Ma L-P, Cheng H-M. Advanced Materials for Energy Storage. *Adv. Mater.* **2010**, 22(8)**:** E28-E62.

2. Simon P, Gogotsi Y. Materials for electrochemical capacitors. *Nat. Mater.* **2008**, 7(11)**:** 845-854.

3. Song Z, Zhou H. Towards sustainable and versatile energy storage devices: an overview of organic electrode materials. *Energy & Environ. Sci.* **2013**, 6(8)**:** 2280-2301.

4. Wang G, Zhang L, Zhang J. A review of electrode materials for electrochemical supercapacitors. *Chem. Soc. Rev.* **2012**, 41(2)**:** 797-828.

5. Winter M, Brodd RJ. What Are Batteries, Fuel Cells, and Supercapacitors? *Chem. Rev.* **2004**, 104(10)**:** 4245-4270.

6. Ji H, Zhao X, Qiao Z, Jung J, Zhu Y, Lu Y*, et al.* Capacitance of carbon-based electrical double-layer capacitors. *Nat Commun* **2014**, 5.

7. Lokhande CD, Dubal DP, Joo O-S. Metal oxide thin film based supercapacitors. *Current Applied Physics* **2011**, 11(3)**:** 255-270.

8. Wei W, Cui X, Chen W, Ivey DG. Manganese oxide-based materials as electrochemical supercapacitor electrodes. *Chem. Soc. Rev.* **2011**, 40(3)**:** 1697-1721.

9. Snook GA, Kao P, Best AS. Conducting-polymer-based supercapacitor devices and electrodes. *J. Power Sources* **2011**, 196(1)**:** 1-12.

10. Frackowiak E, Khomenko V, Jurewicz K, Lota K, Béguin F. Supercapacitors based on conducting polymers/nanotubes composites. *J. Power Sources* **2006**, 153(2)**:** 413-418.

11. Heinze J, Frontana-Uribe BA, Ludwigs S. Electrochemistry of Conducting Polymers—Persistent Models and New Concepts†. *Chem. Rev.* **2010**, 110(8)**:** 4724-4771.

12. Burke A. Ultracapacitors: why, how, and where is the technology. *J. Power Sources* **2000**, 91(1)**:** 37-50.

13. Kötz R, Carlen M. Principles and applications of electrochemical capacitors. *Electrochim. Acta* **2000**, 45(15–16)**:** 2483-2498.

14. Groenendaal L, Jonas F, Freitag D, Pielartzik H, Reynolds JR. Poly(3,4-ethylenedioxythiophene) and Its Derivatives: Past, Present, and Future. *Adv. Mater.* **2000**, 12(7)**:** 481-494.

15. Groenendaal L, Zotti G, Aubert PH, Waybright SM, Reynolds JR. Electrochemistry of Poly(3,4-alkylenedioxythiophene) Derivatives. *Adv. Mater.* **2003**, 15(11)**:** 855-879.

16. Inganäs O, Admassie S. 25th Anniversary Article: Organic Photovoltaic Modules and Biopolymer Supercapacitors for Supply of Renewable Electricity: A Perspective from Africa. *Adv. Mater.* **2014**, 26(6)**:** 830-848.

17. Kearns JT, Roberts ME. Enhanced performance of triarylamine redox electrodes through directed electrochemical polymerization. *J. Mater. Chem.* **2012**, 22(6)**:** 2392-2394.

18. Ma X, Ni X. Copolymerization of EDOT with Pyrrole on TiO2 Semiconductor Films by One-Step Reaction, Structure-Dependent Electronic Properties, and Charge Conduction Models of the Composite Films. *Langmuir* **2014**, 30(8)**:** 2241-2248.

19. Suppes GM, Deore BA, Freund MS. Porous Conducting Polymer/Heteropolyoxometalate Hybrid Material for Electrochemical Supercapacitor Applications. *Langmuir* **2007**, 24(3)**:** 1064-1069.

20. Arico AS, Bruce P, Scrosati B, Tarascon J-M, van Schalkwijk W. Nanostructured materials for advanced energy conversion and storage devices. *Nat Mater* **2005**, 4(5)**:** 366-377.

21. Wang K, Wu H, Meng Y, Wei Z. Conducting Polymer Nanowire Arrays for High Performance Supercapacitors. *Small* **2014**, 10(1)**:** 14-31.

22. Arcila-Velez MR, Roberts ME. Redox Solute Doped Polypyrrole for High-Charge Capacity Polymer Electrodes. *Chem. Mater.* **2014**, 26(4)**:** 1601-1607.

23. Milczarek G, Inganäs O. Renewable Cathode Materials from Biopolymer/Conjugated Polymer Interpenetrating Networks. *Science* **2012**, 335(6075)**:** 1468-1471.

24. Gracia R, Mecerreyes D. Polymers with redox properties: materials for batteries, biosensors and more. *Polym. Chem.* **2013**, 4(7)**:** 2206-2214.

25. Strassberger Z, Tanase S, Rothenberg G. The pros and cons of lignin valorisation in an integrated biorefinery. *RSC Adv.* **2014**, 4(48)**:** 25310-25318.

26. Ragauskas AJ, Beckham GT, Biddy MJ, Chandra R, Chen F, Davis MF*, et al.* Lignin Valorization: Improving Lignin Processing in the Biorefinery. *Science* **2014**, 344(6185).

27. Thakur VK, Thakur MK, Raghavan P, Kessler MR. Progress in Green Polymer Composites from Lignin for Multifunctional Applications: A Review. *ACS Sustainable Chem. Eng.* **2014**, 2(5)**:** 1072-1092.

28. Azadi P, Inderwildi OR, Farnood R, King DA. Liquid fuels, hydrogen and chemicals from lignin: A critical review. *Renew. Sust. Energ. Rev,* **2013**, 21(0)**:** 506-523.

29. Lota G, Milczarek G. The effect of lignosulfonates as electrolyte additives on the electrochemical performance of supercapacitors. *Electrochem. Commun.* **2011**, 13(5)**:** 470-473.

30. Admassie S, Elfwing A, Jager EWH, Bao Q, Inganas O. A renewable biopolymer cathode with multivalent metal ions for enhanced charge storage. *J. Mater. Chem. A* **2014**, 2(6)**:** 1974-1979.

31. Lake M. Liquid Ligninin, LLC, Unpublished data. **2015**.

32. Gosselink RJA, de Jong E, Guran B, Abächerli A. Co-ordination network for lignin—standardisation, production and applications adapted to market requirements (EUROLIGNIN). *Ind. Crops Prod.* **2004**, 20(2)**:** 121-129.

33. Stoklosa RJ, Velez J, Kelkar S, Saffron CM, Thies MC, Hodge DB. Correlating lignin structural features to phase partitioning behavior in a novel aqueous fractionation of softwood Kraft black liquor. *Green Chem.* **2013**, 15(10)**:** 2904-2912.

34. Velez J, Thies MC. Solvated liquid-lignin fractions from a Kraft black liquor. *Bioresour. Technol.* **2013**, 148(0)**:** 586-590.

35. Sixta H, Potthast A, Krotschek AW. Chemical Pulping Processe: Sections 4.1–4.2.5. *Handbook of Pulp*. Wiley-VCH Verlag GmbH, **2008**, pp 109-229.

36. Holladay JE, White JF, Bozell JJ, Johnson D. Top Value-Added Chemicals from Biomass - Volume II—Results of Screening for Potential Candidates from Biorefinery Lignin. *Pacific Northwest National Laboratory, Richland, WA*. **2007**, PNNL-16983.

37. Laurichesse S, Avérous L. Chemical modification of lignins: Towards biobased polymers. *Prog. Polym. Sci.* **2014**, 39(7)**:** 1266-1290.

38. Ajjan FN, Jafari MJ, Rebis T, Ederth T, Inganas O. Spectroelectrochemical investigation of redox states in a polypyrrole/lignin composite electrode material. *J. Mater. Chem. A* **2015**, 3(24)**:** 12927-12937.

39. Kim SK, Kim YK, Lee H, Lee SB, Park HS. Superior Pseudocapacitive Behavior of Confined Lignin Nanocrystals for Renewable Energy Storage Materials. *ChemSusChem* **2014**, 7(4)**:** 1094-1101.

40. Calvo-Flores FG, Dobado JA. Lignin as Renewable Raw Material. *ChemSusChem* **2010**, 3(11)**:** 1227-1235.

41. Jeon J-W, Ma Y, Mike JF, Shao L, Balbuena PB, Lutkenhaus JL. Oxidatively stable polyaniline:polyacid electrodes for electrochemical energy storage. *Phys. Chem. Chem. Phys.* **2013**, 15(24)**:** 9654-9662.

42. Jeon J-W, O'Neal J, Shao L, Lutkenhaus JL. Charge Storage in Polymer Acid-Doped Polyaniline-Based Layer-by-Layer Electrodes. *ACS Appl. Mater. Interfaces* **2013**, 5(20)**:** 10127-10136.

CHAPTER THREE

LIGNIN-COATED CARBON NANOMATERIALS FOR LOW-COST ELECTRICAL ENERGY STORAGE

3.1 Introduction

Growing interest in transition toward greener chemistry and materials, particularly with respect to the use of sustainable, environmentally friendly, and energy efficient technologies[1-3] have motivated research in biomass-derived polymers and chemicals as alternative to petroleum based products. To support the growing capacity of solar and wind energy generation as well as electric or hybrid transportation systems, high-power and low-cost energy storage technologies will be required.[4, 5] Batteries, due to their high energy density, and supercapacitors, due to their high power density, will play a crucial role in these industries as either as individual or combined systems to create high-power and fast responding systems necessary to support emerging transportation systems and overcome the intermittent nature of renewable energy.[5-7] To reduce material cost and expand the potential scale of electrical energy storage, various efforts have focused on the use of widely abundant, environmentally friendly, and cheap, sustainable raw materials.

Carbon is a versatile material that can be synthesized in many forms, such as activated carbon, mesoporous carbon, CNTs, graphene, among others.[3, 8-11] Each form of carbon possesses unique properties of interest to a wide range of industrial/commercial sectors, from lubricants, electronic devices to aircraft. In supercapacitors, a type of high-power density energy storage system, activated carbon has found a niche in commercial systems, while conducting polymers (ECPs) and metal oxides are actively pursued as a

means to increase energy density.[3, 12, 13] Activated carbon systems have seized a marketshare in high power applications due to their chemical stability, long-term cycle life, and fast electrochemical response, as a result of the charge storage mechanism based on the physical adsorption of ions at the high-surface area electrode interface with the electrolyte. Ion adsorption on the polarized electrodes creates an electric double layer (EDL) on the electrode surface, and while no chemical reactions occur, the intrinsic energy density is limited by the accessible surface area.[9, 14] In EDLCs, porosity, pore shape, surface functional groups and electrical conductivity are the most important factors to consider regarding the performance of carbon materials.

Coal-based, coconut shells, phenolic resins, among others are usually the precursors for the synthesis of activated/mesoporous carbons.[15] Each of these will have a different distribution of micropores (<2nm), mesopores (2-50nm) and nanopores/macropores (>50nm) depending on the activation process. A balance between mesoporous and microporous volume is desired for materials with a high specific capacitance and rapid discharge rates.[16-18] In addition to activated carbon, other forms of carbon nanomaterials are being pursued for advanced energy storage materials due to their potential for high surface area and high conductivity, [19] such as CNTs[20] and graphene (GP)[21] (SWCNTs: 200-1250 m^2 g^{-1}, MWCNTs: 430 m^2g^{-1}, $GP_{theoretical}$: 2630 m^2g^{-1})[16].

ECPs and metal oxides are attractive alternatives to high surface area for applications requiring a higher energy density and charge capacity. Because these materials are Faradaic processes, charge can be stored within bulk of the materials

through charge transfer redox reactions in addition to ion adsorption at the electrode-electrolyte interface (pseudocapacitance).[22] Metal oxides, such as RuO_2 and MnO_2, possess high capacitance compared to carbon materials; however, their potential for adaptation in commercial systems is limitation by material scarcity, high cost, complex synthesis methods, and most important, their limitation to low-voltage aqueous electrolytes.[12] Conversely, ECPs such as polypyrrole, polyaniline and poly(3,4-ethylenedioxythiophene) are attractive due to their low-cost, relatively high conductivity, and routine synthesis and processing methods.[23] However, material instability and poor long-term cyclability represent the main obstacles to their commercialization. Several research groups have investigated alternative material designs, such as carbon-ECP[9, 24-26] or metal oxides-ECP[9, 27-29] composite electrodes for increased stability and charge storage, nano/microstructured electrodes for increased contact between electrode and electrolyte,[30] and incorporation of inorganic molecules[31, 32] and redox molecules/polymers[33, 34] as ECP dopants to increase capacitance.

Small redox active molecules or polymers that are non-conductive but can undergo redox reaction by the application of a potential difference have been used as dopants for ECPs or combined with carbon materials to increase the specific energy. In this electrode design, the carbon or ECP serves as a network for the electron transport during the redox reaction process, and the redox molecule/polymer provides additional redox behavior for increased capacitance. Previous work has shown that quinone-type molecules can be incorporated into and ECP film to enhance the electrode redox activity.[35-37] Hydroquinone and other redox active species (*e.g.* catechol, resorcinol) have

been used as additives in the electrolyte[35, 36] for electrochemical grafting on activated carbon electrodes, yielding a notable increase in capacitance with hydroquinone (283 F g^{-1}) compared with the other redox active species.[36] Polypyrrole (PPy) electrodes showed an increase in capacitance from 249 Fg^{-1} to 550 F g^{-1} when synthesized in the presence of 1,4- benzoquinone.[37] However, the small molecules were shown to diffuse out of the electrode over time; therefore, it is expected that the use of polymers may provide a long-term cycle stability advantage as they are more easily confined within the electrode.

Lignin is the second most abundant biopolymer after cellulose, representing between the 10-30% of dry plant mass, and is produced as a by-product of the pulping process of wood.[38, 39] The chemical structure consists of a complex 3D network of phenylpropane units derived from three monolignols: p-hydroxyphenyl (H), guaiacyl (G) and syringyl (S), their ratios vary according to the type of plant (softwood or hardwood). Hardwood, which is commonly used in the paper mills, is known to be formed mainly of G/S units, where S content can vary between 20% to 60%. Lignin is an interesting option as a biorenewable polymer for electrical energy storage due to its redox activity imparted by the presence of phenylpropane subunits with G and S pending groups.[40] The chemical functionality of the recovered lignin is, to some extent, governed by the pulping process, which will lead to different characteristics, properties and functionalities.[40, 41] Currently the most common are chemical pulping; among these, Kraft pulping, which produces Alkali lignin (AL), is based on the addition of sodium hydroxide and sodium sulfide and accounts for the 62% of the global pulping processes. This type of recovered lignin is a hydrophobic polymer soluble in aqueous bases and very poor solubility in inorganic

acids. Sulfite pulping, which results in Sulfonated lignin (SLS), is based on the addition of acid sulfite and accounts for 3.7% of the global pulping processes.[38] This type of recovered lignin is in parts hydrophobic and hydrophilic and therefore, soluble in water. Milzareck and Inganäs[42] show the use of sodium lignosulfonate (SLS) entangled between PPy network during polymerization with capacitance of 450 F g^{-1}, albeit for very thin films. In our previous work,[34] we reported a comparison between polypyrrole films synthesized with Alkali lignin (AL) and SLS; the mixed electrodes (polypyrrole-lignin) show an increase in specific capacitance between 20-30% when synthesized with AL. However, these electrodes exhibited short life upon cycling (lost about 47% of specific charge after 25 cycles),[34] which has been mainly attributed to the overoxidation of polypyrrole and nucleophilic attack by the electrolyte upon cycling.[43] This process causes the loss of contact between polypyrrole and lignin due to the loss of the conductivity. Additionally, quinone groups in lignin might, also, suffer nucleophilic attack or covalent bond breakage upon cycling [43] contributing to the decrease in the electrochemical activity.

In this work, we use nanoporous carbon as a conductive matrix to investigate the electrochemical properties of lignin for electrochemical energy storage applications. A simple ultrasonication/filtration technique was used to prepare carbon/lignin dispersions utilizing: glassy carbon (C2), activated carbon (AC), mesoporous carbon (C500 & MSP), carbon nanopowder (C100) and MesoCarbon MicroBeads (MCMB) (details can be found in **Table B.1**). First, we investigated the effect of the nanocarbon properties on the electrochemical performance of mixed carbon-lignin electrodes. Next, we studied the

influence of electrode processing conditions and lignin type on the electrochemical activity. Finally, asymmetric hybrid supercapacitors were fabricated using the optimal lignin-carbon electrode as the cathode and activated carbon as the anode.

3.2 Experimental methods

3.2.1 Materials

All chemicals were purchased from Fisher Scientific, Sigma-Aldrich, VWR, and MTI Corporation, and used as received unless otherwise stated. Commercially available Alkali Lignin (AL) was purchased from Sigma-Aldrich and Sodium Lignosulfonate (SLS) from VWR. Various carbon materials were used C2, C500, C100, MSP, AC and MCMB, details about these materials can be found in Appendix B **Table B.1**.

3.2.2 Carbon-lignin film preparation

Carbon-lignin films were prepared by dispersing 50 mg of carbon (C2, C500, C100, MSP, AC or MCMB) and 5 mg of conducting graphite (CG) in 10 mL of 0.5M Sulfuric Acid (SA) or 15.3M Acetic Acid (AA) by ultrasonication the solution for various time frames (10 or 20 min), then 1, 5, 10, 20 or 100 mg of SLS or AL were added to the solution and ultrasonicated for other 10 or 20 min, each ultrasonication routine comprised 5min on, 30s off until the set time was reached, an ice bath was used to cool down the solution. A 1 mL syringe was used to take 0.1, 0.5 or 1 mL of this dispersion, which was placed on a glass microfiber paper filter (Whatman GF/F, 25mm), using an O-ring (D= 0.77cm) to give a round shape to the film (**Scheme 3.1**, Steps 1 and 2). Quadruplicates of

each sample were prepared; one (still wet) was taken to perform the electrochemical characterization, the other three were dried overnight in a vacuum oven (98.2 kPa) at 80ºC and weighed (Ohaus DV215CD Semi-micro balance, readability 0.01mg) afterward to determine the average film mass.

3.2.3 Electrochemical analysis

Electrochemical characterization was performed in a 3-electrode Teflon cell (**Scheme 3.1**, Steps 3 and 4) with an electrode area of 0.47 cm^2. Working electrode was Titanium foil (Ti-foil) placed over the composite film, counter electrode a Platinum gauze 52 mesh (Alfa Aesar) and reference electrode Ag/AgCl in 3M NaCl solution. All samples were tested in a VersaSTAT 4 potentiostat/galvanostat and the VersaStudio v2.20.4631 Electrochemistry Software (Princeton Applied Research), in 0.5, 1.5 or 3M H_2SO_4 using cyclic voltammetry (CV) from -0.2 to 1.2 V at various scan rates (3-300 mV s^{-1}), electrochemical impedance spectroscopy (EIS) at 0.7V over a frequency range of 100000 to 0.1 Hz using a perturbation amplitude of 20mV, and charge-discharge (CD) measurements at current densities between 1.7 and 27.2 mA cm^{-2}.

3.2.4 Thermal gravimetric analysis

TGA was performed in a Q500 from TA Instruments on a platinum sample basket previously cleaned with a torch. Every analysis was done with 10 min of purge under dried air and a heating rate of 10ºC/min from room temperature to 800ºC. The samples deposited on a glass microfiber paper filter (MSP/AL-AA, MSP/SLS-SA, and MSP/SLS-AA) were dried and scraped from the substrate to avoid interference. The sample label as

standard is a sample of MSP/CG/SLS powder grained with a mortar and pestle only, which was not subjected to the ultrasonication and filtration process.

3.2.5 Surface morphology

The film surface characterization was performed by Scanning Electron Microscopy (SEM) in a Hitachi SU-6600 Analytical VP FE-SEM at a beam intensity of 2 kV; the samples were placed on a 45º aluminum sample holders with carbon tape. Images were captured at magnifications of x2k, x5k, and x10k.

3.2.6 Brunauer-Emmett-Teller (BET)

Physisorption experiments were performed under Nitrogen, at 77.35K in a Quantachrome Autosorb iQ Gas Sorption Analyzer utilizing a 40-point adsorption/desorption isotherm analysis. The differential pore volume distribution was obtained from the desorption isotherm through Barrett-Joyner-Halenda (BHJ) analysis. Measurements were taken at the Electron Microscopy Laboratory at Clemson University.

3.2.7 Device preparation and characterization

Working and counter electrodes were prepared utilizing similar method as described previously with 50 mg of Mesoporous carbon (MSP) and 5 mg of CG in 10 mL in 15.3 M AA, ultrasonicated for 10 min (5 min on, 30s off), then10 mg of AL were added and sonicated for additional 10 min (5min on, 30s off). 0.5mL of the dispersion was deposited on GF/F (Whatman). While the counter electrode was prepared by

dispersing 10 mg of CG, 5 mg of carboxymethylcellulose (CMC), and 85mg activated carbon (AC) in 10 mL of DI water. The CMC was first left to dissolve in DI water for 4h with constant agitation, and then finely ground CG and AC were added. This solution was sonicated for 40 min (5min on, 30s off). 0.4 mL of this dispersion was deposited on GF/A (Whatman, 21mm). The separator was a Silver 25AR DreamWeaver. Both electrodes and the separator were placed in the vacuum oven (98.2 kPa) at room temperature with 1mL of electrolyte (0.5M H_2SO_4) for 30 min; then they were allowed to soak overnight at ambient temperature and pressure. A MTI CR2025 button cell was prepared and placed in a coin cell apparatus (MTI Corp) to be tested (2-electrode system). CV and EIS were performed as described before; CD measurement between 0.32 and 5.2 mA and cycle life measurement for 2000 cycles from -0.2 to 1 V at 1.3 mA. The mass of the activated carbon was set to 120% the charge of the working electrode determined at a scan rate of 10 mV s^{-1}. The MSP/CG/AL electrode had an approximated mass of 3.18 mg, and the AC/CG/CMC electrode had a mass of 4.08 mg.

3.3 Results and Discussion

A general schematic of the process to fabricate Carbon/Lignin electrodes and the setup of the electrochemical cell is presented in **Figure 3.1**. The films were prepared by dispersing carbon (C2, C100, C500, MSP, AC or MCMB) with conducting graphite (CG) in either sulfuric acid (0.5M SA) or acetic acid (15.3M AA) by ultrasonication for 10 or 20 min. Sulfonated lignin (SLS) or Alkali lignin (AL) was then added to the dispersion and ultrasonicated for another 10 to 20 min (details can be found in the experimental

section). A defined volume of the dispersion was filtered through a glass microfiber membrane and confined to a 0.5 cm^2 electrode by a Teflon O-ring to achieve a target electrode mass (**Figure 3.1**: Step 1). The filter paper was removed from the apparatus (**Figure 3.1**: Step 2), the O-ring was carefully separated from the film, and a piece of titanium foil was placed over the electrode (**Figure 3.1**: Step 3) to be used as the contact for the working electrode. A 3-electrode electrochemical cell was assembled (**Figure 3.1**: Step 4) in a Teflon container with the working electrode assembly (Ti foil + carbon/lignin + paper filter) situated such that the paper filter was accessible to the electrolyte solution (**Figure 3.1**: Step 4 inset). Once the cell was assembled, the electrolyte was added along with the reference electrode and the Pt mesh counter electrode. The experimental design described above provides a very easy and practical method for preparing the electrodes without the need to prepare slurry, coat a current collector or assemble a cell for active material analysis.

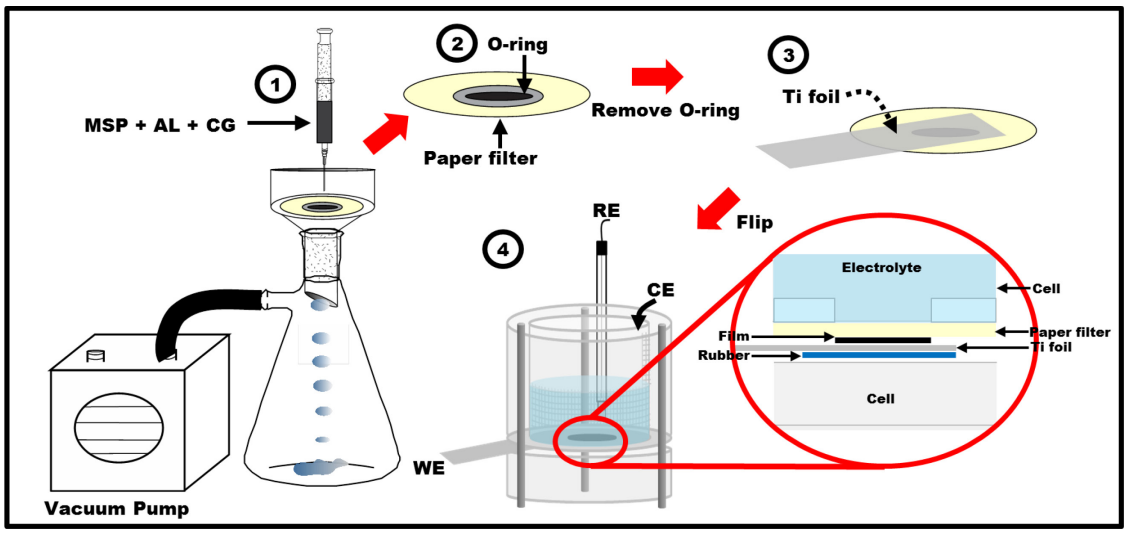

Figure 3.1 Illustrative schematic of the process to prepare Carbon/Lignin electrodes on paper filter and the electrochemical cell setup.

Chemically inert porous carbon nanomaterials were selected as a platform to investigate the electrochemical properties of lignin. Because lignin is not electrically conducting, only a thin layer can be electrochemically addressed, which necessitates a high surface area substrate. A wide range of porous carbon materials were selected, ranging from highly microporous activated carbon (< 2nm pore size) up to mesoporous carbon with predominant pores sizes of 3 nm and 69 nm. First, the influence of the pore size and porosity of the carbon materials on the redox activity of lignin was studied to identify a suitable substrate for determining the effects of lignin composition and lignin type (alkali *vs.* sulfonated) on the electrochemical performance. The metric for determining the most effective carbon nanomaterial to absorb lignin within the internal porous structure was the highest redox activity, which is the integrated charge of the oxidation-reduction processes occurring in lignin (reversible redox peak near 0.55 V).

Figure 3.2a and **3.2b** show the cyclic voltammetry (CV) profiles represented as specific capacitance (F g^{-1}), which is current (A) divided by scan rate (V s^{-1}) and electrode mass (g), *vs.* potential (V) to account for the mass variation in each film. The electrochemical properties of SLS on various carbon nanomaterials, MSP, C100, C500 and AC, are presented at scan rates of 100 mV s^{-1} (**Figure 3.2a**) and 10 mV s^{-1} (**Figure 3.2b**). The physical properties of the carbon nanomaterials can be found in the Appendix B. CV profiles of MCMB and C2 are not shown as they exhibit inferior electrochemical performance compared to C100 but exhibit a similar profile. As shown in **Figure 3.2b**, MSP-lignin mixtures exhibit the highest lignin redox activity as evidenced by the sharp redox couple around 0.55 V for high and low scan rates.

In electrode mixtures with AC and SLS, no redox activity from the lignin is observed, even at the slowest scan rates. Comparatively, AC has the highest surface area (2000 m^2 g^{-1}, pore volume 0.90 cm^3 g^{-1}, **Table B.1**) due to its microporosity, and correspondingly, the smallest pore size (<2nm). As a random aromatic polymer, lignin is too large in solution to be adsorbed within the microporosity of the AC, and likely blocks the accessible surface area by adsorbing on the outer surfaces of the particles. Similarly, mixtures of C500 and SLS showed low lignin redox activity, again, due to the small pore size (4-36nm, **Figure B.1**). Every other carbon nanomaterial exhibits some observable quantity of redox activity in the SLS-carbon electrodes, and the magnitude is directly related to the accessible surface area. For example, MSP (surface area of 86.6 m^2 g^{-1}, pore volume 0.19 cm^3 g^{-1}, pore size 3-69nm from BET, **Figure B.1**) has a notable lower surface area but pores large enough to adsorb lignin and still remain accessible to the

electrolyte. As the surface area of the carbon is decreased for C100 (11.4 $m^2 g^{-1}$ from BET, **Figure B.1**), C2 (2.14 $m^2 g^{-1}$) and MCMB (2.02 $m^2 g^{-1}$), the redox couple associated with lignin decreases due to lower amounts of lignin accessible on the low surface area materials.

The scan rate dependence for the carbon-lignin mixtures can be inferred from **Figures 3.2a** and **3.2b**. First, the decrease in performance of carbon lignin mixtures based on AC and C500 is attributed to ion diffusion limitations within the high-surface area materials; at high scan rates, ions cannot access the inner pores, thus decreasing the measured capacitance. In addition to EDLC, the electrochemical behavior of Faradaic processes (i.e. within the lignin), is also dependent upon scan rate as the presence of ions is required to support the redox processes occurring on the quinone groups. Accordingly, the redox peak separation is increased in MSP at 100mV s^{-1} (oxidation peak: 0.72 V, reduction peak: 0.4 V) compared to 10 mVs^{-1} (oxidation peak: 0.60V, reduction peak: 0.52V). This behavior is common in redox materials, especially proton-dependent redox processes, and peak separation is expected to increase with faster scan rates and as the thickness of the films increase.[43, 44] **Figure 3.2c** shows another representation of scan rate dependence and is calculated as the average specific capacitance (e.g. from **Figures 3.2a** and **3.2b**) for each type of carbon material studied. This representation clearly displays the limitations associated with ion transport in each system. For example, AC has the highest specific capacitance at low scan rate due to the high surface area impacted by its microporosity, but due to diffusional resistances within the particles, the EDLC significantly decreases with increasing scan rate. MSP-lignin mixtures, on the other hand,

display relatively minor scan rate dependence of the capacitance due to the ion accessibility to the larger nanopores. These electrodes exhibit the highest average capacitance at fast scan rate due to the rapid charge transfer processes within the coated SLS layers.

The scan rate-dependent observations are supported by electrochemical impedance spectroscopy (EIS), in which the timescales associated with reaction (charge transfer) and diffusion can be probed. From EIS measurements, the relaxation time constant (τ_c), which is a measure of how fast an electrode can be discharged with 50% efficiency, can be determined. τ_c is defined as the reciprocal of the peak frequency ($\tau_c = 1/f_{peak}$) in the relationship between imaginary capacitance (C_{img}) *vs.* frequency (**Figure 3.2d**). Over the frequency range scanned, AC and C500 (surface area of 471.6 $m^2\ g^{-1}$, pore volume 0.23 $cm^3\ g^{-1}$ from BET, **Figure B.1**) do not exhibit a peak which is probably located at lower frequencies (slower time scales), as is typical in microporous materials. Whereas in the other carbons, τ_c falls within the range of 0.1-1s, and indicates fast discharge capability due to less pore constriction.

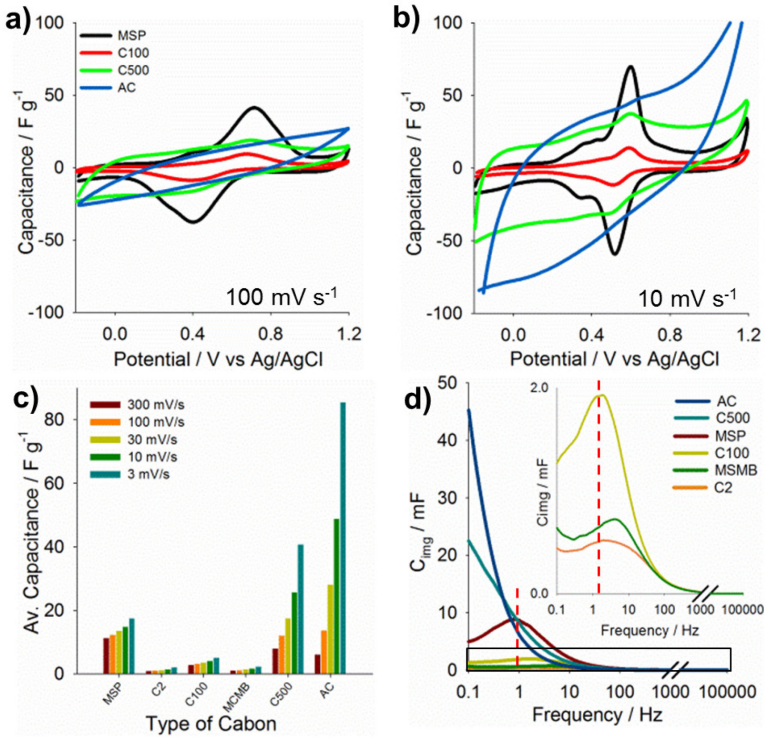

Figure 3.2 Electrochemical properties of SLS- carbon composite electrodes. Cyclic voltammetry profiles normalized to specific capacitance for (a) 100mV s^{-1} and (b) 10mV s^{-1}. (c) Average capacitance (F g^{-1}) *vs.* carbon at various scan rates. (d) Bode plots of imaginary capacitance (C_{img}) *vs.* frequency (Hz).

After determining the effect of pore size on the electrochemical performance of carbon-SLS composite electrodes, we investigated the effects of processing conditions (lignin concentration, mass, sonication, among others) on the electrochemical characteristics of the carbon/SLS films (**Figure 3.3**). The CV profiles normalized to specific capacitance (F g^{-1}) for Carbon/SLS films prepared with various concentrations of SLS are shown in **Figure 3.3a**. At small concentrations of SLS (0.01 wt.%) a weak redox peak can be observed around 0.55V (red curve), which corresponds to a small amount of lignin coated within MSP structure. The intensity of the oxidation-reduction peak couple

increases as the concentration of SLS increases from 0.05 wt.% to a maximum of 0.1 wt.% (yellow curve); further increases in the concentration (0.2 - 1 wt.%) of SLS led to a reduction in the peak intensity. At high concentrations (1 wt.%) SLS is likely to block the access of the electrolyte to the pores because lignin by itself is an insulator material, acting as a resistive layer.

Figure 3.3b presents the specific capacitance (F g^{-1}) as a function of the scan rate (V s^{-1}) for different amounts of dispersed material deposited on the paper filter. For small amounts of material deposited (5.3 mg cm^{-2}), which led to thin films, low scan rate dependence is observed as ions can readily move in and out of the film (low ion diffusion limitations), however, exhibit low average capacitance (~5 F g^{-1}). Conversely, when the mass deposited is increased up to 19.1 mg cm^{-2}, films demonstrated strong scan rate dependence at fast scan rates (100 - 300 mV s^{-1}), as the ions require more time to access the inner structure of thick films. A balance between relatively low scan rate dependence and higher capacitance (~9 F g^{-1}) was found at a mass of 11.5 mg cm^{-2}.

The CV profiles for SLS/carbon films tested in increasing concentration of H_2SO_4 (0.5 M, 1.5 M, 3 M), as specific capacitance (F g^{-1}) *vs.* Potential (V), are presented on **Figure 3.3c**. Two redox peaks are present, including a weak peak around 0.40 V and a strong peak at 0.56 V. These to two peaks correspond to the presence of different redox species in lignin (G and S). Previous works[40] have demonstrated that the major peak (~0.56 V) can be attributed to the presence of G-derived quinones, while the small peak (~0.40 V) can be assigned to S-derived quinones. The peaks exhibit a shift to the right as the concentration of H_2SO_4 increases, for instance, the peak observed at 0.56 V for 0.5 M

H_2SO_4, shifts to 0.58 V in 1.5 M and 0.60 V for 3 M H_2SO_4. It has been demostrated[37] that quinone charge transfer reaction (two electron-two proton) is pH dependent; as the pH of the solution decreases a slight shift to positive potentials is expected.

Moreover, a decrease in the peak intensity at 0.56V is observed as the concentration of H_2SO_4 increases. A similar behavior has been observed in electrodes prepared with conducting polymers[34, 45] where a reduction in the redox activity of lignin is observed, due to the degradation of the G-group upon cycling, owing to the breakage of covalent bonds or nucleophilic attack by the electrolyte. In fact, we have observed a similar CV profile to the 3 M H_2SO_4 (yellow curve), when a single electrode (carbon/SLS) in a 3-electrode cell has been cycled in 0.5 M H_2SO_4 for 2000 charge-discharge cycles, confirming the possibility of degradation and nucleophilic attack by the electrolyte upon cycling. This issue worsens when higher concentrations of acid are used. Consequently, all the previous variables simultaneously and to some extent, depending on the concentration of H_2SO_4, could be contributing to the change in the intensity of the redox peaks. Thus, all following experiments were performed in 0.5 M H_2SO_4.

Ultrasonication is required to ensure proper dispersion/mixing of the carbon nanomaterials with lignin. In general, ultrasonication was performed to disperse the carbon nanomaterial in solution for 10 min (10mL of 0.5 M H_2SO_4), and then again after adding SLS to promote mixing in the solution and intimate contact between the lignin and carbon. **Figure 3.3d** shows the average capacitance (F g^{-1}) of each sonication sequence investigated at various scan rates (mV s^{-1}). Sequences are represented as a'/b', where a' represents the sonication time with carbon and b' represents the sonication time

with carbon and lignin. Each mixing/sonication sequence exhibits a similar scan rate dependence, however, 10'/10' does show significant improvements compared with the other sequences. Notice that 0'/0' was taken just by mixing the sample for 1 min on a vortex mixer, which shows better results than no ultrasonication or mixing after SLS is added (10'/0'). This observation indicates an important point that sonication/mixing does help to trap SLS in the MSP pores. Although, when the dispersion is sonicated too long (10'/20') a decrease in electrochemical performance is observed, which could be due to structural damage occurring in the materials owed to the strength of the ultrasonication process itself which can cause some of the pores to collapse or the lignin structure to degrade. Thus, 10 min ultrasonication before and after adding lignin was determined to be the best option for preparing the composite films.

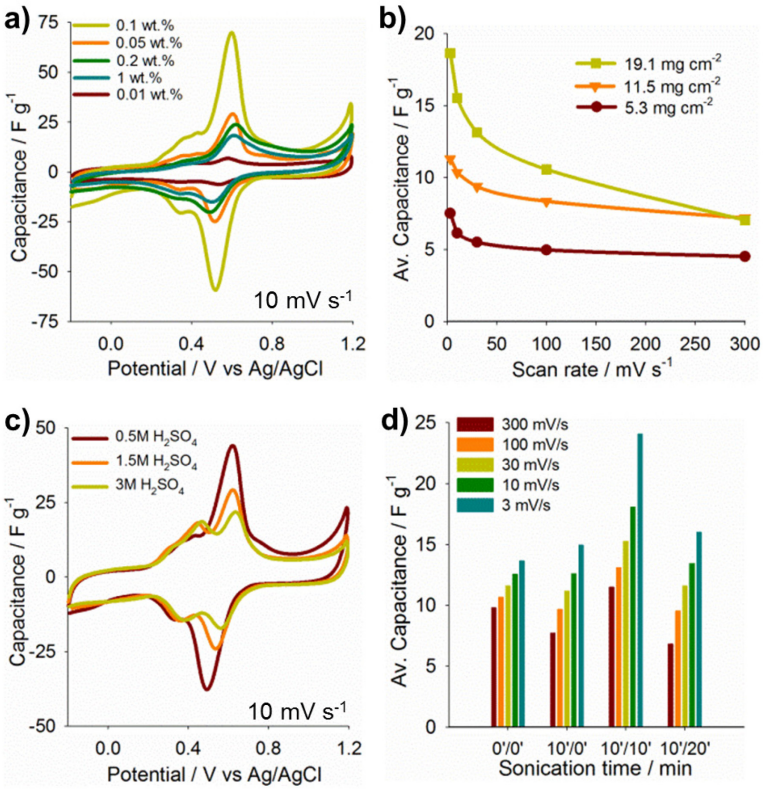

Figure 3.3 Electrochemical properties of MSP/CG/SLS electrodes at various conditions. (a) Cyclic voltammetry profiles normalized to specific capacitance for various SLS loads (b) Average capacitance (F g^{-1}) *vs.* scan rate (mV s^{-1}) varying mass on electrodes. (c) Cyclic voltammetry profiles normalized to specific capacitance of electrodes tested in 0.5, 1.5, 3 M H_2SO_4. (d) Average capacitance of various sonication times at different scan rates. (b), (c) and (d) for MSP/CG/10 mg SLS electrodes.

As mentioned before, SLS has been previously studied as dopant for conducting polymers[34, 40, 42, 45] due to its good solubility in aqueous solutions, however it is only a by-product from the 3.7% of the global pulping processes; on the other hand, AL accounts for the 62%.[38] One downside of AL is the limited solubility in inorganic acids, which represents a challenge for its integration in supercapacitor devices. In our previous work,[34] we studied the incorporation of AL in an ECPs matrix, by utilizing an Acetic

Acid (AA) solution. Therefore, electrodes (MSP/CG/AL) were prepared in a 15.3M AA solution using the processing conditions previously described (**Figure 3.3**). For comparison purposes, electrodes prepared with MSP/CG/SLS were also dispersed in a 15.3M AA, along with MSP/CG/SLS dispersed in 0.5M H_2SO_4. **Figure 3.4a**, presents the CV profiles as specific capacitance (F g^{-1}) *vs*. potential at 100 mV s^{-1} and 10 mV s^{-1} (inset). Electrodes with MSP/CG in SA (red) and MSP/CG in AA (not shown) were prepared for comparison, and as expected, carbon shows the typical square-shape characteristic of EDLC electrodes. Slight differences are observed in the redox peak intensity for MSP/SLS-SA and MSP/SLS-AA, this behavior will be discussed in detail later on (**Figure 3.5**). There is a significant difference between MSP/AL-AA and the rest of the films; peaks are broader and more intense indicating that AL either has more quinone type groups available in the structure or these groups are more easily accessible to the electrolyte; moreover, higher capacitance is observed for films prepared with AL at fast (100mV s^{-1}) and low (10mV s^{-1}) scan rates.

The Nyquist plot, which is a representation of the imaginary (Z'') *vs.* real (Z') impedance obtained from EIS is shown in **Figure 3.4b** and corresponds to electrodes represented on **Figure 3.4a**. The Nyquist plot indicates the time-scales where the process switches from charge transfer (high-frequency range) to mass transfer control (low-frequency range). All the electrodes exhibit a low Ohmic resistance (high-frequency limit of Nyquist plot). MSP-SA demonstrates a very low charge transfer resistance (high-frequency range), consistent with high conductivity in carbon materials. The low-frequency range shows a nearly ideal capacitive behavior (90° line) consistent with a

purely EDLC mechanism. For the rest of the electrodes comprised by SLS or AL, the charge transfer resistance slightly increases (high-frequency range), due to the presence of the charge transfer processes from lignin. The transition between charge transfer and mass transfer control at the low-frequency intercepts (low-frequency limit of semi-circle) occur at 251.2 Hz, 158.2, 158.2, 199.5 Hz for MSP-SA, MSP/SLS-SA, MSP/SLS-AA, MSP/AL-AA, respectively. Notice that the lower the frequency, the longer the time needed for the ion transport within the electrode, consistent with scan rate dependence.

The decrease in the specific capacity (mA h g^{-1}) as a function of increasing current (mA), obtained from the charge-discharge experiments, are presented in **Figure 3.4c**. For comparison purposes, the performance of electrodes made with AC (light blue) were included to highlight the differences with MSP (red) at fast currents. MSP due to the mesoporosity is capable to withstand higher discharge currents compared with AC (highly microporous material) and still keep a fairly constant specific capacity. Conversely, the specific capacity of AC electrodes drops significantly as the discharge current is increased. This behavior is strictly related to the differences in the pore structure between both samples, as explained in **Figure 3.2**. When SLS is added to AC in SA (dark blue), there is a slight increase in the specific capacity due to the presence of lignin, but decreases to zero at high current rates. The differences exhibited in the values for specific capacity between electrodes prepared with AL and SLS is due to the presence of more quinone moieties and higher accessibility of the redox sites to the electrolyte in AL.

Electrodes compared with carbon and SLS have vastly different morphologies when prepared in SA compared to AA. AA is a moderate to poor solvent for SLS, which causes these films to have a higher resistance (**Figure 3.4b**), lower redox peak intensity (**Figure 3.4a**) and a significantly lower specific capacity (**Figure 3.4c**). The effect of the presence of lignin in the morphology of the films was studied by Scanning Electron Microscopy (SEM). As reference **Figure 3.4d** shows the plain MSP-SA film which does not show any significant differences with MSP/SLS-SA (**Figure 3.4e**) and MSP/SLS-AA (not shown), however, MSP/AL-AA shows a quite uniform distribution of lighter spots on the film, lignin is a non-conductive molecule, therefore, under SEM a significant accumulation of lignin would look brighter than the carbon since electrons from the electron beam would be accumulated on the surface of any non-conductive material causing it to look brighter (**Figure 3.4f**). SEM images of the other carbon materials are shown in Appendix B **Figure B.2**.

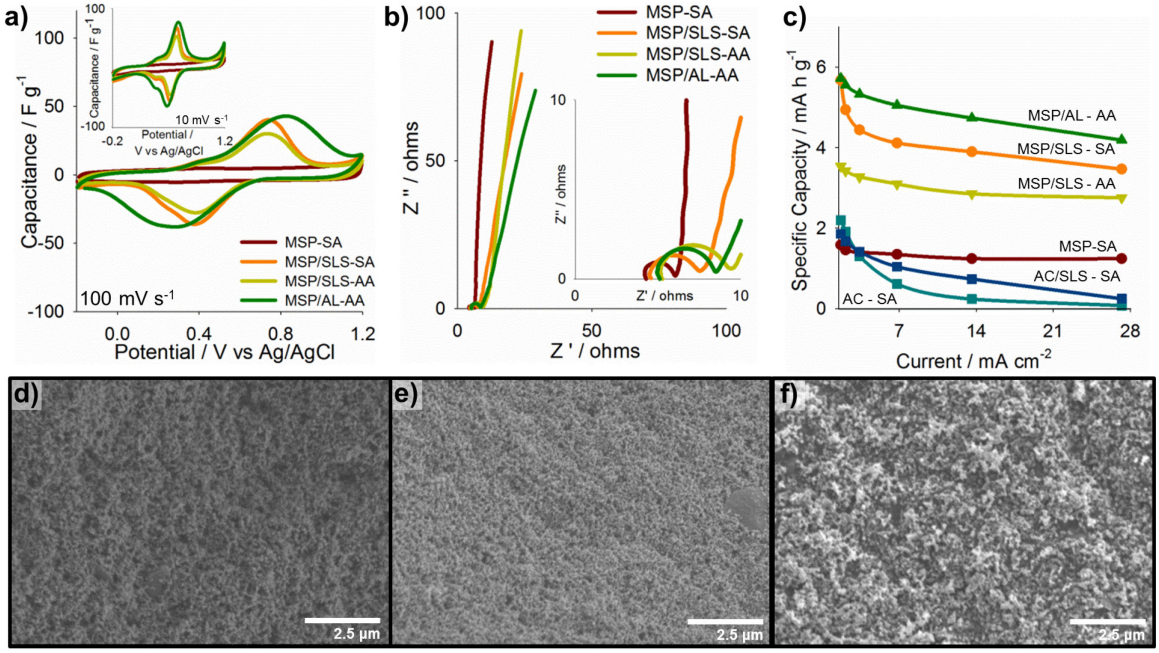

Figure 3.4 Electrochemical properties of MSP and AC electrodes in AA and SA. (a) Cyclic voltammetry profiles at 100 mV s^{-1}, inset 10 mV s^{-1} and (b) Nyquist plot in the frequency range of 10k Hz to 0.1 Hz. of MSP-SA (control), MSP/SLS and MSP/AL prepared in AA and MSP/SLS in SA. (c) Specific capacity *vs*. current including AC-SA (control) and AC/SLS-SA for comparison. Scanning electron microscopy images at x10k of (d) MSP-SA, (e) MSP/SLS-SA and (f) MSP/AL-AA.

To determine the amount of SLS and AL incorporated into the mixed electrodes, thermal gravimetric analysis (TGA) experiments were performed in air up to 800°C (**Figure 3.5**). **Figure 3.5a** and **3.5d** show the Weight Loss % as function of Temperature (°C) and **Figures 3.5b**, **3.5c**, **3.5e** and **3.5f** show the Derivative of the Weight Loss (% $°C^{-1}$) *vs*. Temperature(°C), also known as Derivative Thermogravimetric Analysis (DTG). Each peak in the DTG profile typically indicates the decomposition of particular species. The sample label "standard" is a sample of MSP/CG/SLS powder that was well mixed, but not subjected to the sonication and filtration processes.

A clear difference in the TGA/DTG profiles between the various samples is observed; lignin contains different oxygen functionalities that have various thermal stabilities; therefore, the scission of these functional groups occur at different temperatures.[46] One of the most significant differences between the samples is the shift towards lower temperatures of the MSP/CG peak (**Figure 3.5c** and **3.5f**) from 767, 748, 705, 685 to 662°C for MSP/CG plain powder, MSP/SLS-SA, MSP/SLS-AA, MSP/AL-AA and standard, respectively. The shift in temperature is likely associated with the lignin coating the carbon and preventing aggregation in the dried sample. Therefore, more lignin in the sample increases carbon separation making the carbon easier to combust and decompose. Previous works[47, 48] have shown that the presence of inorganic cations as Na^+ in SLS have an influence on the decomposition temperature by catalyzing dehydration and decarboxylation reactions; also, free sulfonate groups are very active which could weaken the thermal decomposition of carbon.

Figures 3.5b, **3.5c**, **3.5e** and **3.5f** compare the DTG profiles of the standard, SLS, MSP/CG, MSP/SLS-SA, MSP/SLS-AA, and MSP/AL-AA. Samples with SLS show three characteristics peaks between 150 and 400°C that are due to fragmentation of inter-unit linkages such as side chains, H_2O, CO, CO_2 and organic volatiles as CH_2O, CH_4, CH_3OH, SO_2, and R-SH[48-50] that are not observed in MSP/CG (**Figure 3.5b**). Moreover, the standard sample shows a peak between 425 and 550°C that is not present in MSP/CG or SLS by themselves indicating interactions between carbon and lignin due to aromatic rings decomposition; these peaks are also present at lower intensity in MSP/SLS-SA and MSP/SLS-AA. A significant difference between MSP/AL-AA and films prepared with

SLS is the presence of two sharp peaks at 332 and 445°C in MSP/AL-AA and the absence of a broad peak at ~180°C present in all films with SLS. AL, at low temperatures (<200°C) produces a very small amount of volatiles compared with SLS and at higher temperatures (200-450°C) loses aromatics, CO_2 and alkyls molecules.[51] At temperatures higher than 500°C CO, CO_2 and aromatics will decompose; however, lignin, in general, will leave highly condensed aromatic structures and inorganics as ash,[50, 51] about 26.8 wt.% residue, while for MSP/CG the residue is negligible (0.2 wt.%) (**Figure 3.5a**).

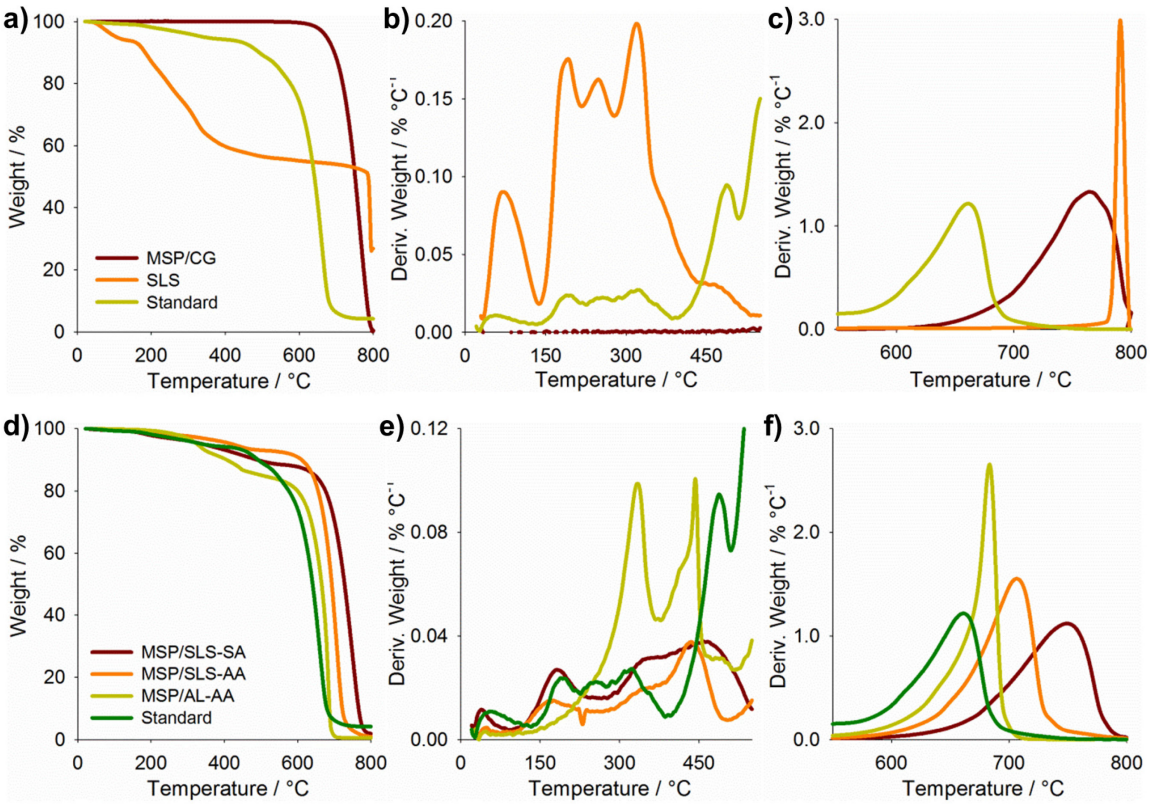

Figure 3.5 Thermal gravimetric analysis (TGA) (a) and DTG (b and c) profiles for MSP/CG plain mixture, SLS and standard. (d) TGA and DTG (e and f) profiles for MSP/CG with SLS or AL in SA or AA and standard.

The amount of lignin (SLS or AL) incorporated in the films was determined by dividing sections of the DTG profiles for the various samples and assigned each of them to either lignin or carbon. A peak fitting software (PeakFit) was used to determine the different Gaussian peaks that gave rise to the DTG profile and integrating the peak area to determine the weight. Details about this method can be found in the Appendix B (**Table B.2**).

The amount of SLS or AL added to MSP/CG mixtures corresponds to 15.4 wt.% of the total solids in the mixture, which does not necessarily mean that this concentration will remain unchanged in the final electrode (after sonication and filtration). Hence, the concentration of SLS or AL were found to be for MSP/SLS-SA 12.5 wt.% of SLS, MSP/SLS-AA 7.7 wt. % of SLS and MSP/AL-AA 14.9 wt.% of AL. These results confirm that AA is not a good solvent for SLS since about half of the total amount of SLS coated MSP. Moreover, the lower electrochemical performance exhibited by MSP/SLS-AA compared with samples prepared from SA correlates to lower mass of SLS in the electrode. Additionally, MSP/SLS-SA and MSP/AL-AA have similar amount of lignin. Supporting that AL has more redox sites accessible to the electrolyte leading to a higher electrochemical performance.

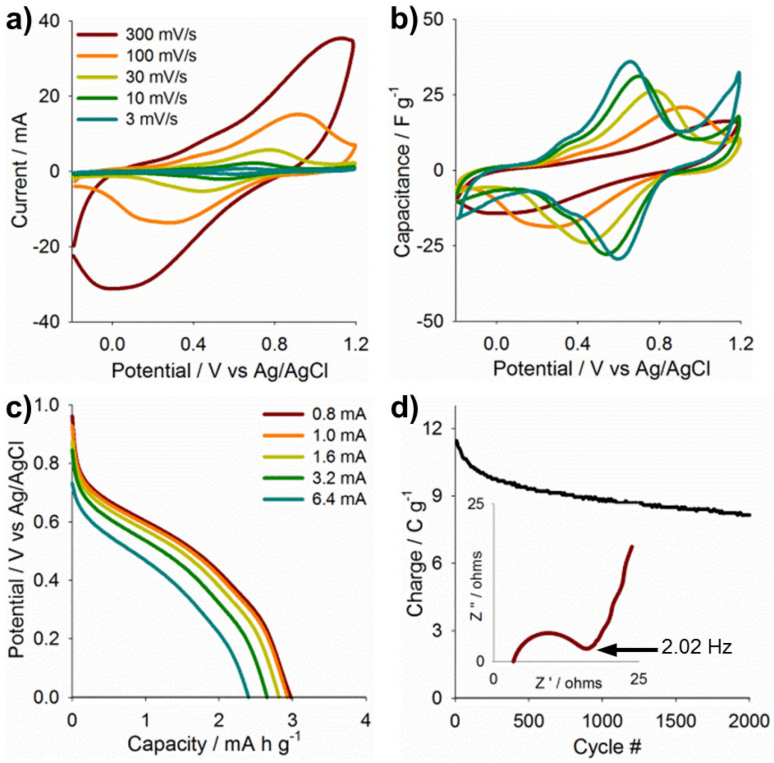

Figure 3.6 Electrochemical performance of asymmetric supercapacitor device (2-electrode cell) with MSP/AL as cathode and activated carbon as anode. (a) Cyclic voltammetry profiles and (b) Cyclic voltammetry profiles normalized to specific capacitance at various scan rates. (c) Supercapacitor discharge profiles. (d) Cycle life stability (charge *vs*. cycle #). Inset: Nyquist plot.

An asymmetric supercapacitor was prepared with MSP/CG/AL as cathode and AC/CG as anode in 0.5M H_2SO_4 (**Figure 3.6**). **Figure 3.6a** and **3.6b** show the cyclic voltammetry profiles as current (mA) *vs*. potential (V) and specific capacitance (F g^{-1}) *vs*. potential (V), respectively, for scan rates between 3 and 300 mV s^{-1}. On a total mass basis, the specific capacitance value is 13.5 F g^{-1} at 3 mV s^{-1}. Notice, the scan rate dependence characterized by the separation between the oxidation and reduction peaks

from AL. At fast scan rates (100 – 300 mV s^{-1}) becomes more difficult for the ions to access the inner structure of the electrode material, accentuating the peak separation as lignin redox process is proton-dependent. **Figure 3.6c** shows the discharge profiles for the asymmetric device as potential (V) *vs.* capacity (mA h g^{-1}) measured from 0 to 1 V for various currents (0.32 to 5.2 mA). For a 60s discharge at 1.3 mA, the specific capacity is 2.8 mA h g^{-1}, which shows small changes when the discharge currents vary between 0.32 and 5.2 mA (2.6 to 3 mA h g^{-1}).

Figure 3.6d shows the change in the specific charge (C g^{-1}) as the device is cycled between -0.2 and 1.0 V for 2000 cycles at 1.3 mA. The device loses about 22% of its original charge after the first 500 cycles, and then a small decay is observed. The decay of the specific charge is related to decrease in the lignin redox activity, as confirmed by cyclic voltammetry performed after the 2000 cycles, where the overall capacitance value drops to 10.6 F g^{-1} at 3mV s^{-1}. The Nyquist plot is presented in **Figure 3.6d** inset; this cell presents low Ohmic series resistance, and a relatively small charge transfer resistance is observed at the high-frequency range, consistent with high conductivity in carbon materials. However, the switching point between charge transfer control to diffusional control (Warburg impedance) occurred at 2.02 Hz, indicating long times for the ion diffusion within the electrodes, consistent with the scan rate dependence of the CV profiles. Even though this device does not show an outstanding performance in terms of capacitance, the important outcome is the possibility of using lignin/carbon composites as a source of increased energy density than the plain carbon material, by tailoring the synthesis and assembly conditions.

3.4 Conclusions

When properly combined with carbon nanomaterials, alkali lignin (AL) is a viable biorenewable material for low-cost electrical energy storage devices, particularly for supercapacitor cathodes. Various carbon materials were investigated as possible platforms to study the electrochemical properties of lignin. First, it was necessary to understand the effect of the pore size on the electrochemical activity of lignin. Intermediate pore sizes >40 nm (mesoporous range) led to optimal redox activity of lignin because the pores are large enough to adsorb lignin while remaining accessible to the electrolyte. Then, to design high-performance electrodes, the processing conditions (sonication, lignin concentration, mass, etc.) were studied and demonstrated to have a strong impact on the electrochemical activity of carbon/lignin electrodes. Additionally, AL shows a higher capacitance when compared with SLS due to a higher accessibility of the redox sites. Finally, the potential application of AL as part of supercapacitor electrodes was shown in the assembly of an asymmetrical supercapacitor device, which represents an important advance towards the use of biopolymer based electrodes in energy storage.

3.5 References

1. Chu S, Majumdar A. Opportunities and challenges for a sustainable energy future. *Nature* **2012**, 488(7411)**:** 294-303.

2. Larcher D, Tarascon JM. Towards greener and more sustainable batteries for electrical energy storage. *Nat Chem* **2015**, 7(1)**:** 19-29.

3. Béguin F, Presser V, Balducci A, Frackowiak E. Carbons and Electrolytes for Advanced Supercapacitors. *Adv. Mater.* **2014**, 26(14)**:** 2219-2251.

4. Liu J, Zhang J-G, Yang Z, Lemmon JP, Imhoff C, Graff GL*, et al.* Materials Science and Materials Chemistry for Large Scale Electrochemical Energy Storage: From Transportation to Electrical Grid. *Adv. Funct. Mater.* **2013**, 23(8)**:** 929-946.

5. Whittingham MS. History, Evolution, and Future Status of Energy Storage. *Proceedings of the IEEE* **2012**, 100(Special Centennial Issue)**:** 1518-1534.

6. Yang Z, Zhang J, Kintner-Meyer MCW, Lu X, Choi D, Lemmon JP*, et al.* Electrochemical Energy Storage for Green Grid. *Chem. Rev.* **2011**, 111(5)**:** 3577-3613.

7. Liu C, Li F, Ma L-P, Cheng H-M. Advanced Materials for Energy Storage. *Adv. Mater.* **2010**, 22(8)**:** E28-E62.

8. Zhai Y, Dou Y, Zhao D, Fulvio PF, Mayes RT, Dai S. Carbon Materials for Chemical Capacitive Energy Storage. *Adv. Mater.* **2011**, 23(42)**:** 4828-4850.

9. Su DS, Schlögl R. Nanostructured Carbon and Carbon Nanocomposites for Electrochemical Energy Storage Applications. *ChemSusChem* **2010**, 3(2)**:** 136-168.

10. Simon P, Gogotsi Y. Capacitive Energy Storage in Nanostructured Carbon–Electrolyte Systems. *Acc. Chem. Res.* **2013**, 46(5)**:** 1094-1103.

11. Kangasniemi KH, Condit DA, Jarvi TD. Characterization of Vulcan Electrochemically Oxidized under Simulated PEM Fuel Cell Conditions. *J. Electrochem. Soc.* **2004**, 151(4)**:** E125-E132.

12. Wang G, Zhang L, Zhang J. A review of electrode materials for electrochemical supercapacitors. *Chem. Soc. Rev.* **2012**, 41(2)**:** 797-828.

13. Augustyn V, Simon P, Dunn B. Pseudocapacitive oxide materials for high-rate electrochemical energy storage. *Energy Environ. Sci.* **2014**, 7(5)**:** 1597-1614.

14. Zhang LL, Zhao XS. Carbon-based materials as supercapacitor electrodes. *Chem. Soc. Rev.* **2009**, 38(9)**:** 2520-2531.

15. Sevilla M, Mokaya R. Energy storage applications of activated carbons: supercapacitors and hydrogen storage. *Energy Environ. Sci.* **2014**, 7(4)**:** 1250-1280.

16. Ghosh A, Lee YH. Carbon-Based Electrochemical Capacitors. *ChemSusChem* **2012**, 5(3)**:** 480-499.

17. Liang C, Li Z, Dai S. Mesoporous Carbon Materials: Synthesis and Modification. *Angew. Chem. Int. Ed.* **2008**, 47(20)**:** 3696-3717.

18. Wang J, Xin HL, Wang D. Recent Progress on Mesoporous Carbon Materials for Advanced Energy Conversion and Storage. *Part. Part. Syst. Char.* **2014**, 31(5)**:** 515-539.

19. Pan H, Li J, Feng Y. Carbon Nanotubes for Supercapacitor. *Nanoscale Research Letters* **2010**, 5(3)**:** 654-668.

20. Titirici M-M, White RJ, Brun N, Budarin VL, Su DS, del Monte F*, et al.* Sustainable carbon materials. *Chem. Soc. Rev.* **2015**, 44(1)**:** 250-290.

21. Singh V, Joung D, Zhai L, Das S, Khondaker SI, Seal S. Graphene based materials: Past, present and future. *Prog. Mater Sci.* **2011**, 56(8)**:** 1178-1271.

22. Abdelhamid ME, O'Mullane AP, Snook GA. Storing energy in plastics: a review on conducting polymers & their role in electrochemical energy storage. *RSC Adv.* **2015**, 5(15)**:** 11611-11626.

23. Snook GA, Kao P, Best AS. Conducting-polymer-based supercapacitor devices and electrodes. *J. Power Sources* **2011**, 196(1)**:** 1-12.

24. Song Y, Liu T-Y, Xu X-X, Feng D-Y, Li Y, Liu X-X. Pushing the Cycling Stability Limit of Polypyrrole for Supercapacitors. *Adv. Funct. Mater.* **2015:** n/a-n/a.

25. Nyholm L, Nyström G, Mihranyan A, Strømme M. Toward Flexible Polymer and Paper-Based Energy Storage Devices. *Adv. Mater.* **2011**, 23(33)**:** 3751-3769.

26. Lota G, Fic K, Frackowiak E. Carbon nanotubes and their composites in electrochemical applications. *Energy Environ. Sci.* **2011**, 4(5)**:** 1592-1605.

27. Yu G, Hu L, Liu N, Wang H, Vosgueritchian M, Yang Y*, et al.* Enhancing the Supercapacitor Performance of Graphene/MnO2 Nanostructured Electrodes by Conductive Wrapping. *Nano Lett.* **2011**, 11(10)**:** 4438-4442.

28. Yang Y, Yuan W, Li S, Yang X, Xu J, Jiang Y. Manganese dioxide nanoparticle enrichment in porous conducting polymer as high performance supercapacitor electrode materials. *Electrochim. Acta* **2015**, 165**:** 323-329.

29. Kumar V, Lee PS. Redox Active Polyaniline-h-MoO3 Hollow Nanorods for Improved Pseudocapacitive Performance. *J. Phys. Chem. C* **2015**, 119(17)**:** 9041-9049.

30. Diaz-Orellana KP, Roberts ME. Scalable, template-free synthesis of conducting polymer microtubes. *RSC Adv.* **2015**, 5(32)**:** 25504-25512.

31. Ćirić-Marjanović G. Recent advances in polyaniline composites with metals, metalloids and nonmetals. *Synth. Met.* **2013**, 170**:** 31-56.

32. Afzal AB, Akhtar MJ, Nadeem M, Hassan MM. Investigation of Structural and Electrical Properties of Polyaniline/Gold Nanocomposites. *J. Phys. Chem. C* **2009**, 113(40)**:** 17560-17565.

33. Zhou Y, Wang B, Liu C, Han N, Xu X, Zhao F*, et al.* Polyanthraquinone-based nanostructured electrode material capable of high-performance pseudocapacitive energy storage in aprotic electrolyte. *Nano Energy* **2015**, 15(0)**:** 654-661.

34. Leguizamon S, Diaz-Orellana KP, Velez J, Thies MC, Roberts ME. High charge-capacity polymer electrodes comprising alkali lignin from the Kraft process. *J. Mater. Chem. A* **2015**, 3(21)**:** 11330-11339.

35. Fic K, Frackowiak E, Beguin F. Unusual energy enhancement in carbon-based electrochemical capacitors. *J. Mater. Chem.* **2012**, 22(46)**:** 24213-24223.

36. Fic K, Meller M, Lota G, Frackowiak E. Quinone/hydroquinone redox couple as a source of enormous capacitance of activated carbon electrodes. *MRS Online Proceedings Library* **2013**, 1505.

37. Arcila-Velez MR, Roberts ME. Redox Solute Doped Polypyrrole for High-Charge Capacity Polymer Electrodes. *Chem. Mater.* **2014**, 26(4)**:** 1601-1607.

38. Sixta H. Handbook of Pulp, vol. 1. Wiley-VCH Verlag GmbH, Weinheim, Germany; 2006.

39. Ragauskas AJ, Beckham GT, Biddy MJ, Chandra R, Chen F, Davis MF*, et al.* Lignin Valorization: Improving Lignin Processing in the Biorefinery. *Science* **2014**, 344(6185).

40. Milczarek G. Lignosulfonate-Modified Electrodes: Electrochemical Properties and Electrocatalysis of NADH Oxidation. *Langmuir* **2009**, 25(17)**:** 10345-10353.

41. Calvo-Flores FG, Dobado JA. Lignin as Renewable Raw Material. *ChemSusChem* **2010**, 3(11)**:** 1227-1235.

42. Milczarek G, Inganäs O. Renewable Cathode Materials from Biopolymer/Conjugated Polymer Interpenetrating Networks. *Science* **2012**, 335(6075)**:** 1468-1471.

43. Niu Z, Zhou W, Chen J, Feng G, Li H, Ma W*, et al.* Compact-designed supercapacitors using free-standing single-walled carbon nanotube films. *Energy Environ. Sci.* **2011**, 4(4)**:** 1440-1446.

44. Futaba DN, Hata K, Yamada T, Hiraoka T, Hayamizu Y, Kakudate Y*, et al.* Shape-engineerable and highly densely packed single-walled carbon nanotubes and their application as super-capacitor electrodes. *Nat Mater* **2006**, 5(12)**:** 987-994.

45. Ajjan FN, Jafari MJ, Rebis T, Ederth T, Inganas O. Spectroelectrochemical investigation of redox states in a polypyrrole/lignin composite electrode material. *J. Mater. Chem. A* **2015**, 3(24)**:** 12927-12937.

46. Suhas, Carrott PJM, Ribeiro Carrott MML. Lignin – from natural adsorbent to activated carbon: A review. *Bioresour. Technol.* **2007**, 98(12)**:** 2301-2312.

47. Yang C, Liu P. Water-Dispersed Conductive Polypyrroles Doped with Lignosulfonate and the Weak Temperature Dependence of Electrical Conductivity. *Ind. Eng. Chem. Res.* **2009**, 48(21)**:** 9498-9503.

48. Lemes AP, Soto-Oviedo MA, Waldman WR, Innocentini-Mei LH, Durán N. Effect of Lignosulfonate on the Thermal and Morphological Behavior of Poly(3-hydroxybutyrate-co-3-hydroxyvalerate). *J. Polym. Environ.* **2010**, 18(3)**:** 250-259.

49. Khan MA, Ashraf SM. Studies on thermal characterization of lignin. *J. Therm. Anal. Calorim.* **2007**, 89(3)**:** 993-1000.

50. Tejado A, Peña C, Labidi J, Echeverria JM, Mondragon I. Physico-chemical characterization of lignins from different sources for use in phenol–formaldehyde resin synthesis. *Bioresour. Technol.* **2007**, 98(8)**:** 1655-1663.

51. Zhang M, Resende FLP, Moutsoglou A, Raynie DE. Pyrolysis of lignin extracted from prairie cordgrass, aspen, and Kraft lignin by Py-GC/MS and TGA/FTIR. *J. Anal. Appl. Pyrolysis* **2012**, 98**:** 65-71.

CHAPTER FOUR

NANOSTRUCTURED POLYACRYLONITRILE/LIGNIN CARBON FIBER ELECTRODES FOR HIGH PERFORMANCE SUPERCAPACITORS

4.1 Introduction

Renewable energy, portable and wearable electronic devices, and electric and hybrid vehicles are a few examples of application areas with increasing demand for high-power density and high-energy density electrical energy storage devices.[1-3] Batteries and supercapacitors have emerged as potential candidates to address the challenges associated with intermittent energy generation from renewable sources, long-term stability in portable and wearable electronics, and safe energy storage in transportation. Among these, supercapacitors are attractive due to long cycle life, higher power density compared to batteries, and good electrical conductivity.[4, 5] The most widely available supercapacitors are electrical double layer capacitors (EDLCs), which store charge based on the physical adsorption of ions at the interface of high surface area electrode materials in an ion-containing electrolyte.[6, 7]

Common materials for EDLCs electrodes are various types of carbon, such as activated carbon,[8] aerogels,[2] nanotubes,[9] graphene,[10, 11] zeolite-templated carbons,[11] fibers,[12] and cloths,[13, 14] due to their general characteristics of lightweight, tunable porosity, high surface area, and high conductivity.[15] Among these materials, activated carbons are the most widely commercialized due to their low cost, establish processing methods, and extremely high surface area; however, mass transfer limitations can arise when inaccessible pores to the electrolyte are developed during the activation process.[16]

A proper balance between macro-, meso- and micropores is required for a combination of high energy density (micropores) and high power density (macropores).[17] Well-ordered templated carbons have also been developed to overcome this challenge, although, the synthesis process tend to be costly, long, and tedious.[18, 19]

Particularly attractive, owing to an easy and scalable synthesis process, as well as mechanical flexibility for use in wearable devices, are carbon fibers.[3] Carbon fibers can be derived from several precursors, such as pitch[20], polyacrylonitrile,[21] and biomass (*e.g.* lignin,[22, 23] cellulose[24]) among others. They possess outstanding specific strength and modulus, as well as excellent electrical and thermal conductivity, which make carbon fibers suitable for applications requiring structural support or flexibility. Synthesized by electrospinning or wet spinning, carbon fibers can be synthesized as discontinuous submicron size fibers (electrospinning) or continuous fibers, generally, in the micron size range (wet spinning).[25]

To enable the used of carbon fibers as supercapacitor electrodes, they must exhibit a micro-/nanostructure that leads to high surface area, otherwise, the electrochemical performance is insufficient. The most common way to introduce meso- and microporosity in carbon fibers is the use of physical or chemical activation with similar processes used for activated carbon synthesis. Physical activation is performed with either CO_2, O_2 or steam as the oxidizing agent at temperatures between 600-1200°C, while chemical activation is performed with either NaOH, KOH, H_3PO_4 or $ZnCl_2$ as oxidizing agents using temperatures between 400-900°C.[15] In general, chemical activation is more efficient than physical activation because it requires a lower

temperature, shorter reaction time, and provides higher micropore volumes with a more narrow pore size distribution compared with physical activation. As a result, chemical activation is often favored over physical activation unless the structural integrity of the electrode material is a concern.[15, 20, 26]

The use of microstructured and activated carbon fibers in supercapacitors has been reported previously.[14, 25, 27-29] For example, Xue *et.al.* [30] compared the effect of physical (CO_2) and chemical (KOH) activation processes on the electrochemical activity of phenol-formaldehyde derived carbon fibers, showing that chemical activation leads to higher surface area (1893 $m^2\ g^{-1}$) and higher specific capacitance (293 F g^{-1} in 6M KOH at 50mV s^{-1}) compared with physical activation (212 F g^{-1} 6M KOH at 50mV s^{-1}). Li *et. al* [31] took advantage of the ternary system Dimethyl sulfoxide (DMSO)-Water(H_2O)-Polyacrylonitrile (PAN) in the coagulation bath of wet spinning to produce PAN carbon fibers with macro- and mesoporosity created by the difference in solubility of PAN in DMSO and H_2O. Porous fibers were generated and later activated with KOH to provide microporosity yielding an average capacitance of ~250 F g^{-1}.

Polyacrylonitrile (PAN) is one of the most common materials utilized for the synthesis of conventional and activated carbon fibers, however, to develop an environmentally friendly and cost-competitive precursor, efforts towards the use of biomass and composite polymers for the synthesis of carbon fibers have gained interest.[25] Lignin is the second most abundant biopolymer after cellulose, comprising between 10-30% of plant dry mass and is produced as a by-product of the chemical pulping process of wood to produce paper.[32] Carbon fibers derived from PAN/lignin polymer blends have

been produced and exhibit micron-size voids due to lignin leaching from the blend during the synthesis process.[33-35] The amount of lignin incorporated into the mixture influences the porosity of the fibers, such that higher concentrations of lignin (up to 45wt.%) lead to larger macro-/mesopores than lower concentrations (10-35 wt.%).[34, 35] The voids are attributed to low viscosities and solid content of the spinning solution, as well as, phase separation during the coagulation bath, resulting in lignin diffusing from the blend to the solution in the coagulation bath. To our knowledge, there are no reports of the use of lignin content to control of the maro-/mesoporosity of PAN/Lignin fibers for designing and optimizing fibrous supercapacitor electrodes.

Here, PAN/lignin fibers were produced via wet spinning and used to create supercapacitor electrodes with macro-/mesoporosity. Porous fibers were then activated with KOH to enhance the microporosity and increase the surface area. The effect of the fiber diameter and chemical activation on the electrochemical activity of the fibers was studied and compared with conventional PAN fibers.

4.2 Experimental methods

4.2.1 Materials

Polyacrylonitrile (PAN) homopolymer with a molecular weight of 150,000 and a glass transition temperature (Tg) of 125°C was used throughout this study. The solvent utilized in this work was dimethyl sulfoxide (DMSO). Both PAN homopolymer and solvent were obtained from Sigma-Aldrich. Softwood Kraft lignin (SKL, indulin) was

provided by Mead-Westwaco. All chemicals used in the electrochemical measurements were purchased from Fisher Scientific unless otherwise stated.

4.2.2 Wet-spinning

Lignin and PAN were dissolved in DMSO at 60°C to make a blend solution with 20 wt.% polymer. The mass ratio of lignin to PAN was 35:65. Fibers were wet spun from blend solution into fibers under coagulant bath comprised of 65 wt.% DMSO/35 wt.% distilled-deionized water maintained at room temperature, and then passed through a water bath. During wet-spinning, the draw down ratio was maintained at 2. After wet spinning, porous fibers were post stretched in a water bath at 80°C, and different draw down ratios of 2 and 4 were obtained.

4.2.3 Carbon fiber synthesis

The precursor fibers were thermo-oxidatively stabilized in air using a heating rate of 0.5°C min^{-1} up to 300°C. Thermally stabilized fibers were carbonized in helium using a graphite furnace (ASTRO HP50-7010) to 1200°C, or 1500°C at a rate of 7°C min^{-1} for 1h.

4.2.4 Sample preparation

The steps to prepare the samples for the electrochemical characterization are presented in **Figure 4.1** as follows:

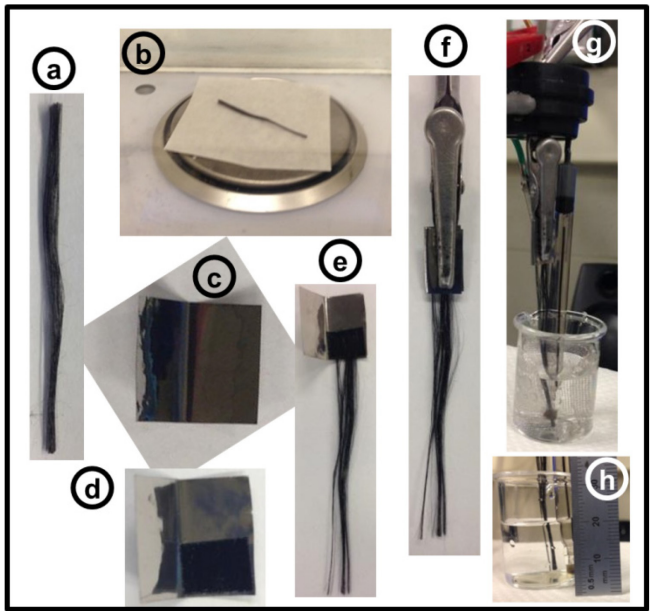

Figure 4.1 Sample preparation steps for electrochemical characterization.

1. The carbon fibers were synthesized in bundles of straight individual fibers (**Figure 4.1**) cut to a length of 4-6 cm to facilitate handling.
2. The sample was weighed in Ohaus DV215CD Semi-micro balance, readability 0.01mg (**Figure 4.1b**).
3. Titanium foil (Ti) was used as current collector (Ti) (**Figure 4.1c**). A piece of carbon tape was laid over the Ti foil (**Figure 4.1d**) to hold in place the bundle of fibers which was gently positioned over it (**Figure 4.1e**).
4. An alligator clip was connected to the Ti foil (**Figure 4.1f**) becoming the working electrode (WE).
5. A 3-electrode cell (**Figure 4.1g**) is assembled comprised by the WE, Ag/AgCl in 3M NaCl solution as reference electrode (RE) and platinum (Pt) gauze 52 mesh (Alfa Aesar) as a counter electrode (CE). The length of the sample in solution was

kept to ~1.5cm of the total length. Therefore, the mass of active material was calculated from the total mass and total length to ~1.5cm (**Figure 4.1h**).

6. The three-electrode cell was connected to a VersaSTAT 4 Potentiostat/Galvanostat and the measurements were taken with VersaStudio v2.42.3 Electrochemistry Software (Princeton Applied Research).

4.2.5 Electrochemical analysis

Electrochemical characterization was performed in a 1.5 M H_2SO_4 solution. 40 cyclic voltammetry cycles were performed between -0.2 to 1.2 V *vs.* Ag/AgCl at 100 mV s^{-1} to allow the electrolyte to completely penetrate the internal structure of the fibers. Next, samples were treated with 0.5 M Ammonium Bicarbonate (NH_4HCO_3) by chronopotentiometry (CP) for 15 min total in intervals of 5 min, unless otherwise stated; the current density was selected according to the specific sample to maintain the potential between 1.0 and 1.25V *vs.* Ag/AgCl during each treatment. Subsequently, deionized (DI) water was used to remove the remaining NH_4HCO_3 and 40 cyclic voltammetry cycles from -0.2 to 1.2V *vs.* Ag/AgCl were used to condition the sample in the electrolyte prior electrochemical characterization. Cyclic voltammetry (CV) experiments were performed from -0.2 to 1.0 V at various scan rates (300, 100, 30, 10, 3 mV s^{-1}), electrochemical impedance spectroscopy (EIS) at 0 V over a frequency range of 10k to 0.1 Hz using a perturbation amplitude of 20 mV, and charge-discharge (CD) measurements at current densities of 0.80, 1.61, 3.23 mA g^{-1} (-0.80, -1.61, -3.23 mA g^{-1}) from 0 to 1 V *vs.*

Ag/AgCl, unless otherwise stated. The samples were characterized before and after electrochemical pretreatment with NH_4HCO_3.

4.2.6 Carbon fiber activation

Stabilized PAN/lignin fibers were chemically activated using a 1 M KOH solution. The samples were soaked in the KOH solution at 60 °C overnight. Then, the fibers were removed and dried in vacuum oven at 85 °C overnight. The activation and carbonization (both simultaneously) were performed in a Thermolyne 79300 tubular furnace under N_2 at a flow rate of 80 mL min^{-1} and a heating rate of 5 °C min^{-1} to 800 °C for 1 h. After cold down the samples were washed with 1 M HCl and deionized water until all the remaining potassium was removed, then dried under vacuum (98.2 kPa) at 80 °C overnight and heat treated to 1200 °C for 1 h at 8 °C min^{-1}.

4.2.7 Surface morphology

The film surface characterization was performed by Scanning Electron Microscopy (SEM) in a Hitachi S4800 High-Resolution SEM at a beam intensity of 5 kV. The samples were frozen with liquid N_2, cut and placed on aluminum sample holders with carbon tape. Images were captured at magnifications of x1.5k, x 2.2k, x5.0k, x40k, x60k. Quartz PCI software and ImageJ were used to take samples measurements.

4.3 Results and discussion

4.3.1 Synthesis of porous PAN/lignin carbon fibers

The synthesis process for the PAN/Lignin carbon fibers (P/L-CF) and PAN/Lignin activated carbon fibers (P/L-ACF) is presented in **Figure 4.2**. The polymer is suspended in a solvent, to form a viscous "spinning dope". In the wet-spinning process, the spinning dope is pumped through a die head, where it is filtered to remove impurities before extruded through a spinneret containing small capillary holes. The spinneret is submerged in a coagulant bath, and the solution immediately enters coagulant bath as it exits the capillary. The coagulant consists of spinning solvent-DMSO, and non-solvent-water. A diffusional interchange between the formed fluid filaments and coagulant causes solvent removal from the fibers and solidification as precipitation occurs. The macro-/mesopores were observed in as-spun fibers after wet spinning due to diffusion of lignin. The following post-stretching step was conducted in water at 80 °C to enhance molecular alignment and reduce fiber diameter; the macro-/mesopores remained after post-stretching. Higher draw down ratio leads to smaller fiber diameter and higher molecular orientation. During thermal stabilization, the cross-linking reactions resulted in the ladder like network structure, which prevented the macro-/mesoporous structure from collapsing during high-temperature carbonization. The hexagonal carbon structure was formed, and marco-/mesopores remained after carbonization.

The chemical activation was performed with KOH, which produces defined micropore size distribution, high micropore volume and high surface area (up to 3000 m^2 g^{-1}) compared with other alkali hydroxide agents, such as NaOH.[15, 26, 36] The activation

mechanism consists of a series of chemical and physical steps involving K, K_2CO_3, K_2O, CO, CO_2, H_2, H_2O that occur from ~400°C to ~800°C during the activation process under an inert atmosphere. A detailed explanation of the reaction mechanism can be found elsewhere.[13, 15] The stabilized fibers were soaked in 1 M solution of KOH at 60°C overnight, and then dried overnight under vacuum at 85 °C. The activation process was performed at 800 °C and a heat treatment step to 1200°C was added to improve the conductivity of the fibers after activation (details can be found in the experimental methods).

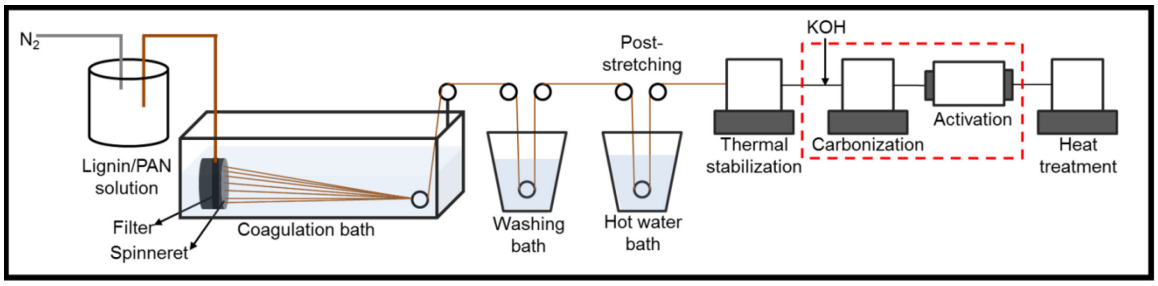

Figure 4.2 Wet-spinning process for the synthesis of PAN/lignin carbon fibers.

Two different sets of porous carbon fibers were prepared: (1) porous PAN/lignin carbon fibers (P/L-CF) with the presence of macro-/mesopores to study the effect of the fiber diameter and chemical treatment on the electrochemical characteristics, and (2) PAN/lignin carbon fibers activated with KOH (P/L-ACF) using the diameter of fibers that led to the best electrochemical performance; both will be discussed in the following sections.

4.3.2 Porous PAN/lignin fibers morphology

As discussed in the previous section, during the wet spinning process of the fibers in the coagulation bath, the solvent (DMSO) diffuses out of the spinning dope and so does lignin due to the difference in concentration, leaving behind voids that are maintained all the way through the carbonized fibers. **Figure 4.3** shows the SEM micrographs of the cross sections of a commercial solid PAN fiber (diameter 8 µm) (**Figure 4.3a**) for comparison purposes, and P/L-CF stabilized at 300°C and carbonized at 1200°C with average diameters of ~8.5µm (**Figure 4.3b**) and ~17µm (**Figure 4.3c**). The range of pores sizes varies from micron to submicron, and the fibers exhibit pores in the cross section, as well as, on the fiber walls. The amount of pores and the pore size can be tuned by changing the ratio of PAN to lignin;[34] however, in this work it was kept to 65wt.% PAN and 35 wt.% lignin.

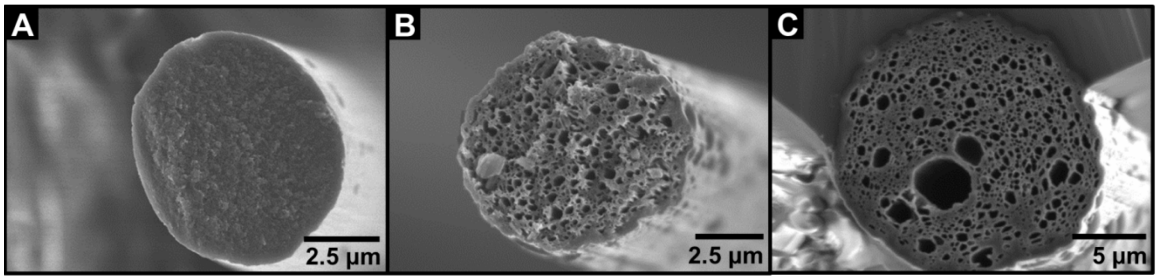

Figure 4.3 SEM images for (a) commercial PAN fiber ~8 µm, (b) PAN/lignin fiber ~8.5 µm, and (c) PAN/lignin fiber ~17 µm average diameter. Stabilized at 300°C and carbonized at 1200°C.

4.3.3 Electrochemical pre-treatment

After carbonization under inert atmosphere (1200-3000°C), the surface of CFs becomes inert due to loss of polar elements on the surface caused by high temperature.[37-39] An anodic oxidation treatment is used to improve the wettability of CF in aqueous systems by increasing the surface free energy, in addition to eliminating impurities that might exist on the surface of the fibers. As a result, the rate of diffusion of ions from the electrolyte to the surface and inner structure of the CFs increases. These treatments at the industrial level are usually carried out with ammonium salts, commonly ammonium bicarbonate (NH_4HCO_3). Acid and alkaline solutions can also be used; however, acid solutions may corrode the equipment, and alkaline solutions may incorporate metallic ions onto the surface and alter the fiber properties, thus ammonium salts are preferred.[38] All samples were treated with 0.5 M NH_4HCO_3 solution (pH 9) in a 3-electrode cell. Each treatment consisted of 5 min chronopotentiometry (CP) at a set current to reach a final voltage of 1.0 V *vs.* Ag/AgCl, but not to exceed a voltage of 1.25 V.

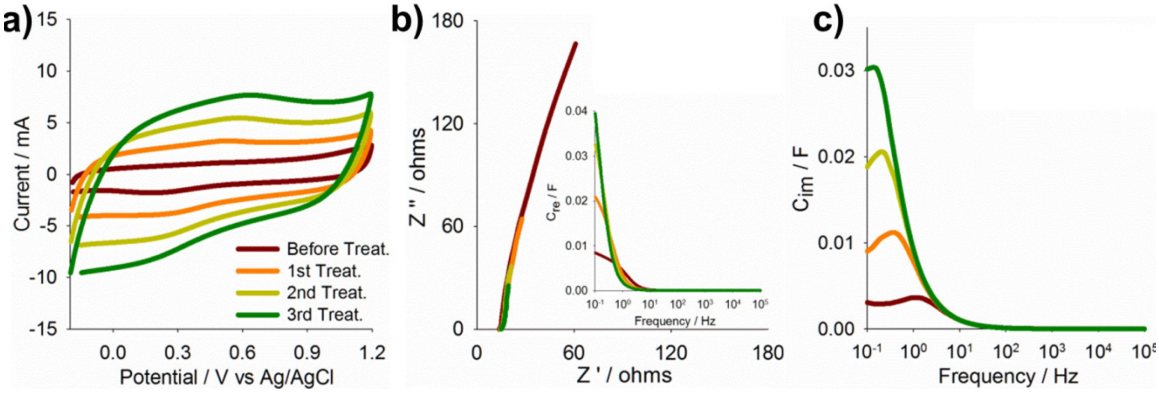

Figure 4.4 Electrochemical pre-treatment of carbon fibers. (a) Cyclic voltammetry profiles of P/L-CF before and after subsequent treatments with NH_4HCO_3 for 5 min. (b) Nyquist plot of Z'' *vs.* Z' (inset: Bode plot of the phase in impedance with frequency). (c) Bode plot of imaginary capacitance (C'') *vs*. frequency.

Figure 4.4 shows the changes in the electrochemical activity of 17µm diameter P/L-CF fibers with subsequent treatments in NH_4HCO_3. **Figure 4.4a** presents the cyclic voltammetry (CV) profiles before and after multiple successive 5 min treatments of applied currents of 3mA, 4 mA, and 4mA for 1st, 2nd, and 3rd treatment, respectively. The current applied during CP was increased to keep the potential between 1.0 and 1.25V *vs.* Ag/AgCl. After three treatments, no significant changes were observed in the CV profiles, thus, each sample was treated for 15 min total in 5 min intervals. The applied current was increased with subsequent treatments because the electrolyte progressively infiltrates the carbon as NH_4HCO_3 reacts with the electrode surface, thereby increasing access to the internal pore structure of the P/L-CFs.

The changes in the kinetic and diffusion control domains are showed in the Nyquist plot (Z'' *vs.* Z') (**Figure 4.4b**). Minimal changes in the Ohmic resistance with subsequent treatments are observed (high-frequency limit EIS) and at all times, the fibers

exhibit low charge transfer resistance (low-frequency side of the semi-circle). The low-frequency intercepts on the Nyquist plots correspond to 1 kHz, 1 kHz, 794.3 Hz, 398.1 Hz for the carbon fiber before treatment, and after subsequent treatments. The low-frequency intercept indicates the transition between kinetic control (charge transfer resistance, high frequencies) and diffusional control (ion transport resistance, low frequencies). After the 2nd treatment, the switching point frequency decreases indicating an increase in the time needed for the ion transport within the electrode. Anodic oxidation increases the accessibility to the microporous regions, therefore, it is expected that the time required for ions to access the inner pores increases. According to the plot of C_{re} (F) *vs.* frequency (Hz) (**Figure 4.4b** inset), the capacitive behavior of the P/L-CFs increases with subsequent treatments due to the increase in accessible surface area. C_{re} increases from 0.0084 F before treatment to 0.0396 F after 3rd treatment and is consistent with the increase in gravimetric capacitance presented in **Figure 4.4a**. The relaxation time (τ_c), which is a measure of how fast the electrode discharges with 50% efficiency, also changes as subsequent treatments are applied (**Figure 4.4c**). It is is defined as the reciprocal of the frequency at the peak ($\tau_c = 1/f_{peak}$) in the C_{im} *vs*. frequency plot. The values τ_c determined from **Figure 4.4c** are 1, 2.5, 5.0, and 7.9 s for sample before treatments, 1st, 2nd, and 3rd treatments, respectively. τ_c increases as the subsequent treatments are applied due to the increased accessibility of the inner pore structure. This evolution in performance exemplifies the tradeoff that exists between large scale and small scale porosity, and the effect of resistive and capacitive behavior.

4.3.4 Effect of fiber diameter

The influence of the diameter on the electrochemical performance of P/L-CFs was studied in 1.5 M H_2SO_4 in a 3-electrode cell after the fibers were conditioned and pretreated with 0.5 M NH_4HCO_3. **Figure 4.5a** shows the specific capacitance (F g^{-1}) as a function of the fiber diameter (μm). The specific capacitance (C_{sp}) is directly related to the specific surface area (S_{SA}) of the fibers (Eq. 4.1) which is inversely proportional to the diameter (D) – and density (ρ) – of the fibers (Eq. 4.2 and 4.3) and approximately follows Eq. 4.4 which is depicted by the red dashed line on **Figure 4.5a** as the change in the double layer capacitance with the reduction of the fiber diameter and correlates to the increase in the surface area.

$$C_{sp} = \frac{\varepsilon S_{SA}}{d} \quad \text{Eq. 4.1}$$

$$S_{SA} = \frac{4}{D\rho} \quad \text{Eq. 4.2}$$

$$C_{sp} \propto \frac{k}{D} \quad \text{Eq. 4.3}$$

$$C \approx \frac{496}{D} \quad \text{Eq. 4.4}$$

The performance of P/L-CFs with different diameters was compared with solid PAN fibers synthesized under the same conditions (stabilization and carbonization) in addition to commercially available PAN fibers. Because commercial PAN fibers (8 μm) are solid and lack surface defects, they possess a low surface area and electrochemical performance (4 F g^{-1}). PAN fibers (8 μm) synthesized in house have more surface defects compared to the commercial fibers; therefore, they show slightly higher capacitance (9 F g^{-1}). PAN/L-CFs 8.5 μm diameter showed the highest capacitance (58.3 F g^{-1}) when

synthesized under standard conditions (stabilization at 300°C and carbonization at 1200°C).

Figure 4.5b shows the CV profiles normalized to specific capacitance (current is divided by the mass and the scan rate) *vs.* potential of PAN/L-CFs at 10 mV s^{-1}. As showed in **Figure 4.5a** coarse PAN/L-CFs (>80 µm) exhibit poor electrochemical activity, whereas thin fibers (<20 µm) show capacitances of 26.8 and 58 F g^{-1} for 17 µm and 8.5 µm diameter fibers, respectively, when carbonized at 1200°C. To improve the conductivity of CFs, the carbonization temperature was increased 1500°C, which led to an increased capacitance of the 8.5 µm fibers up to 70 F g^{-1}. Even without microporosity created by activation, the EDLC of these fibers is fairly high.

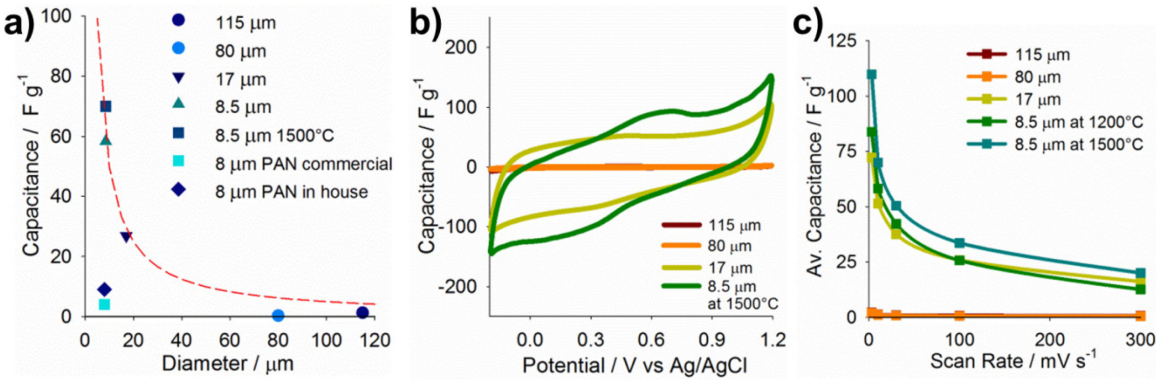

Figure 4.5 Electrochemical characteristics of P/L-CF different diameter. (a) Changes in specific capacitance (F g^{-1}) with diameter (µm) at 10 mV s^{-1}. (b) Cyclic voltammetry profiles normalized to specific capacitance (10mV s^{-1}). (c) Average capacitance (F g^{-1}) as a function of scan rate (mV s^{-1}).

The scan rate (mV s^{-1}) dependence of the average capacitance (F g^{-1}) for the various fibers is shown in **Figure 4.5c**. Thin fibers (17 µm and 8.5 µm) exhibit similar

scan rate dependence (redox activity limited by ion diffusion); at fast scan rates, the inner porosity of the carbon fibers is not accessible due to the timescale required for ion diffusion; therefore, all of the surface of the fibers is not used to store charge at all scan rates. As expected, the highest capacitance that can be achieved occurs at the slowest scan rate (3mV s^{-1}) where capacitance values as high as 72 F g^{-1} and 84 F g^{-1} were obtained from 17 µm and 8.5 µm diameter fibers carbonized at 1200°C. When the 8.5 µm diameter fibers were carbonized at 1500°C to increase their electrical conductivity (from 0.094 S cm^{-1} at 800°C to 0.45 S cm^{-1} at 1500°C), capacitance values up to 110 F g^{-1} (3mV s^{-1}) were achieved.

4.3.5 Activated PAN/lignin carbon fibers

Increasing carbonization temperature alone was not sufficient to obtain acceptable electrochemical performance of P/L-CFs for use in flexible or textile-based wearable energy storage devices. While the addition of lignin provides a template for the formation of macro- and mesopore domains within the internal structure of the PAN fibers, a balance between macro- (>50 nm), meso- (50 - 2 nm) and microporosity (< 2 nm) is required to enable higher energy density carbon fibers. Thus, an activation process was developed to increase microporosity as is commonly applied to carbon materials for applications in supercapacitors.[13, 15, 30] Essentially, P/L-CFs were chemically activated using a standard KOH process. Briefly, PAN/Lignin as-spun fibers were stabilized at 300 °C, then soaked in 1 M KOH overnight at 60 °C, and then dried. Carbonization and activation occurred simultaneously at 800°C. At this temperature the conductivity of the

fibers was low; therefore, a further heat treatment was performed up to 1200°C to improve the electrical conductivity.

Figure 4.6 and **4.7** show the preliminary results obtained from the activation process applied to 8.5 µm diameter P/L-CFs (P/L-ACFs). Prior to activate with KOH, the fibers cannot be fully carbonized to allow the KOH to react with the surface. Thus, the fibers were taken from the stabilization step (at 300°C), where the fibers exist as crosslinked polymers rather than carbonaceous material. During the process of soaking and heating (60°C) within the KOH solution, the fibers attract and curl around each other leading to fused fibers after the activation/carbonization process at (800°C). The final fibers lost part of the macro- and mesoporosity added by lignin, as is shown in **Figure 4.6a**. From the SEM cross-section, the fibers do not appear to be porous at the length scale shown (**Figure 4.6b**) and furthermore, the fused fiber walls show a higher surface roughness than non-activated fibers (**Figure 4.6c**).

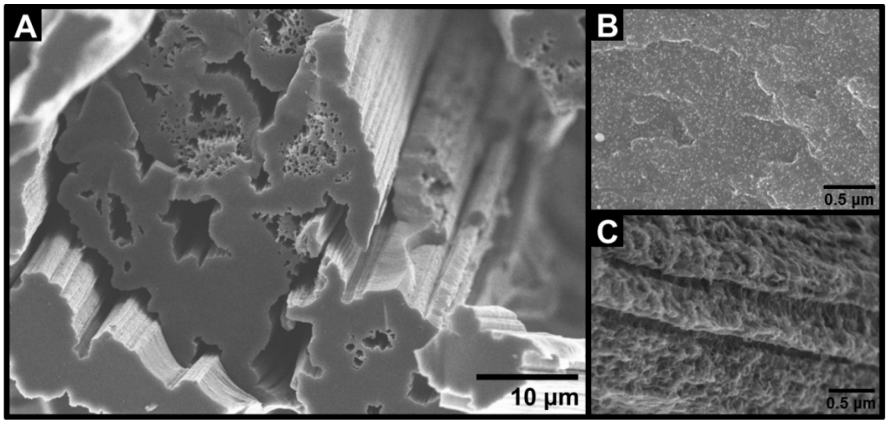

Figure 4.6 Scanning electron microscopy of P/L-ACFs, originally 8.5 µm diameter, activated with KOH. (a) Fuse fibers, (b) cross section, and (c) fiber wall.

The electrochemical performance of the P/L-ACFs shown in **Figure 4.6** is presented in **Figure 4.7**. P/L-ACFs exhibit increased capacitance, as high as 288 F g^{-1} (3 mV s^{-1}), compared with P/L-CFs-1500°C (110 F g^{-1} at 3mV s^{-1}), as shown on the cyclic voltammetry profiles, **Figure 4.7a**. As expected for microporous materials, there is high scan rate dependence between fast (100 mV s^{-1}) and low (3 mV s^{-1}) scan rates. Microporous materials will have a poor performance at fast scan rates as it is difficult for the ions to diffuse into the inner structure of small pores at short time scales (100 mV s^{-1}); however, at slow scan rates (3 mV s^{-1}) longer time for the transport of ions is given, leading to a higher capacitance.

Consistent with the CV profiles characteristics, the charge capacities obtained from the discharge profiles (**Figure 4.7b**) (35 to 89 mA h g^{-1}) are about three-fold higher than the charge capacities of P/L-CFs-1500°C (12 to 25 mA h g^{-1}). Correspondingly, in the specific average capacitance *vs.* diameter plot (**Figure 4.7c**), the capacitance at 10 mV s^{-1} for all the samples studied is compared. It is important to mention that, P/L-CFs denoted by the red dashed line are the same shown in **Figure 4.5**, samples denoted as 8.5 μm P/L-ACF correspond to **Figures 4.6, 4.7a** and **4.7b** while P/L-CF non-act. correspond to a sample subjected to the same process as P/L-ACF without KOH activation. P/L-CF non-act. exhibit very low capacitance (6 F g^{-1} at 10 mV s^{-1}) due to high impedance as confirmed by EIS. The various heat treatments used during the synthesis of the fibers are believed to be affecting the conductivity. Experiments are being performed to understand this behavior. P/L-ACF exhibit more than two-fold higher capacitance (192 F g^{-1} at 10 mV s^{-1}) compared with P/L-CF-1500°C (70 F g^{-1} at 10 mV s^{-1}). Important to notice is that

the electrochemical pre-treatment did not make any difference in P/L-ACFs. The activation process followed by the HCl wash, remove any surface impurity and ensure wettability, therefore, the electrochemical pre-treatment is not needed in this case.

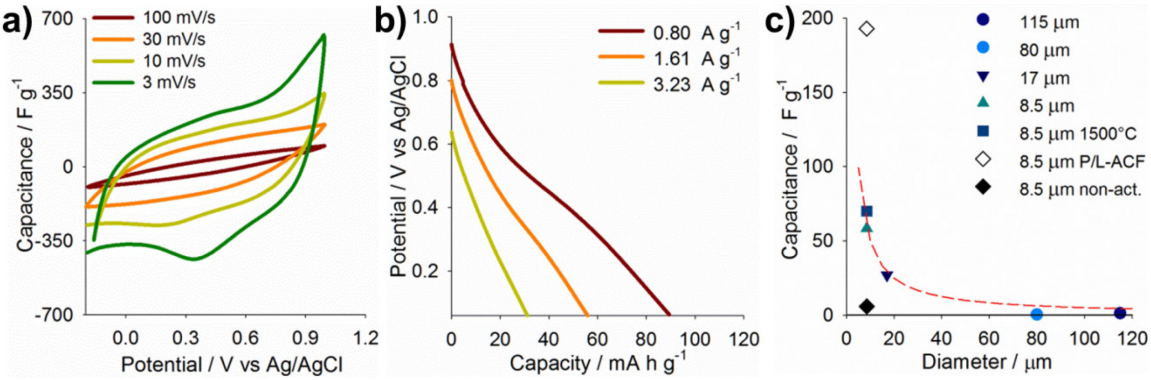

Figure 4.7 Electrochemical characteristics of P/L-ACFs. (a) Cyclic voltammetry profiles normalized to specific capacitance *vs.* potential. (b) Discharge profiles at various currents. (c) Changes in specific capacitance *vs.* diameter at 10 mV s^{-1}.

4.4 Conclusions and future work

The use of lignin as a tool to tune to produce porous carbon fibers has been demonstrated. By controlling the fiber diameter, the capacitance of the final fibers can be significantly improved. Small average fiber diameter (8.5 µm) demonstrated the highest capacitance (~70 F g^{-1} at 10 mV s^{-1}); however, to further increase the electrochemical performance an activation process with KOH was used. P/L-ACF showed a capacitance of 192 F g^{-1} at 10 mV s^{-1}, although the fibers lost the macro- and mesoporosity as they curl together during the KOH soaking process.

The activation process has recently been revised to prevent the macroporosity loss previously observed. After the stabilization at 300°C, the polymer fibers are pre-carbonized at 600°C for 1h to increase the stability of the fibers and freeze the internal structure. Next, the fibers are soaked in KOH overnight under vacuum, then removed from the solution, dried, carbonized/activated at 800°C for 1 h and further heat-treated at 1500°C. This new activation procedure is presently under investigation.

4.5 References

1. Whittingham MS. History, Evolution, and Future Status of Energy Storage. *Proceedings of the IEEE* **2012**, 100(Special Centennial Issue)**:** 1518-1534.

2. Titirici M-M, White RJ, Brun N, Budarin VL, Su DS, del Monte F*, et al.* Sustainable carbon materials. *Chem. Soc. Rev.* **2015**, 44(1)**:** 250-290.

3. Yang P, Mai W. Flexible solid-state electrochemical supercapacitors. *Nano Energy* **2014**, 8**:** 274-290.

4. Yu Z, Tetard L, Zhai L, Thomas J. Supercapacitor electrode materials: nanostructures from 0 to 3 dimensions. *Energy Environ. Sci.* **2015**, 8(3)**:** 702-730.

5. Staaf LGH, Lundgren P, Enoksson P. Present and future supercapacitor carbon electrode materials for improved energy storage used in intelligent wireless sensor systems. *Nano Energy* **2014**, 9**:** 128-141.

6. Wang F, Xiao S, Hou Y, Hu C, Liu L, Wu Y. Electrode materials for aqueous asymmetric supercapacitors. *RSC Adv.* **2013**, 3(32)**:** 13059-13084.

7. Yao F, Pham DT, Lee YH. Carbon-Based Materials for Lithium-Ion Batteries, Electrochemical Capacitors, and Their Hybrid Devices. *ChemSusChem* **2015**, 8(14)**:** 2284-2311.

8. Sevilla M, Mokaya R. Energy storage applications of activated carbons: supercapacitors and hydrogen storage. *Energy Environ. Sci.* **2014**, 7(4)**:** 1250-1280.

9. De Volder MFL, Tawfick SH, Baughman RH, Hart AJ. Carbon Nanotubes: Present and Future Commercial Applications. *Science* **2013**, 339(6119)**:** 535-539.

10. Singh V, Joung D, Zhai L, Das S, Khondaker SI, Seal S. Graphene based materials: Past, present and future. *Prog. Mater Sci.* **2011**, 56(8)**:** 1178-1271.

11. Gu W, Yushin G. Review of nanostructured carbon materials for electrochemical capacitor applications: advantages and limitations of activated carbon, carbide-derived carbon, zeolite-templated carbon, carbon aerogels, carbon nanotubes, onion-like carbon, and graphene. *WIREs Energy Environ.* **2014**, 3(5)**:** 424-473.

12. Su C-I, Wang C-M, Lu K-W, Shih W-C. Evaluation of activated carbon fiber applied in supercapacitor electrodes. *Fiber Polym.* **2014**, 15(8)**:** 1708-1714.

13. Zhang T, Kim CHJ, Cheng Y, Ma Y, Zhang H, Liu J. Making a commercial carbon fiber cloth having comparable capacitances to carbon nanotubes and graphene in supercapacitors through a "top-down" approach. *Nanoscale* **2015**, 7(7)**:** 3285-3291.

14. Wang G, Wang H, Lu X, Ling Y, Yu M, Zhai T*, et al.* Solid-State Supercapacitor Based on Activated Carbon Cloths Exhibits Excellent Rate Capability. *Adv. Mater.* **2014**, 26(17)**:** 2676-2682.

15. Wang J, Kaskel S. KOH activation of carbon-based materials for energy storage. *J. Mater. Chem.* **2012**, 22(45)**:** 23710-23710.

16. Borchardt L, Oschatz M, Kaskel S. Tailoring porosity in carbon materials for supercapacitor applications. *Mater. Horiz.* **2014**, 1(2)**:** 157-168.

17. Inagaki M. Pores in carbon materials-Importance of their control. *New Carbon Materials* **2009**, 24(3)**:** 193-222.

18. Béguin F, Presser V, Balducci A, Frackowiak E. Carbons and Electrolytes for Advanced Supercapacitors. *Adv. Mater.* **2014**, 26(14)**:** 2219-2251.

19. Wang J, Xin HL, Wang D. Recent Progress on Mesoporous Carbon Materials for Advanced Energy Conversion and Storage. *Part. Part. Syst. Char.* **2014**, 31(5)**:** 515-539.

20. Linares-Solano A, Cazorla-Amorós D. Activated Carbon Fibers. *Handbook of Advanced Ceramics, ed. S. Somiya, Academic Press, Elsevier Inc*, **2013**, p 155.

21. Gulgunje PV, Newcomb BA, Gupta K, Chae HG, Tsotsis TK, Kumar S. Low-density and high-modulus carbon fibers from polyacrylonitrile with honeycomb structure. *Carbon* **2015**, 95**:** 710-714.

22. Jin J, Yu B-j, Shi Z-q, Wang C-y, Chong C-b. Lignin-based electrospun carbon nanofibrous webs as free-standing and binder-free electrodes for sodium ion batteries. *J. Power Sources* **2014**, 272**:** 800-807.

23. Wang S-X, Yang L, Stubbs LP, Li X, He C. Lignin-Derived Fused Electrospun Carbon Fibrous Mats as High Performance Anode Materials for Lithium Ion Batteries. *ACS Appl. Mater. Interfaces* **2013**, 5(23)**:** 12275-12282.

24. Chen J, Xu J, Wang K, Cao X, Sun R. Cellulose acetate fibers prepared from different raw materials with rapid synthesis method. *Carbohydr. Polym.* **2016**, 137**:** 685-692.

25. Frank E, Steudle LM, Ingildeev D, Spörl JM, Buchmeiser MR. Carbon Fibers: Precursor Systems, Processing, Structure, and Properties. *Angew. Chem. Int. Ed.* **2014**, 53(21)**:** 5262-5298.

26. Castro-Muñiz A, Suárez-García F, Martínez-Alonso A, Tascón JMD, Kyotani T. Energy storage on ultrahigh surface area activated carbon fibers derived from PMIA. *ChemSusChem* **2013**, 6(8)**:** 1406-1413.

27. Xu B, Wu F, Chen R, Cao G, Chen S, Yang Y. Mesoporous activated carbon fiber as electrode material for high-performance electrochemical double layer capacitors with ionic liquid electrolyte. *J. Power Sources* **2010**, 195(7)**:** 2118-2124.

28. Hu S, Zhang S, Pan N, Hsieh Y-L. High energy density supercapacitors from lignin derived submicron activated carbon fibers in aqueous electrolytes. *J. Power Sources* **2014**, 270**:** 106-112.

29. Jost K, Stenger D, Perez CR, McDonough JK, Lian K, Gogotsi Y*, et al.* Knitted and screen printed carbon-fiber supercapacitors for applications in wearable electronics. *Energy Environ. Sci.* **2013**, 6(9)**:** 2698-2705.

30. Xue R, Yan J, Liu X, Tian Y, Yi B. Effect of activation on the carbon fibers from phenol-formaldehyde resins for electrochemical supercapacitors. *J. Appl. Electrochem.* **2011**, 41(11)**:** 1357-1366.

31. Li Y, Lu C, Zhang S, Su F-Y, Shen W, Zhou P*, et al.* Nitrogen- and oxygen-enriched 3D hierarchical porous carbon fibers: synthesis and superior supercapacity. *J. Mater. Chem. A* **2015**, 3(28)**:** 14817-14825.

32. Sixta H, Potthast A, Krotschek AW. Chemical Pulping Processe: Sections 4.1–4.2.5. *Handbook of Pulp*. Wiley-VCH Verlag GmbH, **2008**, pp 109-229.

33. Choi DI, Lee J-N, Song J, Kang P-H, Park J-K, Lee YM. Fabrication of polyacrylonitrile/lignin-based carbon nanofibers for high-power lithium ion battery anodes. *J. Solid State Electrochem.* **2013**, 17(9)**:** 2471-2475.

34. Dong X, Lu C, Zhou P, Zhang S, Wang L, Li D. Polyacrylonitrile/lignin sulfonate blend fiber for low-cost carbon fiber. *RSC Adv.* **2015**, 5(53)**:** 42259-42265.

35. Xia K, Ouyang Q, Chen Y, Wang X, Qian X, Wang L. Preparation and Characterization of Lignosulfonate–Acrylonitrile Copolymer as a Novel Carbon Fiber Precursor. *ACS Sustainable Chem. Eng.* **2016**, 4(1)**:** 159-168.

36. Babeł K, Jurewicz K. KOH activated lignin based nanostructured carbon exhibiting high hydrogen electrosorption. *Carbon* **2008**, 46**:** 1948-1956.

37. Vickers PE, Watts JF, Perruchot C, Chehimi MM. The surface chemistry and acid–base properties of a PAN-based carbon fibre. *Carbon* **2000**, 38(5)**:** 675-689.

38. Qian X, Wang X, Ouyang Q, Chen Y, Yan Q. Effect of ammonium-salt solutions on the surface properties of carbon fibers in electrochemical anodic oxidation. *Appl. Surf. Sci.* **2012**, 259**:** 238-244.

39. Li J, Wang X, Huang Q, Gamboa S, Sebastian PJ. Studies on preparation and performances of carbon aerogel electrodes for the application of supercapacitor. *J. Power Sources* **2006**, 158(1)**:** 784-788.

CHAPTER FIVE

RIGID, NON-PRESSED, HIGHLY POROUS CARBON AEROGEL SUPERCAPACITOR ELECTRODES

5.1 Introduction

Efforts to reduce our dependence on fossil fuels and reduce the CO_2 emissions have increased the demand for technologies to harvest energy from renewable sources (e.g. wind and solar) and for energy systems to power vehicles.[1, 2] The challenge in this regard is developing highly efficient, low cost and environmentally friendly electrical energy storage devices (EES). Supercapacitors, due to their relatively high energy density and power density, provide an alternative EES to bridge the gap between conventional batteries and capacitors.[2-4] Electrochemical capacitors are classified according to their charge storage mechanism and configuration. Electrochemical double layer capacitors (EDLCs) store charge based on ion adsorption on to the surface of the electrode material, which is generally a high surface area, low resistance material, and are primarily based on highly porous carbons.[5-7] Pseudocapacitors, however, store charge based on a fast oxidation-reduction reactions within electroactive materials, such as conducting polymers[8, 9] and metal oxides.[3, 10, 11] yielding higher energy densities at the cost of reduced cycle life and stability.[12] By contrast, carbon materials exhibit high stability and long cycle life because no electrochemical reactions occur at the electrode interface, and as a result activated carbons are currently used in commercial supercapacitors. However, relatively low energy density is obtained due to the dependence from surface area, carbon structure, pore size distribution, particle size, surface functional groups, as well as, the

type of electrolyte is the motivation for current research.[7, 13] Hybrid capacitors are asymmetric devices comprised of electrodes of each type, in which the anode is typically a high surface area carbon (EDLC), and the cathode is typically a Faradaic material.

Carbon is a versatile material that can be synthesized in many forms.[14] For instance, activated carbons can be synthesized from coconut shells, coals, pitch, and synthetic organic polymers through carbonization and subsequent physical and/or chemical activation to create high surface area materials with combined macro- (>50nm), meso- (50-2nm) and micro- (<2nm) pores. Limitations in mass transfer can occur, especially at high current densities (fast charge-discharge rates), when wormlike pores are developed during the synthesis process; therefore, a balance between micro- and meso-pores volume is desired for high power systems.[3, 6, 7] Carbon nanotubes also represent promising materials since they can be grown directly on the current collector leading to a binder-free alternative materials with very low internal resistance.[15] However, one of their main limitations is relatively small surface area ($<500\ m^2\ g^{-1}$)[2] compared with activated carbons ($700\text{-}2200\ m^2\ g^{-1}$).[6] Therefore, various research efforts have focused on synthesizing composite materials with conducting polymers and metal oxides.[16] Carbon onions are not intrinsically porous, but due to their high conductivity achieved by a high degree of graphitization, they can be used in high power applications.[7] Graphene, which is considered the basic building block of carbon materials, also has a high electrical conductivity and surface area.[2] Efforts to improve energy density have produced materials with low electrode density and poor stability upon cycling.[6] While

each material offers some benefit in power, energy or stability, most carbon are limited by the lack of scalable synthesis as needed to accommodate high energy storage systems.

Particularly attractive as electrode materials for EDLCs are carbon aerogels that are made by controlled pyrolysis of phenolic aerogels. Phenolic aerogels are low-density materials comprised of a three-dimensional polymeric network that forms when the solvent is removed by an extraction process after cross-linking reactions are completed, leading to a porous material, generally with high specific surface area, fine pore size, and, after carbonization, good electrical conductivity.[6, 17-19] The porosity, surface area, and pore volume are highly dependent on the synthesis and processing conditions. There are different ways to synthesize carbon gels from essentially the same list of steps, and some particular changes will determine the name assigned to the final product (i.e. aerogel, xerogel, hydrogel, lyogels).[20]

In this work, we will particularly focus in Resorcinol-Formaldehyde (RF)-derived carbon aerogels. Briefly, carbon gel synthesis involves polycondensation reactions between precursors with a catalyst in aqueous (hydrogels) or organic (lyogels) solvents. A stable crosslinked film is formed by gelation, and the properties (density, rigidity, among others) will vary depending on curing time, reagent concentration, and catalysis. After a solvent exchange, the gels are solidified via supercritical drying with CO_2 (aerogel), subcritical drying with air or N_2 (xerogel), freeze drying or microwave drying. Finally, carbonization (600-1200^{o}C) is used to produce the stable carbon gels, and optionally a physical activation with CO_2 or chemical activation with KOH to increase surface area.[13, 17, 18, 20-26]

The performance of carbon aerogels continues to increase at the synthesis and drying processes are refined (data reported for single electrode measurements). In 2006, Li J. *et al.* showed that RF carbon aerogels could be used as EDLCs electrodes in 6M KOH achieving a specific capacitance of 110 F g^{-1}. Lee Y. J. *et al.* demonstrated that varying the R/C ratio between 20-2000 changes the BET surface area between 165-635 m^2 g^{-1} and the specific capacitance values (at 10mV s^{-1}) in 1M H_2SO_4 from 13-77 F g^{-1}.[18] Inverse emulsion polymerization reactions were shown to be superior to polycondensation reactions, providing surface areas and capacitance values of 1670 m^2 g^{-1} and 150 F g^{-1} compared 189 m^2 g^{-1} and 68 F g^{-1}, in 6M KOH.[13] Wang X. and co-workers[27] showed the use of carbon aerogel microspheres in supercapacitor electrodes with a maximum capacitance (at 2mV s^{-1}) of 187 F g^{-1}. With carbon aerogels activated using CO_2, the surface area could be increased to 2876 m^2 g^{-1} yielding a capacitance of 196 F g^{-1};[28] however, further increasing the surface area up to 3432 m^2 g^{-1} resulted in a decrease in capacitance to 152 F g^{-1}.[19, 29]

In these reports, electrodes are generally prepared by grinding the carbon gel (active material) and preparing slurry with carbon black (graphite or activated carbon), and a binder (PVDF or PTFE) at various ratios (80:10:10 or 75:15:10), coating the slurry on a current collector (nickel foam, stainless steel, among others), thereby adding unnecessary weight to the electrode. In this work, we overcome this challenge by synthesizing carbon foams (aerogels) that function as self-standing electrodes to eliminate the need for a current collector, binder or conductivity enhancers while simultaneously increasing the rate of aerogel synthesis. Carbon veil or alumina felt were

incorporated into the polycondensation reaction mixture to provide mechanical support for the final aerogel. After optimization of the synthesis conditions, processing times were reduced from four days for curing[23] and three days for drying[27] to two days for curing and less than one day for drying. Furthermore, the process described in this paper prevents the negative effects of active material shrinkage due to carbonization that causes the material to separate from the reinforcing fabric and crack. The electrochemical performance of carbon foam aerogel on alumina felt (CFA-AL) and carbon veil (CFA-CV) are reported in single electrode configurations and within symmetric supercapacitors.

5.2 Experimental methods

5.2.1 Materials

Carbon foam aerogels were synthesized by Southern Research Institute. All materials for electrochemical analysis were purchased from Fisher Scientific unless otherwise stated.

5.2.2 Carbon aerogel synthesis process

Excess aluminum acetate ($C_4H_7AlO_5$) (Acros Organics) was dissolved in deionized water and mixed overnight. Resorcinol ($C_6H_6O_2$) (MP Biomedicals) and formaldehyde (CH_2O) (LabChem, Inc.) were dissolved into the aluminum acetate solution to form a resin. The resin was poured into a mold containing a thin carbon veil (Technical Fiber Products) or alumina felt (Zicar Ceramics), sealed, and allowed to cure

for 2 days at 90^0C. Once cured, the infiltrated veil or felt was placed in a gravity oven at 70^0C until dry. Subsequently, the excess material was removed from each surface and the sheet was placed in a furnace, evacuated with a vacuum pump and backfilled with Argon. The samples were heated at a rate of 2.5^0C min^{-1} until the carbonization temperature of ~1050^0C was reached and held for 2 h. This procedure was followed to prepared CFA-AL (carbon foam aerogel – alumina felt) and CFA-CV (carbon foam aerogel – carbon veil). To optimize the process, the resorcinol-aluminum acetate aqueous solution was degassed in vacuum at ~81.3 kPa until bubbles stop forming before adding formaldehyde; this extra step was added for the preparation of CFA-CVT (carbon foam aerogel – carbon veil thin).

5.2.3 Sample preparation

Carbon foam samples were cut with a razor blade in 1.2x1.2 cm squares (1.44 cm^{-2}), weighed (Ohaus DV215CD Semi-micro balance, readability 0.01mg) and placed in a three electrode Teflon cell with a WE testing area of 0.47cm^2. VersaSTAT 4 potentiostat/galvanostat and VersaStudio v2.42.3 Electrochemistry Software (Princeton Applied Research) were used for testing. Working electrode (WE) was Titanium foil (Ti foil) placed under the carbon foam sample, the sides were covered with electric tape to prevent the electrolyte from leaking, and uncovered metal was left to fit the sample (**Figure 5.2**). Platinum gauze 52 mesh (Alfa Aesar) was used as counter electrode (CE), and Ag/AgCl in 3 M NaCl solution as reference electrode (RE).

5.2.4 Electrochemical analysis

Electrochemical characterization was performed in a 0.5M Sulfuric Acid (H_2SO_4) and 3M Potassium Hydroxide (KOH) solutions. 40 cyclic voltammetry cycles were performed between -0.2 to 1.2V vs. Ag/AgCl at 100 mV s^{-1} to allow the electrolyte to wet the internal structure of the carbon foams. Then, samples were treated with 0.5M Ammonium Bicarbonate (NH_4HCO_3) by chronopotentiometry (CP) for 15 min total in intervals of 5 min, unless otherwise stated; the current density was selected according to the specific sample to maintain the potential between 1.0 and 1.25V *vs.* Ag/AgCl during each treatment. Subsequently, deionized (DI) water was used to remove the remaining NH_4HCO_3 and 40 cyclic voltammetry cycles from -0.2 to 1.2V *vs.* Ag/AgCl were used to condition the sample in the electrolyte prior electrochemical characterization. Cyclic voltammetry (CV) experiments were performed from -0.2 to 1.0 V at various scan rates (300, 100, 30, 10, 3 mV s^{-1}), electrochemical impedance spectroscopy (EIS) at 0 V over a frequency range of 10000 to 0.1 Hz using a perturbation amplitude of 20 mV, and charge-discharge measurements at current densities of 0.9, 1.7, 3.5, 6.9, 13.9 mA cm^{-2} (-0.9, -1.7, -3.5, -6.9, -13.9 mA cm^{-2}) from 0 to 1 V vs. Ag/AgCl, unless otherwise stated.

5.2.5 Surface morphology

The film surface characterization was performed by scanning electron microscopy (SEM) in a Hitachi S4800 High-Resolution SEM at a beam intensity of 5 kV; the samples were placed on 45° aluminum sample holders with carbon tape. Images were captured at magnifications of x30, x100, x400, x1.8k, x4.5k x15k, x45k, and x70k.

5.2.6 Brunauer-Emmett-Teller (BET)

Physisorption experiments were performed under Nitrogen, at 77.35K in a Quantachrome Autosorb iQ Gas Sorption Analyzer utilizing a 40-point adsorption/desorption isotherm analysis. The differential pore volume distribution was obtained from the desorption isotherm through Barrett-Joyner-Halenda (BHJ) analysis. Sample size: 0.3013g. Measurements were taken at the Electron Microscopy Laboratory at Clemson University.

5.2.7 Device preparation and characterization

Working and counter electrode were prepared by cutting two square pieces (1 cm^{-2}) and two round pieces (7.1 cm^{-2}) of carbon foam for acid (0.5M H_2SO_4) and basic (6M KOH) symmetrical supercapacitor devices, respectively. Silver 40AR and 25AR DreamWeaver were used as separators for acid and basic devices, respectively. The separators were soaked for 1h in the electrolyte to ensure full wettability. A MTI CR2025 button cell was assembled, and place in a coin cell apparatus (MTI Corp) to be tested (2-electrode system). CV experiments were performed from 0 to 1.0 V at scan rates mentioned before. EIS was performed at the same conditions stated previously. Cycle life experiments were executed for 2000 cycles through charge-discharge cycles between 0 and 1V at 1mA and 1.2mA for acid and basic electrolytes, respectively. The electrodes used in acid media device weighed 2.45 and 2.53mg and for basic media 4.26 and 4.58 mg. Energy and power density were calculated from charge-discharge cycles between 0

to 1.0V from 0.36 to 25.21 A g^{-1} in 6M KOH and from 0.43 to 20.89 A g^{-1} in 0.5M H_2SO_4.

5.3 Results and discussion

5.3.1 Carbon foam synthesis process

Carbon aerogels were synthesized by polycondensation reaction of resorcinol with formaldehyde and aluminum acetate as catalyst followed by pyrolysis. Catalyzing with aluminum acetate, rather than the typical sodium carbonate, results in a low-density gel that cures faster and shrinks very little while drying in air. The dried product can then be wet and redried without noticeable structural degradation. This is likely to produce a more robust superstructure, with shorter meso- and nano-pores, which should result in easier handling and better performance in energy storage applications. Additionally, the formulation described here has shown exceptional processing performance during carbonization after infiltration of a substrate. Typical resorcinol-formaldehyde infiltration and carbonization processes must go through a careful evaluation to prevent tension cracks from forming due to the variation in shrinkage rates between the substrate and the foam during carbonization. This material though has shown compatibility with two different materials, alumina felt and carbon veil, while remaining structurally intact.

Briefly, aluminum acetate is dissolved in DI water overnight, resorcinol is dissolved into this solution, and formaldehyde is then gently added to the mixture. The resin is placed in a mold with alumina felt or carbon veil and sealed to cure for two days at 90 °C. Once cured, the infiltrated veil or felt is placed to dry at 70 °C in a gravity oven.

The excess material is removed, and the sheet is placed in a furnace for carbonization at 1050 °C for 2 h. CFA-AL and CFA-CV were synthesizing following this process. CFA-CVT was made after an aging step was added to stabilize the concentration of catalyst in the solution and an evacuation step was added to control the formation of bubbles, avoiding the development of non-porous skins. This additional step was able to reduce the non-porous skins in the CFA-CVT samples compared with the surface of CFA-AL and CFA-CV. Furthermore, using an excess of alumina acetate and allowing the solution to sit until saturated, leads to a higher aluminum concentration of catalyst compared with CFA-AL and CFA-CV synthesis method, increasing the number of sol formation sites, which decreases the of individual sols in the gel, thus leading to smaller pore sizes and higher surface area.[30-33]

5.3.2 Carbon foam properties

When synthesized within the carbon veil and alumina felt substrates, the carbon aerogel exhibits a three-dimensional interconnected gel structure around the reinforcement fibers, adding stability and some flexibility to the final carbon foam after carbonization. Compared to aerogels coated on planar substrates and foils, where delamination can be problematic, porous networks formed around fibers making up the substrate are mechanically robust. Accordingly, these substrates can be easily integrated into many types of electrochemical cells or device configurations (**Figure 5.2a**). The thickness of the backbone materials was different; alumina felt was 0.1 cm thick while carbon veil 0.019 cm thick, these differences lead to changes in the thickness of the final

carbon foam electrodes. **Figure 5.1** shows the scanning electron microscopy (SEM) images of the various samples: CFA-AL (**Figure 5.1a**, 0.145 cm), CFA-CV (**Figure 5.1b**, 0.037cm) and CFA-CVT (**Figure 5. 1c**, 0.025 cm) taken at magnification of x70 on a 45° aluminum sample holder. The nanostructure of the carbon foams (at the magnifications studied) remained the same regardless the changes in the synthesis process or backbone material (**Figure 5.1b** to **1f**).

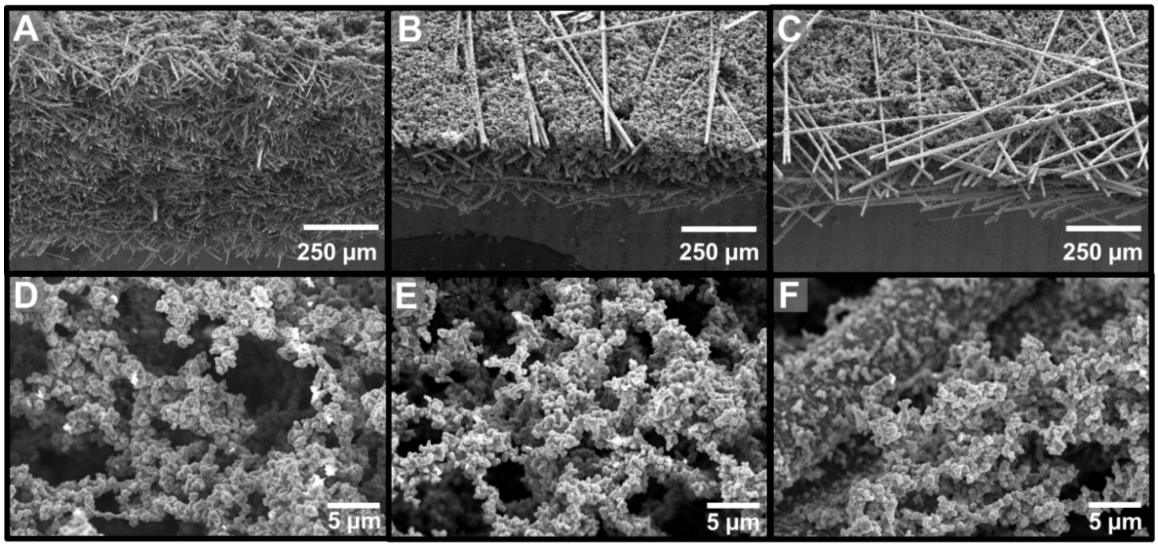

Figure 5.1 Scanning electron microscopy images of CFA-AL (A and D), CFA-CV (B and E) and CFA-CVT (C and F) at a magnification of x70 and x3.5K, respectively.

Interestingly, independent of the changes in the weight of the backbone material, the actual density of the carbonized foams are very similar: 0.117 g cm^{-3} for CFA-CV and 0.128 g cm^{-3} for CFA-AL and CFA-CVT. Conversely, the % of porous carbon (active) material, calculated by differencing the mass of the substrate material added during synthesis with the mass of the final carbon foam does vary depending on the type of backbone material added or changes in the synthesis. The composition of CFA-AL was

36.7% porous carbon material compared to 65.2% for CFA-CV, which is effectively due to the difference in mass of the alumina felt and carbon veil. For CFA-CVT, the % of porous carbon material on the substrate was reduced to 47.6% as the process to remove the excess material from the sheets before carbonization was more aggressive, which also contribute to the reduction of non-porous carbon skins on the sheets surface after carbonization.

Table 5.1. BET surface area, pore volume, and predominant pore size calculated from BHJ for CFA-AL, CFA-CV and CFA-CVT.

Sample	Surface Area [$m^2 g^{-1}$]	Pore Volume [$cm^3 g^{-1}$]	Pore sizes [diameter, nm]
CFA-CV & CFA-AL	664	0.283	3.91 & 67.1
CFA-CVT	660	0.266	3.90 & 34.6

BET measurements were performed under Nitrogen utilizing a 40-point adsorption/desorption isotherm analysis to determine the specific surface area of the carbon aerogels prepared with the two different synthesis methods (*i.e.* the one that leads to CFA-AL and CFA-CV and the one for CFA-CVT). **Table 5.1** shows the BET surface area for CFA-AL, CFA-CV and CFA-CVT. Notice that the surface areas of the samples are very close for the two synthesis methods. However, samples prepared with CFA-CV and CFA-AL present a higher pore volume (0.283 $cm^3 g^{-1}$) with a wider distribution of pores sizes mainly of 3.91 nm and 67.1 nm diameters compared with CFA-CVT which present a lower pore volume (0.266 $cm^3 g^{-1}$) and narrower distribution of pores mainly of 3.90 nm and 34.6 nm consistent with the use of excess catalyst and the degassing step,

which increased the functional surface area by minimizing the formation of macro-porosity and non-porous carbon skins after carbonization.

5.3.3 Electrochemical characterization

Figure 5.2 shows a schematic of the cell set up used for electrochemical measurements on the carbon foam substrates in a 3-electrode configuration. A carbon foam substrate was cut to 1.44 cm^2 and placed on a Ti foil (**Figure 5.2b**). The sides of the Ti foil were covered with electrical tape to prevent the electrolyte from leaking, leaving enough uncovered Ti foil to fit the sample and make contact with the potentiostat as the working electrode (WE). The WE configuration was placed in a Teflon cell as shown in **Figure 5.2c** with an electrolyte contact area of 0.47cm^2 at the base of the cell. The electrolyte is in direct contact with the sample, and the reference electrode (RE) (Ag/AgCl in 3 M KOH) is placed directly above the WE while the platinum mesh counter electrode (CE) is along the side of the Teflon cell.

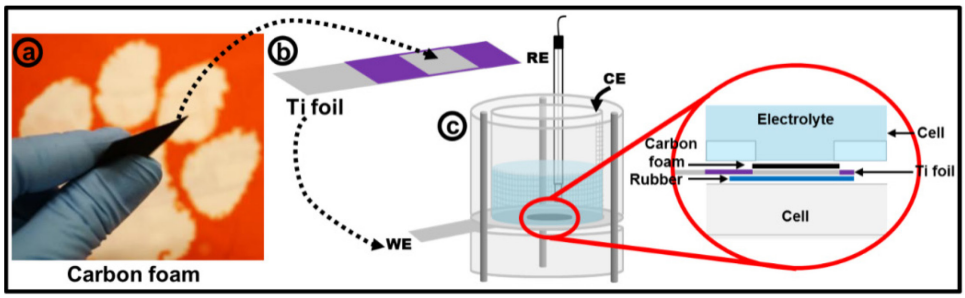

Figure 5.2. Illustrative schematic of the assembly of 3-electrode electrochemical cell for carbon foam characterization.

5.3.4 Electrochemical pre-treatment

Previous works with carbon fibers have indicated that after carbonization under inert atmosphere, the carbon surface becomes "inert" due to the loss of oxygen and related polar groups along the surface. Often, electrochemical anodic oxidation treatment is performed to clean or oxidize the surface of the fibers, thereby increasing the surface free energy (more polar) and wettability (affinity) toward aqueous solvents. As a result, an increase in accessible surface area and/or ion diffusivity is achieved.[22, 24, 34, 35] These treatments at an industrial level are usually carried out with ammonium salts, commonly ammonium bicarbonate (NH_4HCO_3) because acid solutions may cause corrosion and alkaline solutions may incorporate metal ions and alter the properties of the fibers. To reduce the potential for surface damage, ammonium salts are preferred.[34]

The effect of anodic oxidation pre-treatment in 0.5M NH_4HCO_3 solution (pH 9) on the carbon foams was studied. Each treatment consisted of chronopotentiometry for 5 min at a set current, such that a voltage of 1.0 - 1.25 V *vs.* Ag/AgCl was achieved. The required current varied from 4 mA for CFA-AL, 2 mA for CFA-CV, and 3 mA for CFA-CVT. After each treatment, a cyclic voltammetry profile was recorded in a fresh 0.5 M H_2SO_4 and the measured current was normalized to specific capacitance (current is divided by the active mass (g) of the electrode and the scan rate, V s^{-1}). Prior to electrochemical pre-treatment, samples were "conditioned" using cyclic voltammetry to ensure all the electrolyte has completely soaked the internal nanostructure of the samples. While CFA-CV and CFA-AL required many cycles to achieve a steady CV profile, CV profiles of CFA-CVT did not differ significantly during the first ~25 cycles. Furthermore,

the conditioning cycles were performed from -0.2 to 1.2V *vs.* Ag/AgCl to expedite the electrolyte penetrating process, even though the actual CV experiments were performed up to 1.0 V to avoid water decomposition that might lead to an apparent higher capacitance.

On CFA-CV, treatments were applied until a minimal change in CV profile was observed between treatments (**Figure 5.3a**). With additional surface treatments, the average capacitance improved from 43.0 F g^{-1} (no treatments) to 82.3 F g^{-1} (at 10mV s^{-1}) after 4 treatments. Slight changes in performance were also observed in the Nyquist plot presented on **Figure 5.3b**, which shows small changes in the Ohmic resistance (high-frequency limit of EIS) and low charge transfer resistance (low-frequency side of semi-circle in **Figure 5.3**). The low-frequency intercepts of the Nyquist plots occur at frequencies of 100 (no treatment), 398.1, 398.1, 316.22, and 251.19 Hz for samples with successive treatments. Notice that the CFA-CV sample exhibits a change in the frequency at which the electrode switches from kinetic control (high frequency) to mass transfer control (low frequencies). This is also confirmed by the Bode plot of phase Z *vs.* frequency (**Figure 5.3b** inset); as the frequency decreases, the electrochemical behavior switches from resistive (0° phase angle) to capacitive (90° phase angle). The frequency at which the behavior switches increases with treatment for the first three, and decreases after the fourth treatment. When the electrochemical treatments are too long, the surface can become overoxidized and trap ions, which increases the time required for the ion diffusion during the charge-discharge process. Accordingly, future samples were treated for a total of 15 min in NH_4HCO_3 prior to electrical analysis.

Figure 5.3c shows the change in the cyclic voltammetry profile for CFA-CVT electrodes, which exhibit an increase in capacitance from 122.9 to 150.6 F g^{-1} (at 10mV s^{-1}). While the electrochemical anodic oxidation provides a moderate increase in performance, the increase is not as significant as in the case for CFA-CV, where the capacitance nearly doubles. The effect of electrochemical treatment is also displayed in the Nyquist plot (**Figure 5.3d**). The frequency at which the transition between kinetic control and mass control happens, increases from 199.53Hz before treatment to 252.19 Hz after the third treatment indicating that longer times are required for the ion transport within the electrode compared to CFA-CV. This is also confirmed by the Bode plot of phase of *Z vs.* frequency (**Figure 5.3d** inset), which shows a higher frequency switching point after the third treatment. Despite the longer ion transport times, the capacitance of CFA-CVT is double that of CFA-CV, due to the reduction of bubbles that can form during curing and cause non-porous skins during carbonization. Thus, the anodic oxidation treatment has a larger effect on the thicker samples, since the electrolyte is able to wet the internal structure of the CFA-CVT samples easier than CFA-AL and CFA-CV.

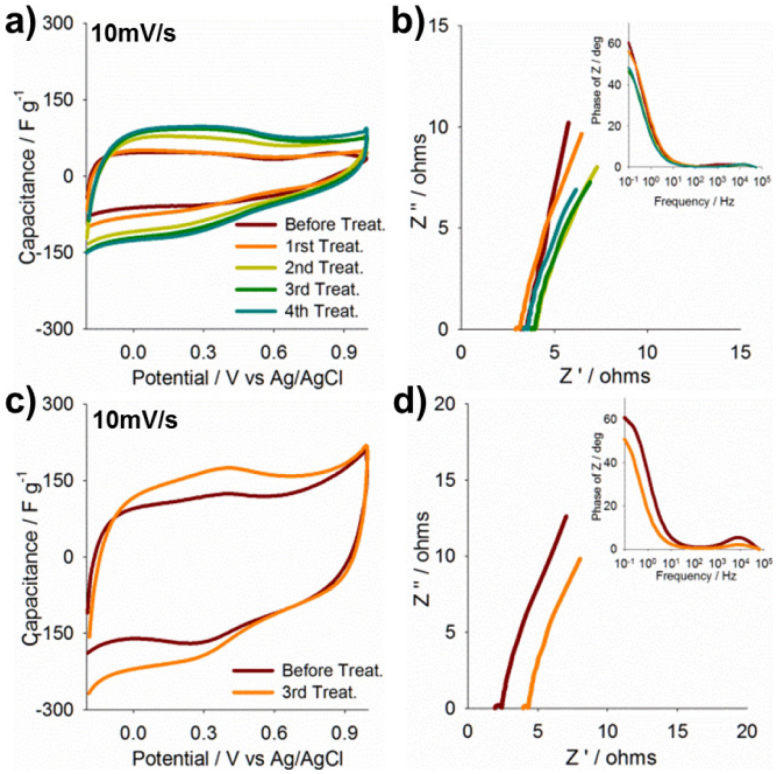

Figure 5.3 Electrochemical pre-treatment of carbon foams. (a) Cyclic voltammetry profile of CFA-CV before and after subsequent treatments in NH_4HCO_3 for 5 min. (b) Nyquist plot of Z'' *vs.* Z' for sample in panel a (inset: Bode plot of the phase in impedance with frequency). (c) Cyclic voltammetry profiles of CFA-CVT before and after 3 subsequent treatments in NH_4HCO_3 for 5 min. (d) Nyquist plot of Z'' *vs.* Z' for sample in panel c (inset: Bode plot of the phase in impedance with frequency). Electrochemical measurements were conducted in a 3-electrode configuration in 0.5 M H_2SO_4.

5.3.5 Electrochemical performance

The electrochemical properties of CFA-AL and CFA-CV are presented in **Figure 5.4. Figure 5.4a** shows the cyclic voltammetry profile as capacitance (F g^{-1}) *vs.* potential (V) of CFA-AL for scan rates between 100 to 10 mV s^{-1}, yielding average capacitances

from 31.7 to 78.3 F g^{-1}, respectively. A scan rate dependence on the capacitance is observed due to mass transfer limitations in the porous carbon electrodes. Due to the small pore size, scan rates below 10 mV s^{-1} are required to achieve a steady profile. As expected, a similar trend is observed in the CV profiles of CFA-CV (**Figure 5.4b**) because the porous carbon aerogel is very similar in each substrate. The average capacitance varies from 46.6 to 82.3 F g^{-1} for scan rates between 100 and 10 mV s^{-1}, respectively. However, the scan rate dependence is lower than that observed in CFA-AL films, presumably due to the thinner substrate. Alumina felt yielded fairly thick carbon foam sheets (0.145 cm) relative to the carbon veil (0.037 cm), which will inevitably require longer times for ions to move through the electrode. At the lowest scan rate investigated (3mV s^{-1}), the electrochemical performance is very similar between CFA-AL (97.7 F g^{-1}) and CFA-CV (98.8 F g^{-1}).

Results presented in the Nyquist plot in **Figure 5.4c** corroborate the results from cyclic voltammetry. Both electrode types exhibited low charge transfer resistance (low-frequency end of semi-circle) due to the high conductivity characteristic of carbon materials. The frequencies at which the kinetic control process switches to mass transport control (low-frequency intercept) occurred at 199.5 and 251.2 Hz for CFA-AL and CFA-CV, respectively, indicating that longer times were required for the ion transport within the CFA-AL electrode, consistent with the high scan rate dependence observed in the cyclic voltammetry profiles. Furthermore, the Bode plot presented in the inset of **Figure 5.4c** clearly shows that CFA-CV electrodes switched between resistive (0° phase angle) and capacitive (90° phase angle) behavior at higher frequencies (faster processes).

Lastly, constant current charge-discharge measurements were performed at currents densities between 0.9 and 13.9 mA cm^{-2}. The discharge capacities of CFA-AL (20.1 and 12.8 mA h g^{-1}) and CFA-CV (19.5 and 13.0 mA h g^{-1}) are very similar and shown in **Figure 5.4d**. The currents we selected such that the device discharges in 60s, and then 15s, which effectively normalizes for the different thicknesses. Because these samples were synthesized by the same process and had similar carbon nanostructures, it is expected that the overall electrode charge capacities are similar for comparable discharge times.

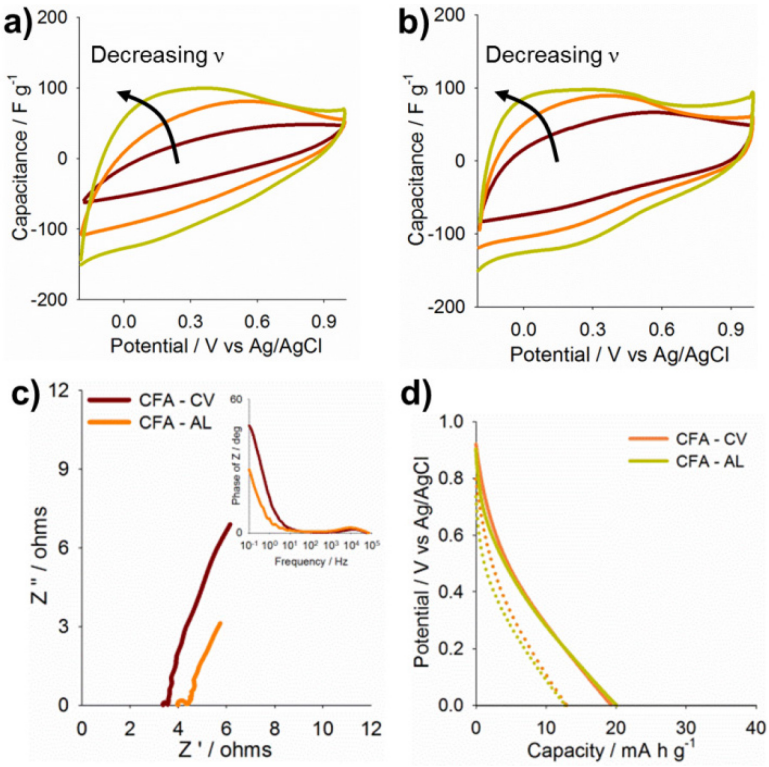

Figure 5.4 Electrochemical properties of CFA-AL, and CFA-CV. Cyclic voltammetry profiles for (a) CFA-AL and (b) CFA-CV normalized by the mass of porous carbon in sample at scan rates between 100 and 10 mV s^{-1}. (c) Nyquist plot of imaginary (Z'') *vs.* real (Z') impedance, inset: Bode plot of the phase in impedance with frequency. (d) Discharge profiles at current densities of (—) 3.5 mA cm^{-2} and (…) 13.9 mA cm^{-2}. Electrochemical measurements were conducted in a 3-electrode configuration in 0.5M H_2SO_4.

CFA-CVT was synthesized with improved catalyst techniques, which increased the functional surface area by minimizing the formation of macro-porosity and non-porous carbon skins after carbonization. **Figure 5.5a** shows the normalized CV profiles of CFA-CVT for scan rates between 100 to10 mV s^{-1}, displaying capacitances between 83.0 to 210.9 F g^{-1} for scan rates from 100 to 10 mV s^{-1}, respectively. The

electrochemical performance is nearly 2.5 fold higher than CFA-AL and CFA-CV, indicating that the reduction in non-porous carbon formation on the surface of the electrodes significantly improves the electrochemical properties of the carbon foams. As seen with previous substrates, these electrodes also exhibit scan rate dependence due to the mesoporosity. From the Nyquist plot shown in **Figure 5.5b**, the kinetically controlled region (low-frequency end of semi-circle) is higher than in CFA-CV. The low-frequency intercept occurs at 63.1 Hz, which is lower than the CFA-CV, indicating longer times are required for ion transport within the electrode. This is likely due to the more evenly distributed catalyst, which caused a finer solid structure with more tortuous diffusion paths.

The discharge characteristics of CFA-CVT are presented in **Figure 5.5c** for current densities between 0.9 and 13.9 mA cm^{-2}, yielding electrode capacities between 60.6 to 28.0 mA h g^{-1}. Compared to CFA-CV, these capacities are 3-fold higher due to the reduction of the nonporous skins on the surface which likely increased the accessibility of ions to the entire structure of the electrode material. The performance of CFA-CV and CFA-CVT is compared through the average capacitance as a function of scan rate depicted on **Figure 5.5d**. CFA-CVT exhibits a higher scan rate dependence compared with CFA-CV, which is consistent with smaller pore size in the carbon nanostructure brought about by changes in the synthesis process. Smaller pore sizes will lead to higher diffusion limitations, but at the same time leads to higher capacitance (258.3 F g^{-1} at 3 mV s^{-1}) compared with CFA-CV (98.8 F g^{-1} at 3 mV s^{-1}). Compared with the performance of similar materials (single electrode measurements) in the literature,[6, 22,

[27, 28] these electrode materials are quite promising even though the carbon foams were not subjected to an activation process. Accordingly, we expect further improvements in performance and carbon nanostructure can be obtained through various post-synthesis activation processes. However, the main advantage compared with previous reports is that our porous carbon aerogels function as self-standing electrodes, which eliminates the need for binder and conductivity enhancer.

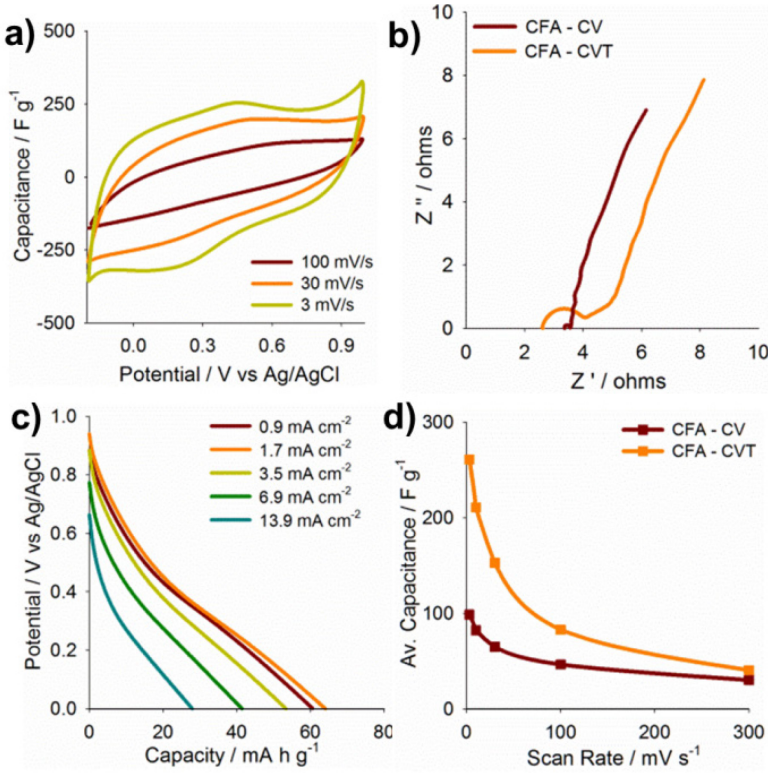

Figure 5.5 Electrochemical performance of CFA-CVT. (a) Cyclic voltammetry profiles normalized by mass of porous carbon in sample at various scan rates. (b) Nyquist plot of imaginary (Z'') *vs.* real (Z') impedance for CFA-CVT and CFA-CV. (c) Discharge profiles with increased current densities (0.9, 1.7, 3.1, 6.9, 13.9 mA cm^{-2}). (d) Scan rate dependence of the average capacitance for CFA-CVT and CFA-CV. Electrochemical measurements were conducted in a 3-electrode configuration in 0.5M H_2SO_4.

A symmetric supercapacitor was prepared with CFA-CVT electrodes (details in experimental section) in 0.5 M H_2SO_4 and 6 M KOH. **Figure 5.6a** shows the normalized CV profiles for scan rates between 300 and 10 mV s^{-1}. On a carbon mass basis, specific capacitance values of 24.35 F g^{-1} and 28.56 F g^{-1} were obtained in 6M KOH and in 0.5M H_2SO_4 (not shown), respectively, at a scan rate of 10 mV s^{-1}. The capacitance is slightly lower than expected from the single electrode value, which could be attributed to internal resistance and device assembly. The Nyquist plot in **Figure 5.6b** shows a small charge transfer resistance (high-frequency range), consistent with high conductivity in carbon materials, and that the transition between kinetic control and mass control occurs at 31.6 Hz. The low-frequency range shows a 90° line (purely capacitive) consistent with a purely EDLC based mechanism. A plot of imaginary capacitance (C_{im}) *vs*. frequency is shown in the inset of **Figure 5.6b**, where the peak indicates the relaxation time (τ_c) and provides a measure of how fast the cell discharges with 50% efficiency. τ_c is defined as the reciprocal of the frequency at the peak ($\tau_c = 1/f_{peak}$). In this device, τ_c is 2.5 s, which is faster than the conventional devices prepared at laboratory scale with activated carbon – conducting graphite – carboxymethyl cellulose (85:10:5) which have a τ_c of 7.9 s.[9] The increase in the device speed is likely due to the absence of current collector and binder, which decreases the internal resistance of the cell.

Carbon materials are known for their cycle life, which can be represented by stability during charge-discharge cycles. **Figure 5.6c** shows the change in the specific capacitance (F g^{-1}) as the device is cycled between 0 and 1.0 V for 2000 cycles at 1.2mA; the capacitance remains unchanged for the whole length of the experiment. Experiments

performed with 0.5M H_2SO_4 exhibit similar behavior and stability to 6M KOH. By investigating charge-discharge behavior over a range of discharge rates, a Ragone plot of the device performance can be constructed to provide a relationship between the energy density (Wh Kg^{-1}) and the power density (W Kg^{-1}), as shown in **Figure 5.6d**. Ragone plots are constructed for two symmetrical devices prepared with CFA-CVT in 0.5 M H_2SO_4 and 6 M KOH. The energy density (E) was obtained from Eq. 5.1[36-38]

$$E = \frac{1}{2m} C(\Delta V)^2 \qquad \text{Eq. 5.1}$$

where C is the capacitance [F] which is calculated from $C = I\,(dV/dt)^{-1}$, I is the discharge current, and dV/dt is the slope of the discharge curve. ΔV potential window utilize in the charge-discharge experiments [V], and m is the mass of the electrode either total mass or mass of the active material [kg]. The power density (P) was calculated from Eq. 5.2[36-38]

$$P = \frac{E}{t} \qquad \text{Eq.5.2}$$

where E is the energy density [Wh Kg^{-1}], and t is the discharge time. Devices in 6M KOH were cycled between 0.36 and 25.2 A g^{-1} while devices in 0.5M H_2SO_4 were cycled between 0.43 and 20.9 A g^{-1}. Under these test conditions, similar energy density and power density relationships were obtained; in 0.5 M H_2SO_4 energy and power densities of 2.0 Wh Kg^{-1} and 2900 W Kg^{-1} were achieved, while in 6 M KOH, energy and power density 2.0 Wh Kg^{-1} and 2400 W Kg^{-1} were determined. The slight differences are related to the nature of the electrolyte; KOH is able to withstand slightly higher currents compared with H_2SO_4. The performance of the devices falls within the range of common carbon materials;[6] however, the main distinction comes from the use of a self-standing

electrode that represents an important advance in the use of carbon aerogels in supercapacitors.

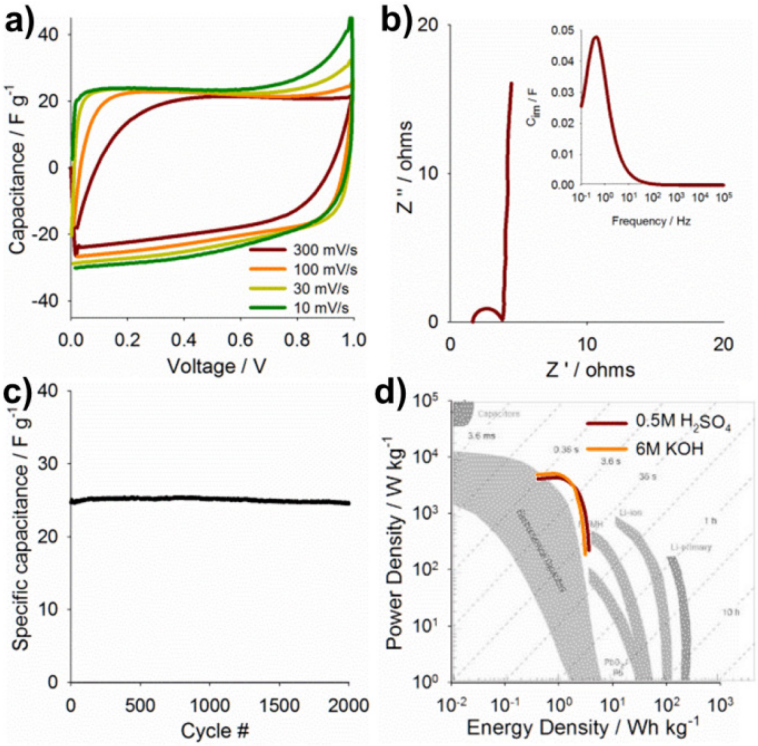

Figure 5.6 Electrochemical performance of CFA-CVT symmetric supercapacitor (2-electrode system) in 6M KOH. (a) Cyclic voltammetry profiles normalized by the % of porous carbon in the sample. (b) Nyquist plot of imaginary impedance (Z'') *vs.* real impedance (Z') (inset: Imaginary capacitance (C_{im}) *vs.* frequency). (c) Device cycle life for 2000 cycles. (d) Ragone plot of symmetrical supercapacitors in 6M KOH and 0.5M H_2SO_4 (Ragone plot at the background adapted by permission from Macmillan Publishers Ltd: Nature Materials ref. [36], copyright 2008).

5.4 Conclusions

Resorcinol-Formaldehyde carbon aerogels reinforced with alumina felt and carbon veil were characterized for applications as self-standing EDLC electrodes. A self-

standing electrode eliminates the need for binder, conductivity enhancer, current collector, preparation time to make the electrodes for supercapacitor devices; hence, the total mass of the device is reduced, and the overall capacitance is increased. The synthesis method was improved to reduce the curing to two days and drying time to one day, which have been the main drawbacks for carbon foam synthesis scale-up. The different substrate materials influenced the final thickness of the self-standing electrodes without altering the 3D carbon nanostructure produced by the polycondensation reaction of RF. Electrochemical anodic oxidation of the samples showed to be beneficial to increase the performance compared to untreated samples. Carbon foams synthesized with an additional degassing step prior mixing formaldehyde in resorcinol-aluminum acetate solution (CFA-CVT) demonstrated approximately 2.5-fold higher capacitance (258 F g^{-1} at 3mV s^{-1}) than carbon foams synthesized without degassing the resorcinol-aluminum acetate solution (CFA-AL 97.7 F g^{-1} and CFA-CV 98.8 F g^{-1} at 3mV s^{-1}). Symmetric supercapacitors exhibit energy densities of 2.0 Wh Kg^{-1} and power densities of 2900 W Kg^{-1} (in 0.5 M H_2SO_4), which is among the highest performance of EDLC energy storage devices.

5.5 References

1. Rao A. Energy and our future: a perspective from the Clemson Nanomaterials Center. *Nanotechnology Reviews* **2015**, 4(5)**:** 79–484.

2. Jiang H, Lee PS, Li C. 3D carbon based nanostructures for advanced supercapacitors. *Energy Environ. Sci.* **2013**, 6(1)**:** 41-53.

3. Yan J, Wang Q, Wei T, Fan Z. Recent Advances in Design and Fabrication of Electrochemical Supercapacitors with High Energy Densities. *Adv. Energy Mater.* **2014**, 4(4)**:** n/a-n/a.

4. Dubal DP, Ayyad O, Ruiz V, Gomez-Romero P. Hybrid energy storage: the merging of battery and supercapacitor chemistries. *Chem. Soc. Rev.* **2015**, 44(7)**:** 1777-1790.

5. Chen T, Dai L. Carbon nanomaterials for high-performance supercapacitors. *Mater. Today* **2013**, 16(7–8)**:** 272-280.

6. Gu W, Yushin G. Review of nanostructured carbon materials for electrochemical capacitor applications: advantages and limitations of activated carbon, carbide-derived carbon, zeolite-templated carbon, carbon aerogels, carbon nanotubes, onion-like carbon, and graphene. *WIREs Energy Environ.* **2014**, 3(5)**:** 424-473.

7. Borchardt L, Oschatz M, Kaskel S. Tailoring porosity in carbon materials for supercapacitor applications. *Mater. Horiz.* **2014**, 1(2)**:** 157-168.

8. Diaz-Orellana KP, Roberts ME. Scalable, template-free synthesis of conducting polymer microtubes. *RSC Adv.* **2015**, 5(32)**:** 25504-25512.

9. Leguizamon S, Diaz-Orellana KP, Velez J, Thies MC, Roberts ME. High charge-capacity polymer electrodes comprising alkali lignin from the Kraft process. *J. Mater. Chem. A* **2015**, 3(21)**:** 11330-11339.

10. Augustyn V, Simon P, Dunn B. Pseudocapacitive oxide materials for high-rate electrochemical energy storage. *Energy Environ. Sci.* **2014**, 7(5)**:** 1597-1614.

11. Jiang J, Li Y, Liu J, Huang X, Yuan C, Lou XW. Recent Advances in Metal Oxide-based Electrode Architecture Design for Electrochemical Energy Storage. *Adv. Mater.* **2012**, 24(38)**:** 5166-5180.

12. Yu G, Xie X, Pan L, Bao Z, Cui Y. Hybrid nanostructured materials for high-performance electrochemical capacitors. *Nano Energy* **2013**, 2(2)**:** 213-234.

13. Halama A, Szubzda B, Pasciak G. Carbon aerogels as electrode material for electrical double layer supercapacitors—Synthesis and properties. *Electrochim. Acta* **2010**, 55(25)**:** 7501-7505.

14. Titirici M-M, White RJ, Brun N, Budarin VL, Su DS, del Monte F*, et al.* Sustainable carbon materials. *Chem. Soc. Rev.* **2015**, 44(1)**:** 250-290.

15. Arcila-Velez MR, Zhu J, Childress A, Karakaya M, Podila R, Rao AM*, et al.* Roll-to-roll synthesis of vertically aligned carbon nanotube electrodes for electrical double layer capacitors. *Nano Energy* **2014**, 8**:** 9-16.

16. Fisher RA, Watt MR, Ready WJ. Functionalized carbon nanotube supercapacitor electrodes: a review on pseudocapacitive materials. *ECS J. Solid State Sci. Technol.* **2013**, 2(10)**:** M3170-M3177.

17. White RJ, Brun N, Budarin VL, Clark JH, Titirici M-M. Always Look on the "Light" Side of Life: Sustainable Carbon Aerogels. *ChemSusChem* **2014**, 7(3)**:** 670-689.

18. Lee YJ, Jung JC, Yi J, Baeck S-H, Yoon JR, Song IK. Preparation of carbon aerogel in ambient conditions for electrical double-layer capacitor. *Curr. Appl. Phys.* **2010**, 10(2)**:** 682-686.

19. Liu N, Shen J, Liu D. Activated high specific surface area carbon aerogels for EDLCs. *Microporous Mesoporous Mater.* **2013**, 167**:** 176-181.

20. Al-Muhtaseb SA, Ritter JA. Preparation and Properties of Resorcinol–Formaldehyde Organic and Carbon Gels. *Adv. Mater.* **2003**, 15(2)**:** 101-114.

21. Pröbstle H, Schmitt C, Fricke J. Button cell supercapacitors with monolithic carbon aerogels. *J. Power Sources* **2002**, 105(2)**:** 189-194.

22. Park H, Seo J, Kim M, Baeck S-H, Shim SE. Development of a carbon foam supercapacitor electrode from resorcinol–formaldehyde using a double templating method. *Synth. Met.* **2015**, 199**:** 121-127.

23. Kim SJ, Hwang SW, Hyun SH. Preparation of carbon aerogel electrodes for supercapacitor and their electrochemical characteristics. *Journal of Materials Science* **2005**, 40(3)**:** 725-731.

24. Li J, Wang X, Huang Q, Gamboa S, Sebastian PJ. Studies on preparation and performances of carbon aerogel electrodes for the application of supercapacitor. *J. Power Sources* **2006**, 158(1)**:** 784-788.

25. Hao P, Zhao Z, Tian J, Li H, Sang Y, Yu G*, et al.* Hierarchical porous carbon aerogel derived from bagasse for high performance supercapacitor electrode. *Nanoscale* **2014**, 6(20)**:** 12120-12129.

26. Liu J, Tian Y, Chen Y, Liang J, Zhang L, Fong H. A surface treatment technique of electrochemical oxidation to simultaneously improve the interfacial bonding strength and the tensile strength of PAN-based carbon fibers. *Mater. Chem. Phys.* **2010**, 122(2–3)**:** 548-555.

27. Wang X, Liu L, Wang X, Bai L, Wu H, Zhang X*, et al.* Preparation and performances of carbon aerogel microspheres for the application of supercapacitor. *J. Solid State Electrochem.* **2010**, 15(4)**:** 643-648.

28. Calvo EG, Lufrano F, Staiti P, Brigandì A, Arenillas A, Menéndez JA. Optimizing the electrochemical performance of aqueous symmetric supercapacitors based on an activated carbon xerogel. *J. Power Sources* **2013**, 241**:** 776-782.

29. Staaf LGH, Lundgren P, Enoksson P. Present and future supercapacitor carbon electrode materials for improved energy storage used in intelligent wireless sensor systems. *Nano Energy* **2014**, 9**:** 128-141.

30. Pekala RW, Mayer ST, Kaschmitter JL, Kong FM. Carbon Aerogels: An Update on Structure, Properties, and Applications. In: Attia YA (ed). *Sol-Gel Processing and Applications*. Springer US: Boston, MA, **1994**, pp 369-377.

31. Pekala R, Alviso C, LeMay J. Organic aerogels: a new type of ultrastructured polymer: Lawrence Livermore National Lab., CA (USA); **1991**.

32. Saliger R, Bock V, Petricevic R, Tillotson T, Geis S, Fricke J. Carbon aerogels from dilute catalysis of resorcinol with formaldehyde. *J. Non-Cryst. Solids* **1997**, 221(2–3)**:** 144-150.

33. Tamon H, Ishizaka H, Mikami M, Okazaki M. Porous structure of organic and carbon aerogels synthesized by sol-gel polycondensation of resorcinol with formaldehyde. *Carbon* **1997**, 35(6)**:** 791-796.

34. Qian X, Wang X, Ouyang Q, Chen Y, Yan Q. Effect of ammonium-salt solutions on the surface properties of carbon fibers in electrochemical anodic oxidation. *Appl. Surf. Sci.* **2012**, 259**:** 238-244.

35. Vickers PE, Watts JF, Perruchot C, Chehimi MM. The surface chemistry and acid–base properties of a PAN-based carbon fibre. *Carbon* **2000**, 38(5)**:** 675-689.

36. Simon P, Gogotsi Y. Materials for electrochemical capacitors. *Nat Mater* **2008**, 7(11)**:** 845-854.

37. Wu Q, Xu Y, Yao Z, Liu A, Shi G. Supercapacitors Based on Flexible Graphene/Polyaniline Nanofiber Composite Films. *ACS Nano* **2010**, 4(4)**:** 1963-1970.

38. Campbell PG, Merrill MD, Wood BC, Montalvo E, Worsley MA, Baumann TF*, et al.* Battery/supercapacitor hybrid via non-covalent functionalization of graphene macro-assemblies. *J. Mater. Chem. A* **2014**, 2(42)**:** 17764-17770.

CHAPTER SIX

SCALABLE, TEMPLATE-FREE SYNTHESIS OF CONDUCTING POLYMER MICROTUBES

6.1 Electrochemical synthesis and grow mechanism of polypyrrole microtubes

6.1.1 Introduction

The performance of portable power systems is currently limited by the properties of the active electrode materials, and further advances in energy storage will require materials that exhibit rapid and efficient charge transfer processes, long-term cycle stability, low-cost and natural abundance. Emerging energy storage devices, such as supercapacitors, have the potential to provide high energy density (charge storage capacity) and high power density (fast charge-discharge rates) to bridge the gap between traditional batteries and high-power capacitors.[1-7] Currently, supercapacitor technologies have attracted interest in four niche applications: renewable energy generation sources to stabilize the variable incoming power; transportation with electric vehicles for regenerative braking system and rapid acceleration;[1, 2, 6, 7] load leveling to prevent power disruptions due to short time fluctuations; and for portable electronics. The general aim of developing new electrical energy storage technology is a positive impact on the world's economy and ecology.[8]

In supercapacitors, many types of electrode materials can be used, ranging from high surface area, inert carbon nanomaterials to Faradaic metal oxides and conducting polymers. Porous carbon nanomaterials rely upon electrical double layer capacitance (EDLC), where the charge is stored physically at the electrode interfaces (non-Faradaic

process).[9] Cells comprising high surface area, inactive electrode materials are referred to as Electrochemical Double-Layer Capacitors (EDLC) and are characterized by high power densities, but are limited by low energy densities. Electroactive conducting polymers (ECPs) and metals oxides[10, 11] have been widely investigated as materials for pseudocapacitors, where the bulk of the material undergoes rapid redox reactions to provide the capacitive response (Faradaic process),[1] providing a higher energy density compared to EDLCs. [12, 13] The trade-off, however, is during charging and discharging, pseudocapacitive materials experience a volume change (swelling-contraction process) due to the ion exchange with the electrolyte, causing poor cycle life (few thousand cycles) compared to carbon-based materials – which undergo ion adsorption-desorption processes – that exhibit stability over hundreds of thousands of cycles. [1, 12]

ECPs (e.g. polypyrrole, polyaniline, and polythiophene derivatives) are highly conductive, easily processable, flexible, have a low environmental impact, and very low cost, especially in comparison to metal oxides,[12] such as ruthenium oxide (RuO_2) – the benchmark standard in pseudocapacitance.[1, 14] Typically, ECPs are stable in the oxidized (p-doped) state, and, therefore, function as a cathode material in a supercapacitor. During oxidation-reduction reactions, counter ions with the opposite polarity transport into and out of the polymer matrix to maintain charge neutrality, resulting in a continual change in volume.[15-17] Although, the potential applications of conducting polymers are wide, the main challenges in the last many years have been creating well-defined shapes[16], which can help mitigate the cycling degradation caused by volumetric changes or increase power densities by providing shorter ion diffusion lengths.[2, 12]

ECPs can be synthesized by oxidative polymerization, which is easily scalable and produces materials that require subsequent processing into electrode films, or by electrochemical polymerization, which leads to chemically-bound films on conductive substrates.[15] The latter is limited by the size of the substrate; however, precise control of the potential, current and state of charge of the resulting polymer is easily achievable.[17] Controlling the structure of ECPs electrodes can lead to improved properties for applications in electrochemistry, electroanalysis, electrocatalysis, energy conversion and storage, chemical, optical and biosensors, drug delivery, protein purification, and actuators, among others.[18-20] A variety of synthesis methods have been developed to generate ECP micro-/nanostructructures, such as nanowires, nanotubes, nanonetworks, nanospheres microcontainers[19, 21-25] and hollow spheres.[26] The most commonly utilized methods are categorized as either hard-template or soft-template approaches, and other more complex techniques, such as nanoimprinting lithography, have also been studied.[18, 27]

In hard-template methods, a pre-formed template with a precisely defined structure is used to guide the growth, morphology and size of the material, which limits the size, morphology, and large-scale production of tailored ECP structures.[28] Common templates used are anodic aluminum oxide membranes, track etched polycarbonate membranes, porous silica, mesoporous zeolites, carbon nanotubes, and highly oriented hydrophilic graphite.[15, 16, 28, 29] This method is effective for synthesizing arrays of aligned polymer micro-/nanotubes and wires with controllable length, thickness, and diameter;[18] the first two of which are controlled by the polymerization time and the latter are

controlled by the size of the pores or channels in the membrane. In chemical polymerization, the membrane is immersed in the solution with the monomer, dopant and/or oxidant allowing the polymerization within the pores.[29] For electrochemical polymerization, a metallic interface is required, which increases the complexity and cost of the process.[15, 16, 29] to obtain the micro-/nanostructures, post-synthesis treatments are required to remove the template, which can damage the structures.

On the other hand, soft-template synthesis, also referred to as template-free or self-assembly,[29] is simple and cheap and does not required a template or potentially harsh post-synthesis treatment.[26] Nanostructure is achieved by self-assembly during polymerization, and is driven by selective control of non-covalent interactions, such as hydrogen bonds, Van der Waals forces, π-π stacking and electrostatic interactions.[18, 29] Templates used include surfactant micelles, colloidal particles, structure-directing molecules,[28] oligomers, bubbles,[19, 21-23, 30-34] interfacial polymerization, dilute polymerization, reverse emulsion polymerization, among others.[18, 35-37] During oxidative polymerization, micelles are formed by dopant and/or monomer-dopant acting as a soft-template to guide the formation of micro-/nanotubes, -wires or -spheres,[18] whereas in electrochemical polymerization the surface potential, reaction rate (applied current), and concentration of surfactants, dopants, all influence the morphology of the final structures. The advantage over the oxidative process is improved control of the shapes; however, the quantity of product is limited by the size of the working electrode.[29] The main challenge is the control of the morphology, orientation, and diameter of the 1D structures.[18]

Various research efforts are underway to improve the controllability of soft-template methods for synthesizing ECP nanostructures. Shi and co-workers[19, 21-23] demonstrated the synthesis of polypyrrole (PPy) microcontainers using bubbles as templates in the presence of various surfactants (β-naphthalenesulfonic acid, (+) & (-) camphorsulfonic acid, sodium dodecyllbenzenesulfonate and polystyrene sulfonic acid). Hydrogen gas formed by reducing protons at the counter electrode led to the formation of gas bubbles on the working electrode, which were stabilized by the anionic surfactant molecules and the growing polypyrrole structures. Compared to planar films, the structured electrodes exhibited improved redox activity and ion transport;[15, 16] however, this method utilizes high potentials that lead to overoxidation of the polypyrrole. The upper voltage limit where polypyrrole overoxidizes depends on the pH of the electrolyte solution; higher pH solutions lower the potential at which overoxidation occurs.[38-42] For this reason Bajpai and co-workers[30, 31] synthesized polypyrrole micro-containers at relatively low potential, 0.8V, which shows low overoxidation rates for pH < 0.1. The general consensus from these reports was that microstructure formation required the use of surfactants to stabilize the bubbles in the solution.

Large scale production of well-aligned arrays of conducting polymers with controllable morphologies and sizes is still a challenge. In this article, a simple approach is demonstrated to prepare large quantities of ECP microtubes utilizing low potentials without the need for a surfactant or substrate based template. Due to its capacity for high power and energy density in supercapacitors, polypyrrole is studied as the electrode material for microtube-based devices. However, since the mechanism for electrochemical

synthesis is similar for various monomers, it is expected that this approach can be applied to other ECPs with relative ease. A discussion of how to control the polymer assembly and microtubes synthesis by changing the substrate geometry is presented, along with the electrochemical properties of the created structures.

6.1.2 Experimental methods

Materials

All chemicals were purchased from Sigma-Aldrich and Fischer Scientific and used as received unless otherwise noted. Pyrrole monomer was purified by distillation.

Substrate preparation

Stainless steel meshes were prepared by cutting 1.2x1.4 cm squares with a 1.3x0.4 cm neck to serve as connection (**Figure 6.1**), sonicated for 10 min in ethanol, dried, weighed (Ohaus DV215CD Semi-micro balance, readability 0.01mg) and treated 15 min (each side) in UV-ozone (Novascan PSD-UV). Parafilm was used to cover the substrates edges and make a 1 cm^2 deposition area.

Microtubes synthesis

Pyrrole monomer (0.09 M solution) was electropolymerized at room temperature in a 0.5 M H_2SO_4 solution (previously degassed with N_2 for 10 min) by chronopotentiometry using currents of 10-16 mA) and charge densities of 1-30 C cm^{-2}.

Electropolymerization was performed in a three-electrode cell with a VersaSTAT 4 potentiostat/galvanostat and VersaStudio v2.20.4631 Electrochemistry Software (Princeton Applied Research). The working electrode was either a stainless steel mesh (McMaster-Carr, Super-Corrosion Resistance Type 316 Stainless Steel Wire Cloth, 40 x 40, 60 x 60, 100 x 100, 200 x 200, 250 x 250, 325 x 325, 400 x 400, **Table C.1**) or stainless steel foil; platinum gauze 52 mesh (Alfa Aesar) was used as the counter electrode, and a Ag/AgCl in 3 M NaCl solution as reference electrode. The platinum mesh was cleaned between each synthesis by rinsing with deionized water and acetone, and the remaining residue removed under the flame of propane torch. In some cases, a 3.3 wt.% Poly(4-Styrene Sulfonic) acid (PSSA) in 0.5M H_2SO_4 solution was also used as a dopant (**Figure C.2**). All samples were dried overnight in a vacuum oven (101.5kPa) at room temperature and weighed afterward to determine film mass. In the two-container experiments, the counter electrode (Pt mesh) was setup in a container separated from the working electrode (Stainless steel M200) and reference electrode (Ag/AgCl in 3 M NaCl). The cells each contained 0.09 M Py in 0.5 M H_2SO_4 and were connected by a salt bridge comprising a filter paper (Fisherbrand Qualitative P8-creped) soaked in the same solution. Chronoamperometry at 10 mA for 30 C cm^{-2} was used to polymerize pyrrole.

Bubble method

M200 mesh substrates were cycled from -0.3 to -0.8V for 1 cycle at 0.1 V s^{-1} in neat 0.5M H_2SO_4 that was previously degassed, leading to the formation of bubbles on

the substrate surface. Electrolyte with pyrrole (0.18 M) was then added to the cell. Chronoamperometry at 10 or 16 mA for 30 C or 60 C was performed.

Large-scale microtubes production

Mesh substrates (M200 and M400) were prepared with dimensions of 4 cm x 1 cm with 1.8 cm x 0.4 cm neck substrates and cleaned as described previously. One side was covered with parafilm, and the substrates were gently rolled into a 1 cm radius of curvature cylinder, leaving the uncovered stainless steel facing the counter electrode at a uniform distance. The experiments were performed with chronoamperometry at 30 mA for 60 C.

Electrochemical analysis

Electrochemical characterization was performed in a 0.5M H_2SO_4 solution (previously degassed with pure dried nitrogen gas for 10min) using cyclic voltammetry from 0 to 0.8 V at various scan rates (300, 100, 30, 10, 3 mV s^{-1}), electrochemical impedance spectroscopy (EIS) at 0.7 V over a frequency range of 10k to 0.1 Hz using a perturbation amplitude of 10 mV, and charge-discharge measurements at current densities of 15, 7.5, 3.75 mA cm^{-2} (-15,-7.5,-3.75 mA cm^{-2}) from 0 to 0.75 V unless otherwise stated.

Surface morphology

The film surface characterization was performed by scanning electron microscopy (SEM) in a Hitachi SU-6600 Analytical VP FE-SEM at a beam intensity of 5 kV; the samples were placed on 45º aluminum sample holders with carbon tape. Images were captured at magnifications of 35x, 90x, 200x, and 300x. Quartz PCI software was used to make all the measurements; this software is calibrated to the microscope. Averages were taken for the diameters and heights presented (between 5-10 specimens depending on the sample).

Supercapacitor testing

A symmetric supercapacitor was assembled in MTI Corp coin cell apparatus using polypyrrole microtubes electrodes deposited on M200 at 10 mA cm^{-2} for 30C cm^{-2}, and a Whatman glass microfiber type A filter soaked in 1 M H_2SO_4 as the separator/electrolyte. Each electrode was charged at 0.4 V prior to analysis. Electrochemical characterization was similar to the single electrode measurements unless otherwise stated. Cyclic voltammetry was performed at scan rates of 100, 50, 20, 10 and 5 mVs^{-1} and charge-discharge measurements were performed at currents of 30, 15, 7.5, 3.75, 1.87 mA cm^{-2} (-30, -15, -7.5, -3.75, -1.87 mA cm^{-2}), from 0 to 0.75 V.

6.1.3 Results and discussion

A general schematic of the setup and process for electropolymerizing polypyrrole microtubes on stainless steel mesh is shown in **Figure 6.1**. Chronopotentiometry was used to control the polymerization because setting the applied current maintains a constant polymerization rate.[16] Stainless steel (SS) mesh substrates were immersed in a solution containing 0.09 M pyrrole and 0.5 M H_2SO_4 along with a reference (Ag/AgCl 3 M NaCl) and counter electrode, and polymer electrodes were grown to a specified charge. Initially, a thin polymer coating forms on the SS mesh wires until a charge of 3 C cm^{-2} is achieved, after which gas bubbles begin to nucleate on the surface on the mesh substrate. Between a deposition charge of 3 and 5 C $cm^{-2,}$ the film continues to grow as the surface become saturated with gas bubbles. Beyond, a charge of 8 C cm^{-2} only microtubes grow perpendicular to the working electrode surface guided by the presence of the gas bubbles. The growth of the microtubes was examined on M200 and M400 substrates to visualize the initial growth process and provide insight into the bubble-guided microtube growth mechanism.

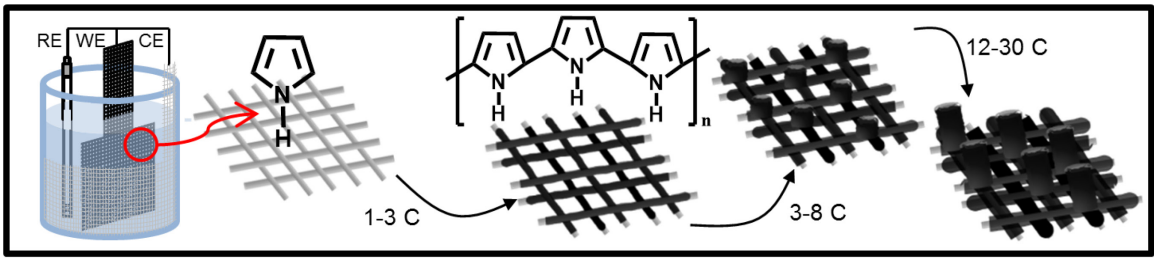

Figure 6.1 Electropolymerization process for synthesizing polypyrrole microtubes on stainless steel mesh.

Scanning electron micrograph (SEM) images are shown in **Figure 6.2** for microtubes grown on M200 substrates at 16 mA cm^{-2} to a final charge of 1, 3, 5, 8, 15 C cm^{-2}. When the polymer coating is forming on the working electrode, protons from the electrolyte are reduced to form hydrogen gas on the Pt counter electrode, which continuously bubble out of solution. At the same time, the hydrogen gas concentration in solution increases and eventually gas bubbles begin to nucleate on the mesh surface, specifically at the joints between two distinct wires. Polymer clusters then begin to form around these bubbles on the surface of the SS mesh wires (**Figure 6.2a**). Above a deposition charge of 3 C cm^{-2}, hydrogen gas bubbles visibly appear (with the naked eye) on the working electrodes and the clusters that had previously formed begin taking the form of a flower (**Figure 6.2b**). As the tubes continue to grow out of the flower-like structures, the bubbles remain at the tip of the tube through the course of the polymerization process. As shown if **Figure 6.2c-e**, the microtubes continue to grow in diameter and length from 5 to 15 C cm^{-2} until the polymerization is stopped. The tube height and diameter a presented as a function of deposition charge in **Figure 6.3**, along with the film thickness on the mesh wires. As shown, the tube height and diameter grow nearly linearly with deposition charge. At 15 C cm^{-2} the microtubes are already well formed; therefore, with increased deposition charge – from 15C cm^{-2} up to 30C cm^{-2} – the microtubes continue to grow with little change in their diameter to the final dimensions shown in **Tables 6.1** and **C.2**. Below, we show that for some substrates, microtubes grow with uniform diameter after about 15 C cm^{-2}.

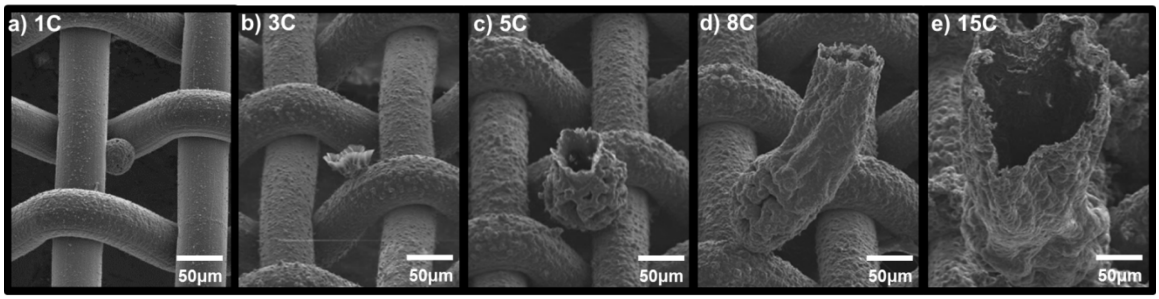

Figure 6.2 Polypyrrole microtubes growth mechanism on M200. SEM image are shown for electrodes grown with total charges of (a) 1 C cm^{-2}, (b) 3 C cm^{-2}, (c) 5 C cm^{-2}, (d) 8 C cm^{-2}, (e) 15 C cm^{-2} at 16 mA cm^{-2}.

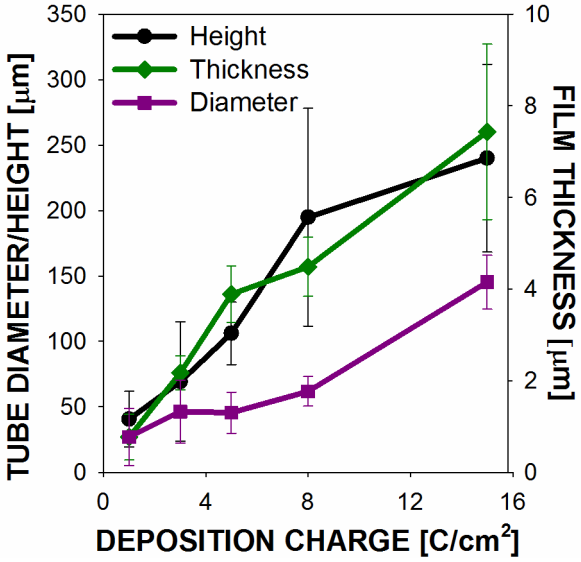

Figure 6.3 Physical dimensions of the polypyrrole microtubes grown on M400 are shown as a function of polymerization charge (1-15 C cm^{-2}), in addition to the thickness of the polymer film on the mesh wires.

To further explain the microtube growth mechanism, a set of experiments were carried out in a two-compartment system where the counter electrode was in a separate container from the reference and the working electrode, and both containers were joined by a salt bridge. All other conditions were kept similar to previous experiments for

growing PPy microtubes. When the counter is separated from the working electrode, microtubes did not grow; which supports the hypothesis that the generation of hydrogen at the counter electrode (from the reduction of protons in solution) leads to the formation of gas bubbles on the counter electrode and also the nucleation of gas bubbles on the working electrode. Furthermore, we showed that when counter electrodes other than Pt were utilized, microtubes could not be achieved.

After demonstrating that the nucleation of gas bubbles on the working electrode were fundamental for the formation of microtubes, a series of experiments adapted from the so-called bubble method[19, 21-23, 30, 31] were performed. As opposed to previous work, our approach did not utilize surfactant molecules, which were previously thought to be required to produce microstructures. These experiments utilized a voltammetric cycle at negative potentials (-0.3 V to -0.8) prior to the addition of the monomer to create H_2 bubbles on the working electrode. Electropolymerization was then performed after monomer addition to generate structures with the shape of balls or bowls, which support previous observations reported in the literature.[19, 21-23, 30, 31] However, this method could not be utilized to create reproducible microtubes. (**Figure C.3**).

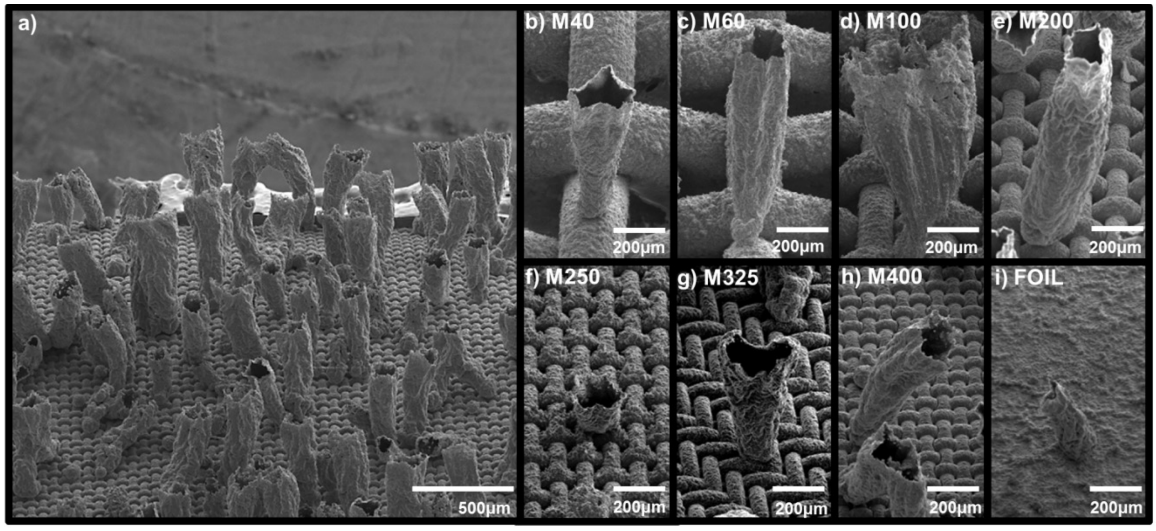

Figure 6.4 Polypyrrole microtubes structures grown on various stainless steel meshes at 10 mA cm^{-2} for 30 C cm^{-2}. SEM images are shown for polypyrrole microtubes grown on (a) M400, (b) M40, (c) M60, (d) M100, (e) M200, (f) M250, (g) M325, (h) M400, and (i) foil for 7.23 C cm^{-2}.

The analysis of the bubbled-guided growth mechanism presented above was carried out on M200 substrates, where fairly uniform growth (with respect to the tube diameter) was observed after the microtube was formed. The dimensions of the stainless steel mesh, however, were shown to have a significant influence on the growth of the polymer structures. While microtubes could be achieved on any mesh, the mesh wire diameter and spacing seemed to affect the growth of the tubes. The microstructure of polymer tubes obtained on various stainless steel substrates are shown in **Figure 6.4**. A generalized presentation of the microtube density and long range order is shown in **Figure 6.4a** shows for microtubes grown on M400 using 10mA cm^{-2} for a total charge of 30C cm^{-2}, which is typical for each mesh. As shown, many tubes are vertically positioned while others appear to collapse on themselves, likely due to the stress upon drying the

aqueous solvent. In **Figure 6.4b** to **6.4i**, SEM images are displayed for selected microtubes on various stainless steel meshes and SS foil, which are grown as previously described. Generally, two kinds of microstructures were found: either a cone-like, which are narrow at the base or cylinder-like microtubes exhibiting a fairly uniform diameter throughout. Stainless steel foil was used as a control to compare the microstructure of polypyrrole electrodes grown on typically used planar substrates and various SS meshes.[19] Several disadvantages have been described for using foil substrates. Most importantly, when relatively thick films are grown, volume changes that occur upon ion insertion and removal during oxidation and reduction processes cause the film to delaminate from the electrode resulting in poor adhesion and poor electrochemical performance. From our experiments, we found poor adhesion on SS foils for films grown with charges greater than 7.23 C cm^{-2}.

Table 6.1 Properties of polypyrrole microtubes on various stainless steel mesh substrates deposited at 10 mA cm^{-2} for 30 C cm^{-2}.

Substrate [mesh]	Film [µm]	Height [µm]	Diameter Top [µm]	Diameter Middle [µm]	Diameter Bottom [µm]	Ratio [D_T to D_M]
M40	12.1	700	200	200	140	2.2
M60	12.0	720	180	220	120	2.7
M100	9.1	720	410	330	160	5.6
M200	15.8	940	210	220	190	1.2
M250	12.6	340	240	210	130	3.0
M325	14.5	620	270	260	180	2.2
M400	17.1	1300	180	160	120	1.9

Tabulated data of various microtube properties are presented in **Table 6.1** for polypyrrole microtubes grown on SS mesh substrates. Each parameter was calculated from measurements made on SEM images, which were taken on substrates positioned at 45º relative to the incident beam. Multiple measurements were recorded for each parameter, and average values are presented. The film thickness was determined by subtracting the diameter of bare stainless steel wire from substrates with polypyrrole films. On average insignificant variation was observed in film thickness since the surface areas of each substrate were similar. Diameters were recorded at varying positions along the microtubes and are designated as bottom (near the substrate), middle and top to quantify the shape of the microtube structures. The ratio of diameter at the top to the middle ($D_T : D_M$) was calculated to reduce the shape to a single number, where a ratio of 1 (as is the case for polypyrrole tubes grown on M200 and M400) indicate cylindrical tubes, whereas a ratio larger than 1 (PPy tubes on M40, M60, M100, M250, M325), indicates conical structures. Tubes with a more pronounced conical shape are represented by larger ratios. On average, microtubes grown with a charge of 30 C cm^{-2} with a cylindrical shape exhibited a height around 1100 μm, while the conical tubes were significantly smaller, with a height dependent upon how conical the tubes were.

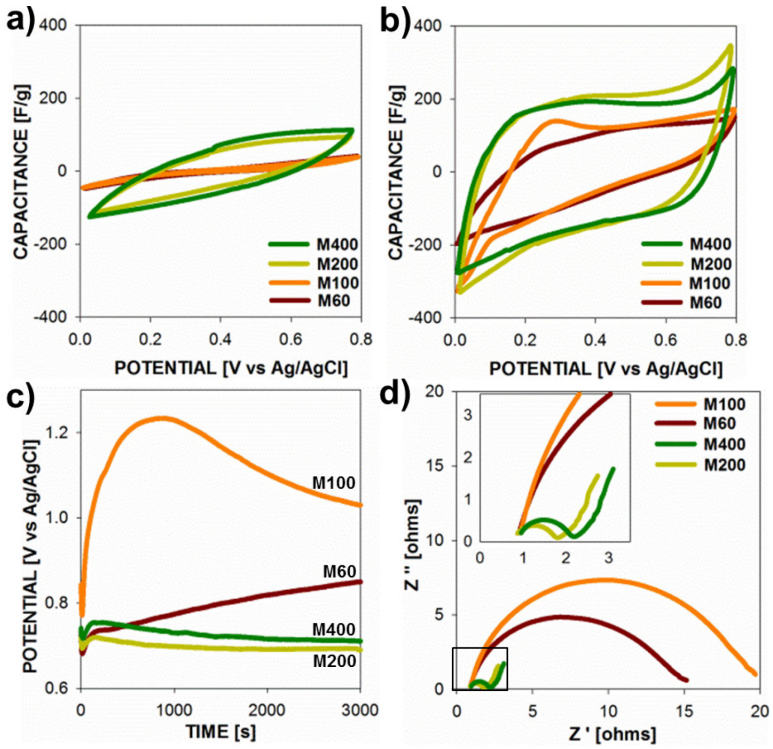

Figure 6.5 Electrochemical properties (specific capacitance *vs.* potential) of polypyrrole microtubes (10 mA cm^{-2}, 30 C cm^{-2}) on stainless steel meshes (M60, M100, M200, M400) recorded at scan rates of (a) 100 mV s^{-1} and (b) 10 mV s^{-1}. (c) Potential required during deposition to maintain the constant current of 10 mA cm^{-2}. (d) Nyquist plot of imaginary *vs.* real impedance from EIS in the frequency range of 10k Hz to 0.1 Hz.

The electrochemical properties of polypyrrole microtubes (10 mA cm^{-2}, 30 C cm^{-2}) are presented in **Figure 6.5** for electrodes grown on M60, M100, M200, M400 SS meshes. **Figures 6.5a** and **6.5b** show the capacitance *vs.* potential plots at a relatively fast scan rate (100 mV s^{-1}) and a slow scan rate (10 mV s^{-1}), respectively, over a potential range between 0 to 0.8 V. Due to the synthesis of relatively thick films (11.98, 9.09, 15.82, 17.06 µm, respectively), a scan rate dependence is observed in the capacitance of each electrode, which is exemplified by the higher specific capacitance observed for low

scan rates (10 mV s^{-1}, **Figure 6.5b**) compared to the higher scan rate (100 mV s^{-1}, **Figure 6.5a**). More on this aspect will be discussed later. Surprisingly, we found that PPy microtubes grown on coarser mesh substrates (larger wire diameters and larger wire spacing) exhibited a poor capacitance compared to electrodes grown on the finer mesh substrates (M200, M400). It is important to note that specific surface area of each substrate is similar (**Table C.1**); however, the electrochemical performance of the microtube electrodes strongly correlates with deposition potential profile (**Figure 6.5c**). That is, when PPy films are grown on M60, M100 SS substrates a higher voltage (above 0.85V) is required during the polymerization to achieve the target current density, which leads to overoxidation and interchain cross-linking, which reduces the electrochemical activity.[38-41] Lower applied current densities, which maintained the polymerization potential below 0.8 V, did not produce microtube structures.

Overoxidation of ECPs produces films with lower conductivity and higher electrode resistances, which is evident by the Nyquist plot presented in **Figure 6.5d**. Regardless of the substrate type, a similar Ohmic series resistance was observed (high-frequency limit of EIS); however, PPy films grown at potentials above 1 V exhibited significantly higher charge transfer resistance (low-frequency side of semi-circle in **Figure 6.5d**), which is consistent with an over-oxidized polymer electrode. In addition to showing higher charge transfer resistances, PPy electrodes exhibit kinetic control over a much larger time scales; the low-frequency intercepts on the Nyquist plots correspond to frequencies of 1.3, 3.2, 39.8, and 31.6 Hz for PPy electrodes on M60, M100, M200, and

M400 SS substrates, respectively. Based on these results, the finer meshes substrates (M200 and M400) were used for subsequent measurements and device fabrication.

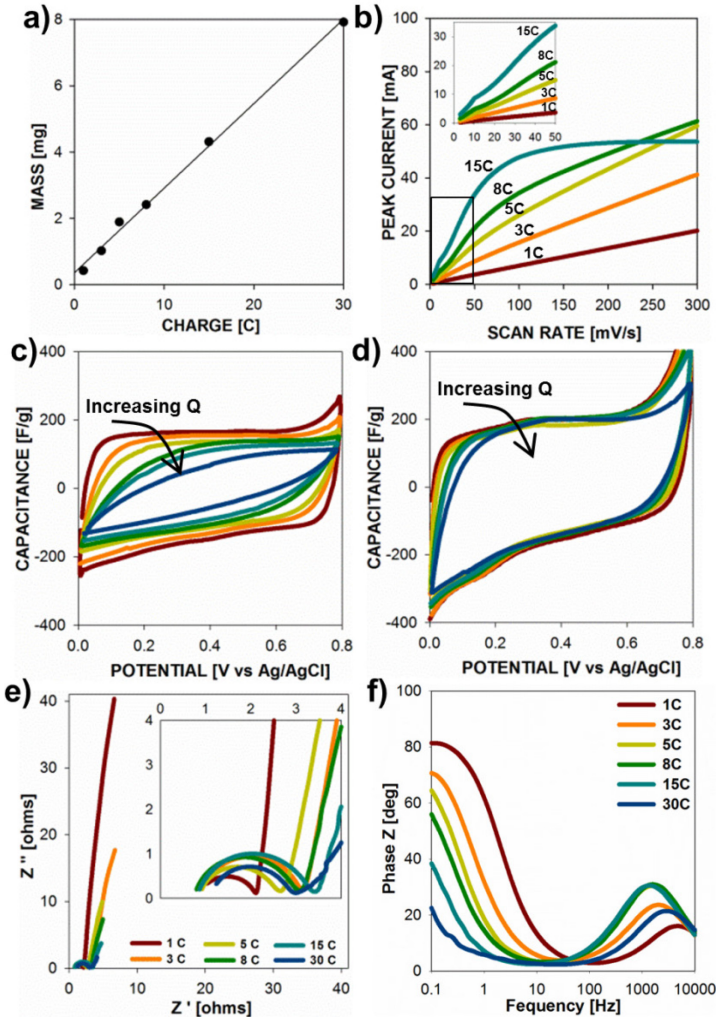

Figure 6.6 Electrochemical properties of polypyrrole microtubes with increasing charge deposited by chronopotentiometry at 16 mA cm^{-2}. (a) Electrode mass *vs.* deposition charge. (b) Peak current *vs.* scan rate for electrodes with increasing deposition charge. Specific capacitances *vs.* voltage at a scan rate of (c) 100 mV s^{-1} and (d) 10 mV s^{-1}. (e) Nyquist Plot of imaginary *vs.* real impedance from EIS measurements for a frequency range of 10k Hz to 0.1 Hz at 0.7 V with an amplitude of 10 mV. (f) Bode plot of the phase in impedance with frequency.

The electrochemical properties of the PPy microtubes grown with increasing deposition charge (structures presented in **Figure 6.2**) are shown in **Figure 6.6**. The electrode mass exhibits a linear correlation with deposition charge indicating a constant coulombic efficiency during electrode synthesis, according to Faraday's law. As shown in **Figure 6.6b**, thin electrodes grown with charge densities of less than 5 C cm^{-2} showed a linear relationship between peak current and scan rate due to the absence of ion-diffusion limitations. Thick microtube electrodes grown with charge densities greater than 8C cm^{-2} displayed a sublinear dependence of peak current with scan rate, due to the increased resistance to ion transport in thick films (tall microtubes). Structures grown with charge densities of 15 C cm^{-2} displayed a peak current plateau at scan rates above 50 mV s^{-1}, illustrating the rate-limitations of thick electrodes. As shown in the insert, each electrode mass displays a linear current-scan rate dependence at low scan rates.

Ion-transport limitations are further clarified in F**igures 6.6c** and **6.6d**, which show the specific capacitance (current/scan rate) *vs*. potential plots at 100mVs^{-1} and 10mVs^{-1}, respectively. At fast scan rates, specific capacitance of the films decreases as Q increases, while these profiles are constant at low scan rates. Data from electrochemical impedance spectroscopy are shown in F**igures 6.6e** and **6.6f.** As the electrode mass increases, the charge transfer resistance increases and the frequency at which the electrodes switch from kinetic control (high frequency) to mass transfer control (low frequency) decreases due to longer time scales required for ion transport within the electrode. The Bode plot of Phase Z *vs.* frequency corroborates the time-scale dependence of the electrochemical processes. As the frequency decreases, the

electrochemical behavior switches from resistive (0° phase angle) to capacitive (90° phase angle). From **Figure 6.6f**, it is clear that the frequency at which the behavior switches decreases with electrodes of increasing mass due to the longer time scales required for ion-diffusion during the charge-discharge processes

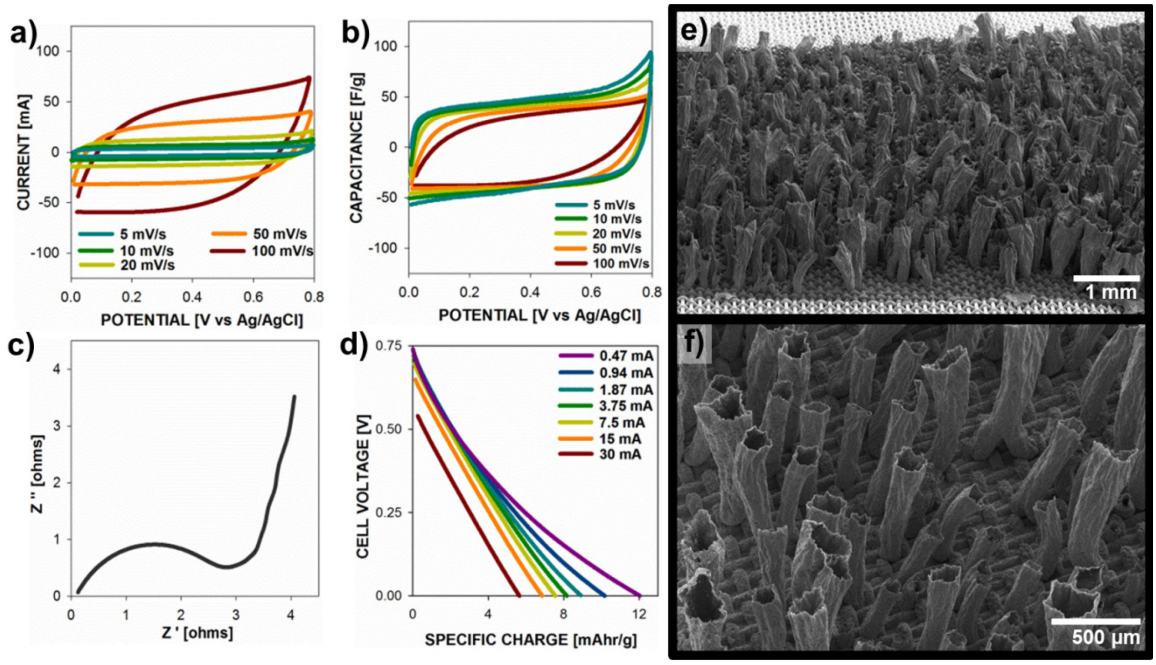

Figure 6.7 Supercapacitor polypyrrole microtubes device, electrodes deposited on M200 at 10 mA cm^{-2} for 30 C cm^{-2}. (a) Cyclic voltammetry (current *vs.* voltage) at various scan rates (100, 50, 20, 10, 5 mV s^{-1}), (b) Specific capacitance *vs.* voltage from profiles shown in a, (c) Nyquist plot of imaginary *vs.* real impedance from EIS measurements, (d) Cell discharge profiles with increased current densities (30, 15, 7.5, 3.75, 1.87, 0.94, 0.47 mA cm^{-2}), (e,f) SEM images of PPy microtubes grow on large-area M200 SS substrates for 60C at 30 mA.

A symmetrical supercapacitor device was built with two polypyrrole microtubes electrodes deposited on M200 at 10 mA cm^{-2} for 30 C cm^{-2}, and their performance is

shown in **Figure 6.7**. **Figures 6.7a** and **6.7b** show the cyclic voltammetry and specific capacitance plots for scan rates between 5-100 mVs^{-1}, displaying a high specific capacitance (on a per mass of active material basis) of 50 F g^{-1}, which is expected for a symmetric cell of electrodes a single electrode capacitance of ~200 F g^{-1}. The Nyquist plot (**Figure 6.7c**) shows that these cells exhibit a low Ohmic series resistance and charge transfer resistance in the given setup. The low-frequency end of the kinetic control was found at 5 Hz and switch from Warburg impedance to nearly ideal capacitance occurred at 0.6 Hz. **Figure 6.7d** shows the specific charge *vs*. cell voltage measured from 0 to 0.75 V for different currents (30, 15, 7.5, 3.75, 1.87 mA cm^{-2}). For a 60s discharge at 7.5 mA cm^{-2}, the specific charge is 7.6 mAh g^{-1} up to a maximum of 12 mAh g^{-1} at 0.47mA cm^{-2}. The performance of the supercapacitor cell (**Figure 6.7b**) is comparable with cells comprising thin PPy electrodes with low scan rate dependence.[43]

After demonstrating that PPy microstructures grown on M200 and M400 SS substrates displayed superior electrochemical performance and more consistent microtube structures compared to those grown on coarse meshes and foils, microtube synthesis was investigated on larger scale substrates to demonstrate the scalability of our process. Using similar current densities and solution conditions as previously examined, PPy microtubes were grown on c.a. 4 cm x 1 cm substrates assembled in a 3-electrode cell. The electrochemical performance of the electrodes were similar to behavior presented in F**igure 6.4**; however, the microtubes surface density of ~560 cm^{-2} obtained on these substrates was notably larger than that achieved on the smaller substrates (1 cm x 1 cm), ~350 cm^{-2}. In the larger substrate system, the distance between the working and counter

electrodes was carefully controlled, which contributed to a higher nucleation density of gas bubbles, and, therefore, microtubes, on the substrate surface.

6.1.4 Conclusions

A template-free synthesis method has been demonstrated, capable of providing control of polypyrrole microtube size and structure by utilizing stainless steel mesh size and electrochemical polymerization conditions (e.g. current density). Polymer microtube synthesis is governed by the nucleation of hydrogen gas bubbles – generated by the reduction of protons on a platinum counter electrode – which guide the formation of polymer structures in a narrow current density range. The mesh size is shown to influence in the structure and electrochemical performance of the microtubes by confining the gas bubble to a specific size. Cylindrical tubes are found on substrates with fine mesh structures (M200-M400) while conical structures, with narrow bases near the mesh, are obtained on larger meshes (<M200). The electrochemical performance of polypyrrole microtubes in a single electrode configuration (~200 F g^{-1}), in addition, the performance of their symmetrical supercapacitor cells (~50 F g^{-1}), were comparable to analogous polypyrrole thin film electrodes. The synthesis of polypyrrole microtubes can be scaled to larger systems by increasing the mesh and electrochemical bath size without any loss in electrochemical performance.

6.2 Influence of temperature and polymerization conditions on the synthesis of conducting polymer microtubes

6.2.1 Introduction

The development and optimization of energy storage technologies has become a challenge to further extend the use of renewable energy sources, portable electronics and electric vehicles.[44-46] Supercapacitors are an attractive option for energy storage due to their potential for high power and high energy densities. To compete with or complement batteries in large scale applications, advances in material performance are needed with respect to energy density and stability.[47]

Supercapacitors are classified as either electrochemical double layer capacitors (EDLCs) or pseudocapacitors based on their energy storage mechanism.[48, 49] EDLCs store charge based on the physical separation of charges at the interface of the electrode and the electrolyte, in what's referred to as the electric double layer.[50] Due to their relatively low cost, established processing technology, chemical stability, and high power capability, activated carbons are currently the only suitable electrode material for commercial EDLCs.[51] However, the energy density, which is related to the charge storage capacity, is limited by the accessible surface area of the carbon, which depends on the pore size distribution, porosity and the electrolyte.[52, 53] Pseudocapacitors, on the other hand, store charge based on fast and reversible redox reactions (Faradaic processes) occurring within the electrodes, which are comprised of electroactive materials, such as electrically conducting polymers (ECPs) and metal oxides. In general, pseudocapacitive materials will have a higher charge storage capacity and energy density compared to

chemically inert carbon. Metal oxides [11, 54, 55] (e.g. RuO_2, MnO_2) typically exhibit high charge capacity through sequential redox reactions but are often limited by high cost, material scarcity, and low voltage operation in aqueous electrolytes. Conversely, ECPs[56] (e.g. polyaniline, poly(3,4 - ethylenedioxythiophene, polypyrrole, among others) are attractive due to their low cost, simple and low-energy synthesis methods, high charge capacity and electrical conductivity.[57] The primary challenge associated with electroactive materials is degradation caused by charge transfer reactions and ion insertion/removal during the charge-discharge processes, which causes material expansion and contraction. As a result, electrodes become mechanically and chemically damaged and exhibit decreasing electrochemical activity after hundreds to thousands of cycles.[16] To overcome these limitations, electrodes are fabricated with controlled micro- and nano-structures to reduce mechanical stresses associated with material expansion and contraction; and at the same time, the power density is increased by reducing ion-transport distances.[4, 58]

Various approaches have been explored to synthesize well-ordered micro- and nanostructured electrodes, which can be classified as hard or soft template methods.[56] Hard template synthesis methods use scaffolds with well-defined structures, such as anodized alumina oxide, mesoporous silica, and polymer latex colloids. Electrode materials are grown within the template, which is later removed by selective etching or calcination; careful handling is required to avoid compromising the structure of the micro-/nanoscale features, which are inherently limited by the predefined template.[59] Soft templates, on the other hand, use surfactants or chemical additives as templates and take

advantage of non-covalent interactions. The growth of the active material is guided by the formation of micelles in solution, which requires strict control of the solution conditions to achieve uniform nanostructures. The main challenges of soft-template methods are: control of the morphology, orientation of features, and synthesis process scalability.[18]

Several research groups have reported the synthesis of ECP microstructures using surfactants as soft templates. Xu and co-workers[60, 61] used p-toluenesulfonic acid in aqueous solutions to synthesize polypyrrole micro/nanohorns on fluorine doped tin oxide glass. Hollow structures were obtained due to the formation of micelles comprised of surfactant and monomer where the shape of the horn was driven by solution pH and polymerization potential. Other approaches to create hollow structures exploit the formation and stabilization of gas bubbles in solution. Applying electrode potentials >1.23V *vs.* SCE generates bubbles via water decomposition, which are stabilized by the surfactant (*e.g.* β-naphthalenesulfonic acid, (+) & (-) camphorsulfonic acid, sodium dodecyl benzenesulfonate and polystyrene sulfonic acid)[19, 21-23] and adsorb on the working electrode surface. Alternatively, H_2 bubbles have been formed and stabilized with surfactants at electrode potentials below -1.0 to -1.6 V *vs.* Ag/AgCl to polymerize pyrrole microstructures.[30, 31] In each case, the use of high electrode potentials resulted in overoxidation of polypyrrole and decreased electrochemical activity.

In previous work,[62] we developed a simple and scalable process for synthesizing polypyrrole (PPy) microtubes on stainless steel meshes without the need for surfactant or hard templates (**Figure 6.9a**). We reported the synthesis mechanism and the effect of mesh properties and current density (deposition potential) on the electrochemical

performance of the films. During the electrochemical polymerization of polypyrrole (**Figure 6.8a**), hydrogen gas is formed on the platinum mesh counter electrode (**Figure 6.8b**) and results in gas bubble nucleation on the stainless steel mesh, where pyrrole (Py) is oxidized to produce polypyrrole.[60, 63] Microtubes are obtained as gas bubbles are incorporated into the growing polymer film (**Figure 6.9b**). In general, we found that the i) microtube density and uniformity increased when polymer microtubes were grown on finer meshes (i.e. smaller wires and wire spacing) and ii) microtube diameter correlated with mesh size. Additionally, for the deposition conditions investigated, optimal electrochemical properties were achieved when electrodes were synthesized at electrode potentials below 0.85 V *vs.* Ag/AgCl (around 25 ºC, 0.1 M PPy, 0.5 M H_2SO_4, 10 mA). Outside a given range of conditions (e.g. low concentrations,[64] low current density, coarse meshes), microtubes could not be obtained without exceeding 0.85 V, which led to the overoxidation of the polymer and decreased electrochemical activity. Furthermore, structures were not obtained at current densities below 10-16 mA cm^{-2} and higher currents led to poor electrochemical properties due to the overoxidation and interchain crosslinking of the polymer.[65]

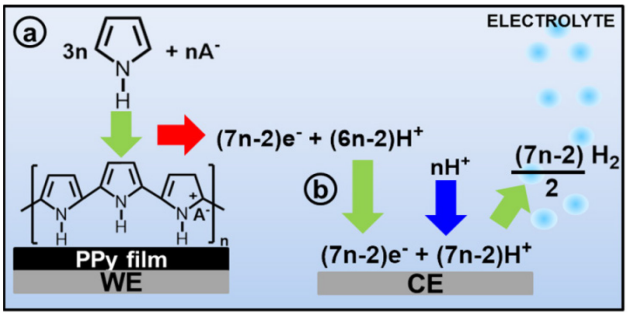

Figure 6.8 Electrochemical polymerization of polypyrrole.

Here, we report the influence of solution temperature, which affects hydrogen solubility and polymerization rate, cell setup and polymerization conditions on the physical structure and electrochemical properties of polymer microtubes. We show that the density of tubes can be increased as the spacing between the working and counter electrodes is decreased and that the tube properties correlated with deposition temperature.

6.2.2 Experimental methods

Materials

All chemicals were purchased from Sigma-Aldrich and Fischer Scientific and used as received unless otherwise noted. Pyrrole monomer was purified by distillation.

Substrate Preparation

Stainless steel mesh substrates (McMaster-Carr, Super-Corrosion Resistance Type 316 Stainless Steel Wire Cloth, 200x200) were prepared by cutting 1.2x1.4 cm rectangles with a 1.3x0.4 cm neck to serve as the connection (**Figure 6.9a**). Substrates were cleaned by sonicating for 10 min in ethanol, dried, weighed (Ohaus DV215CD Semi-micro balance, readability 0.01mg) and treated 15 min (each side) in UV-ozone (Novascan PSD-UV). Parafilm was used to cover the substrates edges and one of the sides to create a 1 cm^2 deposition area.

Microtubes Synthesis

Pyrrole monomer (0.09 M solution) was electropolymerized at various temperatures (4, 14, 24, 34, 60°C) and various distances from the counter electrode (0.5, 1.0, 1.5, 2 cm) in a 0.5 M H_2SO_4 solution (previously degassed with N_2 for 10 min) by chronopotentiometry at 4 mA and charge densities of 12 and 30 C cm^{-2}. Electropolymerization was performed in a 3-electrode cell with a VersaSTAT 4 potentiostat/galvanostat and the VersaStudio v2.40.4 Electrochemistry Software (Princeton Applied Research). The stainless steel mesh substrates were used as the working electrode (WE); platinum gauze 52 mesh (Alfa Aesar) was used as the counter electrode (CE), and a Ag/AgCl in 3 M NaCl solution was used as the reference electrode (RE). The platinum mesh was cleaned between each synthesis by rinsing with deionized water and acetone, and the remaining residue removed by burning with a propane torch. The 3-electrode cell was placed in a cooling bath to control the temperatures at 4 and 14 °C. Experiments at different distances were kept at 24 °C, and experiments at different temperatures were kept at 1 cm distance from CE. The parafilm was removed before the electrochemical analysis, and all samples were dried overnight in a vacuum oven (101.5kPa) at 80°C and weighed after characterization to determine the film mass.

Electrochemical analysis

Electrochemical characterization was performed in a 0.5 M H_2SO_4 solution (previously degassed with pure dried nitrogen gas for 10 min) using cyclic voltammetry from 0 to 0.8 V at various scan rates (300, 100, 30, 10, 3 mV s^{-1}), electrochemical

impedance spectroscopy (EIS) at 0.7 V over a frequency range of 10k to 0.1 Hz using a perturbation amplitude of 10 mV, and charge-discharge measurements at current densities of 14, 7, 3.5mA cm^{-2} (-14,-7,-3.5 mA cm^{-2}) from 0 to 0.8 V unless otherwise stated.

Surface Morphology

The film surface characterization was performed by scanning electron microscopy (SEM) in a Hitachi SU-6600 Analytical VP FE-SEM at a beam intensity of 5 kV; the samples were placed on 45º aluminum sample holders with carbon tape. Images were captured at magnifications of 15x, 20x, 25x, 60x, 90x, and 120x. Quartz PCI software was used to make all the measurements which is calibrated for the microscope. Averages were taken for the diameters and heights presented.

6.2.3 Results and discussion

Figure 6.9 shows a general schematic of the electrochemical set up, synthesis process and electrochemical performance of polypyrrole microtubes.[62] Previously, polypyrrole microtubes were synthesized in a 3-electrode cell (**Figure 6.9a**) solution using chronopotentiometry at a current density of 10 mA cm^{-2}; however, the rate had to be reduced to 4 mA cm^{-2} for polymerization in low-temperature solutions (4°C) to keep the deposition potential below 0.85 V and prevent overoxidation.[66] As polymerization of conducting polymers is also temperature dependent,[65, 67] it was necessary to adjust the synthesis conditions such that microtubes could be obtained over the range of

temperatures. Furthermore, we found that in general, a higher density of microtubes was achieved by covering the back of the electrode (side facing away from the counter electrode) with parafilm in addition to covering the mesh edges, which was necessary to avoid high potential and deposition rates near the edges. Also, because finer mesh substrates showed more uniform microtubes and improved electrochemical activity compared with coarser mesh substrates (**Figure 6.9c**), M200 substrates (1 cm^2) were used for all microtubes grown in this work.

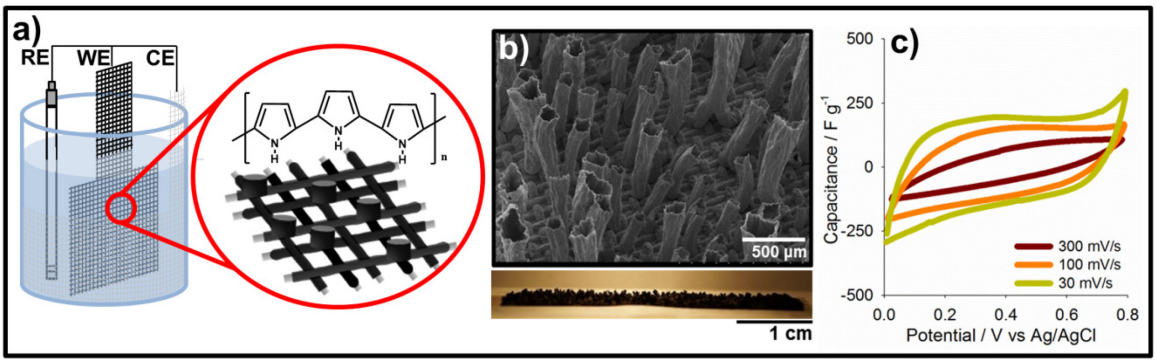

Figure 6.9 Microtube synthesis overview. (a) Electrochemical cell set up and electropolymerization. (b) Polypyrrole microtubes on M200 (4x1cm size substrate). (c) Cyclic voltammetry profiles normalized to capacitance *vs.* potential for microtubes synthesize on M200 at 10mA cm^{-2}, 24°C for 30C cm^{-2}.

The solubility of gasses in liquids is highly dependent on the temperature. In general, the hydrogen solubility in water increases as temperature decreases (calculated based on relationships determined elsewhere[68]), as can be seen on **Figure 6.10a**. Microtubes were synthesized on M200 substrates over a range of temperatures, between 4 °C and 60 °C, for total deposition charges of 12 C cm^{-2} to 30 C cm^{-2}. At temperatures

above 34°C, pyrrole oxidized very quickly in solution resulting in no film formation, which is consistent with previous observations that high temperatures (>30°C) applied during electrochemical synthesis led to polymer dissolution and very thin films with poor adhesion.[69, 70] As a result, solution temperatures were kept below 24 °C for all synthesis experiments. **Figure 6.10a**, shows a plot of the polymerization potential required to achieve a constant current of 4 mA cm^{-2} as function of temperature. As the temperature decreases, the polymerization potential increases and follows the same trend as the hydrogen solubility in water. The chronopotentiometry profiles of electrodes synthesized within this temperature range are shown in **Figure 6.10b**, for electrodes grown to a total charge of 12C cm^{-2}. These plots show two important trends; both the peak potential required during nucleation increases and the steady state current increase as the solution temperature is decreased. Because the same reaction rate is forced in each condition (4 mA cm^{-2}), a higher potential, driving force, is required due to the lower specific reaction rate constant. The peak in potential, which occurs at the onset of polymerization, is attributed to monomer nucleation, and this step is also notably higher at low reaction temperatures.[71, 72] At low temperatures, the rates of the coupling and proton elimination steps for the polymerization of pyrrole decrease, leading to an increase in the potential needed to achieve the set current density (reaction rate).[65]

The polymerization temperature not only affects the synthesis potential but also affects the number of microtubes developed on the mesh substrate (**Figure 6.10c** blue line). Due to the relative large microtubes, the density of tubes on each substrate could be visually determined by observing under a microscope. The number of microtubes

increases with temperature, even though the concentration of hydrogen in solution decreases. Once the concentration of hydrogen in solution reaches the supersaturation value, that varies with temperature,[73] the bubbles will nucleate and grow, leading to the observed increase in the number of microtubes. At low temperature (4°C), the solubility of hydrogen in solution is higher, thus, the saturation point will also be high whereas, at high temperature (24°C), hydrogen will more readily nucleate out of solution in the form of gas bubbles on the working electrode, leading to a higher amount of microtubes, as shown in the insets of **Figures 6.11a** to **6.11c**.

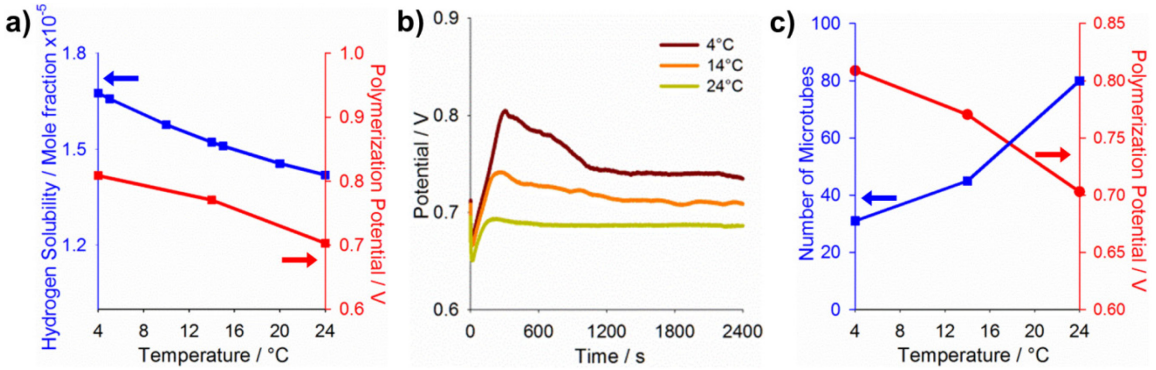

Figure 6.10 Influence of the polymerization temperature in the synthesis of polypyrrole microtubes. (a) Hydrogen solubility in water (blue) and pyrrole polymerization potential as a function of temperature (red). (b) Chronopotentiometry profiles of pyrrole (0.09M in 0.5M H_2SO_4) at various temperatures deposited for 12C cm^{-2} at 4 mA cm^{-2}. (c) Number of microtubes produced as a function of deposition temperature (blue) and pyrrole polymerization potential (red).

The microstructure and physical properties (*i.e.* film thickness, microtube length, and diameter) of the polymer electrodes synthesized at various temperatures were

determined by scanning electron microscopy (SEM). Images were recorded at 45° from the incident beam and are shown in **Figures 6.11a** to **6.11c**. A clear difference in the film morphology can be observed as a function of temperature. Films synthesized at lower temperatures (4 and 14°C) exhibit a rougher surface compared with films at 24°C (**Figures 6.11a**, **6.11b**, and **6.11c**, respectively). The film morphology is highly dependent on the electropolymerization conditions; generally, surface roughness increases as the synthesis potential increases due to lateral and branched growth of the polymer.[67, 74, 75] The thickness of the film formed around the mesh also changes as a function of temperature, from ~15 μm (24°C) down to 8-9 μm (4 °C) (**Figures 6.11d**). Interesting, at lower temperatures (4 and 14°C), the polymer appeared to polymerize to a greater extent on the woven wires (horizontal) compared to the straight wires (vertical), creating an uneven morphology that was challenging to obtain an accurate measure of film thickness.

The length and diameter of the synthesized microtubes (**Figures 6.11e** and **6.11f**) also varied as a function of deposition temperature. An intermediate temperature of 14 °C seemed to be the most efficient for growing microtubes, primarily due to the least amount of polymer formed on mesh from the observations above. Additionally, the longest and most uniform tubes were obtained at this temperature compared to those obtained at 4 °C and 24 °C. At lower temperatures (4 °C), shorter tubes with narrow diameters are achieved, which is likely due to smaller gas bubbles nucleating on the electrode surface. Because the hydrogen solubility is higher in this region, it is less likely that gas bubbles will nucleate on the mesh, leading to fewer and smaller microtubes. At greater

temperatures, monomer diffusivity is higher, and as a result, a higher amount of polymer is formed on the mesh and shorter microtubes are observed.

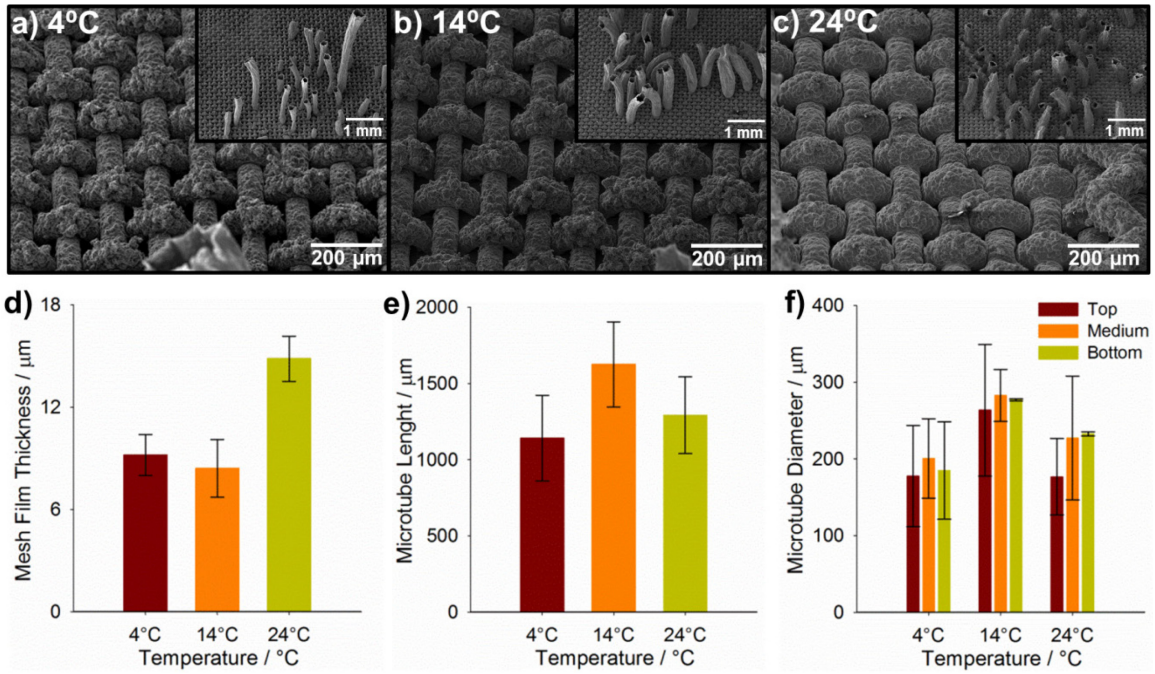

Figure 6.11 Scanning electron microscopy of polypyrrole microtubes synthesized at 4mA cm^{-2} and various temperatures for 30C cm^{-2} at 120x (inset 25x) for (a) 4°C, (b) 14°C, and (c) 24°C. (d) Mesh film thickness. (e) Microtubes length and (f) diameter.

Despite the differences in polymerization potential (**Figure 6.10**) and morphology (**Figure 6.11**) observed for microtubes synthesized at different temperature; the average capacitance (F g^{-1}) as a function of the scan rate (mV s^{-1}) (**Figure 6.12a**) varies only modestly for electrodes synthesised at 4 mA cm^{-2} for 30 C cm^{-2}. The average capacitance is determined from cyclic voltammetry profiles normalized over a range of scan rates from 3 to 300 mV s^{-1}, as shown in **Figure 6.12b** for electrodes synthesized at 24 ºC. Two competing factors affect the electrochemical performance; first, ECPs polymerized at

lower temperature exhibit higher electrical conductivity[67] and second, electrodes polymerized at lower potential have lower inter-polymer crosslinking, which typically leads to higher intrinsic capacitance.[76] As expected, electrodes synthesized at 24 ºC (lowest deposition potential) exhibited the highest intrinsic capacitance, as determined by the capacitance at low scan rates (< 30 mV s^{-1}), where electrical and ion transport do not limit redox activity. Electrodes prepared at low temperatures, however, display the highest capacitance at fast scan rates (> 30 mV s^{-1}) due to their higher electrical conductivity. Nonetheless, the electrochemical performance of each electrode does not vary significantly with temperature, indicating that temperature can be used to tailor the physical properties of the microtubes without negatively affecting electrochemical performance, as long as the synthesis potential is kept below 0.85 V.

It is important to notice that the polymerization potential decreases as the temperature increases (**Figure 6.10c** red line). In our previous work,[62] we found that polymerizations between 0.7 and 0.8V favor optimal electrochemical activity and the formation of more uniform structures. **Figure 6.12b** shows the cyclic voltammetry profile as of specific capacitance (F g^{-1}), which is current (A) divided scan rate (V s^{-1}) and electrode mass (g) *vs.* potential for electrodes synthesized at 4 mA cm^{-2} and 24 ºC for 12 C cm^{-2}. Similar to what is shown in **Figure 6.12a**, there is scan rate dependence as the film is cycled at faster scan rates, which is expected for relatively thick films due to ion diffusion limitations from the bulk of the electrolyte to the film, leading to a decrease in the electrochemical activity of the electrodes; nevertheless, the overall capacitance (~200

F g^{-1}) corresponds to the expected value for polypyrrole films at the experimental conditions.[57]

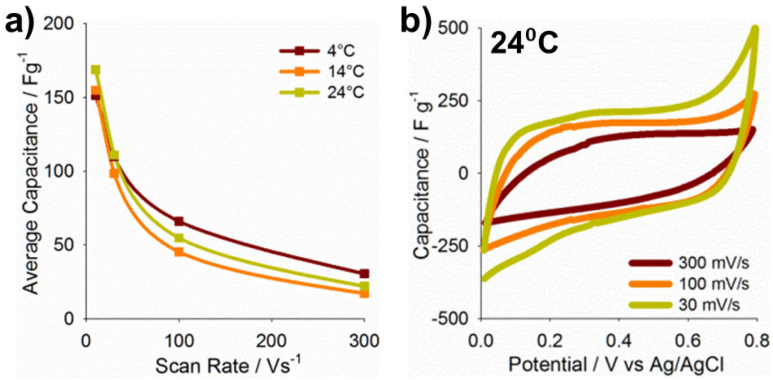

Figure 6.12 Electrochemical performance of polypyrrole microtubes at different temperatures (a) Average capacitance as a function of scan rate for films synthesized at 4mA cm^{-2} for 30C cm^{-2}. (b) Cyclic voltammetry profiles normalized to capacitance *vs.* potential for microtubes synthesized at 4 mA cm^{-2}, 24°C for 12C cm^{-2}.

The spacing between the working electrode and the counter electrode in the electrochemical cell is expected to affect microtube growth because the concentration of hydrogen decreases with distance away from the CE, where it is generated. For microtubes to form, hydrogen must nucleate from the WE. In this experiment, microtubes were synthesized under standard conditions for substrate position ranging from 0.5 and 2 cm away from the CE for a total charge of 30 C cm^{-2}. The morphology of the films and physical features of the microtubes were studied by SEM on 45° sample holders (**Figure 6.13**). **Figures 6.13a** to **6.13c** show the film morphology, as well as a general view of the microtubes extending from the mesh surfaces. No significant differences were observed in the surface morphology because the deposition potential did not vary significantly as

the distance between the WE and CE was increased. The film thickness varies slightly between ~15 ~ 20 µm (**Figure 6.13d**) with no particular correlation with distance; however, mass of polymer deposited slightly increases with WE to CE spacing (0.5 cm: 6.06mg, 1.0cm: 6.64mg, 1.5cm: 7.02mg, 2cm: 7.03mg). At tighter spacing, the average length (**Figure 6.13e**) of the microtubes is smaller and microtubes are more uniform (**Figure 6.13f**), which is likely due to the bubbles formed closer to the CE are more homogeneously distributed on the surface of the electrode when nucleation occurs.

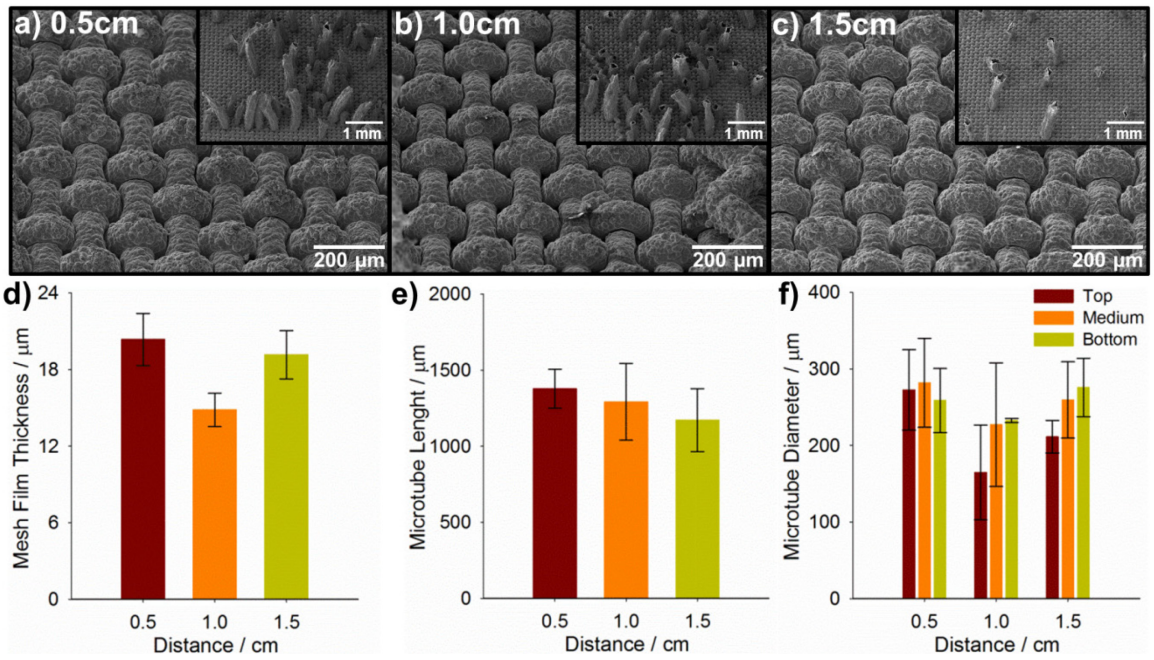

Figure 6.13 Scanning electron microscopy of polypyrrole microtubes synthesized at 4mA cm^{-2} and various distances from CE for 30C cm^{-2} at 120x (inset 25x) for (a) 0.5cm, (b) 1.0cm, and (c) 1.5cm. (d) Mesh film thickness. (e) Microtubes length and (f) diameter.

As the spacing between the WE and CE is increased, the number of microtubes decreases (**Figure 6.14a** red line). When the distance between the WE and CE is 2 cm, very few microtubes form on the substrates (~7 microtubes cm^{-2}), whereas the number of microtubes formed increases significantly as the WE electrode is moved to within 0.5 cm of the CE (up to ~65 microtubes cm^{-2}). The increase in microtube density occurs because the concentration of hydrogen decreases with distance away from the CE where it is generated. When the WE is situated close to the CE, the solution becomes supersaturated quickly after the initial polymerization is applied allowing for hydrogen to uniformly nucleate on the surface of the mesh substrate to create a high density of microstructures. However, it is important to note that the polymerization potential, in this case, remains fairly constant (**Figure 6.14a** blue), thereby causing minimal variability in the electrochemical performance of the samples. **Figure 6.14b**, shows the cyclic voltammetry profiles as specific capacitance ($F\ g^{-1}$) *vs*. potential recorded at a scan rate of 10 $mV\ s^{-1}$ for various CE to WE distances. The electrochemical behavior of the samples is nearly identical, confirming our observations in **Figure 6.14**a and **Figures 6.13a** to **6.13c**. The changes in the spacing between the WE and CE affect the number and physical structure of the microtubes; however, the electrochemical performance of the films is not affected by these differences.

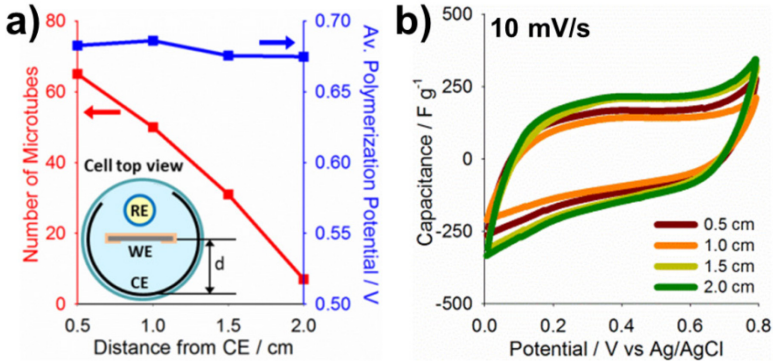

Figure 6.14 Influence of the spacing between the WE and CE in the electrochemical properties of polypyrrole microtubes. (a) Number of microtubes as function of distance synthesized at 4mA cm^{-2}, 24°C for 30C cm^{-2} and changes in average polymerization potential. (b) Cyclic voltammetry profiles normalized to capacitance *vs.* potential at 10 mV s^{-1} for various distances.

6.2.4 Conclusions

The influence of the polymerization temperature and electrochemical cell setup on the synthesis of conducting polymer microtubes in aqueous solutions has been demonstrated. The number of microtubes synthesized increases as the temperature increases from 4 °C to 24 °C while higher temperatures result in overoxidation of the monomer in solution and dissolution of the resulting polymer. However, no significant differences in the electrochemical activity are observed as function of temperature. In general, higher temperature leads to lower polymerization potentials which produce a smoother film, higher intrinsic capacitance (low scan rate performance) and lower conductivity. The number of microtubes on the mesh substrates also increases as the distance between the counter and the working electrode is reduced down to 0.5 cm, yet no significant difference in the electrochemical performance of the electrodes is

observed. The study of these variables is important to understand how to control the growth of polypyrrole microtubes based on template-free methods guided by gas nucleation in solution.

6.3 References

1. Snook GA, Kao P, Best AS. Conducting-polymer-based supercapacitor devices and electrodes. *J. Power Sources* **2011**, 196(1)**:** 1-12.

2. Simon P, Gogotsi Y. Materials for electrochemical capacitors. *Nat. Mater.* **2008**, 7(11)**:** 845-854.

3. Fisher RA, Watt MR, Ready WJ. Functionalized Carbon Nanotube Supercapacitor Electrodes: A Review on Pseudocapacitive Materials. *ECS J. Solid State Sci. Technol.* **2013**, 2(10)**:** M3170-M3177.

4. Yu G, Xie X, Pan L, Bao Z, Cui Y. Hybrid nanostructured materials for high-performance electrochemical capacitors. *Nano Energy* **2013**, 2(2)**:** 213-234.

5. Liu C, Li F, Ma L-P, Cheng H-M. Advanced Materials for Energy Storage. *Adv. Mater.* **2010**, 22(8)**:** E28-E62.

6. Song Z, Zhou H. Towards sustainable and versatile energy storage devices: an overview of organic electrode materials. *Energy Environ. Sci.* **2013**, 6(8)**:** 2280-2301.

7. Evans A, Strezov V, Evans TJ. Assessment of utility energy storage options for increased renewable energy penetration. *Renew. Sust. Energ. Rev,* **2012**, 16(6)**:** 4141-4147.

8. Winter M, Brodd RJ. What Are Batteries, Fuel Cells, and Supercapacitors? *Chem. Rev.* **2004**, 104(10)**:** 4245-4270.

9. Bose S, Kuila T, Mishra AK, Rajasekar R, Kim NH, Lee JH. Carbon-based nanostructured materials and their composites as supercapacitor electrodes. *J. Mater. Chem.* **2012**, 22(3)**:** 767-784.

10. Lokhande CD, Dubal DP, Joo O-S. Metal oxide thin film based supercapacitors. *Curr. Appl. Phys.* **2011**, 11(3)**:** 255-270.

11. Wei W, Cui X, Chen W, Ivey DG. Manganese oxide-based materials as electrochemical supercapacitor electrodes. *Chem. Soc. Rev.* **2011**, 40(3)**:** 1697-1721.

12. Wang G, Zhang L, Zhang J. A review of electrode materials for electrochemical supercapacitors. *Chem. Soc. Rev.* **2012**, 41(2)**:** 797-828.

13. Shukla AK, Banerjee A, Ravikumar MK, Jalajakshi A. Electrochemical capacitors: Technical challenges and prognosis for future markets. *Electrochim. Acta* **2012**, 84(0)**:** 165-173.

14. Kim J-Y, Kim K-H, Kim H-K, Park S-H, Chung KY, Kim K-B. Nanosheet-assembled 3D nanoflowers of ruthenium oxide with superior rate performance for supercapacitor applications. *RSC Adv.* **2014**, 4(31)**:** 16115-16120.

15. Li C, Bai H, Shi G. Conducting polymer nanomaterials: electrosynthesis and applications. *Chem. Soc. Rev.* **2009**, 38(8)**:** 2397-2409.

16. Heinze J, Frontana-Uribe BA, Ludwigs S. Electrochemistry of Conducting Polymers—Persistent Models and New Concepts†. *Chem. Rev.* **2010**, 110(8)**:** 4724-4771.

17. Novák P, Müller K, Santhanam KSV, Haas O. Electrochemically Active Polymers for Rechargeable Batteries. *Chem. Rev.* **1997**, 97(1)**:** 207-282.

18. Long Y-Z, Li M-M, Gu C, Wan M, Duvail J-L, Liu Z*, et al.* Recent advances in synthesis, physical properties and applications of conducting polymer nanotubes and nanofibers. *Prog. Polym. Sci.* **2011**, 36(10)**:** 1415-1442.

19. Qu L, Shi G, Chen Fe, Zhang J. Electrochemical Growth of Polypyrrole Microcontainers. *Macromolecules* **2003**, 36(4)**:** 1063-1067.

20. Yin Z, Zheng Q. Controlled Synthesis and Energy Applications of One-Dimensional Conducting Polymer Nanostructures: An Overview. *Adv. Energy Mater.* **2012**, 2(2)**:** 179-218.

21. Qu L, Shi G, Yuan J, Han G, Chen Fe. Preparation of polypyrrole microstructures by direct electrochemical oxidation of pyrrole in an aqueous solution of camphorsulfonic acid. *J. Electroanal. Chem.* **2004**, 561(0)**:** 149-156.

22. Yuan J, Qu L, Zhang D, Shi G. Linear arrangements of polypyrrole microcontainers. *Chem. Commun.* **2004**(8)**:** 994-995.

23. Qu L, Shi G. Hollow microstructures of polypyrrole doped by poly(styrene sulfonic acid). *J. Polym. Sci., Part A: Polym. Chem.* **2004**, 42(13)**:** 3170-3177.

24. Antony MJ, Jayakannan M. Molecular Template Approach for Evolution of Conducting Polymer Nanostructures: Tracing the Role of Morphology on Conductivity and Solid State Ordering. *J. Phys. Chem. B* **2010**, 114(3)**:** 1314-1324.

25. Reddy ALM, Gowda SR, Shaijumon MM, Ajayan PM. Hybrid Nanostructures for Energy Storage Applications. *Adv. Mater.* **2012**, 24(37)**:** 5045-5064.

26. Wan M. A Template-Free Method Towards Conducting Polymer Nanostructures. *Adv. Mater.* **2008**, 20(15)**:** 2926-2932.

27. Kumar K, Luchnikov V, Nandan B, Senkovskyy V, Stamm M. Formation of self-rolled polymer microtubes studied by combinatorial approach. *Eur. Polym. J.* **2008**, 44(12)**:** 4115-4121.

28. Zhao Y, Liu B, Pan L, Yu G. 3D nanostructured conductive polymer hydrogels for high-performance electrochemical devices. *Energy Environ. Sci.* **2013**, 6(10)**:** 2856-2870.

29. Xia L, Wei Z, Wan M. Conducting polymer nanostructures and their application in biosensors. *J. Colloid Interface Sci.* **2010**, 341(1)**:** 1-11.

30. Bajpai V, He P, Dai L. Conducting-Polymer Microcontainers: Controlled Syntheses and Potential Applications. *Adv. Funct. Mater.* **2004**, 14(2)**:** 145-151.

31. Bajpai V, He P, Goettler L, Dong JH, Dai L. Controlled syntheses of conducting polymer micro- and nano-structures for potential applications. *Synth. Met.* **2006**, 156(5–6)**:** 466-469.

32. Gupta S. Hydrogen bubble-assisted syntheses of polypyrrole micro/nanostructures using electrochemistry: structural and physical property characterization. *J. Raman Spectrosc.* **2008**, 39(10)**:** 1343-1355.

33. Hui F, Li B, He P, Hu J, Fang Y. Electrochemical fabrication of nanoporous polypyrrole film on HOPG using nanobubbles as templates. *Electrochem. Commun.* **2009**, 11(3)**:** 639-642.

34. Mazur M. Preparation of Three-Dimensional Polymeric Structures Using Gas Bubbles as Templates. *J. Phys. Chem. C* **2008**, 112(35)**:** 13528-13534.

35. Huang J, Quan B, Liu M, Wei Z, Jiang L. Conducting Polypyrrole Conical Nanocontainers: Formation Mechanism and Voltage Switchable Property. *Macromol. Rapid Commun.* **2008**, 29(15)**:** 1335-1340.

36. Wang K, Huang J, Wei Z. Conducting Polyaniline Nanowire Arrays for High Performance Supercapacitors. *J. Phys. Chem. C* **2010**, 114(17)**:** 8062-8067.

37. Percec S, Bolas C, Howe L, Brill DJ, Li J. In situ polymerization and morphology of polypyrrole obtained in water-soluble polymer templates. *J. Polym. Sci., Part A: Polym. Chem.* **2012**, 50(23)**:** 4966-4976.

38. Lewis TW, Wallace GG, Kim CY, Kim DY. Studies of the overoxidation of polypyrrole. *Synth. Met.* **1997**, 84(1–3)**:** 403-404.

39. Li Y, Qian R. Electrochemical overoxidation of conducting polypyrrole nitrate film in aqueous solutions. *Electrochim. Acta* **2000**, 45(11)**:** 1727-1731.

40. Park DS, Shim YB, Park SM. Degradation of electrochemically prepared polypyrrole in aqueous sulfuric acid. *J. Electrochem. Soc.* **1993**, 140(3)**:** 609-614.

41. Kumar A, Singh RK, Agarwal K, Singh HK, Srivastava P, Singh R. Effect of p-toluenesulfonate on inhibition of overoxidation of polypyrrole. *J. Appl. Polym. Sci.* **2013**, 130(1)**:** 434-442.

42. Bof Bufon CC, Heinzel T, Espindola P, Heinze J. Influence of the Polymerization Potential on the Transport Properties of Polypyrrole Films. *J. Phys. Chem. B* **2009**, 114(2)**:** 714-718.

43. Qu D, Shi H. Studies of activated carbons used in double-layer capacitors. *J. Power Sources* **1998**, 74(1)**:** 99-107.

44. Larcher D, Tarascon JM. Towards greener and more sustainable batteries for electrical energy storage. *Nat Chem* **2015**, 7(1)**:** 19-29.

45. Titirici M-M, White RJ, Brun N, Budarin VL, Su DS, del Monte F*, et al.* Sustainable carbon materials. *Chem. Soc. Rev.* **2015**, 44(1)**:** 250-290.

46. Dubal DP, Ayyad O, Ruiz V, Gomez-Romero P. Hybrid energy storage: the merging of battery and supercapacitor chemistries. *Chem. Soc. Rev.* **2015**, 44(7)**:** 1777-1790.

47. Yan J, Wang Q, Wei T, Fan Z. Recent Advances in Design and Fabrication of Electrochemical Supercapacitors with High Energy Densities. *Adv. Energy Mater.* **2014**, 4(4)**:** 1300816.

48. Wang K, Wu H, Meng Y, Wei Z. Conducting Polymer Nanowire Arrays for High Performance Supercapacitors. *Small* **2014**, 10(1)**:** 14-31.

49. Wang F, Xiao S, Hou Y, Hu C, Liu L, Wu Y. Electrode materials for aqueous asymmetric supercapacitors. *RSC Adv.* **2013**, 3(32)**:** 13059-13084.

50. Béguin F, Presser V, Balducci A, Frackowiak E. Carbons and electrolytes for advanced supercapacitors. *Adv. Mater.* **2014**, 26(14)**:** 2219-2251.

51. Zhang J, Terrones M, Park CR, Mukherjee R, Monthioux M, Koratkar N*, et al.* Carbon science in 2016: Status, challenges and perspectives. *Carbon* **2016**, 98**:** 708-732.

52. Sevilla M, Mokaya R. Energy storage applications of activated carbons: supercapacitors and hydrogen storage. *Energy Environ. Sci.* **2014**, 7(4)**:** 1250-1280.

53. Zhai Y, Dou Y, Zhao D, Fulvio PF, Mayes RT, Dai S. Carbon Materials for Chemical Capacitive Energy Storage. *Adv. Mater.* **2011**, 23(42)**:** 4828-4850.

54. Jiang J, Li Y, Liu J, Huang X, Yuan C, Lou XW. Recent Advances in Metal Oxide-based Electrode Architecture Design for Electrochemical Energy Storage. *Adv. Mater.* **2012**, 24(38)**:** 5166-5180.

55. Augustyn V, Simon P, Dunn B. Pseudocapacitive oxide materials for high-rate electrochemical energy storage. *Energy Environ. Sci.* **2014**, 7(5)**:** 1597-1614.

56. Abdelhamid ME, O'Mullane AP, Snook GA. Storing energy in plastics: a review on conducting polymers & their role in electrochemical energy storage. *RSC Adv.* **2015**, 5(15)**:** 11611-11626.

57. Leguizamon S, Diaz-Orellana KP, Velez J, Thies MC, Roberts ME. High charge-capacity polymer electrodes comprising alkali lignin from the Kraft process. *J. Mater. Chem. A* **2015**, 3(21)**:** 11330-11339.

58. Pieta P, Obraztsov I, D'Souza F, Kutner W. Composites of conducting polymers and various carbon nanostructures for electrochemical supercapacitors. *ECS J. Solid State Sci. Technol.* **2013**, 2(10)**:** M3120-M3134.

59. Lou XW, Archer LA, Yang Z. Hollow Micro-/Nanostructures: Synthesis and Applications. *Adv. Mater.* **2008**, 20(21)**:** 3987-4019.

60. Bai Y, Xu Y, Wang J, Gao M, Wang J. Interface Effect on the Electropolymerized Polypyrrole Films with Hollow Micro/Nanohorn Arrays. *ACS Appl. Mater. Interfaces* **2014**, 6(7)**:** 4693-4704.

61. Wang J, Xu Y, Yan F, Zhu J, Wang J. Template-free prepared micro/nanostructured polypyrrole with ultrafast charging/discharging rate and long cycle life. *J. Power Sources* **2011**, 196(4)**:** 2373-2379.

62. Diaz-Orellana KP, Roberts ME. Scalable, template-free synthesis of conducting polymer microtubes. *RSC Adv.* **2015**, 5(32)**:** 25504-25512.

63. Qu L, Shi G, Yuan J, Han G, Chen Fe. Preparation of polypyrrole microstructures by direct electrochemical oxidation of pyrrole in an aqueous solution of camphorsulfonic acid. *J. Electroanal. Chem.* **2004**, 561**:** 149-156.

64. Tian Y, Yang F, Yang W. Redox behavior and stability of polypyrrole film in sulfuric acid. *Synth. Met.* **2006**, 156(16–17)**:** 1052-1056.

65. Bof Bufon CC, Heinzel T, Espindola P, Heinze J. Influence of the Polymerization Potential on the Transport Properties of Polypyrrole Films. *J. Phys. Chem. B* **2010**, 114(2)**:** 714-718.

66. Ashrafi A, Golozar MA, Mallakpour S. Morphological investigations of polypyrrole coatings on stainless steel. *Synth. Met.* **2006**, 156(18–20)**:** 1280-1285.

67. Sadki S, Schottland P, Brodie N, Sabouraud G. The mechanisms of pyrrole electropolymerization. *Chem. Soc. Rev.* **2000**, 29(5)**:** 283-293.

68. Lide DR, Haynes WM, Press CRC. *CRC handbook of chemistry and physics*, vol. 96th, 2015-2016. CRC Press: Boca Raton, **2016**, pp 5-149 - 145-152.

69. Rahman SU, Ba-Shammakh MS. Thermal effects on the process of electropolymerization of pyrrole on mild steel. *Synth. Met.* **2004**, 140(2–3)**:** 207-223.

70. Sayyah SM, Abd El-Rehim SS, El-Deeb MM. Electropolymerization of pyrrole and characterization of the obtained polymer films. *J. Appl. Polym. Sci.* **2003**, 90(7)**:** 1783-1792.

71. Talaie A, Boger Z, Romagnoli JA, Adeloju SB, Yuan YJ. Data acquisition, signal processing and modelling: a study of a conducting polypyrrole formate biosensor Part 1: Batch experiment. *Synth. Met.* **1996**, 83(1)**:** 21-26.

72. Shirale DJ, Gade VK, Gaikwad PD, Kharat HJ, Kakde KP, Savale PA*, et al.* The influence of electrochemical process parameters on the conductivity of poly(N-methylpyrrole) films by galvanostatic method. *Mater. Lett.* **2006**, 60(11)**:** 1407-1411.

73. Dapkus KV, Sides PJ. Nucleation of electrolytically evolved hydrogen at an ideally smooth electrode. *J. Colloid Interface Sci.* **1986**, 111(1)**:** 133-151.

74. Partridge AC, Milestone CB, Too CO, Wallace GG. Polypyrrole based cation transport membranes. *J. Membr. Sci.* **1999**, 152(1)**:** 61-70.

75. Patois T, Lakard B, Monney S, Roizard X, Fievet P. Characterization of the surface properties of polypyrrole films: Influence of electrodeposition parameters. *Synth. Met.* **2011**, 161(21–22)**:** 2498-2505.

76. Heinze J, Frontana-Uribe BA, Ludwigs S. Electrochemistry of Conducting Polymers—Persistent Models and New Concepts. *Chem. Rev.* **2010**, 110(8)**:** 4724-4771.

CHAPTER SEVEN

CONCLUSIONS AND RECOMMENDATIONS

The overall goal of this Ph.D. dissertation was to develop straightforward, low-cost approaches for the design of micro- and nano-structured electrodes with enhanced electrochemical performance. Various pathways were followed to fulfill this objective and were organized into two main focus areas. The first one (Chapters 2 and 3) concentrated on the manipulation of the electrode composition through the incorporation of lignin, as a redox polymer, into the active electrode material, for enhanced energy density. The second approach (Chapter 4 to 6) focused on the modification of the electrode structure through changes in the synthesis process of the electrode materials, to improve the electrochemical performance. Overall, we learned to take advantage of redox moieties to manipulate the electrochemical performance of electrode materials, the importance and influence of the polymerization conditions for the synthesis of microstructures, and the structure-performance relationships for the fabrication of high surface area supercapacitor electrodes.

The following sections present the main contributions of each project and recommendations for future work. We highlight possible research pathways and optimization routes, which the author hopes will be useful for new students in Dr. Roberts's research group.

7.1 High charge-capacity polymer electrodes comprising alkali lignin from the Kraft process

Alkali lignin/polypyrrole composite electrodes exhibit 30% higher capacitance than similar electrodes prepared with sulfonated lignin, and 56% higher than electrodes comprised only by polypyrrole. This work represented the first time that alkali lignin is used in composite electrodes with conducting polymers in aqueous solutions. Furthermore, it was found that the differences in the electrochemical behavior of the two types of lignin are related to modifications in the lignin chemistry suffered during the pulping process. Additionally, it was found that as the aromatic phenolic content of lignin polymers increases the electrochemical activity also increases. Moreover, a difference in the morphology of electrodes synthesized with sulfonated lignin in acetic acid and sulfuric acid was found. The electrodes fabricated with acetic acid show an open globular structure, which led to faster charge-discharge processes. Indicating electrodes prepared with sulfonated lignin in acetic acid can discharge faster than the ones prepared with alkali lignin. Therefore, depending on the application (high power or high energy storage), one material or the other can be used in a supercapacitor device.

Interestingly, we found that the optimal concentration of lignin in conducting polymer electrodes is size dependent. For small electrodes (0.02 cm^2), the optimal ratio PPy:Lignin was higher than for larger area electrodes (0.5 cm^2) (Appendix A). This behavior was discovered when stainless steel meshes were used to prepare the composite electrodes. Hence, one possible research pathway could be to investigate the cause of the

size dependence and if this represents any differences in the electrochemical performance and cycle life of the electrodes.

Another potential research route, which was briefly investigated, is the chemical synthesis of polypyrrole/lignin composite electrodes (Appendix A). Polypyrrole/lignin composites were synthesized by chemical polymerization as described in Appendix D. The polymer was deposited onto various substrates (Indium tin oxide, carbon paper, stainless steel, aluminum foil) through a slurry, showing promising results for scalability purposes, since chemical synthesis allows higher production volumes. In this case, lignin:pyrrole ratios and slurry preparation conditions need to be optimized, as well as, improvements in the adhesion between the slurry and the substrate. Also, different conducting polymers such as polyaniline and poly(3,4-ethylenedioxythiophene) could be investigated in composite electrodes with lignin.

One of the main challenges in the preparation of polypyrrole/lignin devices is the lack of options for the negative electrode. Currently, the only option is the use of carbon materials, which possess lower energy storage capacity compared to conducting polymers. Then, a higher amount of carbon is needed on the anode to avoid limitations in the cathode, which increases the overall mass of the device, limiting the specific capacitance. Therefore, it will be useful to investigate possible anode materials based on organic molecules (our research group has done some work in this area) or functionalization of carbon materials with molecules that exhibit redox behavior at negative potentials to enhance the energy density.

7.2 Lignin-coated Carbon Nanomaterials for Low-Cost Electrical Energy Storage

Another challenge related to electrodes prepared with polypyrrole/lignin composites is the cycle life. Electrodes synthesized with conducting polymers are known to have a shorter cycle life, mainly caused by the swelling and shrinking process during charge-discharge, overoxidation, and nucleophilic attack by the electrolyte. These effects are accentuated when combined with lignin due to charge transfer interactions between lignin and polypyrrole. Chapter 3 was focused on the development of a low-cost electrode where the conducting polymer was replaced by porous carbon to study the electrochemical activity of lignin and improve the cycle life. As shown in chapter 2, there are differences in the electrochemical performance of alkali lignin compared with sulfonated lignin. To study these differences, it was found that an intermediate pore size (>40 nm) material is required to adsorb lignin within the internal structure. Moreover, it was demonstrated that the processing conditions such as sonication time, electrolyte, mass, and type of carbon material have a significant influence on the electrochemical performance of the electrodes. Additionally, carbon was able to effectively improve the cycle life of the electrodes. However, current carbon materials exhibit low energy densities, which raise the need for new developments in carbons, conducting polymers, and composites.

To further improve biopolymer/carbon electrodes, one area that could be studied is how well adsorb is lignin within the porous structure of the carbon material. For instance, how long one device can be store and still maintain the electrochemical activity. This measurement can be done for single electrodes or for 2-electrode systems. A simple

way to measure this, could be soaking the electrode in the electrolyte for several days and determine if lignin diffuses out or remains within the carbon structure, measuring the changes in the electrochemical response. Another way is to prepare a supercapacitor device and test it every certain period of time. Moreover, the use of renewable materials in energy storage represents a huge advantage for the development of sustainable technologies. Therefore, future research could be oriented to the use of alternative carbon materials (*e.g.* graphene, CNTs, carbon aerogels, among others) with intermediate pore size (mesoporosity), which could lead to improved electrochemical activity of biopolymer/carbon electrodes.

7.3 Nanostructured polyacrylonitrile/lignin carbon fiber electrodes for high-performance supercapacitors

To the time of dissertation submission, the main findings regarding the use of porous carbon fibers based on PAN/lignin blends were related to the diameter of the fibers. Smaller fiber diameters (8.5 μm) led to higher capacitance compared to thicker fibers (115μm) as the surface area increases with the diameter reduction. Therefore, fibers as thin as 8.5 μm show capacitances of 70 F g^{-1} at 10 mV s^{-1}. Moreover, a chemical activation process with KOH in these fibers led to capacitances of 192 F g^{-1} at 10 mV s^{-1}. Finding the ideal conditions for this activation process has been one of the major challenges we encountered with this project. We believe the various heat treatments (stabilization, pre-carbonization, activation and heat treatment) are causing a decrease in the conductivity of the fibers decreasing their electrochemical performance. Therefore,

we are currently working on improvements to this activation process to avoid the loss of the fiber nanostructure and conductivity.

Future pathways in this work are to change the lignin concentration in the PAN/lignin blend. Until now, 35 wt.% lignin has been used. The limit for the synthesis of stable PAN/lignin fibers is 45 wt.% lignin and the minimum to obtain porous fibers is ~10 wt.% lignin.[1-3] High concentrations of lignin lead to larger macro-/mesopores than low concentrations. Therefore, concentrations between 15-45 wt.% lignin could be used to compare the electrochemical performance and determine the optimal concentration of lignin in the blend. Moreover, porous carbon fibers produced from PAN/Maleic acrylated epoxidized soybean oil (MAESO) and fabricated by Dr. Ogale's graduate student Jing Jin were tested. These fibers showed promising results if similar optimization process as the one with PAN/Lignin fibers is followed. Also, porous carbon fiber mats could be fabricated to create flexible free-standing electrodes or substrates.

7.4 Rigid, non-pressed, highly porous carbon aerogel supercapacitor electrodes

Resorcinol – formaldehyde carbon aerogels reinforced with a backbone material, added during the synthesis process, allowed the fabrication of free-standing electrodes. This eliminated the need for a binder and current collector during supercapacitor assembly. Electrodes exhibited better electrochemical properties when carbon veil was used as backbone material, combined with some slight modifications in the synthesis process. Moreover, the selected backbone materials are lightweight reducing the total weight of the final device. Importantly, the synthesis process of carbon aerogels was

optimized to two days for curing and one day for drying which is faster compared with previous reports.

As future work, the activation of carbon materials to enhance surface area could also be used. The carbon aerogel electrodes exhibit a surface area of ~660 m^2 g^{-1}. Since carbon aerogels have a more delicate structure than carbon fibers, a physical activation with CO_2, steam or O_2 could be more convenient. Chemical activation is more aggressive than physical activation which could damage the 3D structure of the aerogel. By using this procedure, the capacitance of the electrodes could be further increased. Also, resorcinol - formaldehyde could be replaced with more environmentally friendly biomass derived materials (e.g. lignin, cellulose), as suggested in recent reviews.[4]

7.5 Scalable, template-free synthesis of conducting polymer microtubes

Polypyrrole microtubes were synthesized with a free-template method which allows the synthesis of microstructures in various size substrates. This versatility eliminates the size limitations that conventional methods, such as hard templates and soft templates have. To the best of our knowledge, this was the first publication to show polypyrrole microtubes can be synthesized based on the hydrogen gas produced during the electropolymerization of polypyrrole. Different mesh sizes were used to understand the role of the substrate in the synthesis of the microstructure. The mesh size can be used to tune the electrochemical performance of the microtubes. It was found that smaller size meshes (200x200 and 400x400) produce more uniform structures that exhibit higher electrochemical performance. Moreover, the size of the substrate does not limit the

growth of the microtubes. The presence of hydrogen gas in solution plays a fundamental role in the synthesis, as the microtubes grow from the H_2 bubbles that nucleate on the mesh surface. The distance between the counter and working electrode demonstrated to be important, as the working electrode is far from the counter electrode the number of microtubes in solution decreases due to the reduction in the hydrogen concentration.

One point to emphasize is the importance of the platinum mesh counter electrode. The cleaning procedure suggested in Appendix C is fundamental to the successful synthesis of the microtubes, if the counter electrode is not clean, the microtubes will not grow. When the microtubes were synthesized from a mixture of conducting polymer with a polymer dopant (Appendix C), the size and features of the microtubes vary compared with the ones synthesized in the conventional electrolyte. Therefore, a possible pathway could be the use of poly(4-styrenesulfonic acid), p-toluenesufonic acid and sodium dodecyl sulfate which are different types of anionic dopants, to synthesize polypyrrole microtubes. The influence of the dopant in the electrochemical and physical characteristics of the microtubes can be studied. Furthermore, polyaniline and poly(3,4-ethylenedioxythiophene) could be tested to determine if microtubes can be formed.

To change the order of magnitude of the microstructures to possible submicron size, the formation of submicron size bubbles would be needed. A possible option is to scan at negative potentials. A surfactant could be added to the mixture to stabilize the bubbles and later, the conducting polymer monomer could be carefully added. This is similar to what was done in Appendix C to test the "bubble method'; however, for this

case lower currents (< 8 mA), and very small charges (<1C) should be used to avoid the formation of micron-size structures.

7.6 Additional research projects

Other research projects were briefly investigated since they were related to the areas we were studying. One involved the use of an ionic polymer dopant to increase the ion transport within conducting polymer electrodes. The other one consisted in the use of sacrificial groups to control the porosity of conducing polymer films.

On the first project, we used Poly(4-stryrene sulfonic acid) (PSSA) as an ionic polymer dopant for electrochemically polymerized pyrrole electrodes. The objective was to entrap this polymer within conducting polymer chains to invert the doping mechanism and increase ion transport. In polypyrrole (PPy) films, conventionally, the charge compensation occurs by anions and protons from the electrolyte. Anions are bigger in size than protons (H^+) thus, for thick films the charge-discharge process becomes slower as the ion diffusion limitations are higher. We were particularly interested in thick films because they have more practical applications in commercial devices. When PSSA is added to the film, PSS^- will compensate the positive charge developed on PPy (upon charge), while protons from the electrolyte will keep the charge neutrality of the remaining PSS^- groups. Hence, inverting the doping mechanism and increasing the power density in the devices.

We found that this process holds true for thin films (< 5 μm) while thicker films (> 13 μm) do not exhibit any improvement in the electrochemical activity by the addition

of PSSA. We studied changes in PSSA concentration, film thickness, and temperature. The experiments were performed with polypyrrole and polyaniline, both demonstrating similar results. Therefore, our conclusion was that this approach is not suitable for films thicker than ~5 μm.

In the other project, we worked with N-BOC-pyrrole. The objective was to use sacrificial groups (*i.e.* BOC) as a way to control porosity and density in the polymer film; studying the effect of the change in porosity in the electrochemical activity of electrodes. The removal of the BOC group can be done by thermal heating, acid or basic treatments. We worked with thermal heating of N-BOC-polypyrrole films synthesized by electrochemical polymerization. After thermal heating, the polymer (PPy) lost most of the electrochemical activity, which made difficult to test any differences. Therefore, we recommend that future research should be oriented to the study of chemically polymerized N-Boc pyrrole because is easier to handle and higher amounts of polymer can be obtained. A literature review of different deprotection methods use to remove N-Boc groups, experimental conditions, chemical synthesis, and suggestions for future experiments are presented in Appendix E.

7.7 References

1. Dong X, Lu C, Zhou P, Zhang S, Wang L, Li D. Polyacrylonitrile/lignin sulfonate blend fiber for low-cost carbon fiber. *RSC Advances* **2015**, 5(53)**:** 42259-42265.

2. Maradur SP, Kim CH, Kim SY, Kim B-H, Kim WC, Yang KS. Preparation of carbon fibers from a lignin copolymer with polyacrylonitrile. *Synth. Met.* **2012**, 162(5-6)**:** 453-459.

3. Xia K, Ouyang Q, Chen Y, Wang X, Qian X, Wang L. Preparation and Characterization of Lignosulfonate–Acrylonitrile Copolymer as a Novel Carbon Fiber Precursor. *ACS Sustainable Chem. Eng.* **2016**, 4(1)**:** 159-168.

4. White RJ, Brun N, Budarin VL, Clark JH, Titirici M-M. Always Look on the "Light" Side of Life: Sustainable Carbon Aerogels. *ChemSusChem* **2014**, 7(3)**:** 670-689.

APPENDICES

Appendix A

SUPPLEMENTARY INFORMATION FOR HIGH-CHARGE CAPACITY POLYMER ELECTRODES COMPRISING ALKALI LIGNIN FROM THE KRAFT PROCESS

A.1 Effect of H_2SO_4 concentration on electrochemical performance

The influence of H_2SO_4 concentration on the electrochemical performance of the composite films is shown in **Figure A.1**. The films were prepared using a 10mL solution of 15.3M AA, 0.124g of AL, and 69µL of pyrrole monomer. After polymerization, the film was rinsed and tested in sulfuric acid (H_2SO_4) with concentrations: 1M, 0.5M, 0.1M, 0.01M, 0.001M, and 0.0001M. The film was left in the electrolyte solution for 5 min before testing. Cyclic voltammetry shows that high concentrations of H_2SO_4 lead to sharper redox peaks and decreased peak separation, as expected for a proton-dependent process (**Figure A.1a** and **A.1b**).

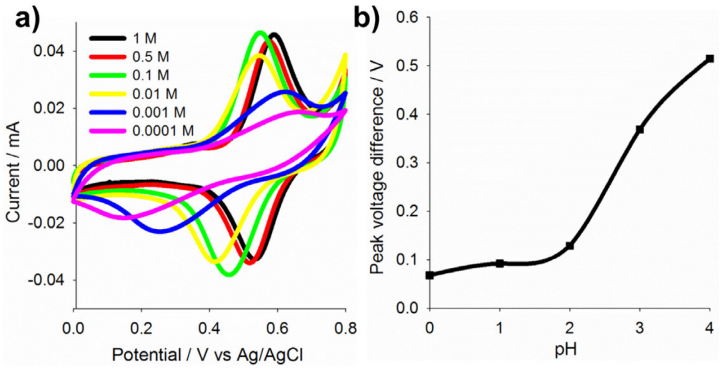

Figure A.1 (a) Cyclic voltammetry profiles for PPy/AL (prepared in 13.5 M AA) for different concentrations of H_2SO_4 testing solution. (b) Voltage difference between cathodic and anodic peaks on (a) *vs.* pH. Measurements were carried out in a 3-electrode cell on Pt working electrodes with Ag/AgCl as reference electrode and Pt mesh as counter electrode.

A.2 Electrochemical characteristics of electrodes prepared in 5M AA polymerization solution

AL/PPy exhibited peculiar behavior when electropolymerized from a 5M AA solution, each electrode type (pure PPy, SLS/PPy, and AL/PPy) was prepared in 5 M AA solutions and tested in 0.5 M H_2SO_4. **Figure A.2** shows that SLS/PPy exhibited the highest capacitance when prepared under these conditions, while AL, which has the highest capacitance at 15.3M AA, showed low capacitance and no redox peak. The standard PPy electrode had lower performance compared to films prepared in H_2SO_4, but was not very different from electrodes prepared in 15.3 M AA. These observations are attributed to the poor solubility of AL in AA at this molarity. SLS and Py showed similar solubility compared to the 15.3 M AA; however, very little AL dissolved under these conditions. The low electrochemical performance is likely due to some solid AL particles finding their way into the film. Currently, the phase behavior of the AL in AA is being investigated to understand this anomaly.

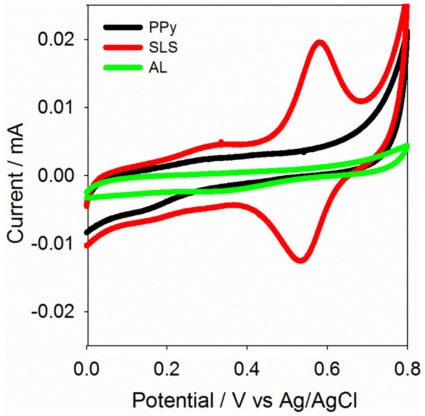

Figure A.2 Cyclic voltammetry profiles of PPy, PPy/SLS, and PPy/AL polymerized from 5 M AA solution. Measurements were carried out in a 3-electrode cell on Pt working electrodes with Ag/AgCl as the reference electrode and Pt as counter electrode.

A.3 Nyquist plots for single electrode and device

Nyquist plots from Electrochemical Impedance Spectroscopy are shown below in **Figure A.3** for single electrode measurements in 0.5 M H_2SO_4 (a) and devices with PPy-lignin cathodes and activated carbon (AC) anodes.

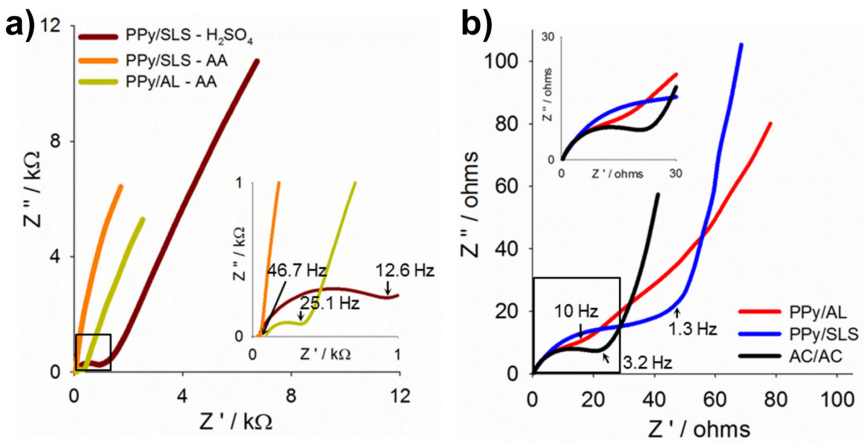

Figure A.3 (a) Nyquist plot of PPy-lignin composite electrodes in 0.5M H_2SO_4 obtained from 3-electrode measurements with Ag/AgCl reference and Pt counter electrodes. (b) Nyquist plot of 2-electrode cells with PPy-Lignin cathodes and AC anodes. Measurements were made using an applied potential of 0.7 V over a frequency range of 10k to 0.1 Hz using perturbation amplitude of 10mV.

A.4 Mass composition of PPy/Lignin films

Electrodes were assumed to be formed with PPy, H_2SO_4 (from polymerization or subsequent testing), acetic acid and either SLS or AL. The resulting film formula composition is of the form:

$$[(PPy)_{x=1}\ (C_2H_3O_2^-)_y\ (SO_4^{-2})_w]\ [Lignin]_z$$

Previous studies[1] have reported approximate "molecular formulas" for AL and SLS. These formulas were used as the lignin monomeric units for the calculations. The molecular formulas were modified to give the approximated sulfur content found in the specific lignin reactants (AL, SLS, and pH fractions 9.5 and 10.5) determined by ICP-AES (**Table 2.1**). The molecular formulas utilized in the calculations are presented on **Table A.1**.

Table A.1 Assumed monomeric units for the different constituents in PPy/Lignin films

Reactant	**Formula**[a]
Pyrrole	C_4H_3N
Acetic Acid	$C_2H_3O_2$
Sulfuric Acid	H_2SO_4
Sulfonated Lignin	$C_{10}H_{12}O_6S_{0.36}$
Alkali Lignin	$C_{10}H_{12}O_3S_{0.19}$
pH 9.5 fraction	$C_{10}H_{12}O_3S_{0.15}$
pH 10.5 fraction	$C_{10}H_{12}O_3S_{0.13}$

[a] Hydrogen was ignored in the calculations

The elemental composition (i.e. weight % of nitrogen, carbon, and oxygen) of the films was determined by EDX, and these values were used to calculate the composition of each species. Electrodes prepared from AA were assumed to have the same doping level (y= 0.61 for x =1), which was found for pure PPY synthesized in AA. Similarly, electrodes prepared from H_2SO_4 were assumed to have the same H_2SO_4 doping level (w=0.09 for x=1), as determined in the reference electrodes. Therefore, the parameters allowed to change during the fitting for the compositions are: (1) the lignin fraction, **z**

(for SLS or AL), and (2) sulfate content, **w** (HSO_4^-/SO_4^{-2}), except in the case of PPy/SLS in H_2SO_4, where w is fixed by the H_2SO_4 dopant level. Using the film formula given above and initial values for the fitting parameters, w and z, the weight % of each element was calculated. A weighted error between the "calculated weight %" and the "EDX weight %" was determined, and w and z were calculated by minimizing the error. A range of compositions is reported to reflex how much the composition can change and still achieve within 5% of the minimum error. Details of the calculations are shown below.

The elemental compositions were calculated by dividing the contribution of each element by the total AMU (Atomic Mass Unit) of the composite (**Eq. A.1-A.2**). (Example for PPy/SLS in AA)

$$\begin{aligned} N_{fxn} &= x \\ C_{fxn} &= 4x + 2y + 10z \\ O_{fxn} &= 2y + 6z + 4w \\ S_{fxn} &= 0.36z + 1w \end{aligned} \qquad A.1$$

$$AMU_T = N_{fxn}\ (AMU_N) + C_{fxn}\ (AMU_C) + O_{fxn}\ (AMU_O) + S_{fxn}\ (AMU_S) \qquad A.2$$

To compare with the EDX results, the wt. % of each element can be calculated using **Eq. A.3**.

$$N\ wt.\% = \frac{N_{fxn}\ (AMU_N)}{AMU_T} \ldots \qquad A.3$$

Equations **A.1-A.3** show the calculations for weight % of C, O, N, S in the electrodes based on the elemental composition of each species, and initial guesses for w and z. A spreadsheet was set to change the values of z and w (x is set to 1, y is determined by reference PPy electrodes) to minimize the error between the elemental analysis values (weight %) from EDX and the calculated values from **Eq. A.1-A.3**. The

range of compositions in **Table 2.1** reflects a variation of parameter analysis in which the error did not significantly change (< 5%). To minimize the influence of the most abundant elements (C, O) within the film, a weighted error was used (**Eq. A.4-A.5**):

$$\%\ individual\ eror = \frac{|EDX_{element} - Calculated|}{EDX_{element}}\ x\ 100 \qquad A.4$$

$$\%\ Weighted\ eror = \sum \frac{Individual\ errors}{EDX_{eac\,h\ element}} \qquad A.5$$

The contributions (wt. %) of each component in the composite film ($[(PPy)_x (C_2H_3O_2^-)_y (SO_4^{-2})_w]$ $[Lignin]_z$) were given by **Eq. A.6** and **A.7**, where MM is the molecular weight of each monomeric unit.

$$MM_{composite} = MM_{PPy}\ (x) + MM_{C2H3O2}\ (y) + MM_{Lignin}\ (z) + MM_{H2SO4}\ (w) \qquad A.6$$

$$wt.\%\ PPy = \frac{MM_{PPy}\ (x)}{MM\ composite}\ x\ 100\ \ldots \qquad A.7$$

A.5 Cycle life of PPy/Lignin electrodes and PPy/Lignin device

The cycle life of PPy/AL single Pt electrode films and PPy/AL-AC device are shown in **Figure A.3**. The single electrode was prepared on a Pt electrode at 20 μA for 3333s (ratio 1:1 wt.% PPy: AL). The PPy/AL for the device was prepared on stainless steel foil as explained in the experimental section (1.34 g L^{-1} AL). It was found that the ideal concentration of AL varies with the size of the electrode: higher area electrodes (0.5 cm^2) required lower concentrations of AL (1.34 g L^{-1}) in solution to obtain optimal hydroquinone/quinone redox behavior, whereas smaller area electrodes (0.02 cm^2) required a higher concentration of lignin (6.7 g L^{-1} AL) to obtain optimal HQ/Q redox behavior. **Figure A.4a** shows the cyclic voltammetry profiles of the device (PPy/AL-AC)

before and after 1700 charge /discharge cycles; HQ/Q groups get irreversibly oxidized, which causes a loss of the characteristic redox peak from AL. After 25 charge/discharge cycles the device starts losing its specific capacitance (**Figure A.4b**), although, the charge drop is slower when compared with the single electrode (Pt) (**Figure A.4c**) indicating that, even though the stability of mixed electrodes is low in solution, it is improved in a 2-electrode cell.

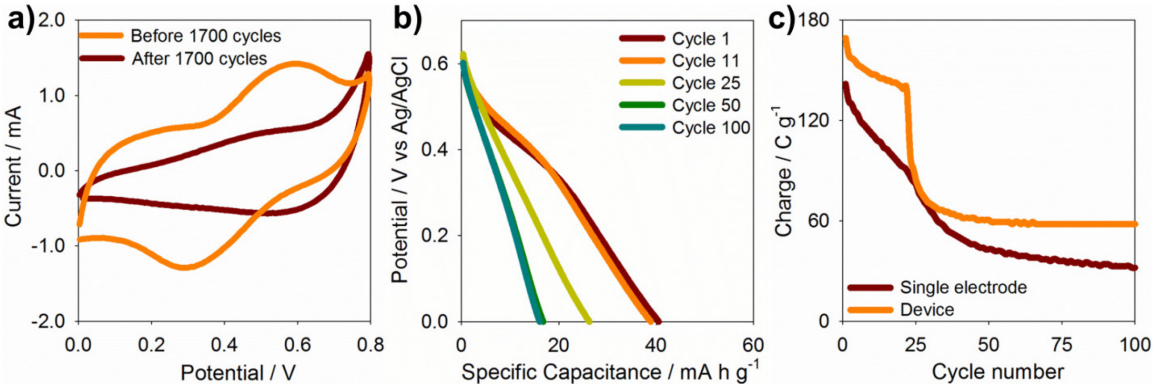

Figure A.4 Cycle life experiments for PPy/AL single electrodes and for asymmetric supercapacitors with PPy/AL and AC device.(a) Cyclic voltammetry profiles of PPy/AL - AC cell before and after 1700 charge/discharge cycles. (b) Discharge profiles for the cell in (a) at 0.46 mA for various cycles. (c) Cycle stability of PPy/AL single electrode and PPy/AL-AC device at 0.46mA.

A.6 Chemical synthesis of polypyrrole/lignin composite electrodes

Chemical synthesis of PPy/AL and PPy/SLS was carried out as described in Appendix D. After synthesizing the polymer composites, a slurry was prepared with N-Methyl-2-pyrrolidone (NMP) as solvent and polyvinylidene fluoride (PVDF) as a binder and conducting graphite to enhance the conductivity in a ratio of 80 wt.% active material,

10 wt.% binder, and 10 wt.% conducting graphite. The slurry was ultrasonicated (**Figure A.5a**) and deposited into a film using a doctor blade (**Figure A.5b**) on carbon/PET, ITO, stainless steel foil and aluminum foil. Once the film was dried, an asymmetric coin cell device with carbon electrode was prepared with 1M H_2SO_4 as electrolyte; the CV profiles for PPY/SLS – Carbon device are shown on **Figure A.5c**.

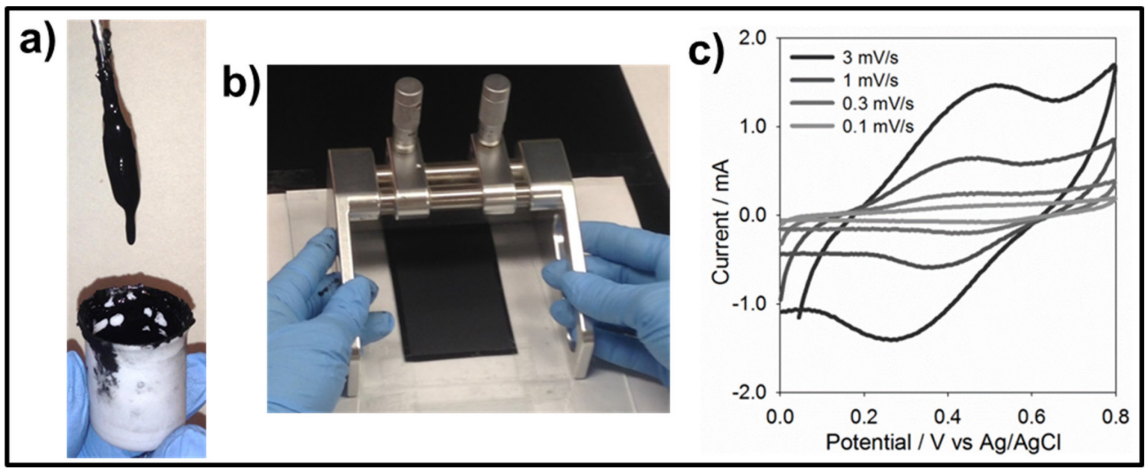

Figure A.5 (a) PPy/AL or PPy/SLS, conducting graphite, PVDF in NMP. (b) Doctor blade film preparation. (c) Cyclic voltammetry profiles for PPy/SLS – Carbon asymmetric device.

A.7 Reference

1. Holladay JE, White JF, Bozell JJ, Johnson D. Top Value-Added Chemicals from Biomass - Volume II—Results of Screening for Potential Candidates from Biorefinery Lignin. *Pacific Northwest National Laboratory, Richland, WA*. **2007**, PNNL-16983.

Appendix B

SUPPLEMENTARY INFORMATION FOR LIGNIN-COATED CARBON NANOMATERIALS FOR LOW-COST ELECTRICAL ENERGY STORAGE

B.1 Carbon materials

Vendor specifications for the various carbon materials used in the preparation of carbon-lignin films are shown in **Table B.1.** The specific surface area (m^2 g^{-1}) for C2 was calculated by estimating the average volume and surface area using the average particle size; approximating the average mass of each particle with the average volume and density value from the literature, finally calculating the specific surface area.

Table B.1 Carbon materials specifications

Carbon material	Short name[a]	Supplier	Catalog #	Particle Size [µm]	Spec. Surface Area [m^2 g^{-1}]
Carbon, glassy	C2	Sigma-Aldrich	484164	2-12	2.14 [b]
Carbon, mesoporous	C500	Sigma-Aldrich	702102	4-6[c]	>500
Carbon, nanopowder	C100	Sigma-Aldrich	633100	<0.1	>100
Carbon, mesoporous	MSP	Sigma-Aldrich	699624	< 0.5	50-100
High Surface Active Carbon for Supercapacitor Electrode	AC	MTI Corp	EQ-AB-520	5	2000
MesoCarbon MicroBeads	MCMB	MTI Corp	MTI EQ-LiB-MCMB	8-33	2.02

[a] Short name used in the paper. [b] Calculated value. [c] From SEMs.

B.2 BET measurements

BET measurements were taken for MSP, C100 and C500. According to the specifications from the supplier, C100 should have a surface area higher than 100 m^2 g^{-1}, however, when BET measurements were taken for this sample; it was found that the surface area is 11.4 m^2 g^{-1} with a pore volume of 0.025 cm^3 g^{-1} and pore size 18.4 Å (in radius). Explaining why the electrochemical activity does not fall within C500 and MSP performances. Experiments were performed twice, and same results were obtained. **Figure B.1** shows the differential pore volume distribution *vs.* pore radius for MSP, C500 and C100. MSP exhibits a surface area of 86.3 m^2 g^{-1} and a total pore volume of 0.19 cm^3 g^{-1} with the majority of the pores concentrated around 14.9 Å and 344.9 Å (in radius). C500 possess a surface area of 471.6 m^2 g^{-1} and a pore volume of 0.23 cm^3 g^{-1} with the majority of the pores concentrated around 20 Å and 179.3 Å (in radius).

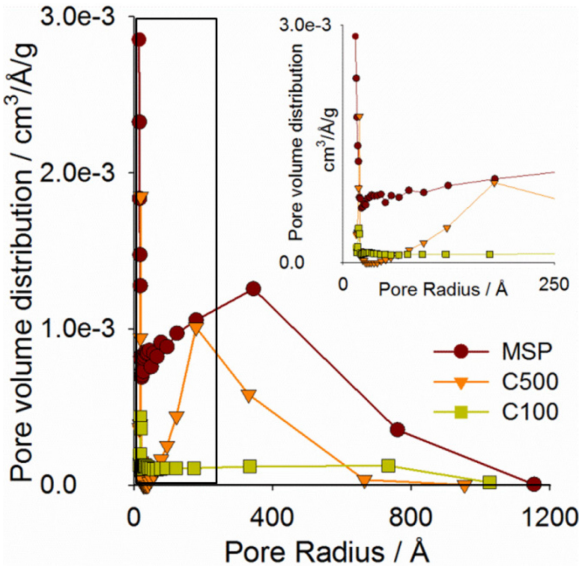

Figure B.1 Differential pore volume distribution for MSP, C500 and C100.

B.3 Film morphology:

Scanning electron microscopy (SEM) images for MSP/SLS, C500/SLS, AC/SLS, C100/SLS films prepared from dispersions in 0.5M H_2SO_4 are shown on **Figures B.2a**, **B.2b**, **B.2c**, and **B.2d**, respectively.

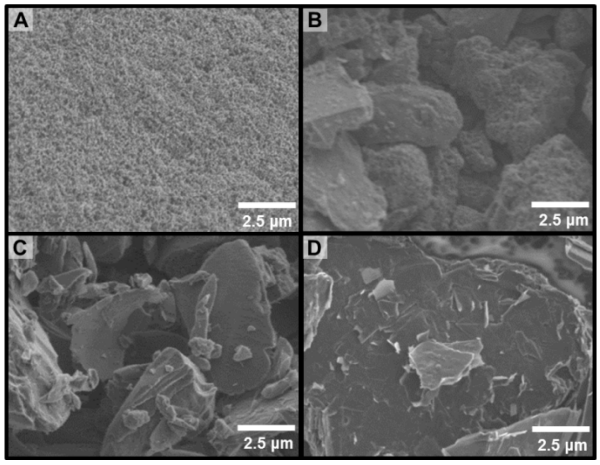

Figure B.2 Scanning electron microscopy images at x10k of (a) MSP/SLS, (b) C500/SLS, (c) AC/SLS, (d) C100/SLS in SA.

B.4 Weight % of sulfonated lignin (SLS) and alkali lignin (AL) in MSP films:

The approximate amount of lignin trapped within the MSP structure was calculated by selecting sections of the DTG curves and assigning them to either lignin or carbon contributions. Peaks below 100°C were considered moisture. Peaks within 100 and ~520°C were considered lignin contribution while peaks within ~520 to 800°C were considered carbon contribution. A peak fitting software (PeakFit) was used to deconvolute the different peaks that gave rise to the DTG curves, assigning each of these peaks to either lignin or carbon. The area under the curve of each peak was calculated to

give the mass contribution of each of the species in the mixture. The final results are shown in **Table B.2**.

Table B.2 Mass composition of SLS and AL in the different samples

Sample	Peak fitting	
	Mass (mg)	**wt.%**
Standard	0.55	16.7
MSP-CG-SLS in SA	0.53	12.5
MSP-CG-SLS in AA	0.32	7.68
MSP-CG-AL in AA	0.46	14.9

Appendix C

SUPPLEMENTARY INFORMATION FOR SCALABLE, TEMPLATE-FREE SYNTHESIS OF CONDUCTING POLYMER MICROTUBES

C.1 Mesh specifications

Table C.1 shows the stainless steel substrates specifications: opening size, wire diameter, specific surface area and open area. Specific surface area is the ratio of actual surface area to planar (substrate) surface area. Open area is calculated considering a planar substrate and is the ratio of the planar area with no wires to the planar substrate area.

Table C.1 Stainless steel mesh substrates specifications

Mesh	Opening Size [mm]	Wire Diameter [mm]	Sp. Surface Area	Open Area [%]
M40	0.38	0.25	2.5	36
M60	0.23	0.19	2.9	29
M100	0.15	0.11	2.8	36
M200	0.074	0.053	2.6	34
M250	0.061	0.041	2.5	36
M325	0.043	0.036	2.9	31
M400	0.038	0.025	2.5	36

C.2 Influence of the polymerization current

Figure C.1 shows the electrochemical characteristics and comparison between the microtubes deposited at different current densities. **Figure C.1a** shows the time evolution in potential during electrode synthesis profile. Each electrode is deposited for the same total charge on a 1 cm^2 substrate (Q [mC] = j [mA cm^{-2}] * t [s]). **Figure C.1b** shows the

cyclic voltammetry profiles indicating no significate difference between the capacitance *vs.* potential plots, although the deposition at 10mA does present slight higher capacitance. **Figure C.1c** EIS of the different films are presented, the series resistance of the films increases as the current density increase. The low-frequency ends of the kinetic control part of the Nyquist plot are 39.81, 79.43, 31.62, 25,12 Hz for 10, 12, 14, 16 mA respectively.

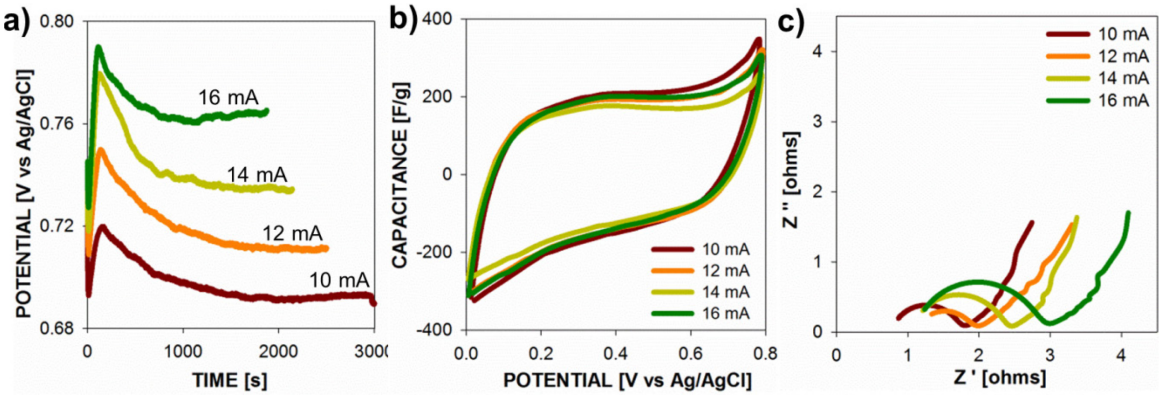

Figure C.1 Electrochemical properties of polypyrrole microtubes deposited by chronopotentiometry on M200 for 30 C cm^{-2} at different current densities (10, 12, 14, 16 mA cm^{-2}). (a) Deposition profiles, (b) Change in specific capacitances at 10 mV s^{-1}, (c) Nyquist Plot.

The **Table C.2** shows the properties of polypyrrole microtubes deposited with increasing current; the thickness of the film increases with the decrease in current. In general, the properties of the microtubes are very similar one to the other as the current increases. Other experiments showed that by increasing the concentration of the monomer from 0.09M to 0.2M, thicker meshes can be obtained.

Table C.2 Properties of polypyrrole microtubes deposited with increasing current*

Sample	Film Thickness [µm]	Height [µm]	Top diameter [µm]	Middle diameter [µm]	Bottom diameter [µm]	Ratio [D_T to D_M]
M200 12mA	14	800	280	290	230	1.6
M200 14mA	12	840	240	230	180	1.7
M200 16mA	11	910	260	260	220	1.4

* Deposition conditions 30C cm^{-2}

Microtubes were also observed when deposited with a ramp chronoamperometry, increase of the current every set time (0.025mA every 13s). Smaller microtubes and smoother surface were obtained in presence of poly(4-styrene sulfonic) acid, as dopant. The polymer disrupts the natural molecular packing of the polypyrrole leading to a smoother surface (**Figure C.2**).

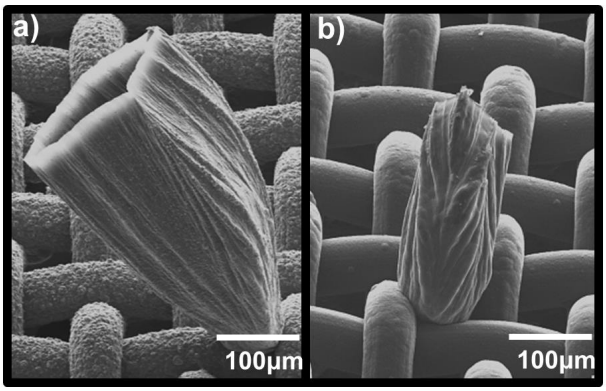

Figure C.2 Polypyrrole microtubes deposited with galvanodynamic deposition from 10 to 12 mA cm^{-2} for 13.3 C cm^{-2} with different dopants. (a) 0.5M H_2SO_4, (b) 3.3 wt. % PSSA.

C.3 Bubble method

The **Figure C.3** shows the SEM image of one of the samples deposited using the so-called bubble method from the literature.[1-6] It is observed that ball-like structures are obtained. However, this is not the same kind of structures achieved with the method presented in this work.

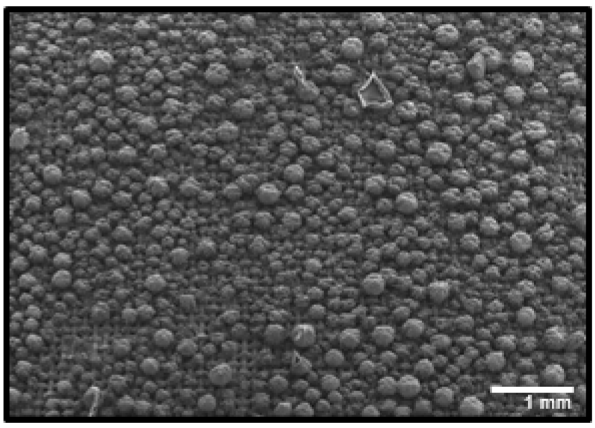

Figure C.3 Bubble method, M200 with 1 cyclic voltammetry cycle from -0.3V to -0.8V at 0.1 V s^{-1} followed by chronopotentiometry at 16mA for 60C.

C.4 Detailed procedure for the synthesis of polypyrrole microtubes

C.4.1 Good practices

- ✓ For the microtubes growth, it is fundamental to be clean and precise when preparing the solutions.
- ✓ Make sure all the containers to be used are properly cleaned!. Use recently distilled pyrrole monomer, avoid to use yellow/brownish monomer.
- ✓ Prepare your own solutions, avoid using solutions that somebody else prepared.

- ✓ Add the monomer right before running the experiments; avoid the use of solutions Py+electrolyte from the day before. Sulfuric acid solutions are fine for long periods of time.

C.4.2 Substrate preparation

- ✓ Cut M200 1.2x1.4 cm and a neck of 0.4x1.3cm

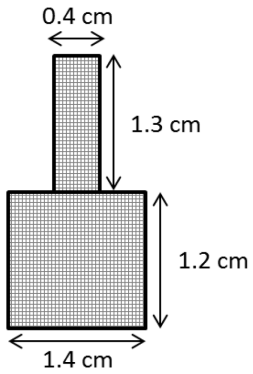

- ✓ Sonicate for 10 min in ethanol, dry the sample with the N_2 gun.
- ✓ Weigh the sample.
- ✓ Treat the sample in UV Ozone for 15 min each side. (30 min total)
- ✓ Cut parafilm (wax paper) with the following specifications (use a sharp blade to make an accurate cut, avoid cutting the edges more than they should)

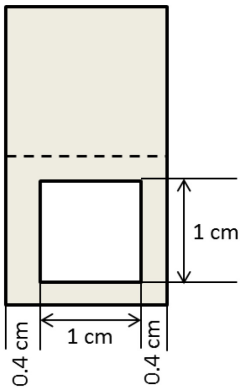

- ✓ Cover the mesh with the parafilm in the following way

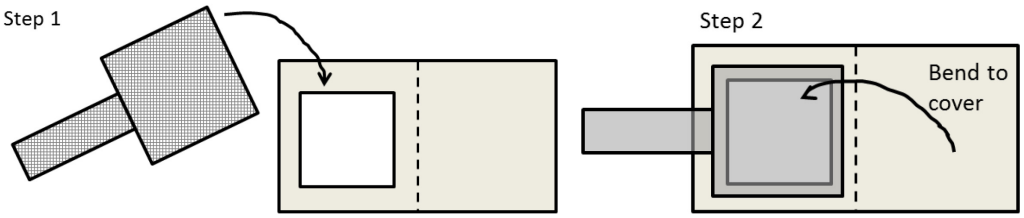

- ✓ To make sure the parafilm is well attached to the substrate, rub the surface by placing a piece of paper (can be the same parafilm protecting paper) over the parafilm and rub with the back of the tweezer, pay special care to the internal edges. *Note*: It has to be paper not kimwipe, otherwise it will stick to the parafilm.

C.4.3 Experiment set up

- ✓ The platinum mesh used as counter electrode (CE), make sure to clean it first with DI water; then acetone, allow the acetone to evaporate; finally, carefully burn the mesh with the torch. **This step is essential.** Pt catalyzes the production of H_2. Therefore, the surface of this mesh has to be clean in other to be able to use the entire surface available.
- ✓ Take the vial with the 10 ml of electrolyte and degassed with N_2 for 10 min. Add the monomer and mixed it for 1 min with the vortex mixer.
- ✓ Take the working electrode (WE) (M200/M400) with one alligator clip. Use the black cap to hang the electrode. Place the CE in the 10 mL beaker. Hang the reference electrode. Connect all the electrodes to their corresponding wire. *Note*: one way to check if there is a good connection between the alligator clip and the

mesh is using the multimeter, one end on the mesh the other one on the alligator wire, resistance should not be higher than ~2Ω.

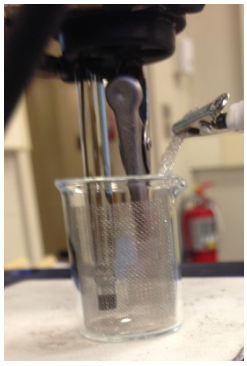

- ✓ Add ~6 extractions of the Py+Electrolyte solution utilizing a disposable Pasteur pipette (~6-7 mL). Make sure the substrate is complete cover as shown in the picture. *Note*: the alligator clip should not be soaked with the electrolyte, it will corrode.

- ✓ Check all connections.
- ✓ Run chronopotentiometry at 10mA for 30C (will take about 50min) make sure the temperature remains constant during the whole experiment.

- ✓ Once done, disconnect everything starting with the WE, RE should be the last one in being disconnected.
- ✓ Wash all the electrodes and beaker with DI water.

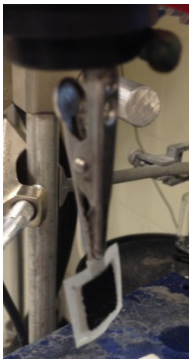

- ✓ Reconnect everything together, this time, add 6 extractions of electrolyte (0.5M H_2SO_4) only (~6-7 mL), to run the characterization experiments which will be: cyclic voltammetry from 0-0.8V at 300, 100, 30, 10, 3 mV s^{-1}; EIS at 0.7 V; and CD set to discharge for 60s.

C.5 References

1. Bajpai V, He P, Dai L. Conducting-Polymer Microcontainers: Controlled Syntheses and Potential Applications. *Adv. Funct. Mater.* **2004**, 14(2)**:** 145-151.

2. Bajpai V, He P, Goettler L, Dong JH, Dai L. Controlled syntheses of conducting polymer micro- and nano-structures for potential applications. *Synth. Met.* **2006**, 156(5–6)**:** 466-469.

3. Qu L, Shi G. Hollow microstructures of polypyrrole doped by poly(styrene sulfonic acid). *J. Polym. Sci., Part A: Polym. Chem.* **2004**, 42(13)**:** 3170-3177.

4. Qu L, Shi G, Chen Fe, Zhang J. Electrochemical Growth of Polypyrrole Microcontainers. *Macromolecules* **2003**, 36(4)**:** 1063-1067.

5. Qu L, Shi G, Yuan J, Han G, Chen Fe. Preparation of polypyrrole microstructures by direct electrochemical oxidation of pyrrole in an aqueous solution of camphorsulfonic acid. *J. Electroanal. Chem.* **2004**, 561(0)**:** 149-156.

6. Yuan J, Qu L, Zhang D, Shi G. Linear arrangements of polypyrrole microcontainers. *Chem. Commun.* **2004**(8)**:** 994-995.

Appendix D

CHEMICAL SYNTHESIS OF POLYPYRROLE AND POLY(3,4-ETHYLENEDIOXYTHIOPHENE)

D.1 Polypyrrole

Chemical synthesis of polypyrrole (PPy) was performed following the synthesis procedure explained by S. Machida and S. Miyata,[1] which is the method we have commonly used to prepare PPy. The yield is between 30 - 50%. To produce more the quantities can be scaled up by maintaining the ratios.

Materials	Reactants	Conditions
- 2 neck 100 mL Round Flask - "x" stir bar - Rubber cap - Round flask wooden ring - Syringe - Hotplate - Ice bath - Thermometer - No. 4 Whatman paper filter - Ceramic Funnel	- Pyrrole monomer - Iron Chloride (III) ($FeCl_3$) - Methanol (CH_3OH) - DI water	- 4°C - Schlenk line (N_2) - Total reaction time 48 hr

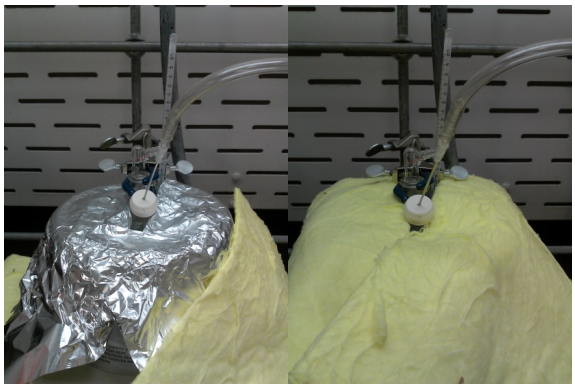

Figure D.1 Chemical polymerization of PPy basic set-up

D.1.1 Procedure

A. The ratios of each of the components in the polymerization are 1:2.33 Py to $FeCl_3$ in a 2.5M solution of $FeCl_3$ in CH_3OH.

B. Vacuum out a 100 mL 1 neck flask by connecting to the Schleck line using a syringe and a rubber cap. Add nitrogen to the flask. Make sure to add the "X" stir bar before sealing the flask. This step is just to make sure the flask is dry.

C. Add the CH_3OH (using a syringe) and bubble with N_2 to remove the excess of O_2 (15min), use a long syringe to reach the liquid while leaving a small syringe on the rubber cap as a vent. Set-up the ice bath and place the thermometer inside to control the temperature. Wait for CH_3OH to get to 4^0C.

D. Make a funnel with the weighing paper to add the $FeCl_3$ to the flask. Wait until all of it is dissolved in CH_3OH. Stir at 700rpm.

E. Add the Py monomer, dropwise using a syringe.

F. Let the reaction run for 6h.

G. Rotovap most of the CH_3OH from the solution.

H. Add DI-water and filter the product using a Whatman No. 4 paper filter.

I. Collect the polymer from the paper filter, place it in a beaker and wash it again with CH_3OH and filter.

J. Repeat procedures H and I as many times as necessary, until the solution is clear. Usually, it takes around 2 times with DI water and 1 last time with CH_3OH.

K. Dry for 24h under vacuum at 80^0C.

D.1.2 Alternative procedure

Some of the problems that might be encountered with the previous procedure are: (1) PPy does not precipitate out of solution or (2) the yield of the reaction is low. Therefore, an alternative procedure we have followed is keeping the same ratios and reactions but modifying the polymerization conditions as follows:

A. The ratios of each of the components in the polymerization are 1:2.33 Py to $FeCl_3$ in a 2.5M solution of $FeCl_3$ in CH_3OH.

B. Vacuum out a 200 mL 1 neck flask, put two syringes one as vent and the other one for the Schleck line connection. Add nitrogen to the flask. Make sure to add the "X" stir bar before sealing the flask.

C. Add the CH_3OH and bubble with N_2 to remove the excess of O_2. Leave the syringe on the rubber cap to allow the air to get out. Set-up the ice bath and place the thermometer inside to control the temperature. Wait for CH_3OH to get to ~4^0C.

D. Make a funnel with the weighing paper to add the $FeCl_3$ to the flask. Wait until all of it is dissolved in CH_3OH.

E. Add the Py monomer, dropwise using a syringe.

F. Let the reaction run for 8h in the ice bath, keeping it at ~4^0C.

G. Take the round flask out of the ice bath and let the reaction run for 40h at room temperature.

H. Rotovap most of the CH_3OH from the solution.

I. Once most of the CH_3OH is gone, add about 100 mL of ice water. This will help to precipitate polypyrrole; especially, when a dopant such as p-Toluenesulfonic acid is added because it improves the solubility of polypyrrole making the extraction more difficult.

J. If after 1h it does not seem like the polymer is precipitating, stir at 60rpm for 1 day.

K. Filter the product using the Whatman No. 4 paper filter.

L. Collect the polymer from the paper filter, place it in a beaker and wash it again with CH_3OH and filter.

M. Repeat procedures H and I as many times as necessary, until the filtrated solution is clear. Usually, it takes around 2 times with DI water and 1 last time with CH_3OH.

N. Dry for 24h under vacuum at 80^0C.

D.1.3 Polypyrrole synthesized with different dopants

Various dopants have been used to synthesize polypyrrole **Table D.1** shows a summary of the reactants ratios (by wt.%). Notice that sulfonated lignin and alkali lignin were also used as dopants with solutions prepared in acetic acid.

Table D.1 Summary of ratios used for the synthesis of polypyrrole

Polymer	**Pyrrole**	**Oxidant ($FeCl_3$)**	**Dopant**	**Solvent**	**Time**
PPy	1	2.33	-	1.1 M of Py in CH_3OH	4.5h
PPy:PSSA	1	2.33	10 mL (1.2 times the amount of pyrrole)	1.5 M of Py in CH_3OH (25mL)	4.5h
PPy:PTSA	1	2.33	0.3	2 M of Py in CH_3OH	48h
PPy in Acetic acid	1	2.33	-	1.1M of Py in a 15.3M Acetic acid solution in water	5h
PPy: SLS	1	2.33	0.5	1.1M of Py in a 15.3M Acetic acid solution in water	5h
PPy:AL	1	2.33	0.5	1.1M of Py in a 15.3M Acetic acid solution in water	5h

D.2 Poly(3,4 Ethylenedioxythiophene) (PEDOT)

PEDOT chemical polymerization procedure is based on the work of P.G. Pickup.[2, 3] The yield is between 80 - 90%. To produce more the quantities can be scaled up by maintaining the ratios.

Materials	Reactants	Conditions
- 100 mL Round Flask - "x" stir bar - Rubber cap - Round flask wooden ring - Syringe - Hotplate - No. 4 Whatman paper filter - Ceramic Funnel	- 3,4-Ethylenedioxythiophene - NaPSS (Sodium Poly(4-Styrene sulfonate)) - $Fe(NO_3)_3$ (Iron II nitrate) - DI water	- Room temperature

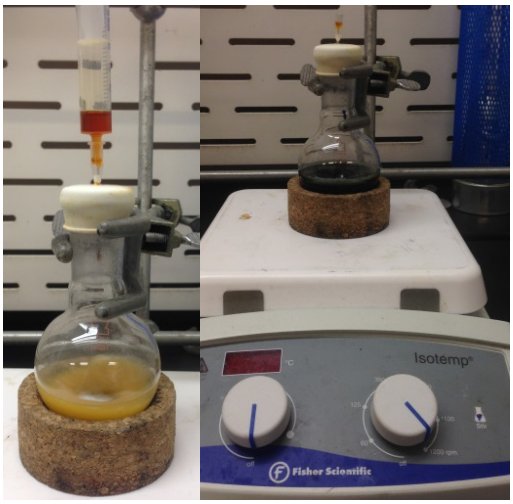

Figure D.2 Chemical polymerization of PEDOT basic set-up

D.2.1 Procedure

A. Pour 15 mL of 0.1M NaPSS in the Round flask, stir this solution until all the NaPSS is dissolved (suggested 1200 rpm).

B. Add 0.8 mL of EDOT to the solution in A. Ultrasonicate the mixture for 10 min and stir for 30 min (suggested 1200 rpm). The solution should be white. Cover the round flask with a rubber cap.

C. Meanwhile, weigh 15.3g of $Fe(NO_3)_3$. Slowly allow to dissolve in 5-7 mL of water (takes about 30 min to dissolve the whole amount). When everything is dissolved, take a syringe and add dropwise the $Fe(NO_3)_3$ to the AB solution while is stirring (suggested 1200 rpm).

D. Let the reaction go for about 6h.

E. Filtrate the product with DI water using a No.4 Whatman paper filter.

F. Collect all the powder and dissolve it in DI water to perform the second filtration, this time with CH_3OH.

G. Collect the PEDOT in a vial; get rid of the excess of solvent utilizing the rotovap for 1 or 2h. Then, place it in the vacuum oven overnight at not more than 80ºC.

D.2.2 Alternative procedure

This method uses a combination of aqueous and organic solvent to dissolve EDOT.[2]

Materials	Reactants	Conditions
- 100 mL Round Flask - "x" stir bar - Rubber cap - Round flask wooden ring - Syringe - Hotplate - No. 4 Whatman paper filter - Ceramic Funnel	- 3,4-Ethylenedioxythiophene - Acetonitrile (ACN) - NaPSS (Sodium Poly(4-Styrene sulfonate)) - $Fe(NO_3)_3$ (Iron II nitrate) - DI water	- Room temperature

A. Prepare a 0.15M EDOT / ACN solution, stir until EDOT is dissolved in the solution.

B. Prepare a 0.15M NaPSS / DI water solution, stir for 20 min until NaPSS is dissolve.

C. Mix solutions A and B in the round flask. Cover the flask with the rubber cap and stir.

D. Dissolve a 10:1 ratio of $Fe(NO_3)_3$ to EDOT in 5 to 7 mL of water. This might take several minutes. When everything is dissolved, take a syringe and add dropwise the $Fe(NO_3)_3$ to the AB solution while is stirring (suggested 1200 rpm).

E. Allow the reaction to run for 2 days.

F. Filtrate the product with DI water using a No.4 Whatman paper filter.

G. Collect all the powder and dissolve it in DI water to perform the second filtration, this time, use CH_3OH to wash the powder.

H. Collect the PEDOT in a vial; get rid of the excess of solvent utilizing the rotovap for 1 or 2h. Then, place it in the vacuum oven overnight at not more than 80ºC.

D.3 References

1. Machida S, Miyata S, Techagumpuch A. Chemical synthesis of highly electrically conductive polypyrrole. *Synth. Met.* **1989**, 31(3)**:** 311-318.

2. Lefebvre M, Qi Z, Rana D, Pickup PG. Chemical Synthesis, Characterization, and Electrochemical Studies of Poly(3,4-ethylenedioxythiophene)/Poly(styrene-4-sulfonate) Composites. *Chem. Mater.* **1999**, 11(2)**:** 262-268.

3. Qi Z, G. Pickup P. High performance conducting polymer supported oxygen reduction catalysts. *Chem. Commun.* **1998**(21)**:** 2299-2300.

Appendix E

N-BOC PYRROLE

E.1 Literature review

The BOC group can be removed from Pyrrole by thermal removal, mild acidic or basic treatment. In the literature, there have been several approaches taken for the removal of this group:

1. By thermal heating at 185^{0}C for 30 min under N_2 and dried under vacuum for 1h @ 150^{0}C.[1]

   According to the TGA made (**Figure E.1**) of the chemically synthesize samples of N-BOC-PPy + PTSA.M + $FeCl_3$ and PPy + PTSA.M + $FeCl_3$, (air, 10^{0}C/min, from 0 to 100^{0}C) synthesized according to the procedure on following sections, the BOC group completely gets removed between ~150-180^{0}C; it seems that most of it goes away after 150ºC. Therefore, this temperature as the maximum temperature to remove the group.

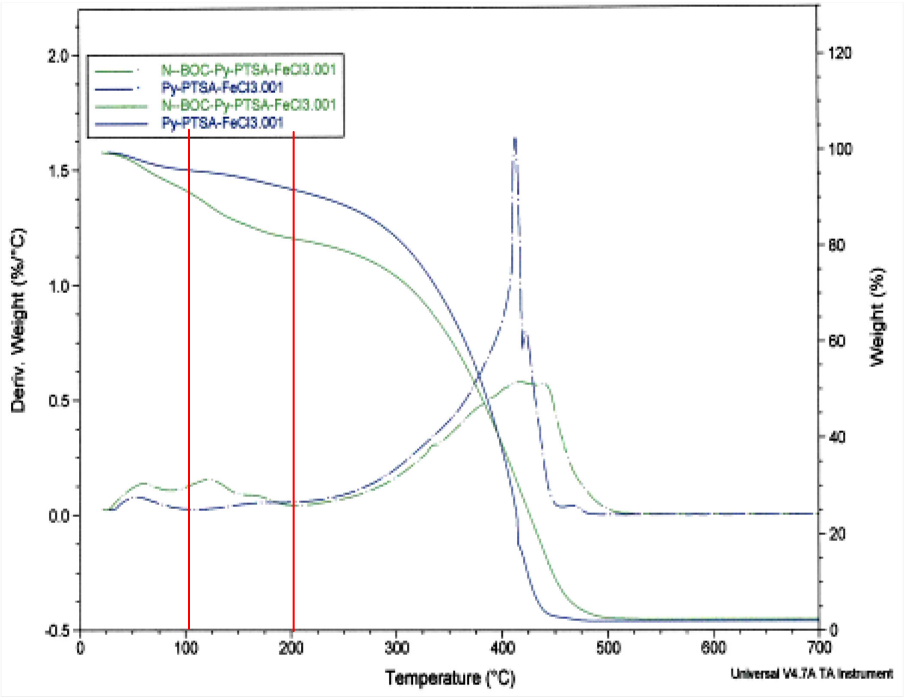

Figure E.1 TGA of chemically synthesize polypyrrole and N-BOC pyrrole.

2. Aqueous phosphoric acid (85%wt.) added to an organic solvent (THF, acetonitrile, toluene, methylene chloride), stirred a room temperature for 4 to 8h. A ratio of 1mL of solvent per 1g of material and 15 equivalents of 85%wt. of phosphoric acid solution. A 50% wt. solution of NaOH was added to keep pH between 7-8. More details in ref. [2]
3. 1mmol of material in 10 mL of water at 100ºC for times between 5-12 min under argon,[3] and under nitrogen between 10 min to 13h reactions.[4] Previous to this work, there was another one showing the use of water at 150ºC under subcritical conditions.[5] All these references show different aromatic and aliphatic molecules

protected by the N-BOC group, they do not show exactly pyrrole, but they show similar type molecules.

4. Deprotection in basic media with sodium methoxide in a mixture of methanol and THF.[6]

E.2 Experiments

So far, we have done experiments with chemical and electrochemical polymerization of N-BOC-pyrrole and compared with same process for just pyrrole, we have only tried to remove the group by thermal treatment: Electrochemical synthesis of N-BOC-Pyrrole: Stainless steel mesh 200x200 with 20 mL propylene carbonate (PC) and 0.1M $LiClO_4$; 20 mL Acetonitrile (MeCN) and 0.1M $LiClO_4$ both with a concentration of N-BOC-PY monomer of 0.1M. Depositions with chronoamperometry at 2.01 V for 1.6C (about 1000s). The CV profiles showed a very poor performance. These samples were heated up to 120^0C overnight. The film tested after heating show poorer CV profiles than before heating.

Improvements: N-BOC-Pyrrole MW= 167.21g/mol, Pyrrole MW= 67.09 g/mol. N-BOC-PY weighs about 2.5 times than Pyrrole. Try with a concentration of 0.25M N-BOC-PY monomer to perform the polymerizations. Since the high voltage needed to polymerize it might be due to the low concentration of monomer in the solutions which takes more voltage applied to polymerize on the substrates.

Run all the experiments in PC which seems to work better than acetonitrile, according to previous results. Clean the film with Ethyl acetate to remove the PC, dried

and heat films up to 150^0C for 30 min, and test. If not change is seen, heat for 1 more hour and test. The test can be performed in PC+0.1M $LiClO_4$.

E.2.1 Chemical synthesis of N-BOC-Pyrrole:

Reactant	MW [g mol^{-1}]	Ratio	Moles	Weight [g]	mL
Pyrrole	67.09	1	0.0149	1	1.034
Iron Chloride III ($FeCl_3$)	162.21	2.3	0.0343	5.564	
Para-Toluenefulfonic acid monohydrate (P-TSA.M)	190.22	0.3	0.00447	0.8506	
Methanol (MeOH)					74.52
N-BOC Pyrrole	167.21	1	0.0149	2.491	2.491
Iron Chloride III ($FeCl_3$)	162.21	2.3	0.0343	5.564	
Para-Toluenefulfonic acid monohydrate (P-TSA.M)	190.22	0.3	0.00447	0.8506	
Methanol (MeOH)					74.52

Materials needed: 1 neck round flask, stir bar, and ice bath.

- Keep polymers in ice bath over 8h and then remove the ice bath and let the reaction go for 40h.
- Once the reaction is done, rotovap most of the MeOH.
- Add 100 mL of ice water, stir (60rpm) overnight to take the polymer out of solution.
- Once is out of solution, filter 2 times with water; 1 time with MeOH and 1 more time with Acetone.
- Dry in vacuum oven at room temperature.

After synthesis, electrodes were prepared with a solution of 5:1 sodium dodecyl sulfate (SDS) to polypyrrole or N-BOC-polypyrrole in water. Sonicated for 10 min the mixture SDS + DI Water, then added polymer, sonicated for 30 min. Deposited 1-2 mL on polyamide filter. Tested one sample without heating and one after heating 120^0C overnight. With this procedure, a reduction in the performance of N-BOC-polypyrrole and polypyrrole after heating was observed.

Improvements: Prepare a mixture of 80% polypyrrole or N-BOC-polypyrrole, 10% conducting graphite (CG) and 10% PVDF in NMP. Allow PVDF to dissolve in NMP at 80^0C for 1h stirring. Finely grain PPy or N-BOC-PY with CG and added to the solution, sonicate all the mixture for 20 min (5 min on – 30s off setup). The NMP will be a hard solvent to remove. The films could also be made with DI water instead of NMP and CMC instead of PVDF. Dissolve the CMC in water for 2h without heating but stirring.

Take one of the 1mL syringe and deposit 0.5mL using a paper filter No. 4 on the base, a GF/F filter over it, placing the white cell o-ring over it. Slowly deposit the mixture over it. Make 5 samples one to be tested at the same moment in the white cell, two other to be heated at 150^0C for 30 min-1h, test one and save the other one for weight and the rest for weight calculations, dry in the vacuum oven. (be careful, the objective is to dry the samples but not remove the BOC group from them, therefore, heat for longer time 72h at around 60-70^0C under vacuum).

E.2.2 Experiments suggested

Besides the experiments suggested above to improve the thermal treatment of the sample for the removal of the N-BOC group, we will like to try the acid/base methods. It is suggested to do this experiments first with the chemically synthesize polypyrrole and N-BOC-Polypyrrole and then try with the electrochemically synthesize films on M200 for thin films 1-2C.

Base on ref.[3-5] boil 10 mL of DI water, add 1mmol of material and stir for 10min, filter this material and prepare the slurry above described to tested over the GF/F, test and compare with the performance of the material that has not been treated. (FT-IR might be needed to determine whether the BOC group was removed or not and compared with standard spectra of polypyrrole). If no differences are observed, run the same experiment for 1h.

Base on ref.[2] prepare a solution of 85%wt. phosphoric acid in water, mix with THF in the proportions described in the reference, add the solution of 50%wt. NaOH and let the reaction go for 4h, stirring at room temperature. Wash and dry the polymer and prepared the slurry as described above. Test and compare with the original material. (FT-IR might be needed to determine whether the BOC group was removed or not and compared with standard spectra of polypyrrole).

E.3 Future work

To control de porosity and density of the polymer film by removal of other types of polymer, could be a polymer that can be removed by thermal treatment, or by UV

radiation, added during the conducting polymer polymerization and then after the film is made remove it, leaving a porous structure. Literature review on this matter needs to be done to find the suitable polymers. The composite film will be done by chemical or electrochemical synthesis. The polymer can also be added to CNT to make bunky paper.

E.4 References

1. Yamamoto T, Yoshizawa M, Mahmut A, Abe M, Kuroda S-i, Imase T*, et al.* Preparation of new π-conjugated polypyrroles by organometallic polycondensations. Synthesis of N-BOC (t-butoxycarbonyl) and N-phenylethynyl polymers, thermal deprotection of the BOC Group, and packing structure of the N-phenylethynyl polymer. *J. Polym. Sci., Part A: Polym. Chem.* **2005**, 43(24)**:** 6223-6232.

2. Li B, Bemish R, Buzon RA, Chiu CKF, Colgan ST, Kissel W*, et al.* Aqueous phosphoric acid as a mild reagent for deprotection of the t-butoxycarbonyl group. *Tetrahedron Lett.* **2003**, 44(44)**:** 8113-8115.

3. Zinelaabidine C, Souad O, Zoubir J, Malika B, Nour-Eddine A. A Simple and Efficient Green Method for the Deprotection of N-Boc in Various Structurally Diverse Amines under Water-mediated Catalyst-free Conditions. *International Journal of Chemistry* **2012**, 4(3).

4. Wang J, Liang Y-L, Qu J. Boiling water-catalyzed neutral and selective N-Boc deprotection. *Chem. Commun.* **2009**(34)**:** 5144-5146.

5. Wang G, Li C, Li J, Jia X. Catalyst-free water-mediated N-Boc deprotection. *Tetrahedron Lett.* **2009**, 50(13)**:** 1438-1440.

6. Jolicoeur B, Chapman EE, Thompson A, Lubell WD. Pyrrole protection. *Tetrahedron* **2006**, 62(50)**:** 11531-11563.